PHOTOPHYSICAL AND STABILITY STUDIES OF NON-FULLERENE ACCEPTOR BASED ORGANIC SOLAR CELLS

Ag

Ag

Ag

MoO$_3$

BHJ Active Layer

ZnO

ITO

$$PCE = \frac{V_{oc}\ J_{sc}\ FF}{P_{in}}$$

Absorption

Wavelength (nm)

ABDUL AZEEZ

DOCTORAL THESIS
2022

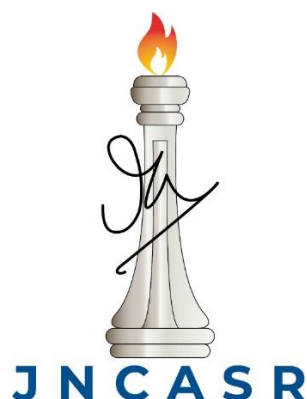# Photophysical and Stability Studies of Non-Fullerene Acceptor Based Organic Solar Cells

A thesis submitted in partial fulfilment for the degree of

Doctor of Philosophy

by

Abdul Azeez

Chemistry and Physics of Materials Unit

School of Advanced Materials

Jawaharlal Nehru Centre for Advanced Scientific Research

(A Deemed University)

Bangalore – 560064

INDIA

July 2022

Declaration

I hereby declare that the matter embodied in the thesis entitled "Photophysical and Stability Studies of Non-Fullerene Acceptor Based Organic Solar Cells" is the result of investigations carried out by me at the Molecular Electronics Laboratory in Chemistry and Physics of Materials Unit, Jawaharlal Nehru Centre for Advanced Scientific Research, Bangalore, India under the supervision of Prof. K. S. Narayan and it has not been submitted elsewhere for the award of any degree or diploma.

In keeping with the general practice in reporting scientific observations, due acknowledgement has been made whenever the work described is based on the findings of other investigators.

(Abdul Azeez)

JAWAHARLAL NEHRU CENTRE FOR ADVANCED SCIENTIFIC RESEARCH

Jakkur, Bangalore 560064, India

K. S. NARAYAN

Professor

PHONE: 91 80 22082822

FAX: 91 80 22082766

e-mail: narayan@jncasr.ac.in

URL: www.jncasr.ac.in/narayan

July 25, 2022

Certificate

I hereby certify that the matter embodied in this thesis entitled **"Photophysical and Stability Studies of Non-Fullerene Acceptor Based Organic Solar Cells"** is the result of the work carried out by Mr. Abdul Azeez at the Molecular Electronics Laboratory in Chemistry and Physics of Materials Unit, Jawaharlal Nehru Centre for Advanced Scientific Research, Bangalore, India, under my supervision and it has not been submitted for the award of any degree or diploma or associateship of any other university or institute.

Prof. K. S. Narayan

(Research Supervisor)

I

This thesis is dedicated to my beloved parents and teachers

III

Acknowledgements

Synopsis

Renewable energy sources are prerequisites to achieving sustainable development goals and net zero-emission. In the context of photovoltaics, conventional silicon solar panels dominated the landscape, with organic and hybrid technologies gaining momentum due to their versatile characteristics of facile-processing, semi-transparency and flexibility. Recent breakthroughs in the design and development of novel non-fullerene molecular acceptors (NFAs), starting from the ITIC in 2015, ushered a new era in bulk-heterojunction (BHJ) photovoltaic research with power conversion efficiencies now approaching 19% for single-junction BHJ organic solar cells (OSCs). The added features of a thicker active layer and higher stability estimates of non-fullerene BHJs as compared to fullerene-based BHJs offer a viable and potential commercial technology in the near future. Several challenges need to be addressed in this regard, such as identifying and mitigating the non-radiative recombination loss pathways and improving the stability. This thesis focuses on enhancing the efficiency and stability of high performing fused-ring electron acceptors IT-4F and Y6 based binary bulk heterojunction OSCs. Along with strategies to improve NFA-based OSCs efficiency, this thesis investigates underlying mechanisms in the device degradation and proposes strategies to mitigate the rapid deterioration of the device performance.

The first part of the thesis focuses on improving the efficiency of non-fullerene acceptor IT-4F based OSCs with inverted device geometry. The contact selectivity improved by introducing an optimized thin $PC_{70}BM$ layer in addition to the electron transport layer ZnO at the cathode interface. The combination of ZnO and $PC_{70}BM$ layers between the cathode and BHJ active layer can reduce charge transport barriers and significantly enhance short-circuit current density and power conversion efficiency (PCE). The analysis of current-voltage characteristics

under dark and illumination conditions indicates a reduced series resistance and enhanced charge collection efficiency in the interlayer device. Impedance spectroscopy (frequency domain measurement) and photocurrent noise spectroscopy (time-domain measurement) were employed to identify the underlying charge transport and recombination dynamics. The equivalent circuit modelling of the impedance spectra shows a significant reduction in the charge transport resistance in the device with a $PC_{70}BM$ interlayer. A low level of photocurrent fluctuations ($\sim 10^{-14}$ Hz^{-1}) in the interlayer device compared with the control device ($\sim 10^{-11}$ Hz^{-1}) correlates with the reduced charge transport barrier identified using the impedance spectroscopy analysis. The study suggests the potential of $PC_{70}BM$ as an interlayer material to further improve the performance of NFA IT-4F based OSCs.

In the next part of the thesis, a comprehensive investigation of light-induced and temperature-induced degradation in non-fullerene acceptor IT-4F based OSCs, focusing on the initial period of operation ('burn-in'), has been studied. Unlike other PV technologies, 'burn-in' degradation is a significant concern in OSCs. In certain combinations of D-A systems, more than half of the initial PCE is lost during the 'burn-in' period. The magnitude of 'burn-in' degradation is largely D-A system-specific and also depends on the device geometry and processing conditions. This investigation focuses on the mechanism of light and temperature-induced degradation in one of the highest stabilities established IT-4F based OSCs with the more stable inverted device geometry. Monitoring current-voltage characteristics upon accelerated aging stresses in inert conditions revealed that significant degradation occurs due to the UV components present in the light illumination. Steady-state optoelectronic measurements and spectroscopic studies provide significant insights into the degradation mechanisms. The building-up of bulk and interfacial charge transport barriers upon accelerated aging was identified using impedance and intensity-modulated photocurrent spectroscopy measurements. Photochemical modifications of the active layer components monitored using FT-IR

spectroscopy indicate weakening conjugation in the acceptor molecule IT-4F due to interaction with UV-light. Further, attempts were made to understand the detrimental effects of the commonly used solvent additive DIO (1,8-diiodooctane) in device degradation. Discerningly tailored experimental condition provides considerable insights into the origin of degradation from different aging stress factors. The study suggests the importance of preventing UV components through suitable barrier layers or through luminescent downshifting to prolong NFA-based OSCs lifetime.

The final section of the thesis focuses on improving the device performance using the ternary blend strategy. Ternary blend strategy in which three photo-active materials constitute the active layer is a route to enhance the photon harvesting without the fabrication complexities of multi-junction devices. Ternary blend devices were fabricated by introducing the acceptor molecule $PC_{70}BM$ as the third component in the PM7 donor and Y6 acceptor based OSCs. Wide-bandgap $PC_{70}BM$ with complementary absorption significantly improved the open-circuit voltage and the PCE of the binary OSCs. Insights into charge transport and recombination dynamics in the devices are analyzed using steady-state and transient techniques. Transient photocurrent results reveal a fast charge carrier extraction in the ternary system with a time constant $\tau \sim 730$ ns, indicating reduced recombination and transport barrier. The role of the third component, $PC_{70}BM$, in the device stability is critical, and it has been found that thermal stress acts as a dominant factor in degradation over the UV light in Y6 acceptor-based devices. The morphological modification of the BHJ active layer indicates a suppressed interfacial recombination due to the third component, $PC_{70}BM$, having a comparatively high thermal transition temperature. Light and temperature-induced degradation studies reveal the optimized BHJ morphology of ternary OSCs in prolonging the device lifetime. This work emphasizes the potential of fullerene derivative acceptor $PC_{70}BM$ in improving the efficiency and stabilizing the NFA based single-junction organic solar cells.

In summary, this thesis suggests methods to enhance device performance of non-fullerene acceptors IT-4F and Y6 based OSCs using interfacial modification and ternary blend strategy. A systematic study of the degradation mechanism in these devices and disintegration of the influence of various aging factors suggests strategies to improve the stability.

Publications

- **Azeez, Abdul**, and K. S. Narayan. *"Insights into the Role of PC70BM As The Third Component In Y6 Acceptor Based Ternary Blend Organic Solar Cells."* Manuscript Under Preparation (2022)

- **Azeez, Abdul**, and K. S. Narayan. *"Dominant Effect of UV-Light-Induced "Burn-in" Degradation in Non-Fullerene Acceptor Based Organic Solar Cells."* The Journal of Physical Chemistry C 125.23 (2021)

- **Azeez, Abdul**, and K. S. Narayan. *"Enhanced device performance via interfacial engineering in non-fullerene acceptor based organic solar cells."* Applied Physics Letters 117.4 (2020)

- Vijayan, Raaghesh, **Abdul Azeez**, and K. S. Narayan. *"Toward reliable high performing organic solar cells: Molecules, processing, and monitoring."* APL Materials 8.4 (2020)

- Vijayan, Raaghesh, **Abdul Azeez**, and K. S. Narayan. *"Enhanced Stability and Optimized Morphology Induced by Electric-Field-Assisted Annealing of Bulk Heterojunction Solar Cells."* Solar RRL 3.10 (2019)

Conference Presentations

- SUNRISE IV – Conference (Online), Spain.
  10-11 February 2022. (**Poster**)

- SUNRISE Symposium (Online), Cambridge University, Cambridge, UK.
  27 April 2021. (**Oral**)

- SUNRISE Symposium (Online), Imperial College London, UK.
  4-5 August 2020. (**Oral**)

- SUNRISE Symposium, Indian Institute of Science (IISc), Bangalore, India.
  12 February 2020. (**Poster**)

- SUNRISE Symposium, Oxford University, Oxford, UK. 7-9 October 2019.
  (**Oral**)

- International Winter School on "Frontiers in Materials Science", JNCASR
  Bangalore, India. December 2-6, 2019. (**Poster - Awarded Best Poster Prize**)

- International Workshop & Conference on Perovskite & Hybrid Photovoltaics
  (ICPHPV). IIT Delhi, India. February 04-08, 2019. (**Poster**)

- JNCASR Annual In-house Symposium-2018, Bangalore, India.
  (**Poster - Awarded Best Poster Prize**)

Contents

1. Organic Solar Cells: An Introduction

2. Materials and Methods

3. Interfacial Engineering of Non-Fullerene Acceptor IT-4F Based Organic Solar Cells

4. Comprehensive Investigation of Light and Temperature Induced Degradation in Non-Fullerene Acceptor IT-4F Based Organic Solar Cells

5. Insights into the Role of PC$_{70}$BM as the Third Component in Y6 Acceptor Based Ternary Blend Organic Solar Cells

6. Summary and Future Directions

Appendices

Appendix A

Appendix B

Appendix C

List of Figures

List of Tables

Glossary of Symbols and Abbreviations

A	Acceptor
AFM	Atomic Force Microscopy
Al	Aluminum
Ag	Silver
Au	Gold
Ba	Barium
BDD	benzo-[1,2-c:4,5-c′]dithiophene-4,8-dione
BDT	benzo [1,2-b:4,5-b′] dithiophene
BHJ	Bulk Heterojunction
BT	Benzothiadiaole
Ca	Calcium
CB	Conduction band
CN	Chloronaphtalene
CPEs	Conjugated polyelectrolytes
CS	Charge Separated
CT	Charge Transfer
D	Donor
DIO	1,8-diiodioctane
DOS	Density of States
DSA	Dynamic Signal Analyzer
DUT	Device under test
E_A	Electron Affinity
E_{CT}	Charge Transfer State Energy
E_g	Optical Bandgap
ENS	Electric Noise Spectroscopy
EL	Electroluminescence
EQE	External Quantum Efficiency
ETL	Electron Transport Layer
f	Frequency in Hz
FF	Fill Factor
FREA	Fused ring electron acceptor
FRET	Forster Resonance Energy Transfer

FTIR	Fourier Transform Infrared Spectroscopy
G	Carrier generation rate
GDM	Gaussian Disorder Model
GIWAXS	Grazing incidence wide-angle X-ray scattering
HOMO	Highest Occupied Molecular Orbital
HTL	Hole Transport Layer
IDT	Indacenodithiophene
IMPS	Intensity Modulated Photocurrent Spectroscopy
IP	Ionization Potential
IS	Impedance Spectroscopy
IQE	Internal Quantum Efficiency
IT-4F	3,9-bis(2-methylene-((3-(1,1-dicyanomethylene)-6-7-difluoro)indanone))-5,5,11,11-tetrakis(4-hexylphenyl)-dithieno[2,3-d:2',3'-d']-s-indaceno[1,2-b:5,6-b']dithiophene
ITIC	3,9-bis(2-methylene-(3-(1,1-dicyanomethylene)-indanone)) 5,5,11,11-tetrakis(4-hexylphenyl)-dithieno[2,3-d:2',3'-d']-s-indaceno[1,2-b:5,6b']dithiophene
ITO	Indium Tin Oxide
J_0	Dark reverse saturation current
$J_{0,rad}$	Dark reverse saturation current in the radiative limit
J_{SC}	Short Circuit Current Density
J-V	Current-Voltage
K_B	Boltzmann constant
k_{ET}	Rate for electron transfer
k_{nr}	(First order) rate constant for nonradiative recombination
KPFM	Kelvin probe force microscopy
Λ	Reorganization energy
LUMO	Lowest unoccupied molecular orbital
MoO_3	Molybdenum trioxide
NDI	Naphthalene diimide
NFA	Non-Fullerene Acceptor
NFREA	Non-fused ring electron acceptor
NPs	Nanoparticles
NPSD	Normalized Power spectral (spectrum) density

OPVs	Organic Photovoltaics
OSC	Organic Solar Cell
P3HT	Poly(3-hexylthiophene)
PBDB-T	poly[(2,6-(4,8-bis(5-(2-ethylhexyl)thiophen-2-yl)-benzo[1,2-b:4,5b′]dithiophene))-alt-(5,5-(1′,3′-di-2-thienyl-5′,7′-bis(2-ethylhexyl)benzo[1′,2′c:4′,5′-c′]dithiophene-4,8-dione)
$PC_{60}BM$	phenyl-C61 -butyric acid methyl ester
$PC_{70}BM$	phenyl-C71 -butyric acid methyl ester
PCE	Power Conversion Efficiency
PEDOT:PSS	Poly(3,4-ethylenedioxythiophene):poly(styrenesulfonate)
PFN	Poly[(9,9-bis(3 0-(N,N-dimethylamino)propyl)-2,7-fluorene)-alt 2,7(9,9dioctylfluorene)]
PL	Photoluminescence
PSD	Power spectral (spectrum) density
PTB7	Polythieno[3,4-b]thiophene/benzodithiophene
q	elementary charge
R	Carrier recombination rate
RMS	Root-mean-square
R-SoXS	Resonant soft X-ray scattering
S_0	Ground state
S_1	First excited singlet state
SCLC	Space Charge Limited Current
SEM	Scanning electron microscopy
SQ	Shockley-Queisser
T	Absolute Temperature in Kelvin
TBOSC	Ternary Blend Organic Solar Cell
TEM	Transmission electron microscopy
TIA	Transimpedance Amplifier
TPC	Transient Photocurrent
UV	Ultra-Violet
V	Voltage
V_{OC}	Open Circuit Voltage
VASE	Variable angle spectroscopic ellipsometry
VB	Valance band

| WF | Work-function |
| ZnO | Zinc Oxide |

Chapter 1

Organic Solar Cells: An Introduction

1.1. Green Energy and Solar Cells

Ever-increasing energy demand combined with the need to reduce CO_2 and other greenhouse gas emissions requires mature renewable energy technologies.[1] It is estimated that global energy consumption is expected to approach 27 TW by 2040.[2] Green energy is a term used to describe the energy that is being generated from natural sources such as Sun, wind and water, which are constantly being replenished.[3] Green energy technologies offering a clean and environmentally friendly alternative to fossil fuel-based energy sources are identified as the solution for sustainable development. The most common green energy sources are solar power, wind power, hydropower, geothermal energy, biomass and biofuels.[4] The enticing fact that the amount of solar power striking the earth in an hour is more than the annual global power consumption is persuasive enough to adopt technologies to harvest sunlight.[5] Photovoltaic (PV) technologies which directly convert light into electricity using suitable materials capable of PV conversion are vital in this regard. Today, solar energy is being harvested in different ways to meet the energy demand at the domestic and industrial levels, such as by using solar cells and solar thermal energy technologies, which directly convert light into electricity.[6-7] The most efficient and widely adopted way of harvesting solar energy is through solar cells. Solar cells are electronic devices that produce current and voltage to generate electric power upon light illumination. A variety of materials can satisfy the requirements of a solar cell, including Silicon, GaAs, CIGS, CdTe, Organic Semiconductors, Perovskites, Dye/TiO_2 and quantum dot

solids.[8-12] The PV technologies or solar cells based on the above-mentioned materials represent a wide spectrum and different generations of solar cells.[13] On the basis of the PV materials used in the solar cells and the technology, four generations of solar cells are defined.[14-15] The oldest commercially available PV technology or solar cells based on c-Si or GaAs wafers constitute the first generation. Thin-film PV technologies such as the ones based on polycrystalline silicon, CdTe and CIGS are referred to as the second generation of solar cells. The third-generation solar cells are the emerging technologies such as organic solar cells and DSSCs, which are not based on conventional p-n junction diode configuration to separate the charge carriers. The fourth-generation solar cell technologies are based on the combination of organic and inorganic materials such as polymer-nanoparticle composites.[14-15] To date, Silicon-based PV technologies are demonstrated to be the most efficient and commercially viable with increasing large industrial and domestic users.[16-18] But many of the remaining technologies are also potential candidates like organic semiconductor and hybrid organic-inorganic perovskite-based PV technologies and are close to successful commercialization.

The core of any thin-film solar cell is the photon absorbing layer (active layer) which absorbs photons of suitable energy and generates electron-hole pairs. The counter electrodes collect these charge carriers, thus providing electric power to the external load. In a conventional p-n junction solar cell, the electric field in the space charge region drives the photogenerated carriers even in the absence of an external bias. The resulting photocurrent in the reverse-bias direction generates a forward current in the presence of an external load (**Figure.1.1**). The combination of these two currents produces a net current (I) in the reverse-bias direction in the solar cell.

$$I = I_L - I_F = I_L - I_0(e^{qV/nK_BT} - 1) \tag{1}$$

where q is the charge of an electron, V is the voltage, K_B is the Boltzmann constant, T is the temperature, I_0 is the saturation current and I_L and I_F are the photocurrent and forward current, respectively. Here *n* is the ideality factor, incorporated for non-ideal or 'practical' diodes, indicating the recombination mechanism in the diode. A conventional p-n heterojunction (junction between two different semiconductors) solar cell is a combination of two materials with different bandgaps, such as GaAs and AlGaAs also work similarly to enhance photon harvesting.[19]
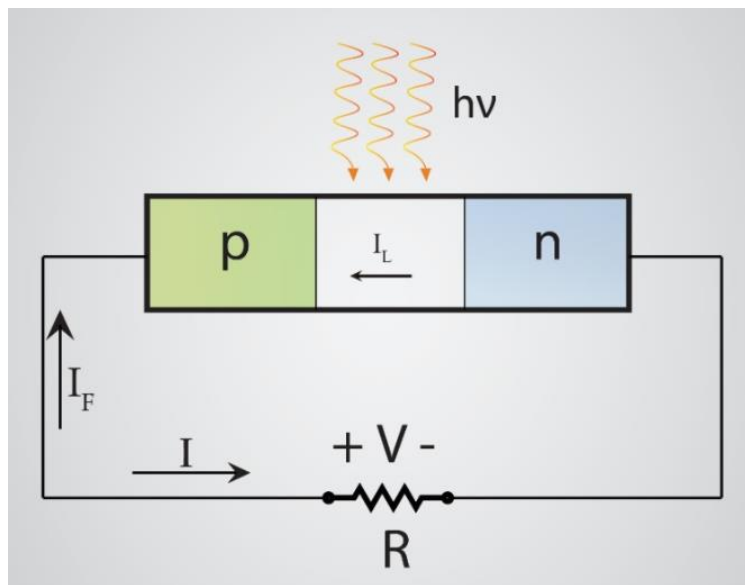
Figure.1.1. Schematic diagram of a conventional *p-n* junction solar cell with a resistive load.

The performance of a solar cell is assessed based on the efficiency and the lifetime of the particular photovoltaic (PV) device. The power conversion efficiency (PCE) of a solar cell is defined by the following equation:

$$PCE = \frac{V_{OC} \times J_{SC} \times FF}{P_{in}} \qquad (2)$$

Where V_{OC}, J_{SC}, FF, and P_{in} represent the open-circuit voltage, short-circuit current density, fill factor and input power, respectively. A detailed discussion of each of these parameters is

3

described in the following subsections. By convention, P_{in} is taken as 100 mW cm^{-2} for the characterization. The V_{OC}, J_{SC} and FF can be determined from the current-voltage (J-V) characteristics of a solar cell under AM1.5 Global, 1 Sun illumination (~100 mW cm^{-2}). **Figure.1.2** show a typical J-V characteristic of a solar cell under simulated AM1.5G illumination (~100 mW cm^{-2}). Inset shows the equation to calculate the FF, and geometrically it defines the 'squareness' of the J-V curve.
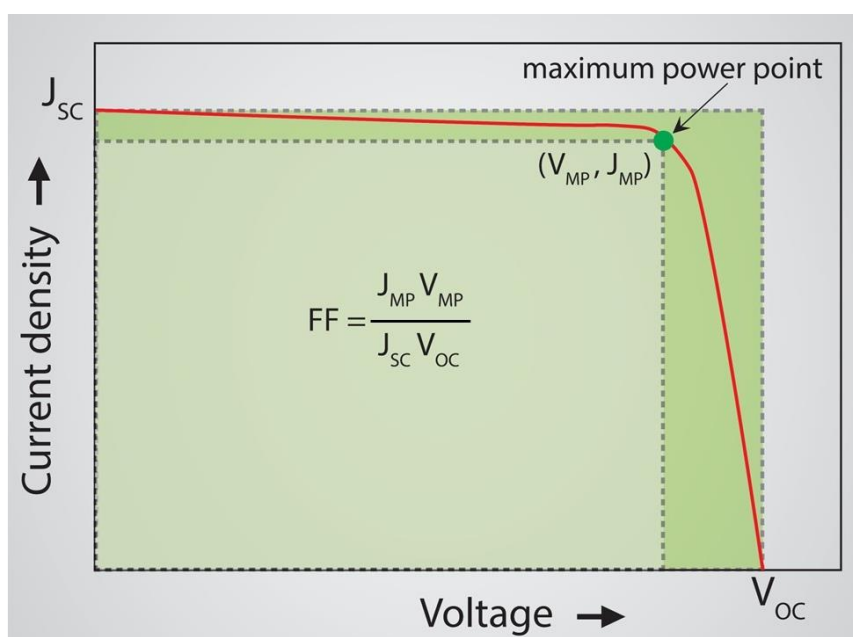
Figure.1.2. Typical current-voltage characteristics of a solar cell under simulated AM1.5G solar illumination (inset shows the equation to calculate device fill factor).

1.2. Organic Semiconductors and Organic Solar Cells

Ever since the discovery of electrical conductivity in organic semiconductors, which began with the observation of electroluminescence in anthracene in the 1960s and later in polyacetylene in 1977, these classes of materials have been of interest over the last five decades.[20-23] Organic semiconductors are carbon-based materials which exhibit semiconducting properties owing to the presence of conjugated molecules. These materials are

earth-abundant and versatile in terms of processing for various applications, making them attractive in optoelectronic applications. Optoelectronic devices based on organic semiconductors can be fabricated on flexible substrates and glass, enabling a niche of applications, including bioelectronics and wearable electronics. Contrary to the inorganic semiconductors such as covalently bonded silicon or III-V, organic semiconductors are based on weak intermolecular forces such as van der Waals interaction, which defines a fundamentally different charge transport mechanism. Organic semiconductors can be classified into small molecules or oligomers and polymers based on the chemical complexity of the material.[24-25] The crucial characteristic of organic semiconductors is the presence of sp^2-hybridized carbon atoms, which form a conjugated system with delocalized π electrons.[26-27] The electronic configuration of the C atom ($1s^2\ 2s^2\ 2p^2$) indicates four valance electrons having sp^2-orbitals in a triangular planar configuration, with the final electron occupying a perpendicular $2p_z$ orbital. The hybridization between the $2p_z$ orbitals results in weaker π (bonding) or π^* (anti-bonding) orbitals. In the ground state of the molecule, the π orbital is occupied and is called as highest occupied molecular orbital (HOMO), and the unoccupied π^* orbital is called the lowest unoccupied molecular orbital (LUMO). The energy difference between the HOMO and LUMO levels is analogous to the bandgap in a crystalline material. The delocalization of these π/π^*-states over many carbon atoms is a measure of conjugation length.[25] The electronic properties of the organic semiconductor are determined by the interaction of these π electrons. For much of the inorganic semiconductors, the quality of band structure and resulting electronic properties are highly sensitive to the defects, indicating processing of these materials is expensive and energy-intense. On the other hand, organic semiconductors are intrinsically semiconducting, and the optoelectronic properties largely depend on the molecule itself than the processing condition, which enables them to be tolerant to defects and impurities. However, low-temperature solution-processed organic

semiconductor thin films also need to be optimal for desired optoelectronic properties as the crystal packing and nanomorphology play a critical role in the performance of devices.[25-26]
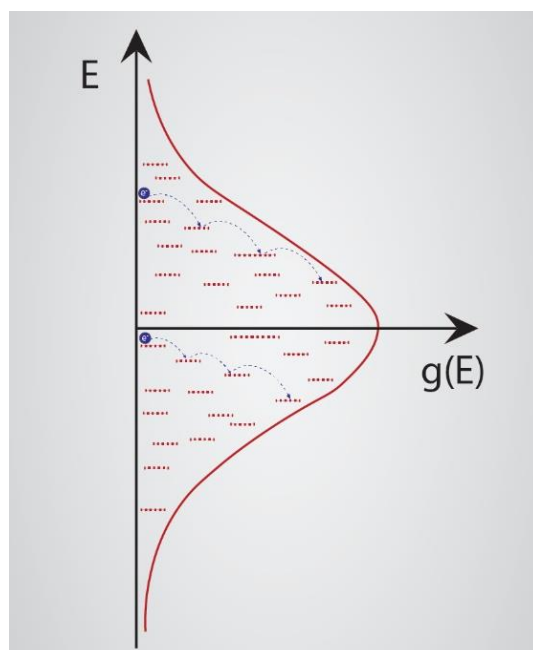
Figure.1.3. Schematic represent the Gaussian disorder model (GDM) and hopping transport of carriers in organic semiconductors.

A set of properties distinguishes organic semiconductors from other crystalline materials, including low dielectric constant (ε_r ~ 3-4), excitonic nature of the photoexcited species exhibiting binding energy (> K_BT) and charge carrier transport via hopping mechanism. Even though the electrons are delocalized within the molecule, in the scale of the intermolecular picture, electrons are localized, and the transport from one π system or molecule to the other is through a hopping mechanism, and each π system acts as a hopping site.[28] This intrinsic characteristic of organic semiconductors, such as disorder and hopping charge transport mechanism, has interesting consequences in the system, such as the increase in mobility with temperature due to the influence of the thermally activated hopping processes.[29] The widely adopted model for the hopping transport in organic semiconductors is the Gaussian disorder

model (GDM) developed by Bassler et al.[30] According to this model, the density of states (DOS) is given by the relation,

$$g(E) = \frac{N_{site}}{\sqrt{2\pi}\sigma} \, exp\left(-\frac{(E-E_0)^2}{2\sigma^2}\right) \tag{3}$$

Where E is the energy, E_0 is the center of the DOS or mean energy N_{site} is the concentration of sites, and σ is the standard deviation of the distribution (**Figure.1.3**). This description of charge transport (GDM) was successful in explaining many experimental observations and photophysical processes in OSCs.[31]
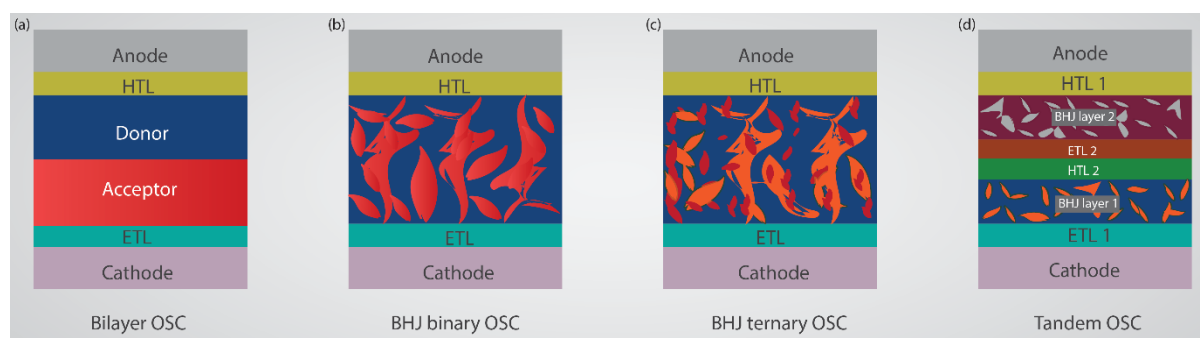
Figure.1.4. Schematic depicting the device architecture of (a) bilayer, (b) binary bulk heterojunction, (c) ternary bulk heterojunction and (d) tandem organic solar cells, respectively.

One of the earliest reports of solar cells using molecular semiconductors is by Tang et al. (1986), where the first bilayer organic solar cell (OSC) was demonstrated by employing organic semiconductor (CuPc and a PDI derivative) as the active layer with an efficiency of ~ 1% under AM2 illumination conditions (75 mW cm^{-2}).[32] The device architecture was thin layers of organic semiconductors sandwiched between counter electrodes. In any thin-film PV technology, the device architecture consists of primarily the active layer sandwiched between counter electrodes. The low-performance metrics of this bilayer OSC are due to the fact that exciton dissociation occurs only at the interface of the donor and acceptor, coupled with low carrier mobility in organic semiconductors leading to poor charge collection. In order to

7

overcome the limitations of bilayer architecture, the concept of bulk heterojunction (BHJ) was introduced.[33] The BHJ concept utilized the inherent phase separation length scales of a two-component polymer mixture. In the bulk heterojunction strategy, a blend of donor polymer and acceptor molecule in a suitable stoichiometry forms the active layer of the OSC with the advantage of an intercalating network of donor and acceptor interface throughout the film (1995 by Heeger and coworkers).[33] The bulk heterojunction strategy of two components can be extended with one more donor (acceptor) element constituting the active layer and is known as the ternary blend OSC.[34-35] Apart from this, BHJ active layers with complementary bandgap can be stacked in tandem with appropriate interconnecting layers to improve the device performance called the tandem organic solar cell.[36] The Schematic in **Figure.1.4** depicts the different types of OSC architecture with representative morphology.

1.3.   Bulk Heterojunction Organic Solar Cells

The concept of bulk heterojunction (BHJ) has enabled the design of donor and acceptor components suited to achieve the high efficiency of OSCs. This strategy has been a prerequisite for recent highest-performing devices that uses the BHJ concept. In this section, an overview of the fundamentals and working principles of BHJ-OSCs are discussed.

1.3.1.   Fundamentals of BHJ Organic Solar Cells

The low device performance of bilayer OSCs is restricted by the limited D-A interface area to roughly a single plane, and weak charge collection as the dissociated carriers have to travel a long distance to reach the respective electrodes.[37] The concept of bulk heterojunction (BHJ) revolutionized the field of OSCs due to the excellent charge generation potential. The BHJ is a blend of donor and acceptor molecules with interpenetrating nano-scale donor-acceptor

phases. BHJ strategy provides a network of D-A interfaces distributed throughout the thin film suitable for exciton dissociation upon photoexcitation.[29] The primary processes involved in BHJ OSCs can be summarized as follows:

1. Photo-absorption

2. Exciton generation

3. Exciton diffusion to the donor-acceptor interface

4. Exciton dissociation into free charge carriers

5. Charge transport

6. Charge collection at the respective electrodes

In brief, upon the photon excitation, photons having energy above the material bandgap will be absorbed, and Frenkel-type singlet excitons will be generated in the active layer almost instantly. The key difference in the OSCs as compared to the inorganic systems is that the photo-absorption leads to the formation of the strongly bound excitons, a localized excited state. In order to maximize the photo absorption, D-A materials with a high absorption coefficient in a wide absorption window are desired. The optimization of different layers with regard to optics in the device architecture is also critical to maximize photo-absorption. The exciton travels to the nearby D-A interface and gets quenched in the femtosecond (*fs*) time scale. This leads to the formation of an interfacial charge transfer (CT) state and eventually the dissociation and formation of spatially separated charge carriers. The critical requirement for this process is the optimum energetic offset larger than the exciton binding energy in the LUMO levels (HOMO levels) for electrons (holes). Further dissociation of the bound charge pair is activated by temperature, leading to the generation of free charge carriers. If the Coulombically bound CT exciton does not dissociate within its lifetime, geminate recombination occurs, leading to an energy loss in the device. In a typical BHJ organic solar cell, geminate recombination of CT exciton occurs in a time scale of 100 *fs-ns*. Further,

additional energy loss due to non-geminate recombination along with the geminate recombination loss can significantly reduce the device performance, including low FF and quantum efficiency. The free charge carriers thus generated travel through the material and eventually collected at the respective electrode giving rise to photocurrent in the external load.[38] **Figure.1.5**. depicts a BHJ organic solar cell device architecture in inverted geometry (anode on top) with the electron transport layer and the hole transport layer.
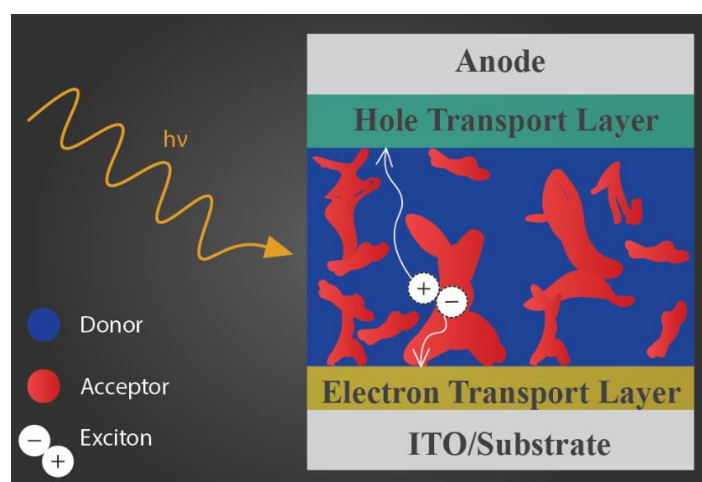
Figure.1.5. Graphical representation of the device architecture of bulk heterojunction organic solar cell in an inverted device geometry.

The photo-physics of organic solar cells, from the phot-excitation to the formation of a charge-separated state (CS), is fundamentally different from that of its inorganic counterpart and necessary to discuss with the timescales involved.[39-40] The photoexcitation almost instantaneously generates excitons which are vibrationally excited and known as hot excitons. The hot excitons relax to the vibrational ground state in ~ 100 *fs* time scale leading to exciton.[41] If the exciton generation occurs in the vicinity of the D-A interface, then the hot exciton dissociates with extra free energy according to the Frank-Condon principle. The singlet excitons generated upon photoexcitation can also diffuse to the D-A interface in the picosecond (*ps*) time scale, and hence the active layer morphology with a sufficient number of D-A

interfaces and optimum domain sizes is necessary for efficient device performance. The diffusion length of excitons in a typical organic solar cell is estimated to be nearly 10 nm.
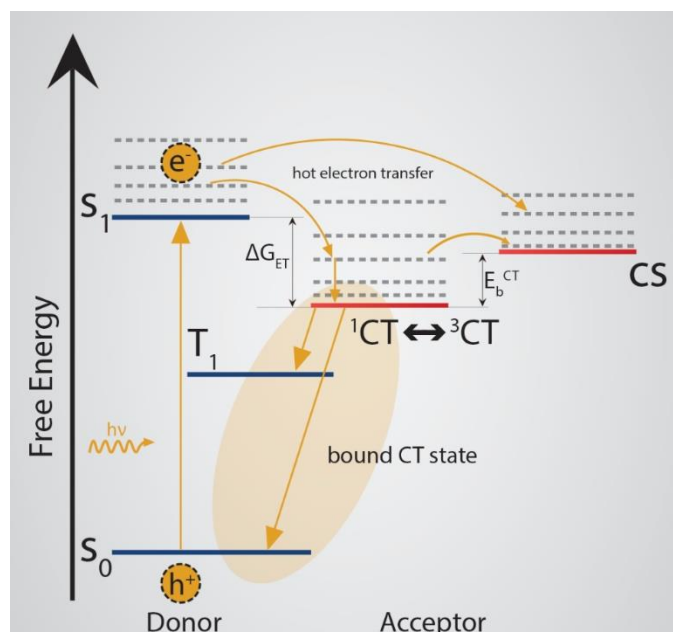
Figure.1.6. The schematic diagram depicts the possible ways to form a charge-separated state (CS) from the singlet exciton in the donor molecule: S_0 and S_1 denote the singlet ground state, and the first excited state, geminate recombination to the triplet state (T_1) from charge transfer (^3CT) state is possible (spin mixing of ^1CT and ^3CT) as indicated (adapted from ref.42).

At this point, instead of diffusing to the D-A interface, the singlet excitons can undergo radiative recombination as well. When a singlet exciton successfully reaches a D-A interface, an ultrafast quasi-adiabatic electron transfer process with a time scale of fewer than 100 *fs* occurs. The electron transfer leads to the formation of a charge-transfer (CT) state in which the electron is in the LUMO of the acceptor and the hole in the HOMO of the donor at the D-A interface. The CT exciton can directly dissociate into free electrons and holes through a hot electron transfer process typically in the timescale of fewer than 50 *fs*. Also, the CT exciton can thermally relax to the ground state CT (timescale ~ *fs-ps*) and eventually, either charge separation or geminate recombination occurs.[42-43] As mentioned earlier, the CT excitons have a Coulombic barrier due to the low dielectric constant of organic semiconductors given by,

$$V = \frac{e^2}{4\pi\varepsilon_0\varepsilon_r r} \qquad (4)$$

where ε_r is the dielectric constant, e is the charge of an electron, ε_0 is the electric permittivity of free space, and r is the electron-hole separation distance. This mutual interaction of CT excitons results in a part of excitons suffering geminate recombination in a time scale of ~ 100 $ps - 100\ ns$.[39, 44]

Immense efforts to understand the exciton formation and dissociation in the BHJ blend coupled with sensitive experimental tools have provided insights into these processes.[41, 45-49] The most important frameworks describing the exciton formation and dissociation in the BHJ blend are Marcus theory of electron transfer and Onsager theory of charge pair dissociation.[47]

The Marcus theory of electron transfer was historically introduced to describe the charge transfer process in electrolytes and was later successfully used to explain the charge transfer in OSCs.[50-51] The semiclassical approach of the Marcus theory treats the nuclear motion classically and the electron coupling quantum mechanically, and the irreversible nature of the charge transfer treats the electron transfer rate as a kinetic parameter rather than a thermodynamic one. The relation between the activation energy barrier with Gibbs free energy and reorganizational energy (Λ) is given by the equation,

$$\Delta G^{\dagger} = \frac{\Lambda + \Delta G^0}{4\Lambda} \qquad (5)$$

ΔG^0 represents the total Gibbs free energy change between the initial and final states or the driving force of the charge transfer process, and the reorganizational energy Λ is the free energy change associated with the relaxation (the reorientation of the dipoles) of the molecular dimer. The electron transfer rate (k_{ET}) according to this framework arrived from the Fermi-Golden rule is expressed by the relation,

$$k_{ET} = \frac{2\pi}{\hbar\sqrt{4\pi\Lambda kT}} V_{ec}^2 \exp\left(-\frac{(\Lambda + \Delta G^0)^2}{4\Lambda kT}\right) \tag{6}$$

Where V_{ec} is the electronic coupling term and can be considered as the intermolecular hopping integral and depends on the extent of electron wave function overlap between donor and acceptor molecules. The Frank-Condon term (exponential term in k_{ET}) shows that as $-\Delta G^0$ increase the rate of electron transfer process also increases, and when $\Lambda = -\Delta G^0$ the reaction occurs without any activation barrier. When $-\Delta G^0 > \Lambda$ the electron transfer rate decreases and is known as the 'inverted regime'. In a modification to electron transfer rate by Holstein et al., assuming $\Delta G^0 = 0$ for the carrier transport, the barrier reduces to $\Lambda/4$ and for thermal activation. Thus, making V_{ec} and Λ are crucial molecular parameters in charge transport processes and molecular design.[51-53]

The Onsager theory of charge pair dissociation takes into account the geminate recombination and quantitatively estimates the bound pair dissociation probability.[54-56] The coulomb capture radius (R_C) is defined as the length scale at which the Coulomb interaction between the electron and hole pair is equal to the thermal energy present given by the relation,

$$R_C = \frac{e^2}{4\pi\varepsilon K_B T} \tag{7}$$

Where e is the charge of the electron, ε is the electric permittivity is the Boltzmann's constant and T is the temperature.[57] In this macroscopic field-dependent CT exciton dissociation framework, the charge pair is assumed to be fully separated if the thermalization length scale is larger than R_C at a given temperature. It is assumed that upon photoexcitation, localized hole and hot electron bound pair are formed, the electron thermalizes to a distance and competition between dissociation and geminate recombination begins in the system. If the thermalization

length scale of the bound pair is less than R_C, then dissociation occurs with a probability $P(F)$ given by,

$$P(F) = \frac{k_d}{k_d + k_f} = \frac{\kappa_d^*(F)}{\kappa_d^*(F) + (\mu\tau)^{-1}} \tag{8}$$

Where k_f is the geminate recombination rate, k_d is the field-dependent dissociation rate, μ is the sum of electron and hole mobilities, τ is the CT exciton lifetime and $k_d = \mu \kappa_d^*(F)$. At the same time, 1- $P(F)$ represents the probability of geminate recombination to the ground state. For homogeneous systems, the estimation of charge dissociation probability using this model was found to be valid, but in organic BHJ systems, this framework results in the overestimation of R_C and the precision of the calculation is limited. Several modifications have been made to this model to include system-specific experimental observation, and each carries its own limitations.[55-56, 58]

The open-circuit voltage is the maximum voltage a solar cell can deliver to the external circuit, and it is an important parameter determining the PCE of a solar cell. Under a steady-state light illumination and open circuit (net current drawn from the device is zero) condition, all the generated free charge carriers accumulate at the respective electrodes forming a potential difference which balances the built-in potential. The carrier generation and recombination will balance each other under this condition, and no net current exists inside the device. The potential difference thus created between the counter electrodes during this quasi-equilibrium state represents the V_{OC} of the device.[59]

$$V_{OC} = \frac{1}{q}(E_{Fn} - E_{Fp}) \tag{9}$$

Where E_{Fn} and E_{Fp} are the electron and hole quasi-Fermi levels, respectively.

In OSCs, the presence of a large number of electronic traps in the tail states within the bandgap causes a shift in the quasi-Fermi levels, unlike crystalline semiconductors. The distribution of photogenerated charge carriers in these trap states results in a downshift of E_{Fn} and upshift of E_{Fp} and consequently a reduced V_{OC} in the device. This makes the direct estimation of V_{OC} from the quasi-Fermi level difficult in OSCs. On the other hand, various factors such as molecular energetics and charge transfer state (CT-state) at the D-A interface influences the V_{OC} directly with a clear correlation. Charge carrier recombination in the device, reverse saturation current, illumination intensity, temperature, the work function of the electrodes, carrier density, energetic disorder, crystallinity, microstructure, and morphology are also among the factors influencing the V_{OC}.[60-62]
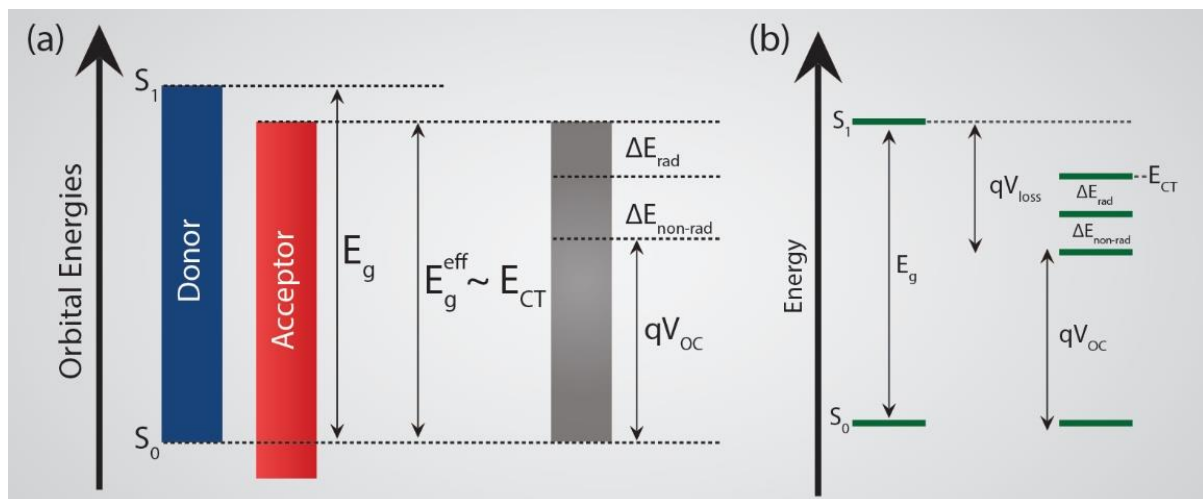
Figure.1.7. The Schematic depicts the orbital energy levels of the donor and acceptor molecules and the open-circuit voltage loss in a typical organic solar cell (adapted from ref.44).

Attempts to quantify and trace the origin of voltage losses in OSCs has been an important aspect since the voltage loss is significant (~ 0.6 – 1.0 eV) as compared to the silicon-based and hybrid perovskite-based solar cells. The main loss in V_{OC} in OSCs is associated with the energetic offset of the donor-acceptor interface and the dominant non-radiative recombination in the system. With the arrival of NFAs, the exciton dissociation and charge generation were

able to achieve with negligible energy offset, indicating high V_{OC} can be obtained by suppressing non-radiative recombination losses effectively.[60]

The V_{OC} can be related to the recombination losses using the following expression,

$$V_{OC} = \frac{1}{q}(E_{CT} - \Delta E_{rad} - \Delta E_{non-rad}) \tag{10}$$

Where E_{CT} is the charge transfer state energy, ΔE_{rad} is the radiative recombination loss which is nearly 0.2 - 0.3 eV, and $\Delta E_{non-rad}$ is the non-radiative recombination loss.[63-64] Here, the upper limit to the V_{OC} is the CT state energy which accounts for the carrier generation loss in the OSCs. According to the principle of detailed balance, every solar cell must have a voltage loss associated with radiative recombination and E_{CT} - ΔE_{rad} sets the maximum achievable V_{OC} in the device.[44] The presence of any additional voltage loss in the device is attributed to the non-radiative recombination and must be reduced to enhance the device performance.[51, 64-65] The non-radiative recombination can include both geminate (mono-molecular) and non-geminate (bimolecular) recombination losses. Geminate recombination refers to the recombination of carriers generated in a single photogeneration event, and non-geminate recombination refers to the recombination between carriers from two independent events. The geminate recombination occurs mostly in the pristine donor or acceptor phase, as the exciton may recombine before successfully reaching a D-A interface.[44, 66-67] Spectroscopically, the geminate and non-geminate recombination dynamics are sensitive to the light intensity and can be distinguished to an extent. This is due to the fact that the CT state, bound charge pair, is nearly localized and immobile at the interface, whereas non-geminate recombination becomes dominant at higher carrier densities or at higher light intensity.[60]

It must be noted that the understanding of the origin and pathways of non-radiative recombination loss in OSC is still low, and strategies to mitigate non-radiative recombination

are an imperative research goal.[68] In order to quantify the non-radiative recombination loss, the quantum yield of electroluminescence emission from the device can be utilized using the relation,

$$\Delta V_{non-rad} = \frac{K_B T}{q} \ln \left(\frac{1}{EQE_{EL}} \right) \tag{11}$$

Where EQE_{EL} is the external electroluminescence quantum efficiency, K_B is the Boltzmann's constant, q is the elementary charge and T is the temperature. The EQE_{EL} of the OSC can be measured by applying forward injection current, and if the non-radiative recombination loss is negligible, then the EQE_{EL} approaches unity.[68-69]

The external quantum efficiency (EQE) of a solar cell is defined as the ratio of the number of charge carriers collected from the solar cell (collected carrier flux) to the number of incident photons (incident photon flux). The EQE provides information on the various processes involved in charge generation and collection in an operating device.[37] Thus, the EQE can be considered as the combined efficiency of six processes in the device:

1. Photon absorption efficiency ($\eta_{PA}(\lambda)$):
2. Exciton diffusion efficiency ($\eta_{ED}(T)$):
3. Charge transfer efficiency ($\eta_{CT}(\lambda)$):
4. Charge dissociation efficiency ($\eta_{CD}(F,T)$):
5. Charge transport efficiency ($\eta_{CP}(F,T)$):
6. Charge collection efficiency ($\eta_{CC}(F)$):

$$EQE \, (\lambda) = \eta_{PA}(\lambda) \, IQE \, (\lambda, T) \tag{12}$$

$$IQE \, (\lambda, T) = \eta_{ED}(T) \, \eta_{CT}(\lambda) \, \eta_{CD}(F,T) \, \eta_{CP}(F,T) \, \eta_{CC}(F) \tag{13}$$

The internal quantum efficiency (IQE) is defined as the ratio of the number of charge carriers collected from the solar cell (collected carrier flux) to the number of photons absorbed. The IQE represent the electrical processes within the device, provided the $\eta_{PA}(\lambda)$ is corrected for
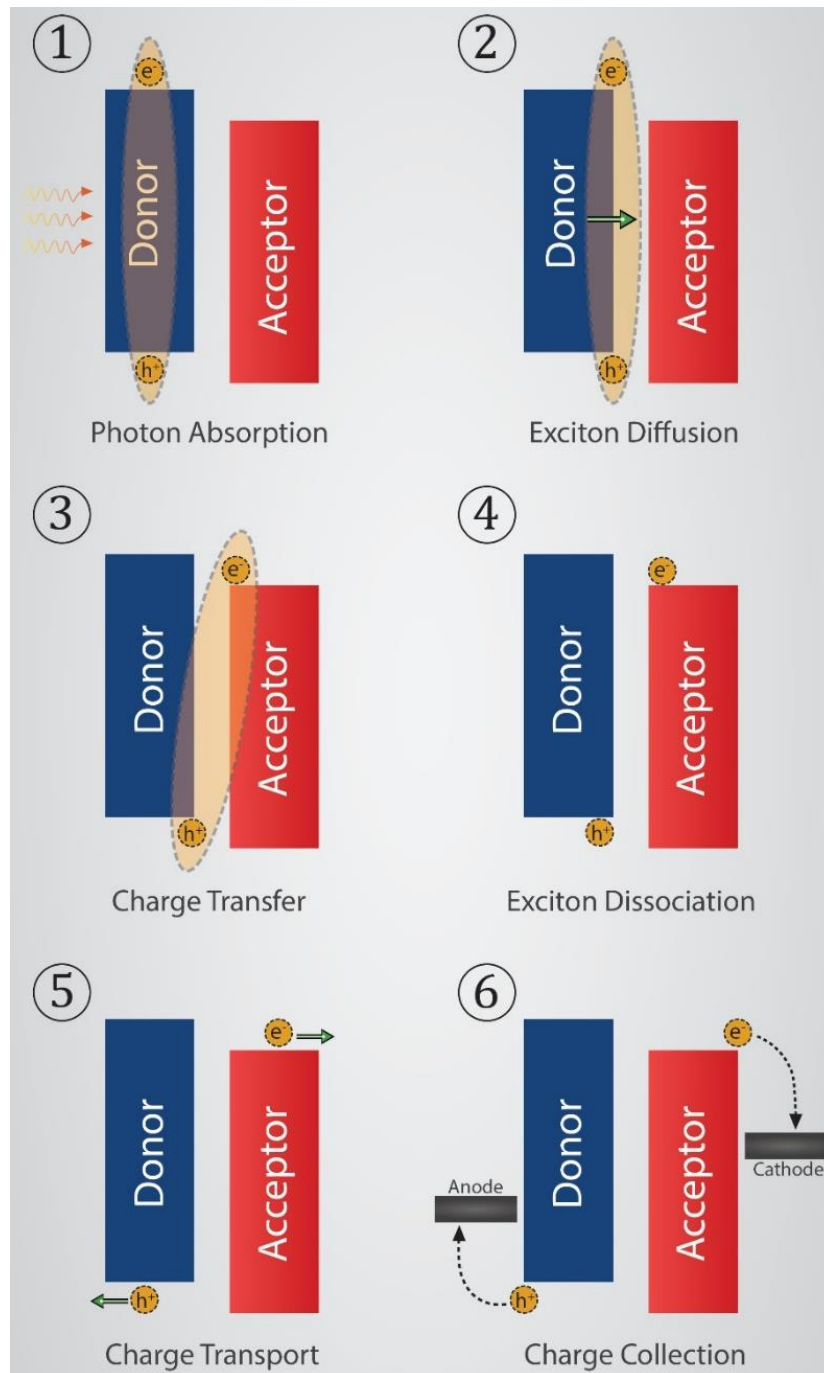
Figure.1.8. Graphical representation of the photophysical processes involved in the photocurrent generation in a bulk heterojunction organic solar cell (efficiency of these processes determines the external quantum efficiency and the magnitude of short circuit current in the device).

parasitic absorption. In order to have high EQE, both optical absorption of the BHJ active layer and IQE needs to be simultaneously optimized. The thickness of the BHJ active layer is another critical parameter in this regard, as the charge carrier collection must balance with the carrier lifetime. In organic semiconductors, the charge carrier mobilities are orders of magnitude less than inorganic counterparts, indicating that thin layers are necessary for efficient carrier extraction. The optimum thickness of the BHJ active layer can be determined by considering the carrier lifetime and transit time. In general, the thickness of the BHJ active layer in OSCs is of the order of ~ 100 nm, a dimension similar to the wavelength of light in the visible region of the spectrum. Another critical parameter is the complex refractive index ($n+ik$) of the various layers in the device as it influences the optical field distribution and, consequently, the shape of the EQE spectrum. It must be noted that the optical distribution in the BHJ active layer is not a simple exponential decay profile as described by the Beer-Lambert law; rather, it is dependent on many other optical properties (n and k) and thickness of the layer. The back electrode reflection of the light makes the cavity resonance critical to enhancing the photon harvesting and high quantum efficiency in the device.[37]

The short-circuit current density can be calculated from the EQE spectra using the relation,

$$J_{SC} = \frac{-q}{hc} \int_{\lambda_1}^{\lambda_2} EQE(\lambda)\, \phi(\lambda)\, \lambda\, d\lambda \tag{14}$$

where q is the elementary charge, h is the Planck's constant, c is the velocity of light, λ is the wavelength and $\phi(\lambda)$ is the AM1.5G spectral radiation.
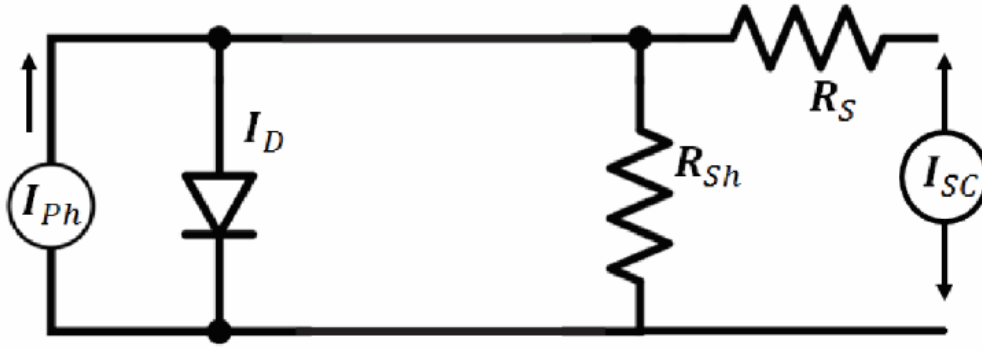
Figure.1.9. The equivalent circuit model of a bulk heterojunction organic solar cell.

The fill factor (FF) of a solar cell is an important parameter determining the device efficiency, and it is calculated using the relation,

$$FF = \frac{J_{MP} \times V_{MP}}{J_{SC} \times V_{OC}}$$

(15)

where J_{MP} and V_{MP} represent the current density and voltage at maximum power point in a typical J-V curve under illumination conditions. Various factors control the FF of a typical organic solar cell, and their influences are usually intertwined, making the estimation difficult.[70-72] The estimation of FF from the equivalent circuit model of an OSC can provide a reasonable insight. An ideal solar cell can be considered as a constant current source with a *p-n* junction diode connected in parallel. This representation must be modified when dealing with practical solar cells having loss channels. Primarily two parasitic resistance, a series resistance element (R_S) and a shunt resistance element (R_{Sh}), are introduced to account for the charge extraction resistance at the active layer-electrode interface and leakage resistance, respectively (**Figure.1.9**).[73] In the circuit model, I_{ph} represents the photocurrent, and I_{SC} is the short circuit current

$$I_{SC} = I_{ph} - I_D - I_{sh}$$

(16)

Importantly, the circuit elements series resistance (R_s), shunt resistance (R_{sh}) and diode are relevant to the device FF.[74] A typical J-V measurement of a solar cell in the dark exhibit *p-n* junction diode characteristics, and under illumination, a combination of dark and photocurrent constitute the J-V curve (**Figure.1.10**).
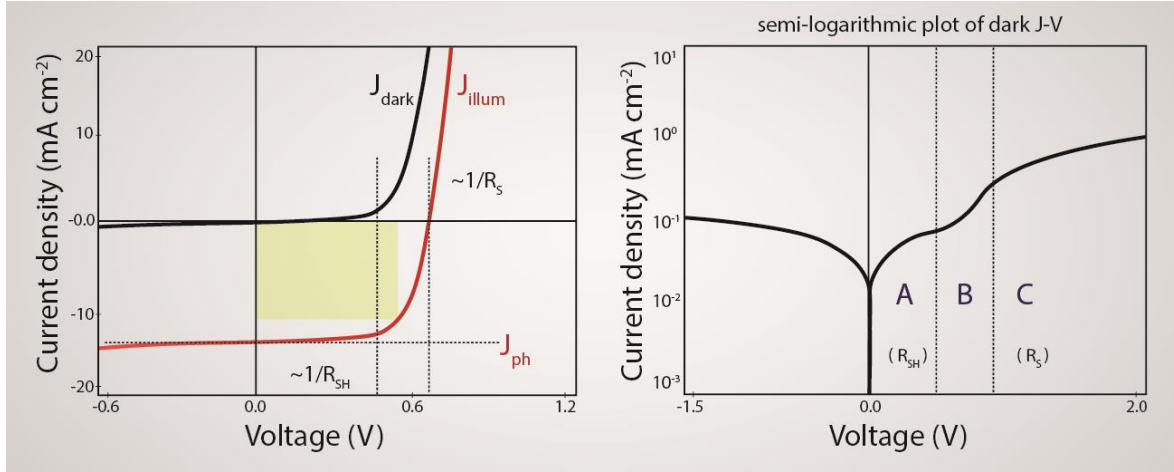
Figure.1.10. Typical current-voltage characteristics of bulk heterojunction organic solar cell under dark and illumination conditions and the same dark J-V curve plotted in a semi-logarithmic scale (adapted from ref.77).

From the equivalent circuit, the J-V curve can be constructed using the relation,

$$J(V) = J_0 \left[\exp\left(\frac{qV}{K_B T}\right) - 1 \right] - J_{ph} \tag{17}$$

Solving this relation at maximum power point can provide an expression for FF of an ideal solar cell without R_s and R_{sh} is given by,

$$FF_0 = \frac{v_{oc} - \ln(v_{oc} + 0.72)}{v_{oc} + 1} \tag{18}$$

Where $v_{oc} = {qV_{oc}}/{K_B T}$ is a dimensionless quantity. The above expression for an OSC will result in significant overestimation and needs to be modified.[75-76] The introduction of parasitic

resistance Rs, which is attributed to the resistance offered by the bulk of the active layer, contacts and the active layer-electrode contact resistance and R_{sh} is attributed to the current leakage induced by the pinhole in the OSCs modifies the expression for J(V) to,

$$J(V) = J_0 \left[\exp\left(\frac{qV}{K_B T}\right) - 1 \right] - J_{ph} + \frac{V - JR_s}{R_{sh}} \tag{19}$$

In this scenario, the J-V curve can be divided into three separate regions, as shown in the semi-logarithmic plot of the dark J-V curve in **Figure.1.10**. Region A is almost a straight line dominated by the shunt resistance, and the slope is given $1/R_{sh}$, followed by an exponential region (region B) governed by the diode characteristics and at higher voltages (region C) another straight line with slope ~ $1/R_s$. The J-V curve under illumination can be visualized as the dark J-V curve moved down by J_{ph}, if the photocurrent does not vary with the applied bias voltage. As mentioned earlier, the FF is the 'squareness' of the J-V curve under illumination in the fourth quadrant, indicating a low R_s and high R_{sh} can modify the slope of regions A and C so as to exhibit a better FF.[74, 77]

The modification of the expression for the J-V characteristic, including the diode ideality factor (*n*), which accounts for the recombination in the device, further modifies the FF. The diode current in a practical solar cell is given by the equation,

$$J(V) = J_0 \left[\exp\left(\frac{qV}{nK_B T}\right) - 1 \right] \tag{20}$$

A system with negligible recombination losses indicates a value of *n* ~1, but in practical solar cells with significant recombination present, the value of *n* will be in the range of 1-2.[78] Many semi-empirical relations based on the equivalent circuit model can be seen in the literature. In essence, the parameters Rs, Rsh, *n,* and J_0 influences the FF of an OSC significantly. The

competition between the carrier extraction and recombination in an OSC can thereby control the device FF, and a nearly ohmic transition at the active layer-electrode interface is essential to achieve high FF in OSCs.[74, 79]

1.3.2. Device Modelling of BHJ Organic Solar Cells

Device modelling of OSCs serves the purpose of providing considerable insights into processes which are difficult to probe using experimental techniques. The underlying principles of device modelling in OSCs are similar to many other thin-film solar cell technologies due to their commonalities. Irrespective of whether inorganic or organic thin-film solar cells, the architecture consists of a thin photo absorber layer, either an intrinsic or doped semiconductor sandwiched between two suitable electrodes.[80] However, the distinct characteristics of organic solar cells stem from the properties of organic semiconductors that can be incorporated into these models to optimize the simulation.[80-82] In general, when a photoactive layer is sandwiched between counter electrodes, a built-in electric field will come into existence that helps the process of charge separation. The simulation of OSCs using the drift-diffusion model is based on the drift and diffusion of the charge carrier population in which the drift of carriers is in response to the electric field, whereas the diffusion represents the random thermal motion of charge carriers due to concentration gradient.[83] The fundamental equations governing the processes are Poisson's equation and continuity equations given below,

$$\frac{\partial^2 \varphi}{\partial x^2} = \frac{-\rho}{\varepsilon} \tag{21}$$

$$\frac{dn}{dt} = G - R + \frac{1}{q}\frac{dJ_n}{dx} \tag{22}$$

$$\frac{dp}{dt} = G - R - \frac{1}{q}\frac{dJ_p}{dx}$$

(23)

Where φ is the electric potential, q is the elementary charge, ρ is the charge carrier density, ε is the electric permittivity in the material, G and R represent the carrier generation and recombination rates, n and p denote the electron and hole density and J_n and J_p are the current density due to electron and hole respectively. Poisson's equation establishes the relation between electric potential and space charge density, while the continuity equations represent the conservation of electron and hole density. Here x is the coordinate normal to the device plane, and t is the time. Under steady-state condition, $dn/dt = dp/dt = 0$ and the continuity equations can be written as,

$$\frac{-1}{q}\frac{dJ_n(x)}{dx} = -D_n\frac{d^2n(x)}{dx^2} - F\mu_n\frac{dn(x)}{dx} = G(x) - R(x,n,p)$$

(24)

$$\frac{1}{q}\frac{dJ_p(x)}{dx} = -D_p\frac{d^2p(x)}{dx^2} + F\mu_p\frac{dn(x)}{dx} = G(x) - R(x,n,p)$$

(25)

Where D_n and D_p represent the diffusivity, μ_n and μ_p represent the mobility of electron and hole, respectively, and F is the electric field. Here the drift and diffusion components of the current are separately represented, and the diffusivity and mobility are related by the Einstein's equation:

$$D_{n,p} = \frac{K_B T \mu_{n,p}}{q}$$

(26)

By applying suitable boundary conditions to the above continuity equations and Poisson's equation for carrier densities and potential at both the contacts, meaningful simulation can be performed, and insights into the underlying physical processes can be obtained.[83]

Approximations based on the mobility-lifetime product which are widely employed in inorganic semiconductor-based solar cells, were also implemented to gain insights into the device physics of OSCs. The charge collection efficiency is dependent on the mobility of the carriers and their lifetime, and a higher mobility-lifetime product $\mu\tau$ is desirable for high photocurrent in the device. Here μ represents the mobility of both electron and hole, and the lifetime of electron and hole is assumed to be nearly the same.

$$\mu\tau = \mu_e\tau_e + \mu_h\tau_h$$

(27)

Under an electric field, the effective length scale a carrier can travel can be approximated as $L_{drift} = \mu\tau$ before the carrier suffers recombination.

Apart from this, higher dimensional such as 2D and 3D modelling can also be found in the literature, which importantly includes the microstructure of the active layer in the simulation.[83]

1.3.3. Principle of Detailed Balance and Shockley-Queisser limit

It is important to discuss in this context the maximum efficiency that can be achieved from a single junction solar cell. According to the thermodynamic principles, the Carnot efficiency is estimated to be ~ 95%, assuming a source of temperature ~ 6000 K (at the surface of the Sun) and a sink of temperature ~ 300 K.[84] But under realistic conditions, this efficiency seems to be very less and the first of its kind of calculation trace back to the seminal paper by Shockley and Quiesser in 1961 when calculated the theoretical limit of efficiency of a single *p-n* junction solar cell.[85-86] The calculation was based on the following assumptions:

i. An ideal photon harvesting in which every single absorbed photon generates an electron-hole pair in the device

ii. Perfect charge collection in the device

iii.   Radiative recombination is the only recombination mechanism in the system

These assumptions imply that all the absorbed photons result in collectable charge carriers and as the recombination process involved in the system is only radiative indicating maximum carrier lifetime. In this scenario, as there is no non-radiative recombination, the splitting of the quasi-Fermi level and the V_{OC} will be maximum. The calculation shows a PCE ~ 30% for an optimal bandgap of ~ 1.1 eV. Many attempts to include real-condition physical processes and to estimate a more accurate practical limit to the efficiency of the solar cell were made in the later years. One such attempt by Archer et al. by considering AM1.5G solar spectra instead of black body radiation, estimates an upper limit of PCE ~ 33.7% for an optimal bandgap of ~ 1.34 eV.[87-88] **Figure.1.11**. shows the dependence of J-V parameters on the bandgap of the absorber and J-V characteristics of such as solar cell under AM1.5G solar illumination.[89]

As far as OSCs are concerned, many loss mechanisms, including significant non-radiative recombination loss and the excitonic nature of the charge pair, set the upper limit much lower than the values predicted in the above calculations. Various empirical models to predict the upper-efficiency limit in BHJ OSCs can be found in the literature, with the calculated PCE ranging from ~10-25%.[90] One such calculation by Coakley and McGehee in 2004 assuming an energy loss of ~ 1 eV during the charge transfer process from donor to acceptor LUMO predicts a PCE ~ 15% for an absorber of bandgap ~ 1.75 eV.[91] By introducing an empirical relation for V_{OC} relating to material energetics, with input mainly from PC$_{60}$BM as the acceptor in combination with a large number of donors, Scharber et al. predicted an upper limit to PCE ~ 10%. The empirical relation used in the calculation was

$$V_{OC} = \frac{1}{e}(E_{HOMO}^{D} - E_{LUMO}^{A}) - 0.3 \tag{28}$$

Where E_{HOMO}^{D} and E_{LUMO}^{A} are donor-HOMO level and acceptor-LUMO level, respectively, with a voltage loss of 300mV.[92] Later, in 2009, Kirchartz et al. calculated the radiative efficiency
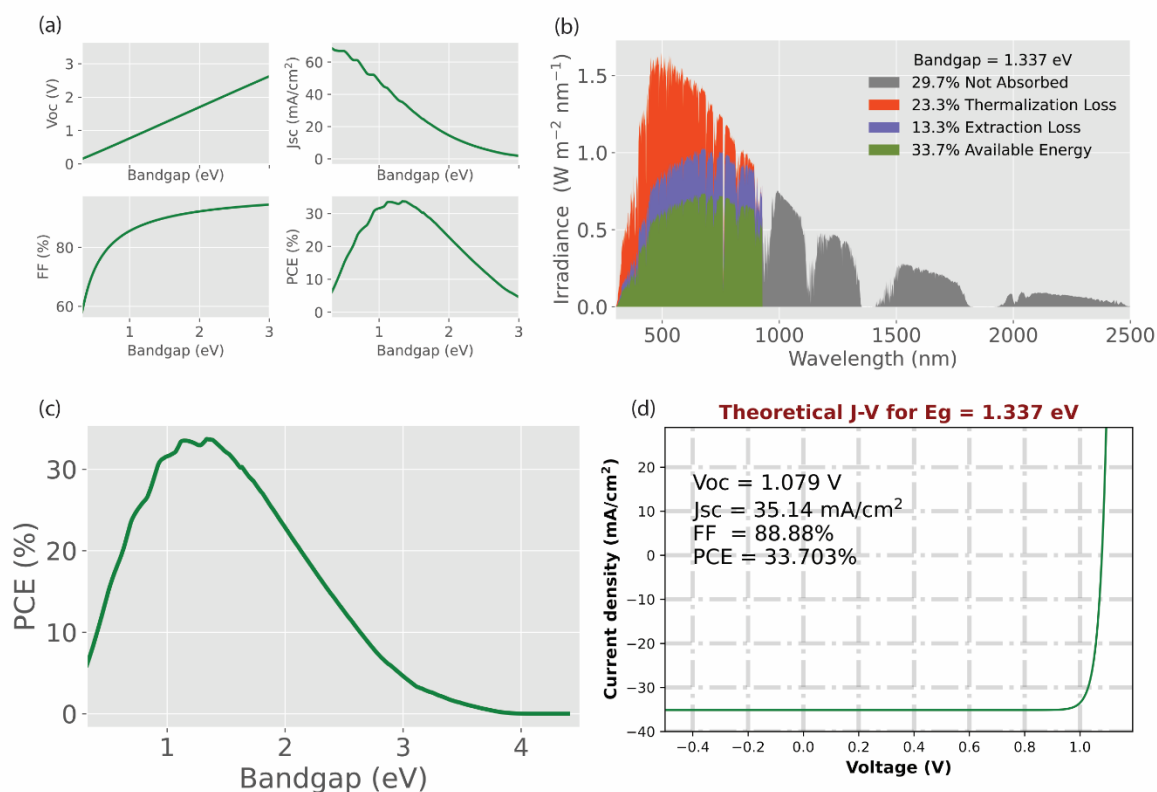
Figure.1.11. Summary of Shockley-Quiesser limit analysis (a) bandgap dependence of J-V parameters, (b) graphical representation of losses in harvesting AM1.5G solar spectra, (c) variation in power conversion efficiency with absorber bandgap and (d) J-V characteristic of a solar cell with ideal bandgap ~1.337 eV under AM1.5G illumination (adapted from ref.89).

limit in BHJ OSCs and proposed that efficiency could exceed 20% and pointed out several loss pathways leading to low PCE (the system used for the analysis only exhibited PCE ~ 4.2%).[93] These pathways are the loss associated with absorption, exciton dissociation losses, non-radiative recombination losses and charge collection loss due to low carrier mobilities. Also, an analysis by Vandewal et al. predicted a PCE ~ 28% by estimating the radiative limit in some low bandgap absorber blends using the detailed balance framework coupled with CT state emission.[94] These series of analyses reveal that under appropriate conditions, even OSCs can have efficiency close to their inorganic counterparts.[90]

With the advent of novel NFAs with significantly reduced recombination losses and carrier generation with a negligible energetic offset, such as ITIC derivatives or Y6 family in combination with PBDB-T series of donors, PCE ~ 20% is predicted to be within reach.[95] This excellent improvement is mainly driven by the development of novel D-A materials, and drift-diffusion simulation studies show that the immediate requirement is the balanced charge carrier mobility of the order of ~ 10^{-3} cm^2/Vs and further reduced non-geminate recombination (rate constant ~ 10^{-12} cm^3/s). This appears to be achievable with the above-mentioned material combinations indicating OSCs will be a front runner in PV technologies in the near future.[95]

1.4. Non-Fullerene Acceptors

Over the years, insights into the device physics of OSCs have been gained from the model system with fullerene derivatives ($PC_{60}BM$ or $PC_{70}BM$) as the acceptor molecule. The arrival of non-fullerene acceptors brought many puzzles that the scientific community still needs to understand, such as the negligible driving force required for the exciton dissociation and challenges such as identifying and mitigating the non-radiative recombination loss pathways.[64] In this section, some of the important non-fullerene acceptors and their salient features in the device perspective are outlined.

1.4.1. Fullerene versus Non-fullerene Acceptors

For the past two decades, OSC research has been dominated by employing fullerene derivatives such as $PC_{60}BM$ or $PC_{70}BM$ as the electron acceptor.[96-97] Advancements in the device performance were achieved largely by the design and synthesis of polymer donors. The polymer:fullerene OSCs were able to achieve PCE of over 11% during this period, and much of the device physics was understood using this model system.[98-99]
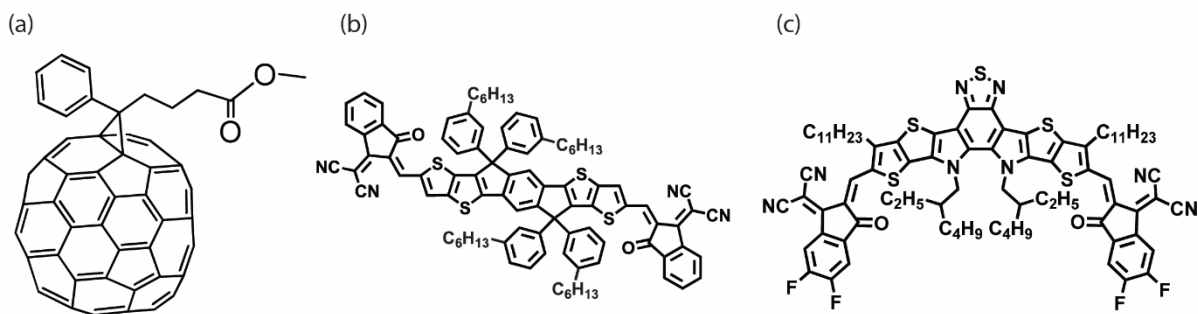
Figure.1.12. The chemical structure of (a) fullerene derivative acceptor molecule PC$_{70}$BM, (b) non-fullerene acceptor molecule ITIC and (c) non-fullerene acceptor molecule Y6, respectively.

The high electron mobility, the spherical structure of the molecule (3D character) and LUMO level are suitable for the exciton dissociation with most of the donors and favourable for balanced charge transport and optimal microstructure. Despite having these remarkable features intrinsically, there were many limitations to the fullerene derivative acceptors.[100] Importantly, these sets of acceptors have no significant absorption in the visible region of the solar spectrum. Apart from this, the chemical modification of the molecule is not straightforward, resulting in synthetic complexity and considerable limitation toward the bandgap tunability (tuning the LUMO level). The Purification of fullerene derivatives, particularly PC$_{70}$BM, is time-consuming, resulting in a high cost of material, making it difficult to achieve commercial viability. Further devices with fullerene derivatives as the acceptor show significantly low thermal stability and photostability.[101] The high sensitivity of fullerene derivatives to light and oxygen sensitivity and rapid aggregation of fullerene molecules in the active layer severely affects the charge transport and limits the device lifetime.[102-103] These factors were constantly persuading the scientific community for the design and development of acceptors with strong absorption in the visible region of the spectrum complementary to the donor and readily tunable electronic energy levels. Many attempts in this direction enabled the development of several sets of high-performing non-fullerene acceptors (NFAs).[104-105]
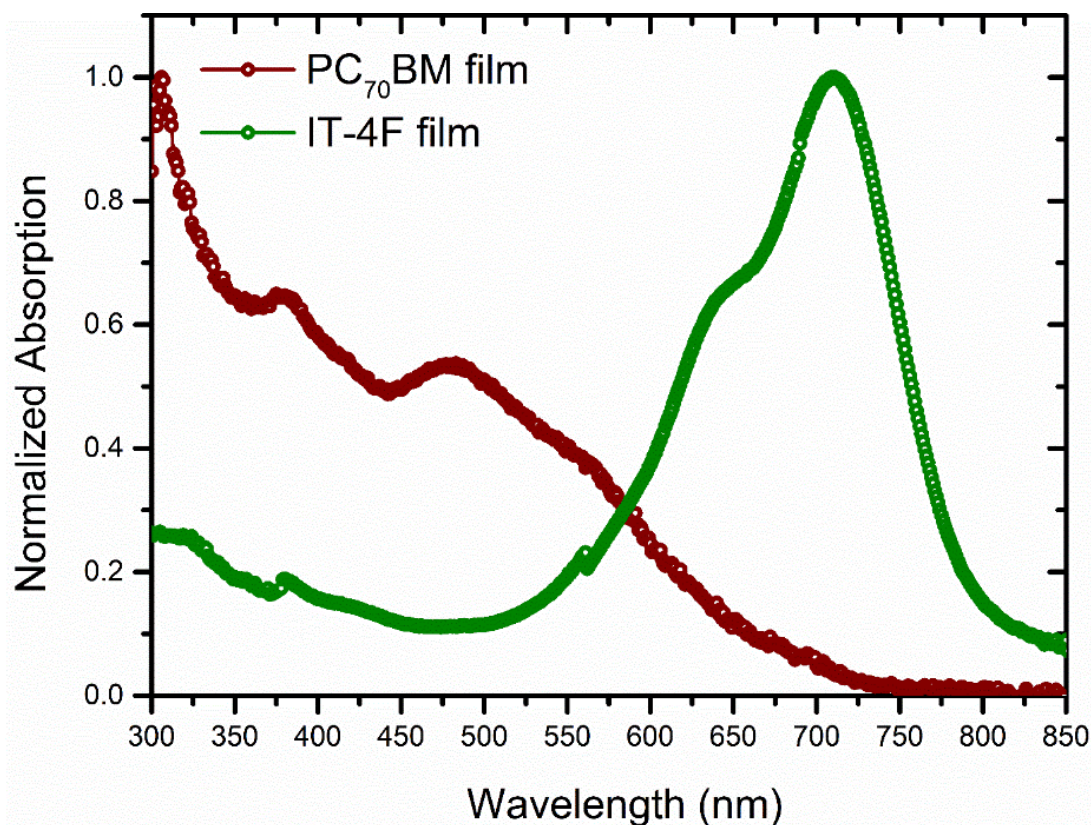
Figure.1.13. Typical normalized absorption spectra of fullerene derivative acceptor molecule PC$_{70}$BM and non-fullerene acceptor IT-4F thin films.

This includes rylene diimides such as perylene diimides (PDI) and naphthalene diimides (NDI), fused ring electron acceptors (FREAs) and non-fused ring electron acceptors (NFREAs).[104, 106-107] The FREAs such as ITIC and Y6 molecules brought in a paradigm shift with excellent improvements in PCE outperforming the fullerene-based devices, and PCE over 19% has been reported to date.[108-111] The development of the ITIC molecule in 2015 thus marked a milestone in the OSC research.[112-113] The major advantages of NFAs over fullerene derivatives are:

- Absorption in the visible and NIR region of the spectrum with a high absorption coefficient (~ 10^5 M^{-1}cm^{-1}).[100, 114]

- Synthetic flexibility to tune the electronic energy levels matching appropriately with the polymer donors.[115]

- Molecular design with strong intramolecular charge transfer effect.[116]

- Molecular design is suitable for fine-tuning crystallinity and miscibility.[117]

- High molecular weight is suitable for robust film formation and excellent thermal stability in the blend.[118]

The absorption spectra and electronic energy levels can be tuned readily by changing the push-pull strength in the NFA molecules. The ease of bandgap tunability in NFAs resulted in the synthesis of a large pool of acceptor molecules with significant enhancement in the PCE.[119] Along with some of the newly developed donors like PBDB-T and D18 having complementary absorption and excellent charge transport properties, it appears that the efficiency of over 20% is within reach using NFAs.[95] **Figure.1.13**. show the normalized absorption spectra of champion fullerene derivative PC$_{70}$BM and the NFA molecule IT-4F. The strong absorption in the visible and NIR region and high absorption coefficient enables superior photon harvesting in NFA-based OSCs. Further, an analysis of the absorption spectra of ITIC derivatives demonstrates excellent tunability and potential to blend with a large spectrum of donors and compatible acceptors in binary and ternary strategies, respectively.[120]

1.4.2. Various Types of Non-Fullerene Acceptors

Rylene diimides

Perylene diimide (PDI) small molecules, perylene diimide (PDI) polymers, and naphthalene diimide (NDI) polymers belong to this class of NFAs.[121] The history of rylene diimides can be traced back to the very first bilayer OSC in which a perylene diimide based acceptor was used by Tang and coworkers in 1986.[32] The early developments in rylene diimides were limited by the PCE of the solar cell employing these acceptors, while fullerene derivatives were performing comparatively better in BHJ OSCs.[112]

31
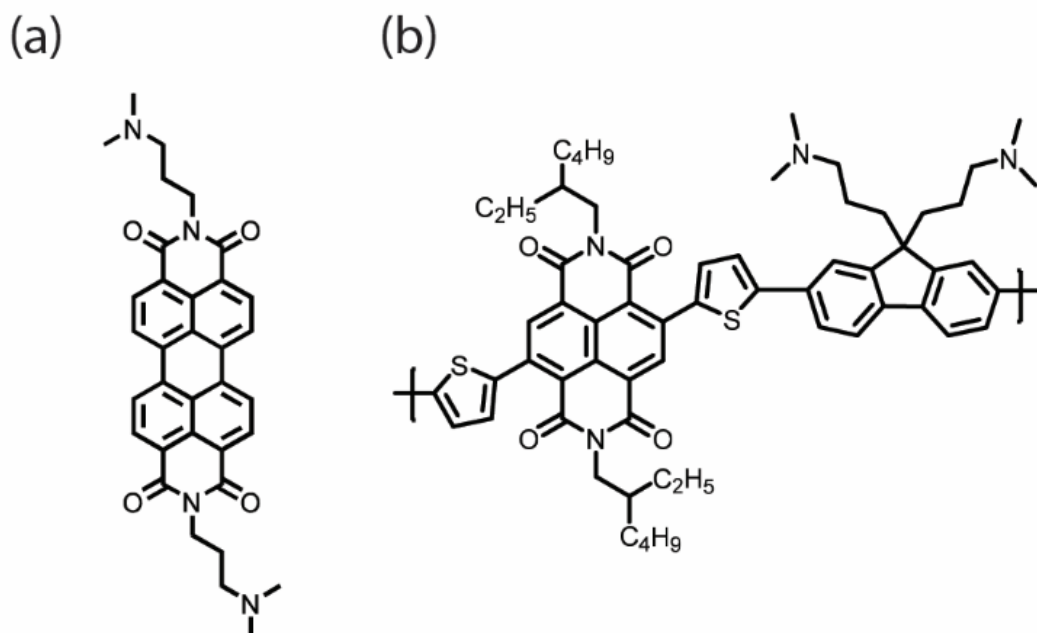
Figure.1.14. The chemical structure of rylene diimide electron acceptors (a) PDIN and (b) PNDITF-3N, respectively.

Despite having strong absorption in the visible region, one of the important reasons behind this efficiency lag for rylene diimides was rapid morphological evolution with strong aggregation behaviour and a tendency to form large crystals in the BHJ active layer. The 3D molecular structure of fullerene derivatives forms intercalating pathways for efficient charge transport with a large number of donors, while the 2D planar structure of rylene diimides with strong aggregation behaviour possessed a poor active layer morphology leading to weak charge separation and transport. Nevertheless, these shortcomings of early NFAs emerged as design rules for the high-efficiency NFAs developed recently.[107, 112, 122]

Fused ring electron acceptors (FREAs)

Acceptors like ITIC and Y6 have multiple fused rings in the core of the molecule, and this central core has some of the key functionalities.[109, 113] The presence of this donor unit in the

core of the molecule primarily enables a strong intramolecular charge transfer effect. The intramolecular charge transfer effect can improve the absorption and extend to the NIR region. Further, the coplanar backbone of the molecule helps the delocalization of π electrons and enables strong intermolecular π-π interactions resulting in improved charge transport. In FREAs importantly, two types of molecular design are present: A-D-A and A-DA'D-A models.
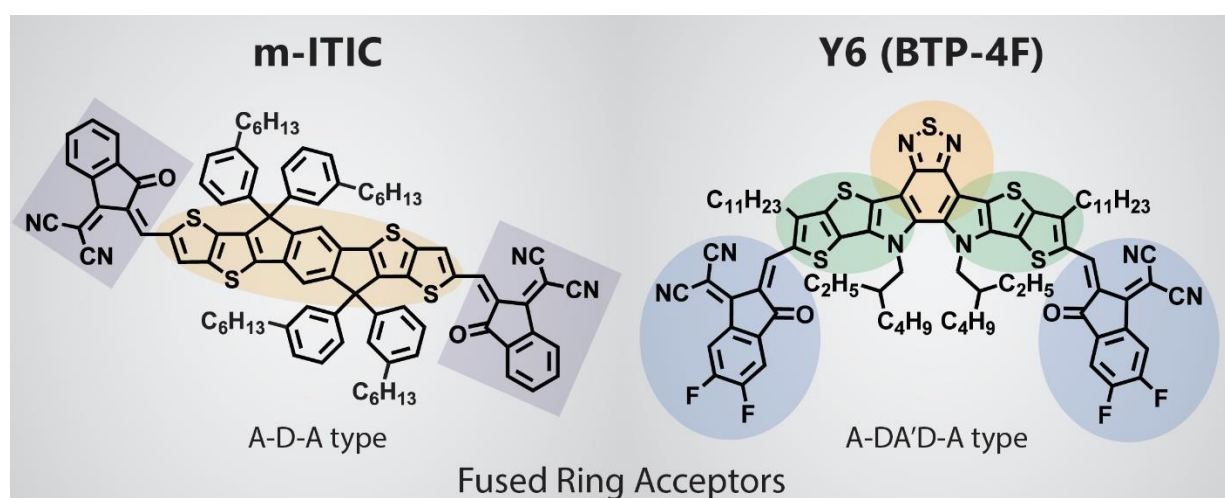
Figure.1.15. The chemical structure of fused-ring electron acceptors m-ITIC and Y6, respectively (adapted from ref.64).

Figure.1.15 show the chemical structure of ITIC and Y6 acceptor molecules, which are employed in recently reported high-efficiency OSCs. The ITIC molecule and its derivatives belong to the A-D-A type, which constitutes a central electron-donating core unit (D) and two electron-withdrawing acceptor units (A) as the end groups. The modification of the push-pull strength of these D and A units can readily tune the electronic energy level and the absorption spectra of the acceptor molecule. The fused core unit in this A-D-A type acceptor molecule is indacenodithiophene (IDT) derivatives which improve absorption to the NIR region. The electron-withdrawing end groups also play a crucial role in deciding the morphology and

solubility of the acceptor and tuning the electronic properties. The molecular design of the Y6 acceptor belongs to an A-DA'D-A design in which an electron deficit benzothiadiaole (BT) unit is incorporated in the fused ring.[123] This modification can improve the D-A interaction and, consequently, the charge carrier mobility. The presence of a pyrrole bridging group with a strong electron-donating tendency help to upshift the HOMO level, thereby reducing the bandgap. At the same time, the large alkyl chain attached to the N atom in the pyrrole group significantly reduces the aggregation behaviour due to steric hindrance.[116]

This feature of narrow bandgap in the Y6 acceptor molecule enabled a strong NIR absorption and enhanced J_{SC} in the devices. These properties arising from the rational design resulted in all the highest PCE-reported OSCs based on FREAs as the acceptor component, surpassing both fullerene derivatives and rylene diimides.

Non-fused ring electron acceptors (NFREAs)

The excellent improvement in PCE of OSCs employing FREAs exceeding 18% indicates the commercialization capabilities in the near future. However, despite having high performance, the commercial viability of FREAs is limited due to high synthetic complexity and production cost. In order to overcome this challenge, concentrated efforts are in place to design and develop non-fused ring electron acceptors (NFREAs) with largely reduced synthetic complexity. The key design strategy in the development of NFREAs is replacing the fused ring core with a single bonded structure. Further, the electronic energy levels and molecular packing can also be readily modified with appropriate units. Recently, an impressive PCE of ~15.2% were able to achieve using NFREA (A14-16) based on a bithiophene-based building block.[124] This efficiency is almost comparable with that of high-performing FREAs with superior photostability, indicating the importance NFREAs in OSC technology development.[125]

Figure.1.16 show non-fused ring electron acceptors DF-PCIC and HF-PCIC, when blended with suitable donors PBDB-T and PBDB-T-F, respectively, exhibit PCE > 10%. Both the NFREA molecules have an A-D-D'-D-A type structure, and HF-PCIC is designed to overcome the low J_{SC} in devices with acceptor molecule DF-PCIC. In DF-PCIC, the central non-fused ring core unit is connected to two cyclopentadithiophene units by single bonds, whereas in the HF-PCIC is a modification with a strong electron-withdrawing end group to increase the intramolecular charge transfer effect. The molecules exhibit similar absorption spectra to that of ITIC molecule and performance parameters close to it with significantly reduced synthetic complexity.[125-127]
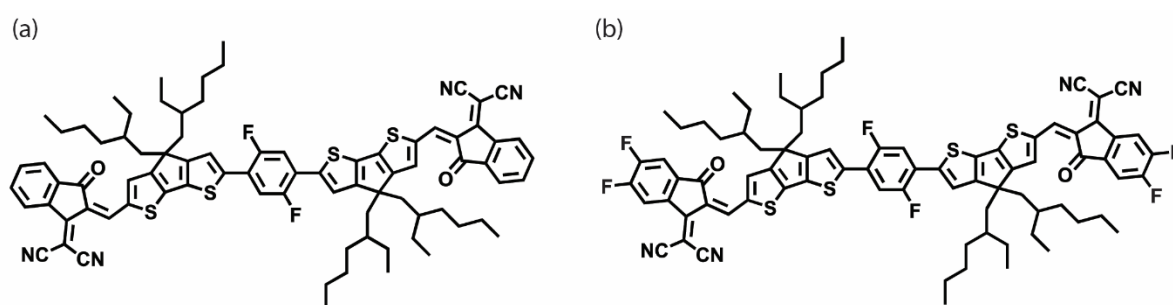
Figure.1.16. The chemical structure of non-fused ring electron acceptors (a) DF-PCIC and (b) HF-PCIC, respectively.

From the device point of view, the excellent performance of NFAs employed OSCs is characterized by the exciton dissociation with a small energy offset. **Figure.1.17** show the electronic energy levels of PC$_{70}$BM molecule, NFAs ITIC and Y6, along with the most compatible and one of the high-performing donor PM6. This indicates that a blend of donor PM6 and non-fullerene acceptor ITIC shows excellent exciton dissociation and high PCE despite a negligibly small energetic offset. The low energetic disorder of NFAs can be attributed to the sharp absorption onset and reduced voltage loss. For a good OSC, the blend

morphology is critical in which importantly, optimum domain size and purity are necessary. Apart from this, percolate, and continuous charge transport pathways and a favourable molecular orientation are also important. The planar conformation and better molecular packing lead to a more stable morphology of NFA based OSCs. On the other hand, the phase purity in the blend is better for fullerene derivatives due to their spherical geometry, but the phase purity can be improved in NFAs as well by improving the molecular crystallinity. **Table.1.1** show the J-V parameters of the highest efficiency reported systems to date using various types of NFAs along with the champion fullerene derivative acceptor $PC_{70}BM$-based system. The high short circuit current density and PCE are obtained when FREAs are blended with suitable donors.[107]
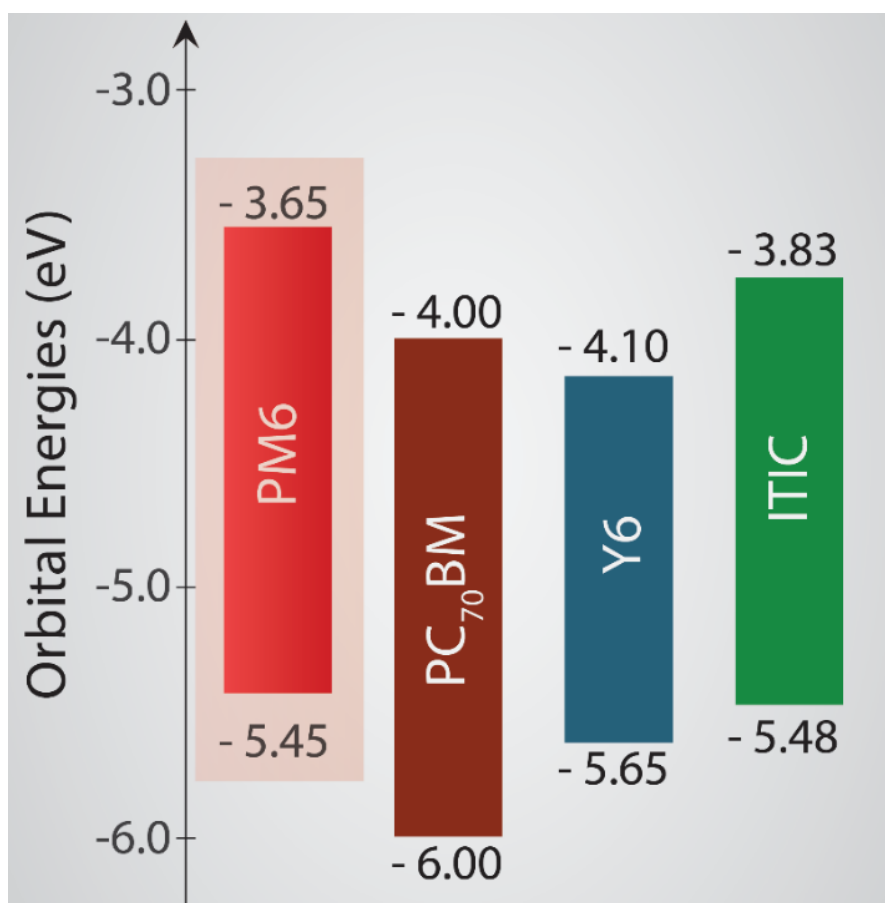
Figure.1.17. Orbital energy diagram of donor PM6 and acceptors $PC_{70}BM$, Y6 and IT-4F.

Table.1.1. The performance parameters of highest efficiency reported NFAs belonging to various types of molecular designs along with the champion fullerene derivative-based OSC.

Donor(s)	Acceptor	V_{OC}	J_{SC}	FF	PCE	Reference
DR3TSBDT:PTB7-Th	$PC_{70}BM$	0.772	23.31	70.44	12.10	98
PDBT-T1	6a[a]	1.001	12.53	71.7	8.98	128
PBDB-T-2Cl	IT-4F[b]	0.890	20.58	78.0	14.29	111
PBDB-T-2F	Y6[b]	0.856	25.73	76.8	16.94	129
PBDB-T-2F	L8-BO[b]	0.870	25.72	81.5	18.32	130
PBDB-T-2F	HF-PCIC[c]	0.910	17.81	70.77	11.49	127
PBDB-T-2F	A14-16[c]	0.876	21.8	79.8	15.2	124

(a) Rylene diimide, (b) fused-ring electron acceptor and (c) non-fused ring electron acceptor.

1.5. Ternary Blend Organic Solar Cells

Ternary strategy in which a blend of three photoactive materials constituting the active layer of OSC has shown to improve the device performance.[131-133] Ternary and tandem strategies are generally adopted to improve binary OSCs device performance further.[134-135] Due to significantly reduced fabrication complexity, single-junction BHJ OSCs are preferred over tandem device architecture. In this regard, ternary blend organic solar cells (TBOSCs) are ideal due to improved photon harvesting and facile device fabrication processes.[136] TBOSCs have several advantages over binary devices, summarized in **Figure1.18**. The highest PCE reported single-junction OSCs to date are based on ternary blend strategy, whether its fullerene

derivative or non-fullerene molecule as the acceptor component (see **Table.1.2**).[98, 137] TBOSCs based on a combination of polymers and small molecules along with all-polymer and all-small molecule blends have significantly improved device performance.[132] A small molecule as the third component in a polymer/small molecule binary BHJ has been shown to optimize the morphology by improving crystallinity along with improving the overall absorption.[131, 138] The polymer-polymer-small molecule TBOSCs are set forth to improve the absorption of the blend as the polymer donors usually exhibit a narrow absorption window.[139] The third component, usually a polymer donor, in this case, assists the charge transport and dissociation, along with broadening the absorption window. As a natural extension to the all-polymer binary BHJ OSCs, all-polymer TBOSCs are also introduced, which show superior device performance.[136] All small-molecule TBOSCs are interesting due to the superior reproducibility of high-performing devices owing to the characteristics of small molecules such as well-defined structure, molecular weight and high purity.[140-141]
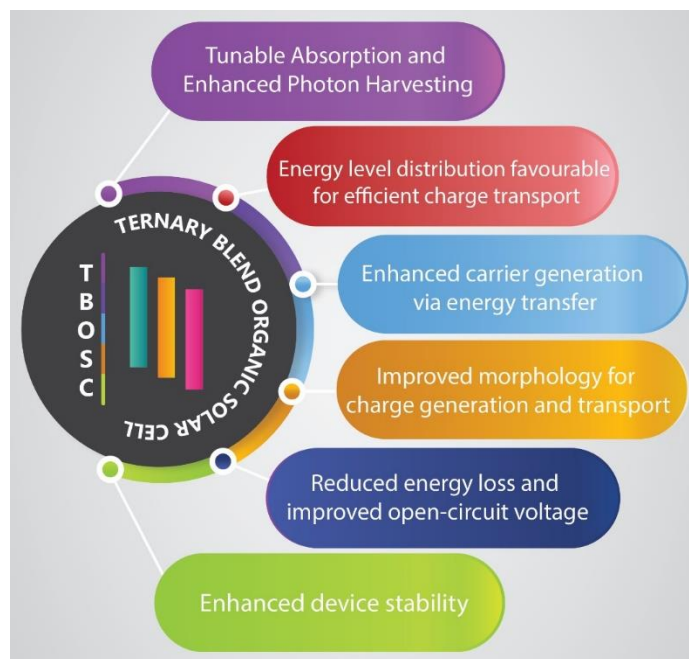
Figure.1.18. Infographic depicting the advantages of ternary blend organic solar cells over binary organic solar cells.

Rational choice of the third component in an optimal amount can enhance the photon harvesting and, subsequently, the device performance metrics of the binary device. Morphological modification brought in by the third component has shown to improve the device stability in specific combinations of donor-acceptor (D-A) systems. Though ternary strategy is a well-established technique in BHJ OSCs, with the development of NFAs, this technique has consistently improved the device efficiency of the binary system on many champion D-A combinations.[142] Apart from the enhanced absorption window broadening and morphological modifications of the active layer, different device engineering strategies for these high-performing ternary devices can also push the PCE further. In this regard, a comprehensive understanding of the role of the third component in charge transport physics is necessary. The presence of the third component (either a donor or an acceptor) in a D-A system can impact the device physics of the OSC in different ways depending on the electronic energy levels and various other molecular properties.[132-133]

Table.1.2. The performance parameters of highest efficiency reported ternary blend organic solar cells and the corresponding binary devices in which the third component was introduced.

Binary Components	Third Component	V_{OC} (V)	J_{SC} (mA cm^{-2})	FF (%)	PCE (%)	Reference
PTB7-Th:Y6		0.67	20.16	56.77	7.71	[143]
PTB7-Th:Y6	PC$_{70}$BM	0.67	24.68	58.02	9.55	[143]
PM6:Br-ITIC		0.937	18.53	72.7	12.63	[144]
PM6:Br-ITIC	J71	0.930	19.39	78.4	14.13	[144]
PM6:IT-4F		0.869	20.26	77.4	13.62	[145]

PM6:IT-4F	N7IT	0.890	22.54	74.8	15.02	[145]
PM7:IT-4F		0.890	20.58	78.0	14.29	[111]
PM7:IT-4F	PC$_{60}$BM	0.875	20.7	77.2	14.0	[146]
PM7:IT-4F	PC$_{70}$BM	0.872	21.2	77.3	14.3	[146]
PM6:Y6		0.820	25.20	76.1	15.7	[109]
PM6:Y6	PC$_{70}$BM	0.861	25.10	77.2	16.7	[146]
PM6:Y6	D18	0.852	25.55	72.8	15.85	[147]
PM6:Y6	ITIC	0.879	25.50	74.20	16.6	[148]
PM6:Y6	BTP-M	0.875	26.56	73.46	17.03	[149]
PM6:Y6	IT-4F	0.844	25.40	75.9	16.27	[150]
PM6:Y6	BTF	0.853	26.11	74.22	16.53	[151]
PM6:Y6	J71	0.850	25.55	76.0	16.50	[152]
PM6:Y6	S3	0.856	25.86	79.17	17.53	[153]
PM6:Y6	AQx-3	0.870	26.82	77.2	18.01	[129]
PM6:BTP-4F-12		0.850	24.50	77.9	16.2	[154]
PM6:BTP-4F-12	MeIC	0.863	25.40	79.2	17.4	[154]
PM6:BTP-eC9		0.845	26.81	77.5	17.58	[155]

PM6:BTP-eC9	BTP-F	0.858	26.99	79.7	18.45	[155]
PM6:N3		0.837	25.81	73.9	15.98	[156]
PM6:N3	PC$_{70}$BM	0.840	26.85	78.0	17.60	[157]
PM6:C9		0.852	26.58	76.73	17.38	[158]
PM6:C9	PM6-Si30	0.870	26.90	78.04	18.27	[158]
PM7:Y6		0.868	24.98	71.42	15.49	[159]
PM7:Y6	PC$_{70}$BM	0.868	25.44	75.66	16.71	[159]
D18-Cl:Y6		0.881	25.53	75.88	17.07	[160]
D18-Cl:Y6	Y6-1O	0.900	25.87	76.92	17.91	[160]
D18-Cl:L8-BO		0.888	25.10	77.80	17.37	[155]
D18-Cl: L8-BO	L8-BO-F	0.902	25.30	78.30	17.83	[155]
D18-Cl:N3		0.859	27.85	75.70	18.13	[161]
D18-Cl:N3	PC$_{60}$BM	0.849	28.22	78.0	18.69	[161]
PBQx-TF:eC9-2Cl		0.868	25.9	78.6	17.7	[162]
PBQx-TF:eC9-2Cl	F-BTA3	0.879	26.7	80.9	19.0	[162]
D18:L8-BO		0.907	24.9	78.5	17.7	[135]
D18:L8-BO	PM6	0.896	26.7	81.9	19.6	[135]
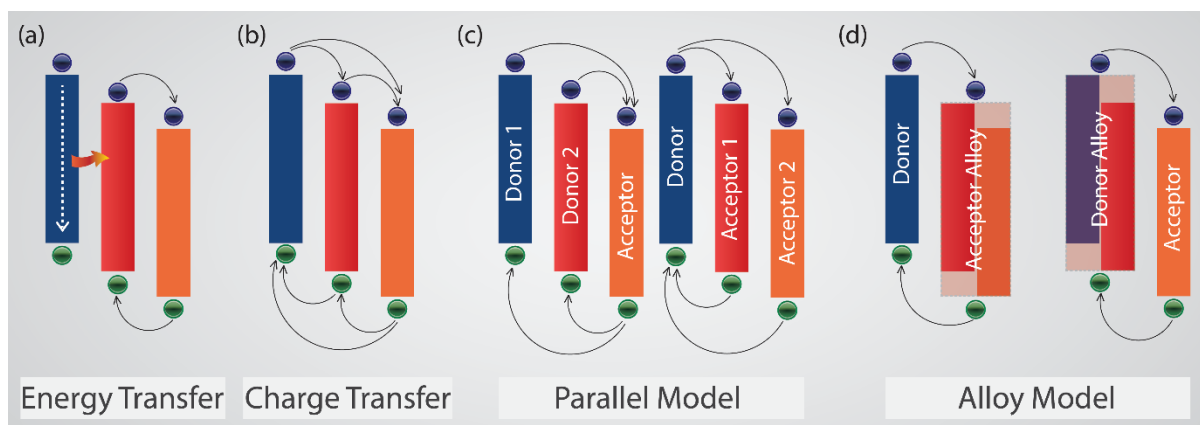
Figure.1.19. Graphical representation depicting the various charge transport models in a ternary blend organic solar cell using orbital energy levels of constituent elements (adapted from ref.163).

Multiple charge transport models have been proposed depending on the alignment of electronic energy levels of the third component in the binary system. These are charge transfer, energy transfer, parallel-like and alloy models.[163] The charge transfer mechanism refers to an ideal step-like alignment of energy levels, the overlap between the emission of one component and absorption of another can lead to energy transfer. Efficient charge transfer between the components equivalent to two D-A systems refers to the parallel-like model. In the case of the alloy model, either a donor alloy (or acceptor alloy) establishes charge transport with the acceptor (or donor), similar to a single D-A system. On the other hand, optimization of active layer morphology is a deciding factor in enhancing the efficiency and stability aspects of the ternary device. Efforts to correlate the distribution of the third component in a bi-continuous D-A phase to the device performance and morphological stability still need a neat framework. The thermal properties and miscibility of various constituting components are crucial in extracting the best performance of the device. Further, the weight ratio of individual components in the BHJ and its correlation to the device parameters, specifically the V_{OC}, needs to be understood.[164]
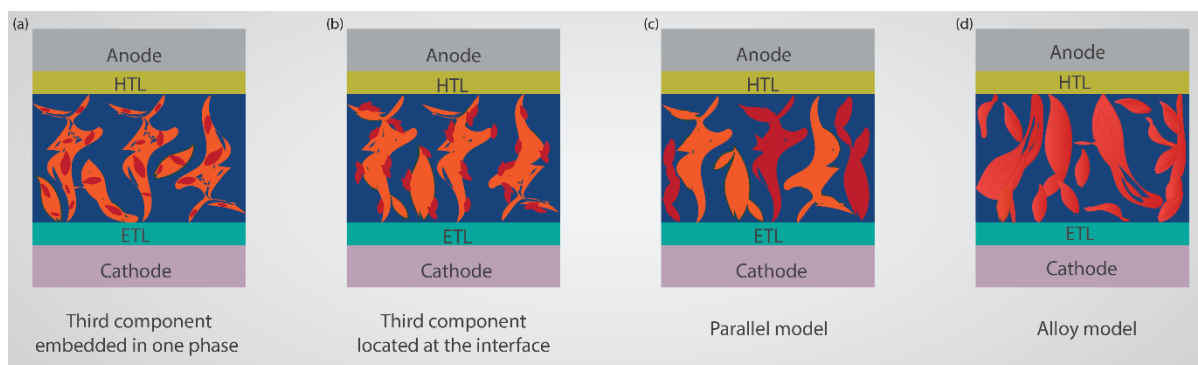
Figure.1.20. Graphical representation depicting the various charge transport models in a ternary blend organic solar cell using the morphology of the bulk heterojunction active layer in inverted device architecture (adapted from ref.163).

The presence of multiple chromophores in the BHJ blend provides the advantage of the possibility of energy transfer between the constituent components in the blend. The fluorescence or Forster resonance energy transfer (FRET) mechanism is an effective strategy to enhance the performance of BHJ OSCs.[132] FRET is a process in which a donor transfers energy to an acceptor non-radiatively through dipole-dipole interaction. The necessary condition for FRET to occur in a system is that the emission spectrum of the FRET donor must overlap with the absorption spectra of one of the constituent elements in the system. Apart from this, for an efficient FRET, the donor and acceptor elements must be within a specific length scale called the Forster radius (R_0). The value of R_0 is system dependent and can vary from nearly 1 nm to 10 nm. The fluorescence lifetime and quantum yield of the donor and the quenching efficiency of the acceptor also influence the FRET occurrence in the blend.[132, 164-165]

$$D^* + A \rightarrow D + A^*$$
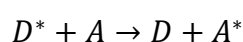
The rate constant of FRET is given by the expression,

43
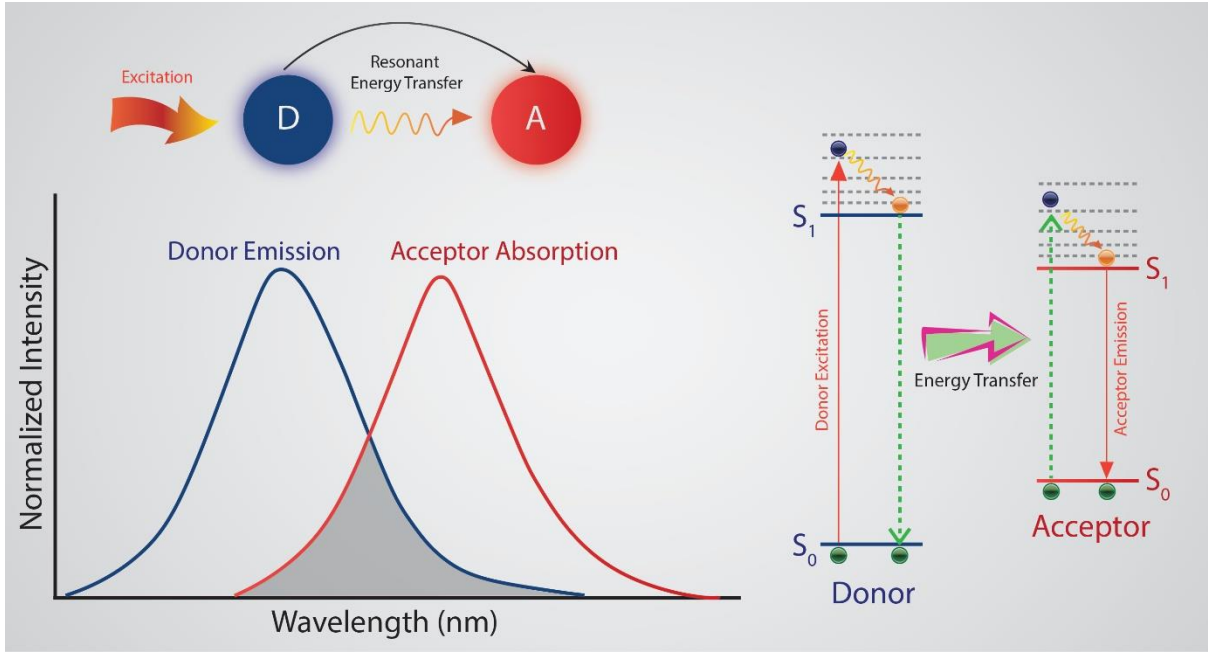
Figure.1.21. Schematic diagram depicting the FRET mechanism in a ternary blend organic solar cell.

$$K_{FRET} = \frac{1}{\tau_D} \left(\frac{R_0}{R}\right)^6 \tag{29}$$

Where τ_D is the fluorescence lifetime of the FRET donor in pristine form and R is the distance between the donor and acceptor.

The FRET efficiency can be calculated as,

$$E_{FRET} = \frac{1}{1 + \left(R/R_0\right)^6} = 1 - \frac{\tau_{DA}}{\tau_D} \tag{30}$$

here τ_{DA} is the lifetime of the donor emission in presence of the acceptor. The steady-state photoluminescence (PL), time-resolved photoluminescence (TRPL) and transient absorption spectroscopy (TAS) can be used as experimental tools to probe the FRET mechanism in a blend. The presence of FRET in the BHJ system can benefit in several ways, including enhanced exciton diffusion length. For instance, McGehee et al. showed that in a strongly

Coulomb coupled D-A system, exciton harvesting over a distance of more than 25 nm is possible with an order of magnitude increase in the effective exciton diffusion length.[166] Thus, the FRET mechanism in a BHJ system can improve the $J_{SC,}$ whereas the effect of FRET on V_{OC} and FF still needs to be uncovered in detail.

1.6.   Stability of Organic Solar Cells

The unprecedented efficiency improvements in OSCs with the arrival of small molecule non-fullerene acceptors reaffirmed the potential for successful commercialization.[129, 167] At this juncture, the stability of the OSC is the major concern as the performance of these devices degrades rapidly compared to the inorganic counterpart (Si, CdTe).[168] In comparison with the tremendous efforts toward efficiency enhancement, the stability aspects are less explored in the OSCs, and there is a need for a fundamental understanding of the degradation mechanism. [169-170] To put in perspective, some of the high-performing D-A combinations with initial PCE above 15% degrade within a day, even in dark conditions.[171] This section briefly discusses the general degradation behaviour in OSCs along with the factors causing degradation. Further, the stability aspects of NFA-based systems and the impediments to achieving a long life compared to the inorganic solar cells will be outlined.

1.6.1. Degradation Process in Organic Solar Cells

As mentioned earlier, the deterioration of device performance in OSCs is substantially faster as compared to inorganic or hybrid PV technologies. The important reason behind this rapid degradation can be attributed to the intrinsic instability of organic semiconductors.[169, 172] The degradation pattern in OSCs comprises two stages: (1) an exponential decay in device performance during the initial period of an operation termed the 'burn-in' degradation,

followed by (2) a comparatively slow decay in device performance until the failure of the device termed as the long-term degradation (**Figure.1.22**).[169] The 'burn-in' degradation is substantial in OSCs as compared to other PV technologies, and even with high-performing NFAs, it has been reported to ~50% drop in efficiency within a timescale of 24 hours in dark conditions.[171, 173]
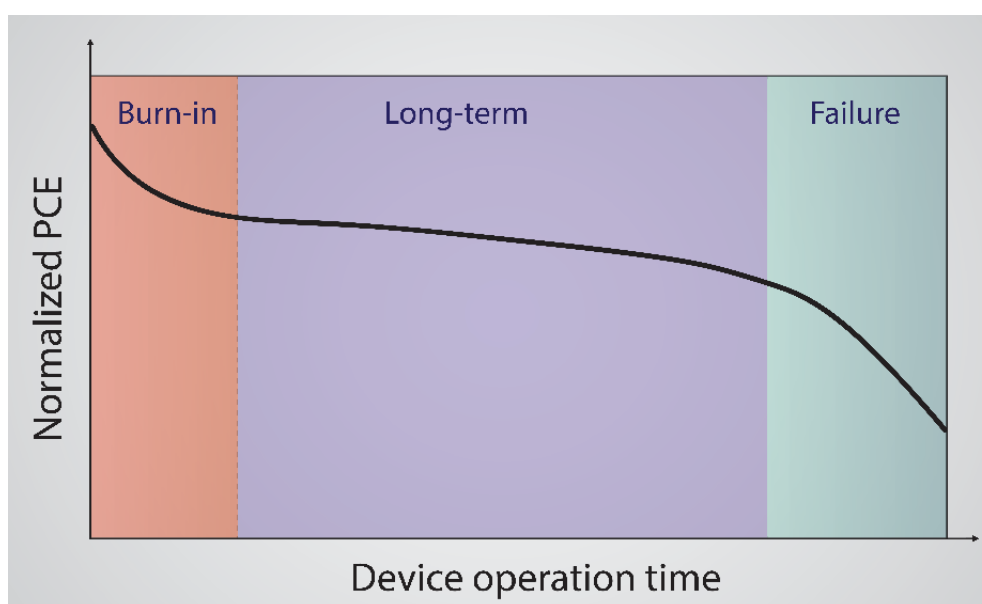
Figure.1.22. Schematic depicting the various stages of degradation in a typical organic solar cell (adapted from ref.169).

Understanding the degradation in general and the 'burn-in' degradation, in particular, is important for the commercial viability of OSCs as it needs to perform consistently throughout their lifetime.[174-175] Various intrinsic and extrinsic factors contribute to the degradation of OSCs and are summarized in **Figure.1.23**.[174] The extrinsic factors include light, heat, oxygen ingression, moisture, and electrical and mechanical stress. The intrinsic factors are degradation in the dark due to chemical reactions between different layers and the chemical stability of the OSC constituents. In OSCs based on fullerene derivatives as the acceptor, aggregation and

vertical stratification of PCBM molecules upon thermal stress have shown to reduce the D-A interface and consequently a reduced charge transport and performance.[172, 176] The aggregation and crystallization of PCBM molecules within the active layer result in fullerene aggregates of size on a microscale, significantly reducing the interpenetrating D-A interfaces and reduction in J_{SC}.[177] The aggregation tendency can be reduced by using solvent additives during solution processing, and the introduction of specially designed cross-links can also reduce the aggregate formation. The dimerization of $PC_{60}BM$ acceptor molecules under illumination conditions is a detrimental effect which modifies the electronic properties and is identified as the reason behind J_{SC} loss in degraded OSCs.[103, 178-179] The use of $PC_{70}BM$ or higher adduct fullerenes as acceptors can significantly reduce the detrimental effect due to photo-dimerization, and it must be noted that the dimerization can be reversed in PCBM at elevated temperatures.[103]

Figure.1.23. Infographic depicting the various factors causing degradation in organic solar cells.

The device degradation due to extrinsic factors can be substantially minimized with the encapsulation of the device.[180] Some of the commonly used encapsulants include ethylene-vinyl acetate (EVA), UV-cured epoxy, polyisobutylene (PIB) and organic materials such as PMMA, and PVMK. The major benefit of the encapsulation technique is that it can prevent oxygen and moisture ingression into the active layer and interfacial layers in the device.[180-181] This will reduce the unwanted photochemical and thermochemical modifications of the constituent materials and oxidation of the electrodes. The encapsulation barrier layer requires chemical stability, mechanical strength, high photostability and thermal stability.[180] Otherwise, the disintegration of this barrier layer and its reaction with various layers in the device can have a further detrimental impact on device performance. Many UV-curable resin-based encapsulants suffer from photodegradation and thermal oxidation, and a high processing temperature of the encapsulant layer is not desirable.[169, 180-182]

1.6.2. Stability Aspects of NFA based Organic Solar Cells

The stability of NFA acceptor based OSCs is highly dependent on the material properties of the acceptor molecule employed. But in general, the stability of NFA based devices is superior to their fullerene-based counterparts.[120, 170, 172] Recently, Stephen R. Forrest et al. reported an extrapolated device lifetime of ~ 30 years after accelerated aging studies in NFA BT-CIC based devices.[183] Earlier, in a similar analysis along with long-term J-V monitoring, Brabec and coworkers estimated ~ 10 years of a lifetime for IT-4F based inverted OSCs.[167] The essential takeaway from these results is the potential of high performing NFA based OSCs ability to perform intrinsically similar to the inorganic counterpart. As promising efficiency is obtained using recently developed NFAs, understanding stability implications in these systems are extremely important. The thermal stability of NFA based OSCs is superior compared to the

fullerene counterpart, partly due to the anisotropic molecular structure with rigid backbones, making them less mobile in the blend.[120] The thermal transition temperature of the NFA molecule plays a critical role in morphological stability, and in general, a high thermal transition temperature is desired (>100°C).[169, 184] High thermal transition temperature can slow down the diffusion and crystallization of the component providing stable morphology over a long period.[184] Apart from this, the parameters such as miscibility, crystallinity, domain size and purity and morphological evolution during the operation, such as mixing and de-mixing of the constituents, are also critical.[184] Some of the early stability reports in NFA based BHJs demonstrate that the optimal miscibility, domain size, domain purity along with balanced nucleation, aggregation and crystallization can be achieved due to the synthetic flexibility of NFAs.[120]

1.6.3.   Challenges to improving the stability

The availability of a vast amount of D-A combinations combined with system-specific degradation mechanisms makes it challenging to propose a general set of frameworks for long-term stability applicable to all OSCs.[184-185] A general framework to identify and eliminate rapidly degrading combinations may help to isolate and concentrate on combinations which are promising, and this requires a detailed understanding of degradation and its relation with material properties. The significant 'burn-in' degradation in most of the OSCs is another major challenge that needs to be addressed.[174] A set of design rules for 'burn-in' free OSCs requires detailed investigations to understand the degradation mechanism induced by various contributing factors. The intrinsic chemical stability of NFAs needs to be improved by considering the effects of interaction with interlayers and photo-thermal stress.[172] The fragile C=C in NFAs tends to weaken in a short period of operation due to the interaction with

interlayers in the presence of external stress factors such as light, heat, moisture and oxygen.[174, 186-187] The morphological instabilities of NFA based devices are largely dependent on the compatibility with the choice of donor molecule, and it is important to screen the potential of a particular NFA with the material properties. This requires an in-depth understanding of the morphology formation and evolution in BHJ OSCs. The planar conformations of NFAs combined with the insights on molecular packing and interaction from single crystals of NFAs can shed more light on desired film formation. The real operation condition of OSCs further involves thermal and light cycles, and the impact of this phenomenon is particularly important.[188] Effective encapsulation techniques with facile processing requirements need to be developed to minimize the effect of extrinsic factors.[180-181] Along with it, optimizing the device by simultaneously considering both efficiency and long-term stability is necessary for high performing OSCs.[174-175]

1.7.   Thesis Outline

This thesis focuses on device processing strategies to enhance the efficiency and stability of high performing fused-ring electron acceptors IT-4F and Y6-based binary bulk heterojunction OSCs. Along with strategies to improve NFA-based OSCs efficiency, this thesis investigates underlying mechanisms in the device degradation and proposes routes to mitigate the same.

The first part of the thesis focuses on improving the efficiency of NFA IT-4F-based inverted OSCs, in which ZnO is the cathode interlayer. The contact selectivity at the cathode interface improved by introducing a thin $PC_{70}BM$ interlayer along with the standard electron transport layer ZnO. The combination of ZnO and $PC_{70}BM$ layers between the cathode and bulk heterojunction active layer can reduce charge transport barriers and significantly enhance short-circuit current density and PCE. Impedance spectroscopy and electrical noise measurements

reveal reduced charge transport barriers at the cathode interface due to the presence of the interlayer. The study suggests the potential of $PC_{70}BM$ as an interlayer material to further improve the performance of NFA IT-4F-based OSCs.

In the next part of the thesis, a comprehensive investigation of light-induced and temperature-induced-degradation in NFA IT-4F based OSCs with emphasis on the initial period of operation ('burn-in') has been studied. Unlike other PV technologies, 'burn-in' degradation is a significant concern in OSCs. In certain combinations of D-A systems, more than half of the initial PCE is lost during the 'burn-in' period. The magnitude of 'burn-in' degradation is largely D-A system-specific and depends on device geometry and processing conditions. In this investigation, the mechanism of light and temperature-induced degradation in one of the highest stability established IT-4F based OSCs with the more stable inverted geometry. Monitoring current-voltage characteristics upon accelerated aging stresses in inert conditions revealed that significant degradation occurs due to the UV components present in the light illumination. Steady-state optoelectronic measurements and spectroscopic studies provide significant insights into the degradation mechanisms, including the bulk and interfacial charge transport barriers. Further, attempts were made to understand the detrimental effects of the commonly used solvent additive DIO (1,8-diiodooctane) in device degradation. Discerningly tailored experimental condition provides considerable insights into the origin of degradation from different aging stress factors. The study suggests the importance of preventing UV components through suitable barrier layers or through luminescent downshifting to prolong NFA-based OSCs lifetime.

The final section of the thesis focuses on improving the device performance using the ternary blend strategy. Ternary blend strategy in which three photoactive components constitute the active layer is a route to enhance photon harvesting without the fabrication complexities of multi-junction devices. We introduced the acceptor molecule $PC_{70}BM$ as the third component

in the Y6 acceptor based OSCs. Wide-bandgap $PC_{70}BM$ with complementary absorption significantly improved the open-circuit voltage and the PCE of the binary OSCs. Insights into charge transport and recombination dynamics in the devices are analyzed using steady-state and transient techniques. The morphological modification in the BHJ active layer due to the third component $PC_{70}BM$, having a comparatively high thermal transition temperature, reduced the interfacial recombination and rapid degradation of the Y6 based binary counterpart. Light and temperature-induced degradation studies reveal the optimized morphology of ternary BHJ OSCs in prolonging the device lifetime. This work pinpoints the potential of fullerene derivative acceptor $PC_{70}BM$ in improving the efficiency and stabilizing the NFA based single-junction organic solar cells.

In summary, the thesis describes methods to improve the device performance of non-fullerene acceptors IT-4F and Y6 based OSCs using interfacial modification and ternary blend strategy. In addition to this, a systematic study of degradation mechanism in these devices and disintegration of the influence of various aging factors along with implications toward strategies to improve the stability.

References:

1.   Desa, U. N., Transforming Our World: The 2030 Agenda for Sustainable Development. **2016**.

2.   Conti, J.; Holtberg, P.; Diefenderfer, J.; LaRose, A.; Turnure, J. T.; Westfall, L., International Energy Outlook 2016 with Projections to 2040. USDOE Energy Information Administration (EIA), Washington, DC (United States …: 2016.

3.   What Is Green Energy? https://www.twi-global.com/technical-knowledge/faqs/what-is-green-energy.

4.   Goswami, D. Y.; Kreith, F., *Energy Efficiency and Renewable Energy Handbook*; CRC press, 2015.

5.   Lewis, N. S.; Nocera, D. G., Powering the Planet: Chemical Challenges in Solar Energy Utilization. *Proceedings of the National Academy of Sciences* **2006**, *103*, 15729-15735 0027-8424.

6.   Smets, A. H. M.; Jäger, K.; Isabella, O.; Swaaij, R. A.; Zeman, M., *Solar Energy: The Physics and Engineering of Photovoltaic Conversion, Technologies and Systems*; UIT Cambridge, 2015.

7.   Luo, F. L.; Hong, Y., *Renewable Energy Systems: Advanced Conversion Technologies and Applications*; Crc Press, 2017.

8.   Polman, A.; Knight, M.; Garnett, E. C.; Ehrler, B.; Sinke, W. C., Photovoltaic Materials: Present Efficiencies and Future Challenges. *Science* **2016**, *352*, aad4424 0036-8075.

9.   Liu, F.; Zeng, Q.; Li, J.; Hao, X.; Ho-Baillie, A.; Tang, J.; Green, M. A., Emerging Inorganic Compound Thin Film Photovoltaic Materials: Progress, Challenges and Strategies. *Materials Today* **2020**, *41*, 120-142 1369-7021.

10.   Ansari, M. I. H.; Qurashi, A.; Nazeeruddin, M. K., Frontiers, Opportunities, and Challenges in Perovskite Solar Cells: A Critical Review. *Journal of Photochemistry and Photobiology C: Photochemistry Reviews* **2018**, *35*, 1-24 1389-5567.

11.   Gong, J.; Sumathy, K.; Qiao, Q.; Zhou, Z., Review on Dye-Sensitized Solar Cells (Dsscs): Advanced Techniques and Research Trends. *Renewable and Sustainable Energy Reviews* **2017**, *68*, 234-246 1364-0321.

12.   Sogabe, T.; Shen, Q.; Yamaguchi, K., Recent Progress on Quantum Dot Solar Cells: A Review. *Journal of Photonics for Energy* **2016**, *6*, 040901 1947-7988.

13.   Nayak, P. K.; Mahesh, S.; Snaith, H. J.; Cahen, D., Photovoltaic Solar Cell Technologies: Analysing the State of the Art. *Nature Reviews Materials* **2019**, *4*, 269-285 2058-8437.

14.   Asim, N.; Sopian, K.; Ahmadi, S.; Saeedfar, K.; Alghoul, M. A.; Saadatian, O.; Zaidi, S. H., A Review on the Role of Materials Science in Solar Cells. *Renewable and Sustainable Energy Reviews* **2012**, *16*, 5834-5847 1364-0321.

15.   Sharma, S.; Jain, K. K.; Sharma, A., Solar Cells: In Research and Applications—a Review. *Materials Sciences and Applications* **2015**, *6*, 1145.

16.   Piotr Bojek, H. B., Iea (2021), Solar Pv, Iea, Paris **2021**.

17.   Crystalline Silicon Photovoltaics Research. *Solar Energy Technologies Office*.

18.   Photovoltaics Report. *Fraunhofer Institute for Solar Energy Systems, ISE with support of PSE Projects GmbH*.

19.   Neamen, D. A., *Semiconductor Physics and Devices: Basic Principles*; McGraw-hill, 2003.

20.   Chiang, C. K.; Fincher Jr, C. R.; Park, Y. W.; Heeger, A. J.; Shirakawa, H.; Louis, E. J.; Gau, S. C.; MacDiarmid, A. G., Electrical Conductivity in Doped Polyacetylene. *Physical review letters* **1977**, *39*, 1098.

21.   Pope, M.; Kallmann, H. P.; Magnante, P. J., Electroluminescence in Organic Crystals. *The Journal of Chemical Physics* **1963**, *38*, 2042-2043 0021-9606.

22.   Helfrich, W.; Schneider, W. G., Recombination Radiation in Anthracene Crystals. *Physical Review Letters* **1965**, *14*, 229.

23.   Silinsh, E. A., Introduction: Characteristic Features of Organic Molecular Crystals. In *Organic Molecular Crystals*, Springer: 1980; pp 1-46.

24.   Haneef, H. F.; Zeidell, A. M.; Jurchescu, O. D., Charge Carrier Traps in Organic Semiconductors: A Review on the Underlying Physics and Impact on Electronic Devices. *Journal of Materials Chemistry C* **2020**, *8*, 759-787.

25.   Myers, J. D.; Xue, J., Organic Semiconductors and Their Applications in Photovoltaic Devices. *Polymer Reviews* **2012**, *52*, 1-37 1558-3724.

26.   Coropceanu, V.; Cornil, J.; da Silva Filho, D. A.; Olivier, Y.; Silbey, R.; Brédas, J.-L., Charge Transport in Organic Semiconductors. *Chemical reviews* **2007**, *107*, 926-952 0009-2665.

27.   Brütting, W., Introduction to the Physics of Organic Semiconductors. *Physics of organic semiconductors* **2005**, 1-14.

28.   Forrest, S. R., *Organic Electronics: Foundations to Applications*; Oxford University Press, USA, 2020.

29.   Kippelen, B.; Brédas, J.-L., Organic Photovoltaics. *Energy & Environmental Science* **2009**, *2*, 251-261.

30.   Bässler, H., Charge Transport in Disordered Organic Photoconductors. A Monte Carlo Simulation Study. *Physica Status Solidi B (Basic Research);(Germany)* **1993**, *175*.

31.   Coehoorn, R.; Pasveer, W. F.; Bobbert, P. A.; Michels, M. A. J., Charge-Carrier Concentration Dependence of the Hopping Mobility in Organic Materials with Gaussian Disorder. *Physical Review B* **2005**, *72*, 155206.

32.   Tang, C. W., Two-Layer Organic Photovoltaic Cell. *Applied physics letters* **1986**, *48*, 183-185 0003-6951.

33.   Yu, G.; Gao, J.; Hummelen, J. C.; Wudl, F.; Heeger, A. J., Polymer Photovoltaic Cells: Enhanced Efficiencies Via a Network of Internal Donor-Acceptor Heterojunctions. *Science* **1995**, *270*, 1789-1791 0036-8075.

34.   Zhao, F.; Wang, C.; Zhan, X., Morphology Control in Organic Solar Cells. *Advanced Energy Materials* **2018**, *8*, 1703147.

35.   Maturová, K.; van Bavel, S. S.; Wienk, M. M.; Janssen, R. A. J.; Kemerink, M., Morphological Device Model for Organic Bulk Heterojunction Solar Cells. *Nano letters* **2009**, *9*, 3032-3037 1530-6984.

36.   Ameri, T.; Dennler, G.; Lungenschmied, C.; Brabec, C. J., Organic Tandem Solar Cells: A Review. *Energy & Environmental Science* **2009**, *2*, 347-363.

37.   Tress, W., Device Physics of Organic Solar Cells. **2011**.

38.   Ogawa, S., *Organic Electronics Materials and Devices*; Springer, 2015.

39.   Etzold, F.; Howard, I. A.; Mauer, R.; Meister, M.; Kim, T.-D.; Lee, K.-S.; Baek, N. S.; Laquai, F., Ultrafast Exciton Dissociation Followed by Nongeminate Charge Recombination in Pcdtbt: Pcbm Photovoltaic Blends. *Journal of the American Chemical Society* **2011**, *133*, 9469-9479 0002-7863.

40.   Balawi, A. H.; Kan, Z.; Gorenflot, J.; Guarracino, P.; Chaturvedi, N.; Privitera, A.; Liu, S.; Gao, Y.; Franco, L.; Beaujuge, P., Quantification of Photophysical Processes in All-Polymer Bulk Heterojunction Solar Cells. *Solar RRL* **2020**, *4*, 2000181 2367-198X.

41.   Grancini, G.; Maiuri, M.; Fazzi, D.; Petrozza, A.; Egelhaaf, H.-J.; Brida, D.; Cerullo, G.; Lanzani, G., Hot Exciton Dissociation in Polymer Solar Cells. *Nature materials* **2013**, *12*, 29-33 1476-4660.

42.   Shivanna, R.; Rajaram, S.; Narayan, K. S., Role of Charge-Transfer State in Perylene-Based Organic Solar Cells. *ChemistrySelect* **2018**, *3*, 9204-9210 2365-6549.

43.   Vithanage, D. A.; Devižis, A.; Abramavičius, V.; Infahsaeng, Y.; Abramavičius, D.; MacKenzie, R. C. I.; Keivanidis, P. E.; Yartsev, A.; Hertel, D.; Nelson, J., Visualizing Charge Separation in Bulk Heterojunction Organic Solar Cells. *Nature communications* **2013**, *4*, 1-6 2041-1723.

44.   Menke, S. M.; Ran, N. A.; Bazan, G. C.; Friend, R. H., Understanding Energy Loss in Organic Solar Cells: Toward a New Efficiency Regime. *Joule* **2018**, *2*, 25-35 %@ 2542-4351.

45.   Kurpiers, J.; Ferron, T.; Roland, S.; Jakoby, M.; Thiede, T.; Jaiser, F.; Albrecht, S.; Janietz, S.; Collins, B. A.; Howard, I. A., Probing the Pathways of Free Charge Generation in Organic Bulk Heterojunction Solar Cells. *Nature communications* **2018**, *9*, 1-11 2041-1723.

46.   Bakulin, A. A.; Rao, A.; Pavelyev, V. G.; van Loosdrecht, P. H. M.; Pshenichnikov, M. S.; Niedzialek, D.; Cornil, J.; Beljonne, D.; Friend, R. H., The Role of Driving Energy and Delocalized States for Charge Separation in Organic Semiconductors. *Science* **2012**, *335*, 1340-1344 0036-8075.

47.   Clarke, T. M.; Durrant, J. R., Charge Photogeneration in Organic Solar Cells. *Chemical reviews* **2010**, *110*, 6736-6767 0009-2665.

48.   Andermann, A. M.; Rego, L. G. C., Energetics of the Charge Generation in Organic Donor–Acceptor Interfaces. *The Journal of Chemical Physics* **2022**, *156*, 024104 0021-9606.

49.   He, Y.; Wang, B.; Lüer, L.; Feng, G.; Osvet, A.; Heumüller, T.; Liu, C.; Li, W.; Guldi, D. M.; Li, N., Unraveling the Charge-Carrier Dynamics from the Femtosecond to the Microsecond Time Scale in Double-Cable Polymer-Based Single-Component Organic Solar Cells. *Advanced energy materials* **2022**, *12*, 2103406 1614-6832.

50.   Marcus, R. A., On the Theory of Oxidation-Reduction Reactions Involving Electron Transfer. I. *The Journal of chemical physics* **1956**, *24*, 966-978 0021-9606.

51.   Jungbluth, A.; Kaienburg, P.; Riede, M., Charge Transfer State Characterization and Voltage Losses of Organic Solar Cells. *Journal of Physics: Materials* **2022**, *5*, 024002 2515-7639.

52.   Shuai, Z.; Li, W.; Ren, J.; Jiang, Y.; Geng, H., Applying Marcus Theory to Describe the Carrier Transports in Organic Semiconductors: Limitations and Beyond. *The Journal of Chemical Physics* **2020**, *153*, 080902 0021-9606.

53.   Godovsky, D., Modeling the Ultimate Efficiency of Polymer Solar Cell Using Marcus Theory of Electron Transfer. *Organic Electronics* **2011**, *12*, 190-194 1566-1199.

54.   Onsager, L., Initial Recombination of Ions. *Physical Review* **1938**, *54*, 554.

55.   Braun, C. L., Electric Field Assisted Dissociation of Charge Transfer States as a Mechanism of Photocarrier Production. *The Journal of chemical physics* **1984**, *80*, 4157-4161 0021-9606.

56.   Limpinsel, M.; Wagenpfahl, A.; Mingebach, M.; Deibel, C.; Dyakonov, V., Photocurrent in Bulk Heterojunction Solar Cells. *Physical Review B* **2010**, *81*, 085203.

57.   Pelzer, K. M.; Darling, S. B., Charge Generation in Organic Photovoltaics: A Review of Theory and Computation. *Molecular Systems Design & Engineering* **2016**, *1*, 10-24.

58.   Mihailetchi, V. D.; Koster, L. J. A.; Hummelen, J. C.; Blom, P. W. M., Photocurrent Generation in Polymer-Fullerene Bulk Heterojunctions. *Physical review letters* **2004**, *93*, 216601.

59.   Elumalai, N. K.; Uddin, A., Open Circuit Voltage of Organic Solar Cells: An in-Depth Review. *Energy & Environmental Science* **2016**, *9*, 391-410.

60.   Azzouzi, M.; Kirchartz, T.; Nelson, J., Factors Controlling Open-Circuit Voltage Losses in Organic Solar Cells. *Trends in Chemistry* **2019**, *1*, 49-62 2589-5974.

61.   Qi, B.; Wang, J., Open-Circuit Voltage in Organic Solar Cells. *Journal of Materials Chemistry* **2012**, *22*, 24315-24325.

62.   Tang, Z.; Wang, J.; Melianas, A.; Wu, Y.; Kroon, R.; Li, W.; Ma, W.; Andersson, M. R.; Ma, Z.; Cai, W., Relating Open-Circuit Voltage Losses to the Active Layer Morphology and Contact Selectivity in Organic Solar Cells. *Journal of Materials Chemistry A* **2018**, *6*, 12574-12581.

63.   Yao, J.; Kirchartz, T.; Vezie, M. S.; Faist, M. A.; Gong, W.; He, Z.; Wu, H.; Troughton, J.; Watson, T.; Bryant, D., Quantifying Losses in Open-Circuit Voltage in Solution-Processable Solar Cells. *Physical review applied* **2015**, *4*, 014020.

64.   Hou, J.; Inganäs, O.; Friend, R. H.; Gao, F., Organic Solar Cells Based on Non-Fullerene Acceptors. *Nature materials* **2018**, *17*, 119-128 1476-4660.

65.   Zhang, J.; Tan, H. S.; Guo, X.; Facchetti, A.; Yan, H., Material Insights and Challenges for Non-Fullerene Organic Solar Cells Based on Small Molecular Acceptors. *Nature Energy* **2018**, *3*, 720-731 2058-7546.

66.   Lakhwani, G.; Rao, A.; Friend, R. H., Bimolecular Recombination in Organic Photovoltaics. *Annual review of physical chemistry* **2014**, *65*, 557-581 0066-426X.

67.   Bergqvist, J.; Tress, W.; Forchheimer, D.; Melianas, A.; Tang, Z.; Haviland, D.; Inganäs, O., New Method for Lateral Mapping of Bimolecular Recombination in Thin-Film Organic Solar Cells. *Progress in Photovoltaics: Research and Applications* **2016**, *24*, 1096-1108 %@ 1062-7995.

68.   Qian, D.; Zheng, Z.; Yao, H.; Tress, W.; Hopper, T. R.; Chen, S.; Li, S.; Liu, J.; Chen, S.; Zhang, J., Design Rules for Minimizing Voltage Losses in High-Efficiency Organic Solar Cells. *Nature materials* **2018**, *17*, 703-709 1476-4660.

69.   Chen, X.-K.; Qian, D.; Wang, Y.; Kirchartz, T.; Tress, W.; Yao, H.; Yuan, J.; Hülsbeck, M.; Zhang, M.; Zou, Y., A Unified Description of Non-Radiative Voltage Losses in Organic Solar Cells. *Nature Energy* **2021**, *6*, 799-806 2058-7546.

70.   Mauer, R.; Howard, I. A.; Laquai, F., Effect of Nongeminate Recombination on Fill Factor in Polythiophene/Methanofullerene Organic Solar Cells. *The Journal of Physical Chemistry Letters* **2010**, *1*, 3500-3505 1948-7185.

71.   Proctor, C. M.; Love, J. A.; Nguyen, T. Q., Mobility Guidelines for High Fill Factor Solution-Processed Small Molecule Solar Cells. *Advanced Materials* **2014**, *26*, 5957-5961 0935-9648.

72.   Zhang, Y.; Dang, X. D.; Kim, C.; Nguyen, T. Q., Effect of Charge Recombination on the Fill Factor of Small Molecule Bulk Heterojunction Solar Cells. *Advanced Energy Materials* **2011**, *1*, 610-617 1614-6832.

73.   Gupta, D.; Mukhopadhyay, S.; Narayan, K., Fill Factor in Organic Solar Cells. *Solar Energy Materials and solar cells* **2010**, *94*, 1309-1313.

74.   Qi, B.; Wang, J., Fill Factor in Organic Solar Cells. *Physical Chemistry Chemical Physics* **2013**, *15*, 8972-8982.

75.   Green, M. A., Solar Cell Fill Factors: General Graph and Empirical Expressions. *Solid State Electronics* **1981**, *24*, 788-789 0038-1101.

76.   Green, M. A., Accuracy of Analytical Expressions for Solar Cell Fill Factors. *Solar cells* **1982**, *7*, 337-340 0379-6787.

77.   Servaites, J. D.; Ratner, M. A.; Marks, T. J., Organic Solar Cells: A New Look at Traditional Models. *Energy & Environmental Science* **2011**, *4*, 4410-4422.

78.   Sze, S. M.; Li, Y.; Ng, K. K., *Physics of Semiconductor Devices*; John wiley & sons, 2021.

79.   Bartesaghi, D.; Pérez, I. D. C.; Kniepert, J.; Roland, S.; Turbiez, M.; Neher, D.; Koster, L., Competition between Recombination and Extraction of Free Charges Determines the Fill Factor of Organic Solar Cells. *Nature communications* **2015**, *6*, 1-10 2041-1723.

80.   Li, D.; Song, L.; Chen, Y.; Huang, W., Modeling Thin Film Solar Cells: From Organic to Perovskite. *Advanced Science* **2020**, *7*, 1901397 2198-3844.

81.   Koster, L. J. A.; Smits, E. C. P.; Mihailetchi, V. D.; Blom, P. W. M., Device Model for the Operation of Polymer/Fullerene Bulk Heterojunction Solar Cells. *Physical Review B* **2005**, *72*, 085205.

82.   Davids, P. S.; Campbell, I. H.; Smith, D. L., Device Model for Single Carrier Organic Diodes. *Journal of Applied Physics* **1997**, *82*, 6319-6325 0021-8979.

83.   Kirchartz, T.; Nelson, J., Device Modelling of Organic Bulk Heterojunction Solar Cells. *Multiscale Modelling of Organic and Hybrid Photovoltaics* **2013**, 279-324.

84.   Belghachi, A., Theoretical Calculation of the Efficiency Limit for Solar Cells. *Solar Cells-New Approaches and Reviews* **2015**, 47-76.

85.   Shockley, W.; Queisser, H. J., Detailed Balance Limit of Efficiency of P-N Junction Solar Cells. *Journal of applied physics* **1961**, *32*, 510-519 0021-8979.

86.   Queisser, H. J., Detailed Balance Limit for Solar Cell Efficiency. *Materials Science and Engineering: B* **2009**, *159*, 322-328 0921-5107.

87.   Haverkort, J. E. M.; Garnett, E. C.; Bakkers, E. P. A. M., Fundamentals of the Nanowire Solar Cell: Optimization of the Open Circuit Voltage. *Applied Physics Reviews* **2018**, *5*, 031106 1931-9401.

88.   Archer, M. D.; Bolton, J. R., Requirements for Ideal Performance of Photochemical and Photovoltaic Solar Energy Converters. *Journal of Physical Chemistry* **1990**, *94*, 8028-8036 0022-3654.

89.   Chuang, C. M., Shockley-Queisser-Limit. *Github* **2016**.

90.   Giebink, N. C.; Wiederrecht, G. P.; Wasielewski, M. R.; Forrest, S. R., Thermodynamic Efficiency Limit of Excitonic Solar Cells. *Physical Review B* **2011**, *83*, 195326.

91.   Coakley, K. M.; McGehee, M. D., Conjugated Polymer Photovoltaic Cells. *Chemistry of materials* **2004**, *16*, 4533-4542 0897-4756.

92.   Scharber, M. C.; Mühlbacher, D.; Koppe, M.; Denk, P.; Waldauf, C.; Heeger, A. J.; Brabec, C. J., Design Rules for Donors in Bulk-Heterojunction Solar Cells—Towards 10% Energy-Conversion Efficiency. *Advanced materials* **2006**, *18*, 789-794 0935-9648.

93.   Kirchartz, T.; Taretto, K.; Rau, U., Efficiency Limits of Organic Bulk Heterojunction Solar Cells. *The Journal of Physical Chemistry C* **2009**, *113*, 17958-17966 1932-7447.

94.   Vandewal, K.; Tvingstedt, K.; Inganäs, O., Charge Transfer States in Organic Donor–Acceptor Solar Cells. In *Semiconductors and Semimetals*, Elsevier: 2011; Vol. 85, pp 261-295 %@ 0080-8784.

95.   Firdaus, Y.; Le Corre, V. M.; Khan, J. I.; Kan, Z.; Laquai, F.; Beaujuge, P. M.; Anthopoulos, T. D., Key Parameters Requirements for Non-Fullerene-Based Organic Solar Cells with Power Conversion Efficiency> 20%. *Advanced Science* **2019**, *6*, 1802028 2198-3844.

96.   He, Y.; Li, Y., Fullerene Derivative Acceptors for High Performance Polymer Solar Cells. *Physical chemistry chemical physics* **2011**, *13*, 1970-1983.

97.   Li, C.-Z.; Yip, H.-L.; Jen, A. K. Y., Functional Fullerenes for Organic Photovoltaics. *Journal of Materials Chemistry* **2012**, *22*, 4161-4177.

98.   Kumari, T.; Lee, S. M.; Kang, S.-H.; Chen, S.; Yang, C., Ternary Solar Cells with a Mixed Face-on and Edge-on Orientation Enable an Unprecedented Efficiency of 12.1%. *Energy & Environmental Science* **2017**, *10*, 258-265.

99.   Huang, J.; Carpenter, J. H.; Li, C. Z.; Yu, J. S.; Ade, H.; Jen, A. K. Y., Highly Efficient Organic Solar Cells with Improved Vertical Donor–Acceptor Compositional Gradient Via an Inverted Off-Center Spinning Method. *Advanced Materials* **2016**, *28*, 967-974 0935-9648.

100.   Li, S.; Liu, W.; Li, C. Z.; Shi, M.; Chen, H., Efficient Organic Solar Cells with Non-Fullerene Acceptors. *Small* **2017**, *13*, 1701120 1613-6810.

101.   Zhao, W.; Qian, D.; Zhang, S.; Li, S.; Inganäs, O.; Gao, F.; Hou, J., Fullerene-Free Polymer Solar Cells with over 11% Efficiency and Excellent Thermal Stability. *Advanced materials* **2016**, *28*, 4734-4739 0935-9648.

102.   Pan, Q.-Q.; Li, S.-B.; Duan, Y.-C.; Wu, Y.; Zhang, J.; Geng, Y.; Zhao, L.; Su, Z.-M., Exploring What Prompts Itic to Become a Superior Acceptor in Organic Solar Cell by Combining Molecular Dynamics Simulation with Quantum Chemistry Calculation. *Physical Chemistry Chemical Physics* **2017**, *19*, 31227-31235.

103.   Piersimoni, F.; Degutis, G.; Bertho, S.; Vandewal, K.; Spoltore, D.; Vangerven, T.; Drijkoningen, J.; Van Bael, M. K.; Hardy, A.; D'Haen, J., Influence of Fullerene Photodimerization on the Pcbm Crystallization in Polymer: Fullerene Bulk Heterojunctions under Thermal Stress. *Journal of Polymer Science Part B: Polymer Physics* **2013**, *51*, 1209-1214 0887-6266.

104.   Li, H.; Wang, J.; Wang, Y.; Bu, F.; Shen, W.; Liu, J.; Huang, L.; Wang, W.; Belfiore, L. A.; Tang, J., The Progress of Non-Fullerene Small Molecular Acceptors for High Efficiency Polymer Solar Cells. *Solar Energy Materials and Solar Cells* **2019**, *190*, 83-97 0927-0248.

105.   Cheng, P.; Li, G.; Zhan, X.; Yang, Y., Next-Generation Organic Photovoltaics Based on Non-Fullerene Acceptors. *Nature Photonics* **2018**, *12*, 131-142 1749-4893.

106.   Yan, C.; Barlow, S.; Wang, Z.; Yan, H.; Jen, A. K. Y.; Marder, S. R.; Zhan, X., Non-Fullerene Acceptors for Organic Solar Cells. *Nature Reviews Materials* **2018**, *3*, 1-19 % @ 2058-8437.

107.   Zhang, G.; Zhao, J.; Chow, P. C. Y.; Jiang, K.; Zhang, J.; Zhu, Z.; Zhang, J.; Huang, F.; Yan, H., Nonfullerene Acceptor Molecules for Bulk Heterojunction Organic Solar Cells. *Chemical reviews* **2018**, *118*, 3447-3507 0009-2665.

108.   Liu, Q.; Jiang, Y.; Jin, K.; Qin, J.; Xu, J.; Li, W.; Xiong, J.; Liu, J.; Xiao, Z.; Sun, K., 18% Efficiency Organic Solar Cells. *Science Bulletin* **2020**, *65*, 272-275.

109.   Yuan, J.; Zhang, Y.; Zhou, L.; Zhang, G.; Yip, H.-L.; Lau, T.-K.; Lu, X.; Zhu, C.; Peng, H.; Johnson, P. A., Single-Junction Organic Solar Cell with over 15% Efficiency Using Fused-Ring Acceptor with Electron-Deficient Core. *Joule* **2019**, *3*, 1140-1151 2542-4351.

110.   Zhang, S.; Qin, Y.; Zhu, J.; Hou, J., Over 14% Efficiency in Polymer Solar Cells Enabled by a Chlorinated Polymer Donor. *Advanced Materials* **2018**, *30*, 1800868 0935-9648.

111.   Zhang, Y.; Yao, H.; Zhang, S.; Qin, Y.; Zhang, J.; Yang, L.; Li, W.; Wei, Z.; Gao, F.; Hou, J., Fluorination Vs. Chlorination: A Case Study on High Performance Organic Photovoltaic Materials. *Science China Chemistry* **2018**, *61*, 1328-1337 1869-1870.

112.   Armin, A.; Li, W.; Sandberg, O. J.; Xiao, Z.; Ding, L.; Nelson, J.; Neher, D.; Vandewal, K.; Shoaee, S.; Wang, T., A History and Perspective of Non-Fullerene Electron Acceptors for Organic Solar Cells. *Advanced Energy Materials* **2021**, *11*, 2003570 1614-6832.

113.   Lin, Y.; Wang, J.; Zhang, Z. G.; Bai, H.; Li, Y.; Zhu, D.; Zhan, X., An Electron Acceptor Challenging Fullerenes for Efficient Polymer Solar Cells. *Advanced materials* **2015**, *27*, 1170-1174 0935-9648.

114. Lin, H.; Chen, S.; Li, Z.; Lai, J. Y. L.; Yang, G.; McAfee, T.; Jiang, K.; Li, Y.; Liu, Y.; Hu, H., High-Performance Non-Fullerene Polymer Solar Cells Based on a Pair of Donor–Acceptor Materials with Complementary Absorption Properties. *Advanced Materials* **2015**, *27*, 7299-7304 0935-9648.

115. Li, S.; Ye, L.; Zhao, W.; Zhang, S.; Mukherjee, S.; Ade, H.; Hou, J., Energy-Level Modulation of Small-Molecule Electron Acceptors to Achieve over 12% Efficiency in Polymer Solar Cells. *Advanced materials* **2016**, *28*, 9423-9429 0935-9648.

116. Wei, Q.; Liu, W.; Leclerc, M.; Yuan, J.; Chen, H.; Zou, Y., A-Da′ Da Non-Fullerene Acceptors for High-Performance Organic Solar Cells. *Science China Chemistry* **2020**, *63*, 1352-1366 1869-1870.

117. Yang, Y.; Zhang, Z.-G.; Bin, H.; Chen, S.; Gao, L.; Xue, L.; Yang, C.; Li, Y., Side-Chain Isomerization on an N-Type Organic Semiconductor Itic Acceptor Makes 11.77% High Efficiency Polymer Solar Cells. *Journal of the American Chemical Society* **2016**, *138*, 15011-15018 0002-7863.

118. Wang, T.; Wang, X.; Yang, R.; Li, C., Recent Advances in Ternary Organic Solar Cells Based on Förster Resonance Energy Transfer. *Solar RRL* **2021**, *5*, 2100496 2367-198X.

119. Wadsworth, A.; Moser, M.; Marks, A.; Little, M. S.; Gasparini, N.; Brabec, C. J.; Baran, D.; McCulloch, I., Critical Review of the Molecular Design Progress in Non-Fullerene Electron Acceptors Towards Commercially Viable Organic Solar Cells. *Chemical Society Reviews* **2019**, *48*, 1596-1625.

120. Gurney, R. S.; Lidzey, D. G.; Wang, T., A Review of Non-Fullerene Polymer Solar Cells: From Device Physics to Morphology Control. *Reports on Progress in Physics* **2019**, *82*, 036601 0034-4885.

121.   Li, C.; Wonneberger, H., Perylene Imides for Organic Photovoltaics: Yesterday, Today, and Tomorrow. *Advanced Materials* **2012**, *24*, 613-636 0935-9648.

122.   Sun, H.; Chen, F.; Chen, Z.-K., Recent Progress on Non-Fullerene Acceptors for Organic Photovoltaics. *Materials Today* **2019**, *24*, 94-118 1369-7021.

123.   Zou, X.; Wen, G.; Hu, R.; Dong, G.; Zhang, C.; Zhang, W.; Huang, H.; Dang, W., An Insight into the Excitation States of Small Molecular Semiconductor Y6. *Molecules* **2020**, *25*, 4118 1420-3049.

124.   Ma, L.; Zhang, S.; Zhu, J.; Wang, J.; Ren, J.; Zhang, J.; Hou, J., Completely Non-Fused Electron Acceptor with 3d-Interpenetrated Crystalline Structure Enables Efficient and Stable Organic Solar Cell. *Nature communications* **2021**, *12*, 1-12 2041-1723.

125.   Yang, M.; Wei, W.; Zhou, X.; Wang, Z.; Duan, C., Non-Fused Ring Acceptors for Organic Solar Cells. *Energy Materials* **2021**, *1*, 100008.

126.   Li, S.; Zhan, L.; Liu, F.; Ren, J.; Shi, M.; Li, C. Z.; Russell, T. P.; Chen, H., An Unfused-Core-Based Nonfullerene Acceptor Enables High-Efficiency Organic Solar Cells with Excellent Morphological Stability at High Temperatures. *Advanced Materials* **2018**, *30*, 1705208 0935-9648.

127.   Li, S.; Zhan, L.; Zhao, W.; Zhang, S.; Ali, B.; Fu, Z.; Lau, T.-K.; Lu, X.; Shi, M.; Li, C.-Z., Revealing the Effects of Molecular Packing on the Performances of Polymer Solar Cells Based on a–D–C–D–a Type Non-Fullerene Acceptors. *Journal of Materials Chemistry A* **2018**, *6*, 12132-12141.

128.   Meng, D.; Fu, H.; Xiao, C.; Meng, X.; Winands, T.; Ma, W.; Wei, W.; Fan, B.; Huo, L.; Doltsinis, N. L., Three-Bladed Rylene Propellers with Three-Dimensional Network Assembly for Organic Electronics. *Journal of the American Chemical Society* **2016**, *138*, 10184-10190 0002-7863.

129.   Liu, F.; Zhou, L.; Liu, W.; Zhou, Z.; Yue, Q.; Zheng, W.; Sun, R.; Liu, W.; Xu, S.; Fan, H., Organic Solar Cells with 18% Efficiency Enabled by an Alloy Acceptor: A Two-in-One Strategy. *Advanced Materials* **2021**, *33*, 2100830 0935-9648.

130.   Li, C.; Zhou, J.; Song, J.; Xu, J.; Zhang, H.; Zhang, X.; Guo, J.; Zhu, L.; Wei, D.; Han, G., Non-Fullerene Acceptors with Branched Side Chains and Improved Molecular Packing to Exceed 18% Efficiency in Organic Solar Cells. *Nature Energy* **2021**, *6*, 605-613 2058-7546.

131.   Yu, R.; Yao, H.; Hou, J., Recent Progress in Ternary Organic Solar Cells Based on Nonfullerene Acceptors. *Advanced Energy Materials* **2018**, *8*, 1702814 1614-6832.

132.   Zhao, C.; Wang, J.; Zhao, X.; Du, Z.; Yang, R.; Tang, J., Recent Advances, Challenges and Prospects in Ternary Organic Solar Cells. *Nanoscale* **2021**, *13*, 2181-2208.

133.   Gasparini, N.; Salleo, A.; McCulloch, I.; Baran, D., The Role of the Third Component in Ternary Organic Solar Cells. *Nature Reviews Materials* **2019**, *4*, 229-242 2058-8437.

134.   Zheng, Z.; Wang, J.; Bi, P.; Ren, J.; Wang, Y.; Yang, Y.; Liu, X.; Zhang, S.; Hou, J., Tandem Organic Solar Cell with 20.2% Efficiency. *Joule* **2022**, *6*, 171-184 2542-4351.

135.   Zhu, L.; Zhang, M.; Xu, J.; Li, C.; Yan, J.; Zhou, G.; Zhong, W.; Hao, T.; Song, J.; Xue, X., Single-Junction Organic Solar Cells with over 19% Efficiency Enabled by a Refined Double-Fibril Network Morphology. *Nature Materials* **2022**, 1-8 1476-4660.

136.   Benten, H.; Nishida, T.; Mori, D.; Xu, H.; Ohkita, H.; Ito, S., High-Performance Ternary Blend All-Polymer Solar Cells with Complementary Absorption Bands from Visible to near-Infrared Wavelengths. *Energy & Environmental Science* **2016**, *9*, 135-140.

137.   Zhan, L.; Li, S.; Li, Y.; Sun, R.; Min, J.; Bi, Z.; Ma, W.; Chen, Z.; Zhou, G.; Zhu, H., Desired Open-Circuit Voltage Increase Enables Efficiencies Approaching 19% in Symmetric-Asymmetric Molecule Ternary Organic Photovoltaics. *Joule* **2022**, *6*, 662-675 2542-4351.

138.   Baran, D.; Kirchartz, T.; Wheeler, S.; Dimitrov, S.; Abdelsamie, M.; Gorman, J.; Ashraf, R. S.; Holliday, S.; Wadsworth, A.; Gasparini, N., Reduced Voltage Losses Yield 10% Efficient Fullerene Free Organic Solar Cells with> 1 V Open Circuit Voltages. *Energy & environmental science* **2016**, *9*, 3783-3793.

139.   Liu, X.; Yan, Y.; Yao, Y.; Liang, Z., Ternary Blend Strategy for Achieving High-Efficiency Organic Solar Cells with Nonfullerene Acceptors Involved. *Advanced Functional Materials* **2018**, *28*, 1802004 1616-301X.

140.   An, Q.; Zhang, F.; Yin, X.; Sun, Q.; Zhang, M.; Zhang, J.; Tang, W.; Deng, Z., High-Performance Alloy Model-Based Ternary Small Molecule Solar Cells. *Nano Energy* **2016**, *30*, 276-282 2211-2855.

141.   Chang, Y.; Chang, Y.; Zhu, X.; Zhou, X.; Yang, C.; Zhang, J.; Lu, K.; Sun, X.; Wei, Z., Constructing High-Performance All-Small-Molecule Ternary Solar Cells with the Same Third Component but Different Mechanisms for Fullerene and Non-Fullerene Systems. *Advanced Energy Materials* **2019**, *9*, 1900190 1614-6832.

142.   Bi, P.; Hao, X., Versatile Ternary Approach for Novel Organic Solar Cells: A Review. *Solar RRL* **2019**, *3*, 1800263 2367-198X.

143.   Yin, Z.; Mei, S.; Chen, L.; Gu, P.; Huang, J.; Li, X.; Wang, H.-Q.; Song, W., Efficient Ptb7-Th: Y6: Pc71bm Ternary Organic Solar Cell with Superior Stability Processed by Chloroform. *Organic Electronics* **2021**, *99*, 106308 1566-1199.

144.   An, Q.; Wang, J.; Zhang, F., Ternary Polymer Solar Cells with Alloyed Donor Achieving 14.13% Efficiency and 78.4% Fill Factor. *Nano Energy* **2019**, *60*, 768-774 2211-2855.

145.   Liu, T.; Ma, R.; Luo, Z.; Guo, Y.; Zhang, G.; Xiao, Y.; Yang, T.; Chen, Y.; Li, G.; Yi, Y., Concurrent Improvement in J Sc and V Oc in High-Efficiency Ternary Organic Solar

Cells Enabled by a Red-Absorbing Small-Molecule Acceptor with a High Lumo Level. *Energy & Environmental Science* **2020**, *13*, 2115-2123.

146.   Pan, M.-A.; Lau, T.-K.; Tang, Y.; Wu, Y.-C.; Liu, T.; Li, K.; Chen, M.-C.; Lu, X.; Ma, W.; Zhan, C., 16.7%-Efficiency Ternary Blended Organic Photovoltaic Cells with Pcbm as the Acceptor Additive to Increase the Open-Circuit Voltage and Phase Purity. *Journal of Materials Chemistry A* **2019**, *7*, 20713-20722.

147.   Liu, Z., Enhancing the Photovoltaic Performance with Two Similar Structure Polymers as Donors by Broadening the Absorption Spectrum and Optimizing the Molecular Arrangement. *Organic Electronics* **2021**, *93*, 106153 1566-1199.

148.   Su, Z.; Zhang, Z.; Xie, G.; Zhang, Y.; Zhang, X.; Zhang, W.; Zhang, J., Over 16.5% Efficiency in Ternary Organic Solar Cells by Adding an Alloyed Acceptor with Energy Transfer Process. *Dyes and Pigments* **2021**, *192*, 109434 0143-7208.

149.   Zhan, L.; Li, S.; Lau, T.-K.; Cui, Y.; Lu, X.; Shi, M.; Li, C.-Z.; Li, H.; Hou, J.; Chen, H., Over 17% Efficiency Ternary Organic Solar Cells Enabled by Two Non-Fullerene Acceptors Working in an Alloy-Like Model. *Energy & Environmental Science* **2020**, *13*, 635-645.

150.   An, Q.; Ma, X.; Gao, J.; Zhang, F., Solvent Additive-Free Ternary Polymer Solar Cells with 16.27% Efficiency. *Sci. Bull* **2019**, *64*, 504-506.

151.   Ma, Y.; Zhou, X.; Cai, D.; Tu, Q.; Ma, W.; Zheng, Q., A Minimal Benzo [C][1, 2, 5] Thiadiazole-Based Electron Acceptor as a Third Component Material for Ternary Polymer Solar Cells with Efficiencies Exceeding 16.0%. *Materials Horizons* **2020**, *7*, 117-124.

152.   Xie, G.; Zhang, Z.; Su, Z.; Zhang, X.; Zhang, J., 16.5% Efficiency Ternary Organic Photovoltaics with Two Polymer Donors by Optimizing Molecular Arrangement and Phase Separation. *Nano Energy* **2020**, *69*, 104447 2211-2855.

153.   An, Q.; Wang, J.; Ma, X.; Gao, J.; Hu, Z.; Liu, B.; Sun, H.; Guo, X.; Zhang, X.; Zhang, F., Two Compatible Polymer Donors Contribute Synergistically for Ternary Organic Solar Cells with 17.53% Efficiency. *Energy & Environmental Science* **2020**, *13*, 5039-5047.

154.   Ma, X.; Wang, J.; Gao, J.; Hu, Z.; Xu, C.; Zhang, X.; Zhang, F., Achieving 17.4% Efficiency of Ternary Organic Photovoltaics with Two Well-Compatible Nonfullerene Acceptors for Minimizing Energy Loss. *Advanced Energy Materials* **2020**, *10*, 2001404 1614-6832.

155.   Li, Y.; Cai, Y.; Xie, Y.; Song, J.; Wu, H.; Tang, Z.; Zhang, J.; Huang, F.; Sun, Y., A Facile Strategy for Third-Component Selection in Non-Fullerene Acceptor-Based Ternary Organic Solar Cells. *Energy & Environmental Science* **2021**, *14*, 5009-5016.

156.   Jiang, K.; Wei, Q.; Lai, J. Y. L.; Peng, Z.; Kim, H. K.; Yuan, J.; Ye, L.; Ade, H.; Zou, Y.; Yan, H., Alkyl Chain Tuning of Small Molecule Acceptors for Efficient Organic Solar Cells. *Joule* **2019**, *3*, 3020-3033 2542-4351.

157.   Qin, Y.; Xu, Y.; Peng, Z.; Hou, J.; Ade, H., Low Temperature Aggregation Transitions in N3 and Y6 Acceptors Enable Double-Annealing Method That Yields Hierarchical Morphology and Superior Efficiency in Nonfullerene Organic Solar Cells. *Advanced Functional Materials* **2020**, *30*, 2005011 1616-301X.

158.   Peng, W.; Lin, Y.; Jeong, S. Y.; Genene, Z.; Magomedov, A.; Woo, H. Y.; Chen, C.; Wahyudi, W.; Tao, Q.; Deng, J., Over 18% Ternary Polymer Solar Cells Enabled by a Terpolymer as the Third Component. *Nano Energy* **2022**, *92*, 106681 2211-2855.

159.   Gao, J.; Wang, J.; An, Q.; Ma, X.; Hu, Z.; Xu, C.; Zhang, X.; Zhang, F., Over 16.7% Efficiency of Ternary Organic Photovoltaics by Employing Extra Pc71bm as Morphology Regulator. *Science China Chemistry* **2020**, *63*, 83-91 1869-1870.

160.   Ma, X.; Zeng, A.; Gao, J.; Hu, Z.; Xu, C.; Son, J. H.; Jeong, S. Y.; Zhang, C.; Li, M.; Wang, K., Approaching 18% Efficiency of Ternary Organic Photovoltaics with Wide

Bandgap Polymer Donor and Well Compatible Y6: Y6-1o as Acceptor. *National science review* **2021**, *8*, nwaa305 2095-5138.

161.   Jin, K.; Xiao, Z.; Ding, L., 18.69% Pce from Organic Solar Cells. *J. Semicond* **2021**, *42*, 060502.

162.   Cui, Y.; Xu, Y.; Yao, H.; Bi, P.; Hong, L.; Zhang, J.; Zu, Y.; Zhang, T.; Qin, J.; Ren, J., Single-Junction Organic Photovoltaic Cell with 19% Efficiency. *Advanced Materials* **2021**, *33*, 2102420 0935-9648.

163.   Xu, X.; Li, Y.; Peng, Q., Recent Advances in Morphology Optimizations Towards Highly Efficient Ternary Organic Solar Cells. *Nano Select* **2020**, *1*, 30-58 2688-4011.

164.   Doumon, N. Y.; Yang, L.; Rosei, F., Ternary Organic Solar Cells: A Review of the Role of the Third Element☆. *Nano Energy* **2022**, 106915 2211-2855.

165.   Mohapatra, A. A.; Tiwari, V.; Patil, S., Energy Transfer in Ternary Blend Organic Solar Cells: Recent Insights and Future Directions. *Energy & Environmental Science* **2021**, *14*, 302-319.

166.   Scully, S. R.; Armstrong, P. B.; Edder, C.; Fréchet, J. M. J.; McGehee, M. D., Long-Range Resonant Energy Transfer for Enhanced Exciton Harvesting for Organic Solar Cells. *Advanced Materials* **2007**, *19*, 2961-2966 0935-9648.

167.   Du, X.; Heumueller, T.; Gruber, W.; Classen, A.; Unruh, T.; Li, N.; Brabec, C. J., Efficient Polymer Solar Cells Based on Non-Fullerene Acceptors with Potential Device Lifetime Approaching 10 Years. *Joule* **2019**, *3*, 215-226.

168.   Cheng, P.; Zhan, X., Stability of Organic Solar Cells: Challenges and Strategies. *Chemical Society Reviews* **2016**, *45*, 2544-2582.

169.   Mateker, W. R.; McGehee, M. D., Progress in Understanding Degradation Mechanisms and Improving Stability in Organic Photovoltaics. *Advanced materials* **2017**, *29*, 1603940.

170.   Li, W.; Liu, D.; Wang, T., Stability of Non-Fullerene Electron Acceptors and Their Photovoltaic Devices. *Advanced Functional Materials* **2021**, *31*, 2104552 1616-301X.

171.   Upama, M. B.; Wright, M.; Mahmud, M. A.; Elumalai, N. K.; Soufiani, A. M.; Wang, D.; Xu, C.; Uddin, A., Photo-Degradation of High Efficiency Fullerene-Free Polymer Solar Cells. *Nanoscale* **2017**, *9*, 18788-18797.

172.   Speller, E. M.; Clarke, A. J.; Luke, J.; Lee, H. K. H.; Durrant, J. R.; Li, N.; Wang, T.; Wong, H. C.; Kim, J.-S.; Tsoi, W. C., From Fullerene Acceptors to Non-Fullerene Acceptors: Prospects and Challenges in the Stability of Organic Solar Cells. *Journal of Materials Chemistry A* **2019**, *7*, 23361-23377.

173.   Li, N.; Perea, J. D.; Kassar, T.; Richter, M.; Heumueller, T.; Matt, G. J.; Hou, Y.; Güldal, N. S.; Chen, H.; Chen, S., Abnormal Strong Burn-in Degradation of Highly Efficient Polymer Solar Cells Caused by Spinodal Donor-Acceptor Demixing. *Nature communications* **2017**, *8*, 1-9.

174.   Azeez, A.; Narayan, K. S., Dominant Effect of Uv-Light-Induced "Burn-in" Degradation in Non-Fullerene Acceptor Based Organic Solar Cells. *The Journal of Physical Chemistry C* **2021**, *125*, 12531-12540 1932-7447.

175.   Vijayan, R.; Azeez, A.; Narayan, K., Toward Reliable High Performing Organic Solar Cells: Molecules, Processing, and Monitoring. *APL Materials* **2020**, *8*, 040908.

176.   Vijayan, R.; Azeez, A.; Narayan, K. S., Enhanced Stability and Optimized Morphology Induced by Electric-Field-Assisted Annealing of Bulk Heterojunction Solar Cells. *Solar RRL* **2019**, *3*, 1900120.

177.   Hsieh, Y.-J.; Huang, Y.-C.; Liu, W.-S.; Su, Y.-A.; Tsao, C.-S.; Rwei, S.-P.; Wang, L., Insights into the Morphological Instability of Bulk Heterojunction Ptb7-Th/Pcbm Solar Cells Upon High-Temperature Aging. *ACS Applied Materials & Interfaces* **2017**, *9*, 14808-14816 1944-8244.

178.   Distler, A.; Sauermann, T.; Egelhaaf, H. J.; Rodman, S.; Waller, D.; Cheon, K. S.; Lee, M.; Guldi, D. M., The Effect of Pcbm Dimerization on the Performance of Bulk Heterojunction Solar Cells. *Advanced Energy Materials* **2014**, *4*, 1300693 1614-6832.

179.   Heumueller, T.; Mateker, W. R.; Distler, A.; Fritze, U. F.; Cheacharoen, R.; Nguyen, W. H.; Biele, M.; Salvador, M.; von Delius, M.; Egelhaaf, H.-J., Morphological and Electrical Control of Fullerene Dimerization Determines Organic Photovoltaic Stability. *Energy & Environmental Science* **2016**, *9*, 247-256.

180.   Corsini, F.; Griffini, G., Recent Progress in Encapsulation Strategies to Enhance the Stability of Organometal Halide Perovskite Solar Cells. *Journal of Physics: Energy* **2020**, *2*, 031002.

181.   Uddin, A.; Upama, M. B.; Yi, H.; Duan, L., Encapsulation of Organic and Perovskite Solar Cells: A Review. *Coatings* **2019**, *9*, 65.

182.   Matteocci, F.; Cinà, L.; Lamanna, E.; Cacovich, S.; Divitini, G.; Midgley, P. A.; Ducati, C.; Di Carlo, A., Encapsulation for Long-Term Stability Enhancement of Perovskite Solar Cells. *Nano Energy* **2016**, *30*, 162-172.

183.   Li, Y.; Huang, X.; Ding, K.; Sheriff, H. K. M.; Ye, L.; Liu, H.; Li, C.-Z.; Ade, H.; Forrest, S. R., Non-Fullerene Acceptor Organic Photovoltaics with Intrinsic Operational Lifetimes over 30 Years. *Nature communications* **2021**, *12*, 1-9 2041-1723.

184.   Qin, Y.; Balar, N.; Peng, Z.; Gadisa, A.; Angunawela, I.; Bagui, A.; Kashani, S.; Hou, J.; Ade, H., The Performance-Stability Conundrum of Btp-Based Organic Solar Cells. *Joule* **2021**, *5*, 2129-2147 2542-4351.

185.   Guo, J.; Wu, Y.; Sun, R.; Wang, W.; Li, J.; Zhou, E.; Guo, J.; Wang, T.; Wu, Q.; Luo, Z., Photooxidation Analysis of Two Isomeric Nonfullerene Acceptors: A Systematic Study of Conformational, Morphological, and Environmental Factors. *Solar RRL* **2021**, *5*, 2000704 2367-198X.

186.   Tournebize, A.; Mattana, G.; Gorisse, T. r. s.; Bousquet, A.; Wantz, G.; Hirsch, L.; Chambon, S., Crucial Role of the Electron Transport Layer and Uv Light on the Open-Circuit Voltage Loss in Inverted Organic Solar Cells. *ACS applied materials & interfaces* **2017**, *9*, 34131-34138.

187.   Classen, A.; Heumueller, T.; Wabra, I.; Gerner, J.; He, Y.; Einsiedler, L.; Li, N.; Matt, G. J.; Osvet, A.; Du, X., Revealing Hidden Uv Instabilities in Organic Solar Cells by Correlating Device and Material Stability. *Advanced Energy Materials* **2019**, *9*, 1902124.

188.   Lee, H. K. H.; Durrant, J. R.; Li, Z.; Tsoi, W. C., Stability Study of Thermal Cycling on Organic Solar Cells. *Journal of Materials Research* **2018**, *33*, 1902-1908 0884-2914.

Chapter 2

Materials and Methods

2.1 Materials

The BHJ active layer in the organic solar cells constituting the charge generation and transport needs careful design and optimization. The BHJ layer is a blend of donor polymer and an acceptor molecule covering a large portion of the solar-spectral range in an optimized ratio. The extent of commonality in terms of solubility parameters and film formation tendency forms basic design criteria. Homogenous films with the added feature of a vertical gradient in the donor to acceptor distribution are desired. The orbital energy levels, the density of states distribution, absorption window, absorption coefficient, charge carrier mobility, and the compatibility of each material, such as miscibility and complementary absorption, are some of the properties of BHJ components that play a decisive role in the device performance. The active layer materials used in this thesis are: donor polymer PBDB-T-2Cl and acceptor molecules IT-4F, Y6 and $PC_{70}BM$. The orbital energy levels and the band gap of these materials are summarized in **Table.2.1**. The PBDB-T series of polymers fall in a suitable category of donor materials with complementary absorption and suitable electronic energy levels compatible with the most recently reported high-performing NFAs. The main building blocks of PBDB-T polymer are the BDT and BDD units, along with conjugated side chains on the BDT unit. The conjugation and rigidity of the BDT and BDD units help the aggregation, while strong π-π stacking results in better phase purity in the film.[1]
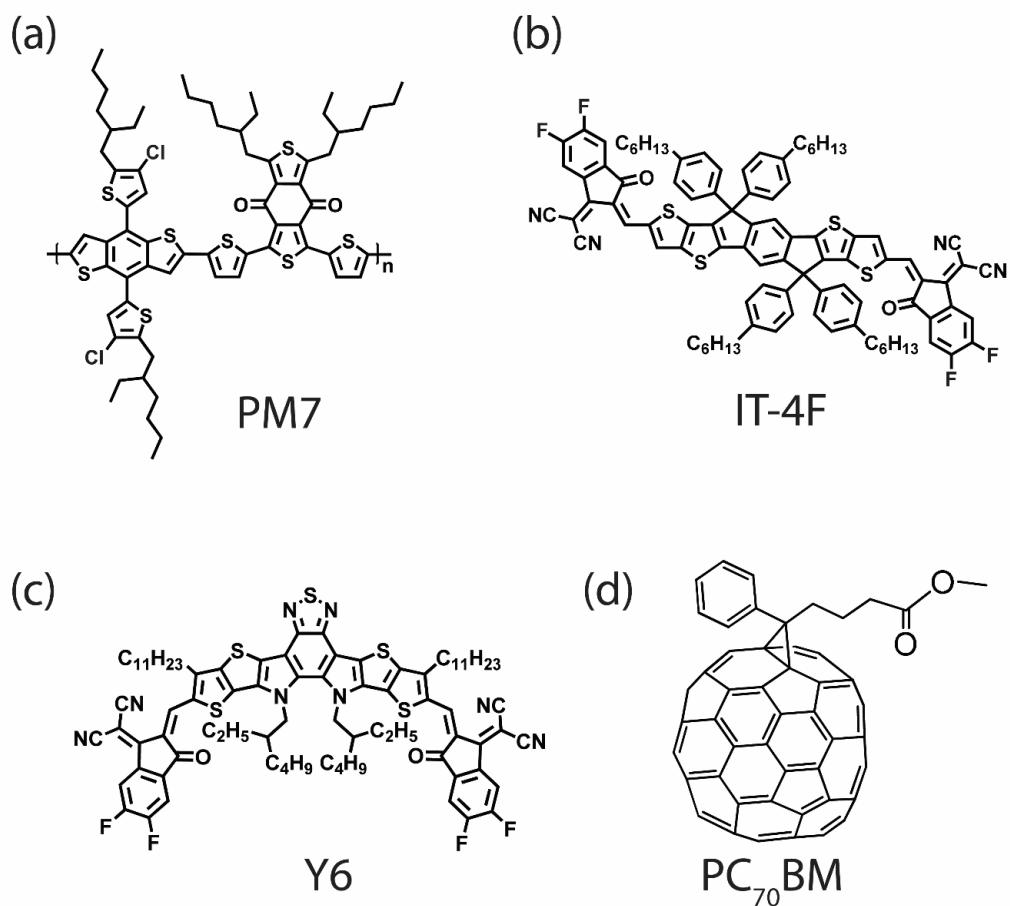
Figure.2.1. The chemical structure of (a) donor PBDB-T-2Cl, acceptors (b) IT-4F, (c) Y6 and (d) PC$_{70}$BM respectively.

Table.2.1. List of donor and acceptor molecules with corresponding orbital energy levels.

Material	HOMO (eV)	LUMO (eV)	E$_g$ (eV)	Reference
PBDB-T	-5.34	-3.32	2.02	2
PBDB-T-2Cl (PM7)	-5.52	-3.57	1.95	2-5
ITIC	-5.48	-3.83	1.65	6
IT-4F	- 5.66	-4.14	1.52	3, 6-7
Y6	-5.65	-4.02	1.63	8
PC$_{70}$BM	-6.0	-4.0	2.0	9

The molecular optimization strategies involve modifying all three parts of the polymer to obtain well-matched energy level shifting and enhanced absorption. The fluorination or chlorination of donor polymers can effectively modulate the π electronic properties of the organic semiconductor and act as an important molecular design strategy. The small size and high electronegativity of fluorine help reduce the steric hindrance in the molecular packing along with modifying the π electron behaviour and improving crystallinity. The crystallinity improvement arises from the non-covalent intermolecular and intramolecular interactions of fluorine atoms which improve the charge transport. Further, reduction in the Coulombic barrier between the electron and hole also occurs due to the high polarization of fluorinated molecules. Due to these advantages, the fluorinated PBDB-T polymer: PBDB-T-2F, commonly known as PM6, is one of the best donors compatible with many high-performing NFAs.[7] The chlorinated version of PBDB-T polymer, PBDB-T-2Cl, commonly known as PM7, is also a suitable donor with similar properties. Even though the electronegativity of chlorine is less than that of fluorine, chlorination help to downshift the orbital energy levels better than fluorination due to the presence of an empty *3d* orbital. PBDB-T-2Cl has a downshifted HOMO level and upshifted LUMO level as compared to PBDB-T-2F donor (**Table.2.1**). The increased intramolecular charge transfer effect as a result of the higher dipole moment of the chlorine-carbon bond results in the absorption broadening of the PBDB-T-2Cl in comparison with PBDB-T-2F.[10] Apart from the above-mentioned favourable modifications, the chlorination strategy is cost-effective compared to fluorination, and hence PBDB-T-2Cl was chosen as the donor polymer throughout the studies in this thesis.

2.1. Fabrication of Organic Solar Cells

The device architecture of the OSC consists of BHJ active layer, buffer layers and counter electrodes. In general, the OSCs are fabricated in normal or inverted architecture. The normal device architecture consists of **ITO/PEDOT** : **PSS/BHJ active layer/PFN Br/Al**, whereas the inverted device architecture is **ITO/ZnO/BHJ active layer/MoO$_3$/Ag**. The buffer layers (ETL and HTL) can vary depending on the D-A combination, and additional buffer layers could also be present in the device. The choice of D-A combination is the most important part while fabricating a high-performing device, and the choice of buffer layers and electrodes is also critical. The processing conditions and fabricating procedure become crucial for a given D-A combination in extracting the best performance. The D-A ratio, processing solvent, spin coating method, thickness of the active layer and various treatments of the layer such as thermal annealing and solvent vapour annealing are critical in optimizing the BHJ active layer. In order to control the BHJ active layer morphology, solvent additives are also used in some cases. The common solvent additives used in BHJ-OSC fabrication include DIO (1,8-diiodooctane) and CN (chloronaphthalene).
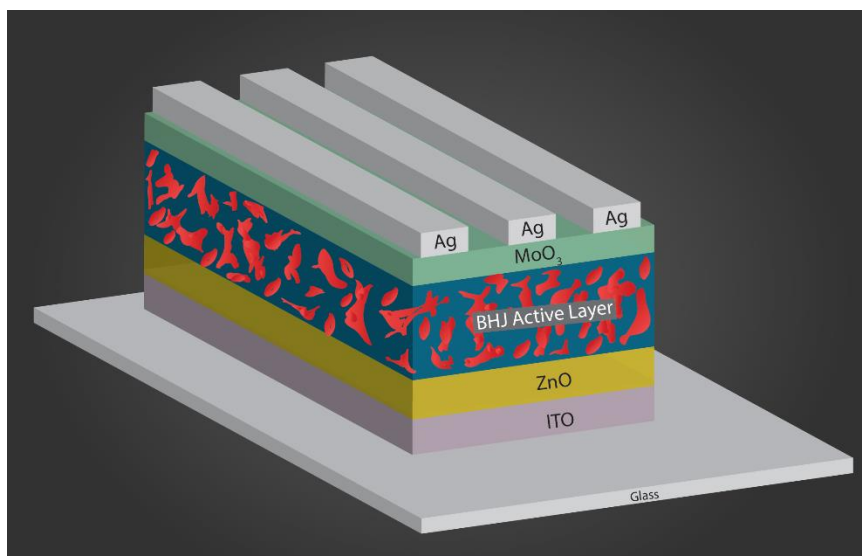
Figure.2.2. A typical inverted device architecture of bulk heterojunction organic solar cell.

In this thesis, mostly OSCs are fabricated in an inverted device geometry with Ag as the anode which is on top of the stack (**Figure.2.2**). The choice of inverted device geometry help to avoid the acidic PEDOT:PSS layer coming in contact with the BHJ active layer and ITO layer, and it is identified as a cause for various degradation mechanisms. This indicates that the inverted device geometry is comparatively more stable than the normal device architecture. Since a significant amount of study in this thesis is related to device stability, the standard device fabrication is restricted to inverted architecture unless otherwise specified. Apart from the elimination of the acidic buffer layer, in inverted geometry, the top electrode materials used are more ambient stable high work function metals such as Ag. The buffer layers or charger transport/extraction layers are used in the device to obtain a near-ohmic transition at the active layer–electrode interface and to tune the polarity of charge collection. The cathode buffer layer (ETL) in this architecture is usually selected as ZnO due to its versatile characteristics such as high electron mobility, ease of synthesis, transparency and high optical transmission. The anode buffer layer (HTL) used in this architecture is the transition metal oxide MoO_3 in order to facilitate the hole extraction. Among the various wet thin film deposition techniques, the spin coating method is the most commonly adopted technique in lab-scale device fabrication. In the spin coating technique, the solution is dispensed onto the substrate, which is already placed on a rotating chuck and rotated with a definite speed so as to achieve the desired thickness. The spin coating technique can provide uniform thin films with thickness varying from the nm-µm range for small substrates. The relation between the thickness of the film and the speed of rotation is given by,

$$d_f \propto \frac{1}{\sqrt{\omega}}$$

(31)

Where d_f is the final thickness and ω is the angular velocity or rotation speed. This inverse relation can provide a rough estimate of the thickness, and profilometry can be used for the

optimization of the film thickness. Also, spin coating varies depending on whether the chuck is rotating or stationary while the dispensation of solution from the pipette. In static spin coating, the rotation of the substrate begins immediately after the solution is dispensed, whereas in dynamic spin-coating, the substrate is maintained in a state of rotation during the solution is dispensed onto the substrate. The dynamic dispense is usually preferred as it gives less time for the evaporation of the solvent while the thin film is formed. For very low spin speed and a viscous solution that needs full coverage on the substrates, the static spin coating is desired.

Table.2.2. List of buffer layer materials with corresponding orbital energy levels.

Material	HOMO (eV)	LUMO (eV)	Reference
ZnO	-7.6	-4.3	[11-12]
MoO_3	-5.3	-2.3	[12]

The OSC device fabrication begins with the precleaning and patterning of the ITO substrates. After patterning, the ITO-coated substrates are thoroughly cleaned with DI water and dried. Then the substrates are sequentially sonicated for 15 minutes each with acetone and isopropyl alcohol and dried by passing N_2 gas. To ensure a clean surface by removing impurities and contaminants and also to improve the surface wettability, plasma cleaning is performed for nearly 5-10 minutes. The Zinc oxide (ZnO) sol-gel precursor was spin-coated on precleaned indium tin oxide (ITO) substrates to obtain ~ 40 nm ZnO film. The ZnO sol-gel precursor was prepared by dissolving 100 mg Zinc acetate dihydrate [$Zn(CH_3COO)_2.2H_2O$] in 1 ml of 2-methoxy ethanol and 28 µl ethanolamine as a stabilizer. Zinc acetate dihydrate, 2-methoxy ethanol and ethanolamine all were procured from Sigma Aldrich. The ZnO layer was thermally annealed in air at 200 °C for half an hour to obtain crystalline ZnO from the gel film. The

crystallinity of ZnO is critical for the performance of OSC as it controls the optoelectronic properties of the film. Even though the most common way of obtaining the ZnO layer is through the sol-gel method, various other ways, including solution processing from nanoparticle dispersion, spray pyrolysis, and metal-organic chemical vapour deposition (MOCVD), and atomic layer deposition (ALD), can also be used. The ZnO-coated ITO substrates were then transferred to a nitrogen-rich glove box for the deposition BHJ active layer. After the coating of the BHJ layer and post-processing such as thermal annealing, the devices (electrode area ≈ 9 mm^2) were completed by thermal evaporation of ~ 8 nm layer of molybdenum oxide (MoO$_3$) and a 100 nm layer of silver at a base pressure of 10^{-6} mbar.

Table.2.3. List of electrode materials with corresponding work function values.

Material	Work function (eV)
ITO	4.7
Al	4.1
Ag	4.6
Au	5.1

2.2. Characterization of Organic Solar Cells

The primary characterization of an OSC is the determination of device PCE under AM1.5G (air mass 1.5 global) illumination conditions. The AM1.5G solar spectrum has an integrated power of 100 mWcm^{-2}. By convention, AM1.5G solar spectrum was adopted as the standard illumination condition and is equivalent to average solar irradiation at mid-latitudes. The current-voltage characteristic of the OSC under AM1.5G illumination condition can be used to extract the parameters V_{OC}, J_{SC}, FF and the PCE. Light measurements were performed at one

sun illumination (AM 1.5 G) provided by a Newport class AAA solar simulator. A source meter (Keithley 2420) interfaced with data acquisition software (Oriel Instruments I−V test station) was used to perform solar cell characterization. During the measurement, only the active area (9 mm^2) of the device is exposed to the light. The remaining area was covered using black tape to avoid any inconsistency in the measurement.

The intensity-dependent J-V characteristic were studied using neutral density filters (NDFs) coupled with a Newport class AAA solar simulator. A source meter (Keithley 2420) interfaced with data acquisition software (Oriel Instruments I−V test station) was used to determine the J-V parameters at different intensity levels.

For external quantum efficiency (EQE) measurements, a light source (Zolix LSH T150 tungsten halogen lamp) coupled with a monochromator (SPEX 500M) was used to illuminate the device area. The EQE was measured under short circuit conditions using Lock-in Amplifier (SRS SR830). The light intensity was calibrated using a silicon detector (UDT Instruments).

Absorption spectra of pristine and BHJ thin films were obtained using a PerkinElmer Lambda 750 UV/Vis/NIR spectrometer. Fourier transform infrared (FT-IR) spectra of films were collected on a Bruker IFS 66v/S FT-IR spectrometer using potassium bromide (KBr) disks.

For SCLC mobility measurement, electron-only devices were fabricated with the architecture ITO/ZnO/BHJ active layer/LiF/Al. Zinc oxide (ZnO) nanoparticle dispersion (purchased from Sigma Aldrich) in ethanol was spin-coated on precleaned and patterned indium tin oxide (ITO) substrates to obtain 40 nm ZnO film. ZnO layer was thermally annealed in air at 120 °C for half an hour. For PM7:Y6 and PM7:Y6:PC$_{70}$BM, BHJ solutions of 1:1.2 and 1:1.2:0.2 ratio of donor and acceptors with polymer concentration at 16 mg/ml in chloroform solvent. The devices (electrode area ≈ 9 mm^2) were completed by thermal evaporation of a ~1 nm layer of LiF and a 100 nm layer of Aluminium at a base pressure of 10^{-6} mbar. The charge carrier

mobility was determined by fitting the dark J-V characteristic to the Mott-Gurney law (single carrier SCLC model): $J = 9\mu\varepsilon_0\varepsilon_r V^2/8d^3$, where J is the measured current density, μ is the charge carrier mobility, ε_0 is the electric permittivity of vacuum, ε_r is the dielectric constant, d is the thickness of the active layer, and V is the applied voltage.

2.3. Impedance Spectroscopy

Impedance spectroscopy (IS) is a facile and powerful tool to study the charge transport and recombination dynamics in OSCs. The concept of impedance can be traced back to the 1880s when Oliver Heaviside first introduced it and later the development of the complex representation of impedance by A.E Kennelly and C.P Steinmetz. In general, IS has been a widely used tool to understand charge transfer and transport mechanisms in electrochemical systems, including DSSCs.[13] Recently, an increasing interest in employing this technique in OSCs has been witnessed due to the simplicity of the measurement and swift analysis capability.[14] In this technique, the frequency-dependent electrical resistance (impedance-$Z(\omega)$) of the system under investigation is probed by applying a small sinusoidal (AC) voltage perturbation with varying frequency and simultaneously looking into the response of the system to it. The interaction of the electromagnetic field with the system results in energy storage, energy dissipation and relaxation processes. The condition of small signal response is to ensure that the system does not undergo a permanent change during the measurement, and the linearity of the measured current and the applied voltage signal is maintained. The electrical perturbation can be applied along with DC bias or under illumination conditions if the system is photoresponsive to gain further insights into the relaxation processes involved.[14-17] The impedance response $Z(\omega)$, to an applied voltage $V(\omega, t)$ is given by,

$$Z(\omega) = \frac{V(\omega, t)}{I(\omega, t)} = \frac{V_0}{I_0} e^{i\theta} \tag{32}$$

$$V(\omega, t) = V_0 e^{i\omega t}, \ I(\omega, t) = I_0 e^{i(\omega t - \theta)}$$

Where $I(\omega, t)$ is the output current from the device under test, V_0 and I_0 represent the amplitude of voltage and current signals, respectively, and θ represents the phase difference between the input voltage signal and output current. The real and imaginary parts of the complex impedance can be determined using the relations below,

$$Z(\omega) = Z'(\omega) + i\, Z''(\omega) \tag{33}$$

$$Z'(\omega) = |Z|Cos\theta, \ Z''(\omega) = |Z|Sin\theta \tag{34}$$

$$|Z| = \sqrt{(Z')^2 + (Z'')^2} \tag{35}$$

Where $Z'(\omega)$ and $Z''(\omega)$ represents the real and imaginary part of the complex impedance $Z(\omega)$. The impedance response from a system can be visualized in a variety of ways and is most commonly represented using the Nyquist plot (Cole-Cole plot) and Bode plots. The Nyquist plot is a complex diagram with an x-axis representing the $Z'(\omega)$ and the y-axis representing the negative of $Z''(\omega)$. In Bode plots, the x-axis represents the frequency, and the y-axis represents the magnitude of impedance or the phase. For a quick analysis of the relaxation processes involved in the system, the Nyquist plot is beneficial, and the results are usually represented in this form, whereas Bode plots contain the frequency dependence explicitly in contrast to the Nyquist plot.

The analysis of the impedance data is primarily performed using equivalent circuit modelling (ECM), in which the impedance response is reproduced using circuit elements such as resistors, capacitors and inductors. The ECM is a powerful strategy as it allows for a quick assessment of features in the Nyquist plot to the physical processes governing the system and provides the choice of circuit elements that are meaningful with respect to the system under investigation. **Figure.2.3.** show Nyquist plot corresponding to some common circuit elements and simple combinations.

Table.2.4. List of common circuit elements used in ECM of impedance spectroscopy and the corresponding impedance.

Circuit Element	Impedance $Z(\omega)$
Resistor (R)	R
Capacitor (C)	$\dfrac{1}{i\omega C}$
Inductor (L)	$i\omega L$
Constant phase element (CPE)	$\dfrac{1}{(i\omega)^n Q_n}$

When a small voltage perturbation is applied to a pure resistor element, it corresponds to a point in the real axis (Z') of the Nyquist plot as the voltage and current are in phase.

$$Z_R(\omega) = \frac{V_0 e^{i\omega t}}{\left(V_0 e^{i\omega t}/R\right)} = R \tag{36}$$

In case of a pure capacitor element the phase difference is $-\pi/2$ and it corresponds to a vertical line parallel to y-axis from the origin.

$$Z_C(\omega) = \frac{1}{i\omega C} \qquad (37)$$

The form of Nyquist plot for a parallel R-C circuit corresponds to a semicircle (**Figure.2.3b**) and multiple parallel RC-element with different values corresponds to multiple semi-circles (**Figure.2.3d**) in Nyquist plot representation. The non-ideal elements which are commonly included to represent dispersive processes in ECM are the Warburg element (W) accounts for the impedance from the diffusion of redox species, and the constant phase element (CPE) for non-ideal capacitance.
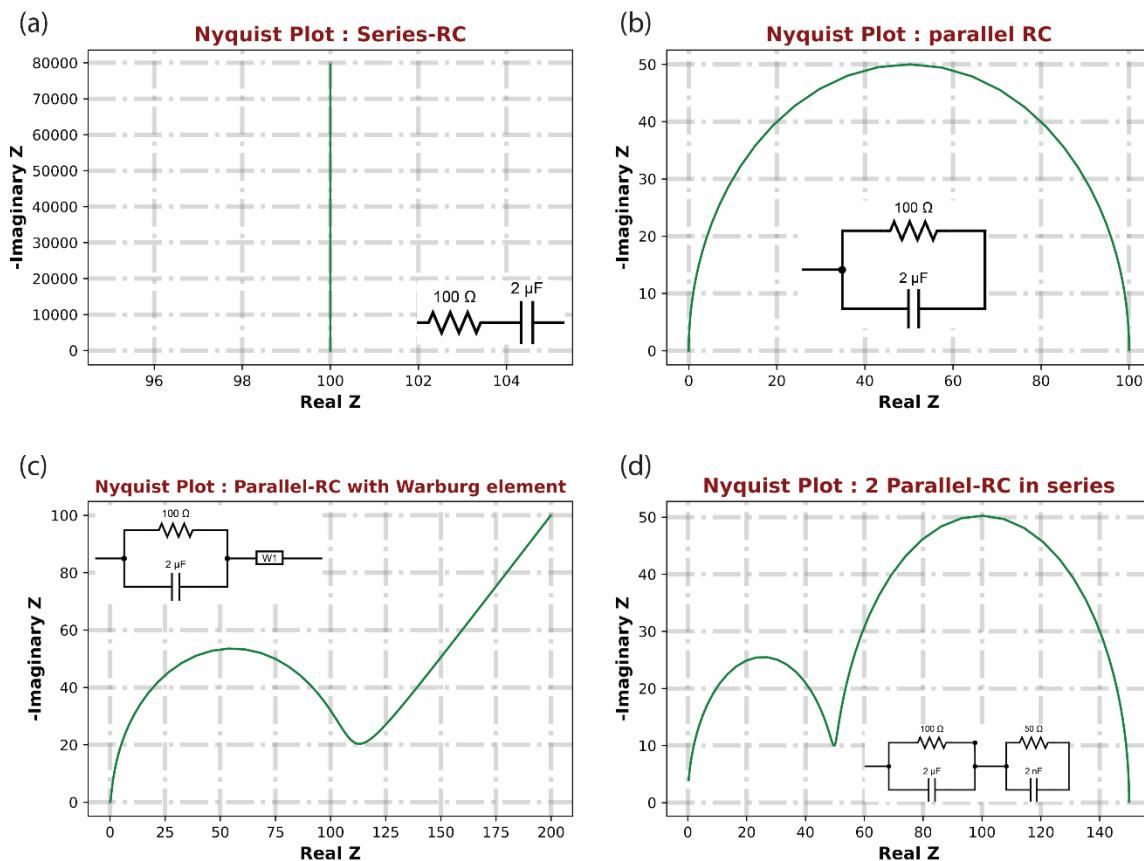
Figure.2.3. The impedance spectroscopy Nyquist plots of some of the important basic circuits with resistor, capacitor and Warburg element.

The IS can provide insights into the charge transport and recombination dynamics in OSCs and has been widely adopted recently. A typical IS response of an OSC corresponds to a semicircle in the Nyquist plot with information on resistive and capacitive processes in the device. This method can easily identify multiple relaxation processes with different timescales in an OSC. The parameters such as charge transport and recombination resistance, geometrical and chemical capacitance, charge carrier lifetime and mobility can be extracted from the impedance spectra along with information on bulk and interfacial properties. Relaxation processes with different timescales can be simultaneously visualized as multiple semicircular arcs in the Nyquist plot. The performance losses associated with non-ohmic contact in the devices can make the analysis challenging. The selection of components for ECM also needs to be appropriate while interpreting the data.
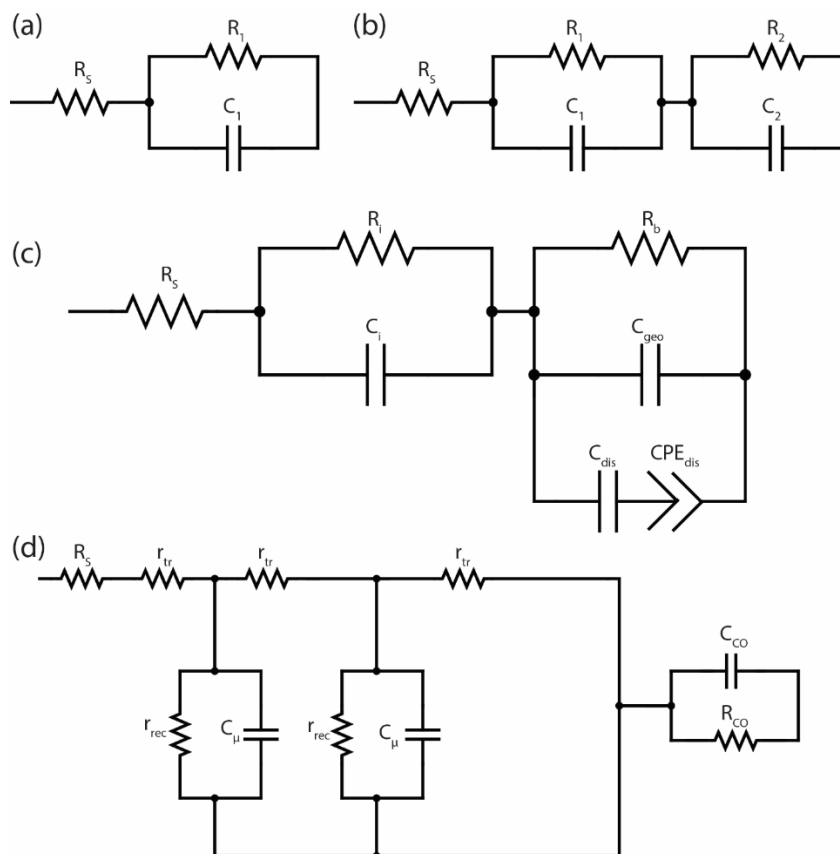
Figure.2.4. Some of the important equivalent circuit models used to analyze and interpret the impedance spectroscopy response of the organic solar cell.

Various equivalent circuit models can be found in the literature to interpret the impedance spectra of OSCs (**Figure.2.4**). As a rule of thumb, it is desired to use a minimum number of circuit elements needed to fit the experimental spectra. The most commonly used circuit model is a single parallel RC connected in series with another resistor element. The series resistance in this R_S-RC model accounts for the resistance contribution from the electrode contacts, and this element is common in all ECMs and graphically represents the shift from the origin along the x-axis. The parallel RC elements represent the charge transport resistance in the device and geometric capacitance originating from the device geometry, respectively. The model with two parallel RC elements (R_s-R_1C_1-R_2C_2) is also widely used to interpret the impedance spectra of OSCs. In this model, resistance elements R_1 and R_2 account for the charge transport and recombination resistance, respectively.[18] The capacitance elements C_1 and C_2 represent geometric and chemical capacitance, respectively. Interpretations in which each parallel RC unit accounts for the bulk and interfacial processes can also be found in the literature.[19] Specific modifications introduced in the devices from the control device also lead to the introduction of appropriate circuit elements in the equivalent circuit model.[20-21]

2.4. Intensity Modulated Photocurrent Spectroscopy

Intensity-modulated photocurrent spectroscopy (IMPS) is a complementary approach to impedance spectroscopy and has been utilised to gain insights into the charge transport and trap-assisted recombination processes in OSCs. Contrary to IS, IMPS involves the application of a small perturbation of light intensity in superposition with a large DC illumination and measuring the corresponding modulated photocurrent response from the device. The light intensity modulation over a range of frequencies generates a steady-state AC photocurrent $I_{ph}(\omega)$ with a characteristic profile of the device under test. It has been demonstrated that

suitable modelling to the IMPS result performed without a background illumination can even extract the trap density profile of the system.[22-24]
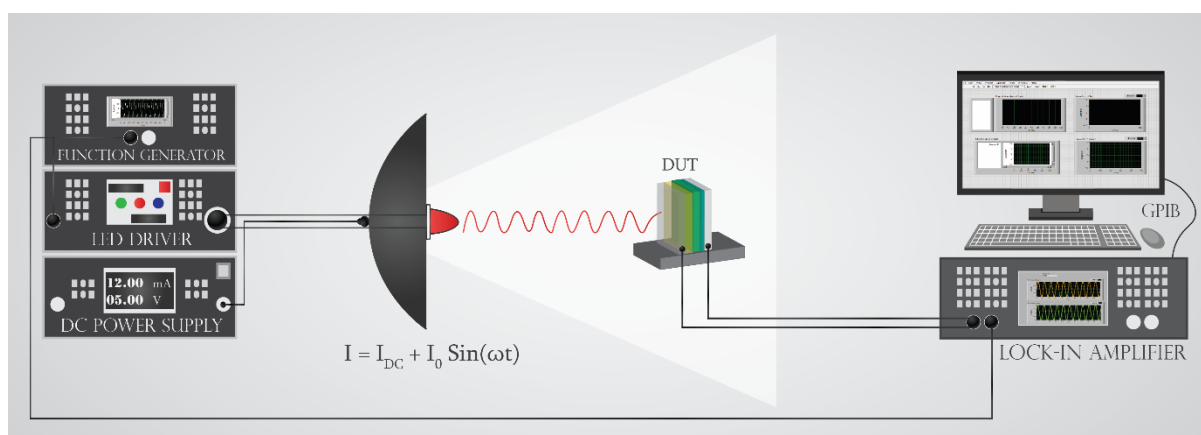
Figure.2.5. Schematic depicting the experimental setup of the IMPS measurement in an organic solar cell.

In general, the photocurrent response from an OSC to a superimposition of small sinusoidal perturbation ($I_0 \, Sin(\omega t)$) in the presence of larger CW illumination (I_{DC}) show a universal maximum and decays at higher frequencies. The frequency response of the photocurrent and the phase shift of the modulated photocurrent can be utilised to extract information on various photophysical processes in the OSC. The low-frequency components of $I_{ph}(\omega)$ are known to be directly linked with the trap-assisted non-geminate recombination processes in the device. Further analysis of IMPS data involves equivalent circuit modelling using passive elements similar to the IS modelling and visualization in the Cole-Cole plot representation.[22, 25]

Intensity-modulated photocurrent spectroscopy (IMPS) was carried out in a home-built experimental setup. A low-noise LED (with different wavelengths) is used as a modulation light source to generate modulated photocurrent. A function generator (Tektronix AFG 1022) was used to drive the LED, and the photocurrent response was collected using a Lock-in amplifier (SR830) interfaced using LabView software.

2.5. Electric Noise Spectroscopy

The measurable inherent noise from the electronic devices can provide insights into the charge transport processes in an operating device. The electric noise spectroscopy (ENS) is a valuable tool in this regard, and a careful analysis of the photocurrent fluctuations in OSCs monitored over a short time interval (μs-ms time scale) provides information on charge transport recombination and extraction processes. It must be noted that fluctuation in the current or voltage signal is stochastic in nature, but the statistical properties and features can be independent of time. The ENS technique has been widely used in devices based on inorganic semiconductors, and it is found to be useful in understanding charge transport in disordered systems with hopping carrier transport mechanisms.[26-29] In this technique, fluctuations in the signal are recorded from the device under test (DUT), which can be analysed in the time domain and compared with multiple data sets obtained from various external conditions applied to DUT during measurement. The most useful and interesting analysis of the noise spectra is carried out in the frequency domain by converting the time domain data into the frequency domain through digital signal processing techniques such as fast fourier transform (FFT), which results in power spectral density (PSD). **Figure.2.6** show the schematic of the experimental setup used for the noise measurement and typical time-domain data along with its PSD.

The noise from a pure resistor element is known as Johnson noise or white noise, and the power spectral density is given by, $S_V = 4K_B TR$. Where R is the resistance, K_B is the Boltzmann's constant and T is the temperature. The term white noise indicates the frequency independence of the noise PSD. Other than the Johnson noise, various other noise features such as shot noise, flicker noise or *1/f* noise are also observed in electronic devices. The shot noise is due to the quantization of electric charge and is associated with the current in finite systems such as quantum dots and quantum wires. The flicker noise or *1/f* noise is common to almost all electronic devices with inverse frequency dependence. The origin of the *1/f* noise can be

attributed to the fluctuations in the mobility of the carriers or due to the fluctuations in the carrier density as a result of imperfection in the system.[17, 30] Various models describing the *1/f* noise can be found in literature including Hooge's model and Kleinpenning model.[31] According to Hooge's model, the PSD is given by the relation,

$$\frac{S_I(f)}{I^2} = \frac{\alpha_H}{fN} \tag{38}$$

Where $S_I(f)$ is the fluctuation in the current, N is the carrier concentration, f is the frequency and α_H is the Hooge's parameter. In general, the noise spectra of an OSC exhibit a *1/f* behaviour with the value of Hooge's parameter between 0.8-1.4. **Figure.2.6c** demonstrate both white noise and *1/f* behaviour measured from an OSC under illumination condition.
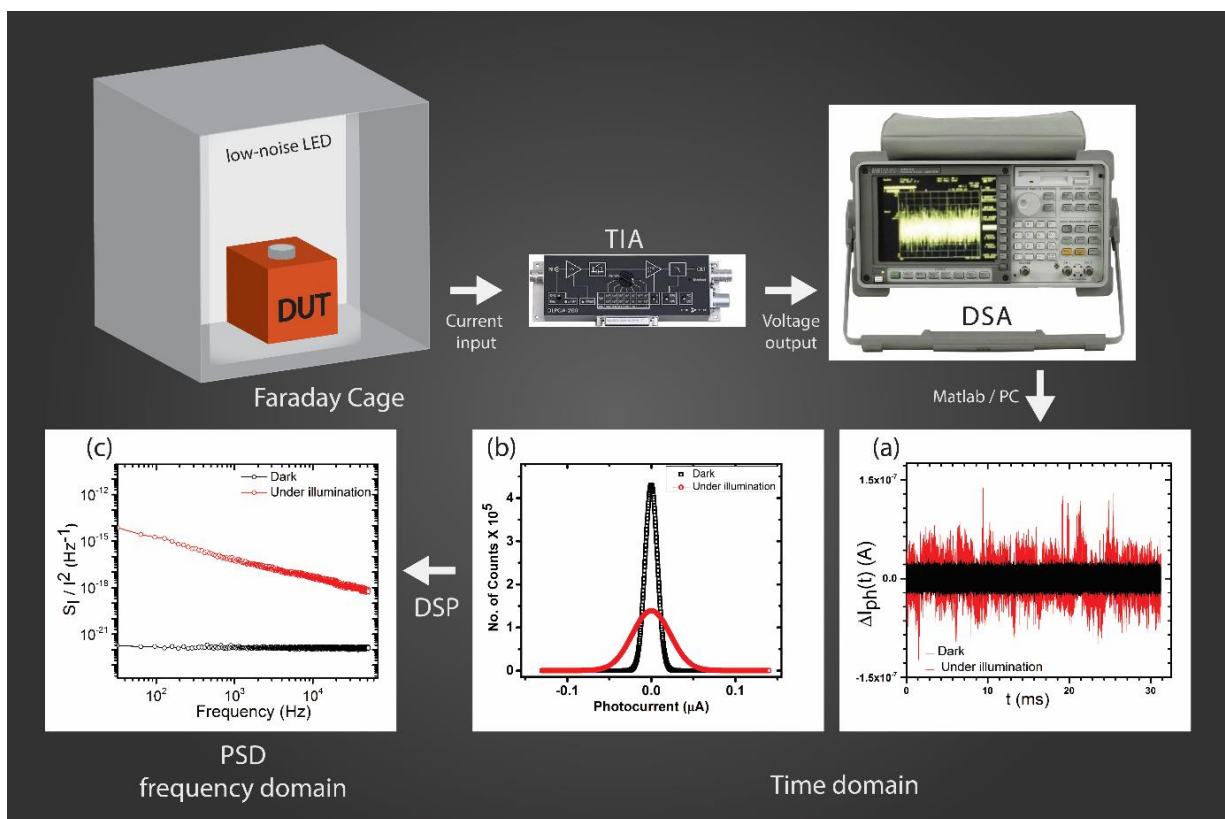
Figure.2.6. The experimental setup for electric noise spectroscopy along with a typical noise characteristic of organic solar cells in time and frequency domain (frequency domain result obtained through digital signal processing).

Noise measurements were carried out in an electrically shielded and grounded environment using a Faraday cage. A low-noise white LED (under steady-state DC light levels of ~ 10 mW/cm^2) driven by rechargeable DC batteries is used to illuminate the device under test (DUT). The output of the amplified current (from low-noise trans-impedance preamplifier, Femto DLPCA-200) was sampled by a dynamic signal analyzer (Agilent 35670A). The time-series data sampled above the Nyquist rate corresponds to an upper-frequency limit in the measurement range. The lower frequency limit is determined by the total time span of one sampled data set (or frame). Each frame is normalized by the gain at the preamplifier before its Fourier transform, the modulus square of which gives the PSD. The PSD is averaged by the total number of captured frames (50) for each set of results. The data processing and analysis were verified with waveforms captured in the signal analyzer for periodic as well as an aperiodic waveform. Control measurements verified the effectiveness of the electrical shielding with the background noise ($\sim 10^{-26}$ A^2/Hz) largely limited by the preamplifier noise.

2.6. Transient Photocurrent Measurement

Transient electrical measurements are important tools to probe the photophysical processes in OSCs due to the various range of time scales involved. Transient photocurrent (TPC) and transient photovoltage (TPV) techniques can provide information on charge carrier extraction time and carrier lifetime in OSCs.[32-33] In the TPC technique, the device is perturbed by a short light pulse (usually sub-ns pulse) using a pulsed laser and the corresponding decay in the photocurrent response is studied using an oscilloscope.[33] During the TPC measurement, the device is held at short-circuit condition, and the TPC decay profile provides information on carrier extraction time and charge carrier density.[34] The TPC measurement on BHJ OSCs is

carried out using a sub-ns pulsed laser (AlphaLas) of wavelength ~ 532 nm, and the transient profile is recorded using an oscilloscope (Keysight MDO).

2.7. Electroluminescence Measurement

The charge carrier injection into the OSC by applying external current to the device results in bimolecular recombination of the carriers at the D-A interface. The luminescence produced in this fashion is known as electroluminescence (EL) and can provide valuable information about the device, including CT-state dynamics.[35] The EL measurement is more useful compared to the PL emission because the carrier injection from the CT state in the D-A interface and the emission represent the CT state of the blend. Whereas in PL spectra, the emission from the individual components of the blend can dominate, and the CT emission can be suppressed.[36-38]

The EL measurements in OSCs were carried out using a source meter (Keithley 2400) which is used to apply voltage bias to the device, and the subsequent emission from the device was acquired using a spectrometer (Hamamatsu) and SpecEvaluation software.

2.8. Morphological Characterization using Atomic Force Microscopy

Atomic force microscopy (AFM) is a powerful tool to probe the morphology and texture of thin-film samples. The history of AFM can be traced back to Binnig and Quate when they demonstrated the concept of AFM in 1986, and later Wickramsinghe et al. developed an AFM setup with a vibrating cantilever technique in 1987.[39-40] AFM belongs to the class of scanning probe microscopy (SPM) techniques with sub-nm resolution in imaging. When a cantilever with an atomically sharp tip comes in the proximity of the sample, the short-range force of interaction between them produces deflection in the cantilever.
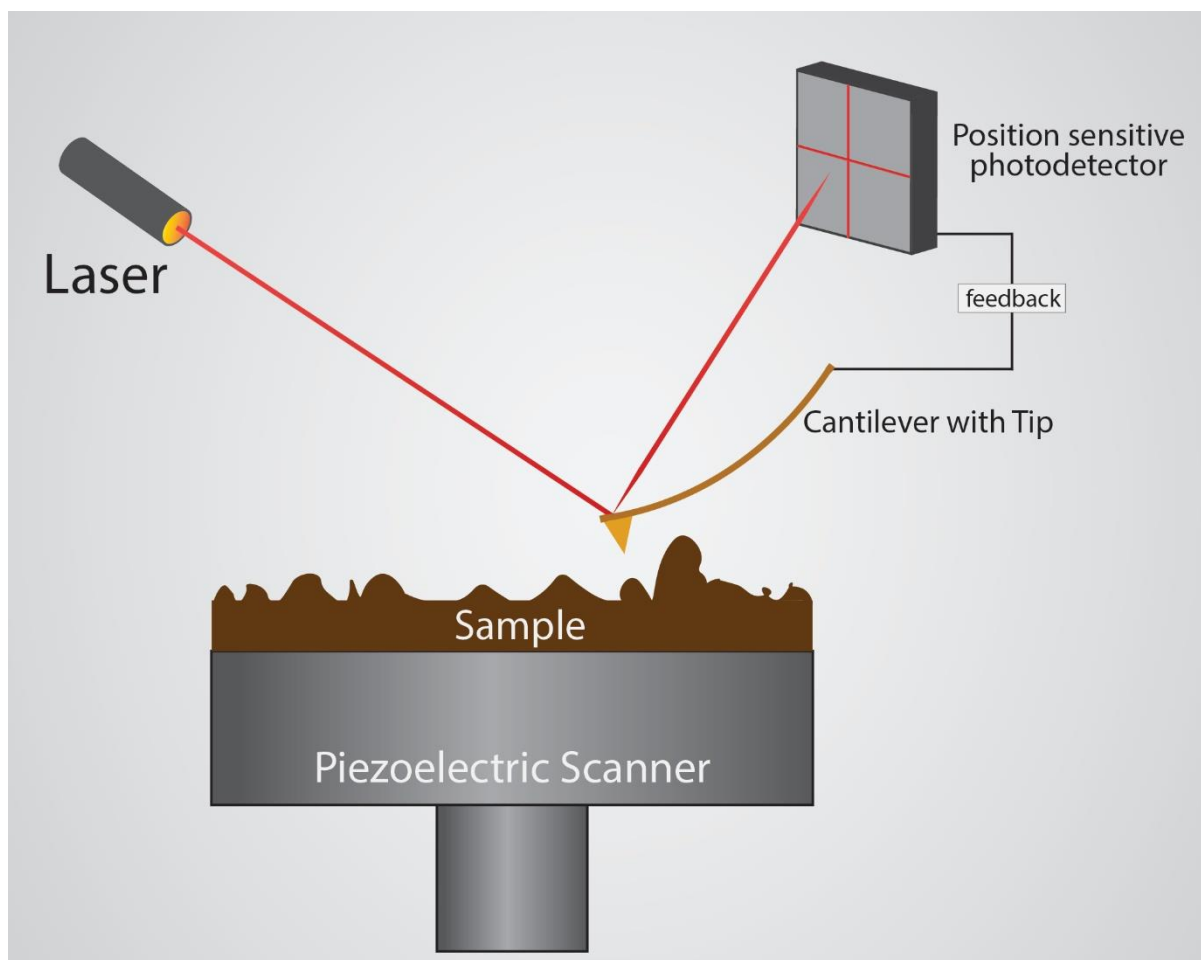
Figure.2.7. Schematic of the AFM experimental setup used to probe the surface morphology of organic thin films.

This deflection is recorded using a laser beam and a position-sensitive detector arrangement to decipher the information on the surface (**Figure.2.7**). The AFM can be operated in different ways, such as contact mode and non-contact mode or 'tapping' mode. In contact mode, the tip of the cantilever comes in direct contact with the sample surface, and the deflection of the cantilever is monitored, or the force of interaction is maintained constant using a feedback loop. But this mode of operation has a disadvantage in that the tip can be damaged as it is dragged over the sample surface, and the sample itself can undergo permanent damage. In non-contact mode, the tip is made to oscillate close to its resonant frequency while scanning without making direct contact with the sample surface. By keeping the amplitude and frequency of the

oscillation constant, any interaction with the sample surface as the tip scan over it results in amplitude change and is recorded to gain the topography information. In comparison, the non-contact mode provides better resolution with minimum surface damage. AFM imaging is an extensively used tool to probe the surface morphology of organic thin films.[41-42] Insights into the device performance - morphology correlation can be gained using AFM imaging of BHJ films and serve as a valuable tool along with other complementary techniques such as KPFM, TEM, SEM, R-SoXS, GIWAXS and VASE.[43-46]

For surface imaging, a JPK Instruments Nanowizard 3 Atomic Force Microscope (AFM) was used. The AFM head was mounted on an inverted microscope (Carl Zeiss). Feedback was controlled using a four-quadrant position detector measuring the deflection of the 810 nm laser from the AFM cantilever as the tip was scanned over the surface. The scans were performed using Cr-Pt conductive cantilever tips procured from BudgetSensors with a force constant of 40 N/m and resonant frequency ~ 300kHz.

Additional methods and modifications to the stated techniques have also been used in the course of the studies. These are described in the relevant sections of the different chapters.

References

1.   Zheng, Z.; Yao, H.; Ye, L.; Xu, Y.; Zhang, S.; Hou, J., Pbdb-T and Its Derivatives: A Family of Polymer Donors Enables over 17% Efficiency in Organic Photovoltaics. *Materials Today* **2020**, *35*, 115-130 1369-7021.

2.   Fan, Q.; Liu, T.; Gao, W.; Xiao, Y.; Wu, J.; Su, W.; Guo, X.; Lu, X.; Yang, C.; Yan, H., Overcoming the Energy Loss in Asymmetrical Non-Fullerene Acceptor-Based Polymer Solar Cells by Halogenation of Polymer Donors. *Journal of Materials Chemistry A* **2019**, *7*, 15404-15410.

3.   Zhang, S.; Qin, Y.; Zhu, J.; Hou, J., Over 14% Efficiency in Polymer Solar Cells Enabled by a Chlorinated Polymer Donor. *Advanced Materials* **2018**, *30*, 1800868 0935-9648.

4.   Fan, Q.; Zhu, Q.; Xu, Z.; Su, W.; Chen, J.; Wu, J.; Guo, X.; Ma, W.; Zhang, M.; Li, Y., Chlorine Substituted 2d-Conjugated Polymer for High-Performance Polymer Solar Cells with 13.1% Efficiency Via Toluene Processing. *Nano Energy* **2018**, *48*, 413-420 2211-2855.

5.   Li, S.; Zhan, L.; Zhao, W.; Zhang, S.; Ali, B.; Fu, Z.; Lau, T.-K.; Lu, X.; Shi, M.; Li, C.-Z., Revealing the Effects of Molecular Packing on the Performances of Polymer Solar Cells Based on a–D–C–D–a Type Non-Fullerene Acceptors. *Journal of Materials Chemistry A* **2018**, *6*, 12132-12141.

6.   Yu, R.; Yao, H.; Hou, J., Recent Progress in Ternary Organic Solar Cells Based on Nonfullerene Acceptors. *Advanced Energy Materials* **2018**, *8*, 1702814 1614-6832.

7.   Zhao, W.; Li, S.; Yao, H.; Zhang, S.; Zhang, Y.; Yang, B.; Hou, J., Molecular Optimization Enables over 13% Efficiency in Organic Solar Cells. *Journal of the American Chemical Society* **2017**, *139*, 7148-7151 0002-7863.

8.   Yuan, J.; Zhang, Y.; Zhou, L.; Zhang, G.; Yip, H.-L.; Lau, T.-K.; Lu, X.; Zhu, C.; Peng, H.; Johnson, P. A., Single-Junction Organic Solar Cell with over 15% Efficiency Using Fused-Ring Acceptor with Electron-Deficient Core. *Joule* **2019**, *3*, 1140-1151 2542-4351.

9.   Chen, G.; Sasabe, H.; Sano, T.; Wang, X.-F.; Hong, Z.; Kido, J.; Yang, Y., Chloroboron (Iii) Subnaphthalocyanine as an Electron Donor in Bulk Heterojunction Photovoltaic Cells. *Nanotechnology* **2013**, *24*, 484007 0957-4484.

10.   Zhang, Y.; Yao, H.; Zhang, S.; Qin, Y.; Zhang, J.; Yang, L.; Li, W.; Wei, Z.; Gao, F.; Hou, J., Fluorination Vs. Chlorination: A Case Study on High Performance Organic Photovoltaic Materials. *Science China Chemistry* **2018**, *61*, 1328-1337 1869-1870.

11.   Liang, Z.; Zhang, Q.; Jiang, L.; Cao, G., Zno Cathode Buffer Layers for Inverted Polymer Solar Cells. *Energy & Environmental Science* **2015**, *8*, 3442-3476.

12.   Wang, K.; Liu, C.; Meng, T.; Yi, C.; Gong, X., Inverted Organic Photovoltaic Cells. *Chemical Society Reviews* **2016**, *45*, 2937-2975.

13.   Lvovich, V. F., *Impedance Spectroscopy: Applications to Electrochemical and Dielectric Phenomena*; John Wiley & Sons, 2012.

14.   Von Hauff, E., Impedance Spectroscopy for Emerging Photovoltaics. *The Journal of Physical Chemistry C* **2019**, *123*, 11329-11346.

15.   Bisquert, J., Theory of the Impedance of Electron Diffusion and Recombination in a Thin Layer. *The Journal of Physical Chemistry B* **2002**, *106*, 325-333.

16.   Fabregat-Santiago, F.; Garcia-Belmonte, G.; Mora-Sero, I.; Bisquert, J., Characterization of Nanostructured Hybrid and Organic Solar Cells by Impedance Spectroscopy. *Physical chemistry chemical physics* **2011**, *13*, 9083-9118.

17.   Azeez, A.; Narayan, K., Enhanced Device Performance Via Interfacial Engineering in Non-Fullerene Acceptor Based Organic Solar Cells. *Applied Physics Letters* **2020**, *117*, 043302.

18.   Azeez, A.; Narayan, K. S., Enhanced Device Performance Via Interfacial Engineering in Non-Fullerene Acceptor Based Organic Solar Cells. *Applied Physics Letters* **2020**, *117*, 043302 %@ 0003-6951.

19.   Zhou, H.; Zhang, Y.; Seifter, J.; Collins, S. D.; Luo, C.; Bazan, G. C.; Nguyen, T. Q.; Heeger, A. J., High-Efficiency Polymer Solar Cells Enhanced by Solvent Treatment. *Advanced materials* **2013**, *25*, 1646-1652 0935-9648.

20.   Gehan, T. S.; Ellis, C. L. C.; Venkataraman, D.; Bag, M., Origin of Low Open-Circuit Voltage in Surfactant-Stabilized Organic-Nanoparticle-Based Solar Cells. *ACS Applied Materials & Interfaces* **2020**, *12*, 8183-8188 1944-8244.

21.   Rana, A.; Kumar, A.; Chand, S.; Singh, R. K., Hole Transport Layer Influencing the Charge Carrier Dynamics During the Degradation of Organic Solar Cells. *Journal of Applied Physics* **2019**, *125*, 053102 0021-8979.

22.   Bag, M.; Narayan, K., Universality in the Intensity-Modulated Photocurrent in Bulk-Heterojunction Polymer Solar Cells. *Physical Review B* **2010**, *82*, 075308.

23.   Byers, J. C.; Ballantyne, S.; Rodionov, K.; Mann, A.; Semenikhin, O. A., Mechanism of Recombination Losses in Bulk Heterojunction P3ht:Pcbm Solar Cells Studied Using Intensity Modulated Photocurrent Spectroscopy. *ACS Applied Materials & Interfaces* **2011**, *3*, 392-401.

24.   Gao, Y.; Wise, A. J.; Thomas, A. K.; Grey, J. K., Spectroscopic and Intensity Modulated Photocurrent Imaging of Polymer/Fullerene Solar Cells. *ACS Applied Materials & Interfaces* **2016**, *8*, 285-293.

25.   Grimm, R. T.; Deb, P.; Walwark Jr, D. J.; Viets, C.; Grey, J. K., Implications of Trap-Assisted Nongeminate Charge Recombination on Time-and Frequency-Domain Photocurrent Degradation Signatures of Organic Solar Cells. *The Journal of Physical Chemistry C* **2020**, *124*, 16838-16848.

26.   Vandamme, L. K. J., Noise as a Diagnostic Tool for Quality and Reliability of Electronic Devices. *IEEE Transactions on Electron Devices* **1994**, *41*, 2176-2187.

27.   Harsh, R.; Narayan, K. S., Noise Spectroscopy of Polymer Transistors. *Journal of Applied Physics* **2015**, *118*, 205502.

28.   Barone, C.; Lang, F.; Mauro, C.; Landi, G.; Rappich, J.; Nickel, N. H.; Rech, B.; Pagano, S.; Neitzert, H. C., Unravelling the Low-Temperature Metastable State in Perovskite Solar Cells by Noise Spectroscopy. *Scientific Reports* **2016**, *6*, 34675.

29.   Singh, A.; Nayak, P. K.; Banerjee, S.; Wang, Z.; Wang, J. T.-W.; Snaith, H. J.; Narayan, K. S., Insights into the Microscopic and Degradation Processes in Hybrid Perovskite Solar Cells Using Noise Spectroscopy. *Solar RRL* **2018**, *2*, 1700173.

30.   Bag, M.; Vidhyadhiraja, N.; Narayan, K., Fluctuations in Photocurrent of Bulk Heterojunction Polymer Solar Cells—a Valuable Tool to Understand Microscopic and Degradation Processes. *Applied Physics Letters* **2012**, *101*, 043903.

31.   Hooge, F. N.; Kleinpenning, T. G. M.; Vandamme, L. K. J., Experimental Studies on 1/F Noise. *Reports on Progress in Physics* **1981**, *44*, 479-532.

32.   Fu, J.; Chen, S.; Yang, K.; Jung, S.; Lv, J.; Lan, L.; Chen, H.; Hu, D.; Yang, Q.; Duan, T., A "Σ-Hole"-Containing Volatile Solid Additive Enabling 16.5% Efficiency Organic Solar Cells. *Iscience* **2020**, *23*, 100965 2589-0042.

33.   Palomares, E.; Montcada, N. F.; Méndez, M.; Jiménez-López, J.; Yang, W.; Boschloo, G., Photovoltage/Photocurrent Transient Techniques. In *Characterization Techniques for Perovskite Solar Cell Materials*, Elsevier: 2020; pp 161-180.

34.   Yang, K.; Chen, S.; Fu, J.; Jung, S.; Ye, J.; Kan, Z.; Hu, C.; Yang, C.; Xiao, Z.; Lu, S., Molecular Lock Induced by Chloroplatinic Acid Doping of Pedot: Pss for High-Performance Organic Photovoltaics. *ACS Applied Materials & Interfaces* **2020**, *12*, 30954-30961 1944-8244.

35.   Shivanna, R.; Rajaram, S.; Narayan, K. S., Role of Charge-Transfer State in Perylene-Based Organic Solar Cells. *ChemistrySelect* **2018**, *3*, 9204-9210 2365-6549.

36.   Vandewal, K.; Tvingstedt, K.; Gadisa, A.; Inganäs, O.; Manca, J. V., Relating the Open-Circuit Voltage to Interface Molecular Properties of Donor: Acceptor Bulk Heterojunction Solar Cells. *Physical Review B* **2010**, *81*, 125204.

37.   Tvingstedt, K.; Vandewal, K.; Gadisa, A.; Zhang, F.; Manca, J.; Inganas, O., Electroluminescence from Charge Transfer States in Polymer Solar Cells. *Journal of the American Chemical Society* **2009**, *131*, 11819-11824 0002-7863.

38.   Seeland, M.; Rösch, R.; Muhsin, B.; Gobsch, G.; Hoppe, H., Electroluminescence as Characterization Tool for Polymer Solar Cells and Modules. *Energy Procedia* **2012**, *31*, 167-172 1876-6102.

39.   Binnig, G.; Quate, C. F.; Gerber, C., Atomic Force Microscope. *Physical review letters* **1986**, *56*, 930.

40.   Martin, Y.; Williams, C. C.; Wickramasinghe, H. K., Atomic Force Microscope–Force Mapping and Profiling on a Sub 100-Å Scale. *Journal of applied Physics* **1987**, *61*, 4723-4729 0021-8979.

41.   Liu, F.; Zhao, W.; Tumbleston, J. R.; Wang, C.; Gu, Y.; Wang, D.; Briseno, A. L.; Ade, H.; Russell, T. P., Understanding the Morphology of Ptb7: Pcbm Blends in Organic Photovoltaics. *Advanced Energy Materials* **2014**, *4*, 1301377 1614-6832.

42.   Maturová, K.; Van Bavel, S. S.; Wienk, M. M.; Janssen, R. A. J.; Kemerink, M., Description of the Morphology Dependent Charge Transport and Performance of Polymer: Fullerene Bulk Heterojunction Solar Cells. *Advanced Functional Materials* **2011**, *21*, 261-269 1616-301X.

43.   Zhao, F.; Wang, C.; Zhan, X., Morphology Control in Organic Solar Cells. *Advanced Energy Materials* **2018**, *8*, 1703147 1614-6832.

44.   Vijayan, R.; Azeez, A.; Narayan, K. S., Enhanced Stability and Optimized Morphology Induced by Electric-Field-Assisted Annealing of Bulk Heterojunction Solar Cells. *Solar RRL* **2019**, *3*, 1900120.

45.   Upama, M. B.; Elumalai, N. K.; Mahmud, M. A.; Wright, M.; Wang, D.; Xu, C.; Uddin, A., Effect of Annealing Dependent Blend Morphology and Dielectric Properties on the Performance and Stability of Non-Fullerene Organic Solar Cells. *Solar Energy Materials and Solar Cells* **2018**, *176*, 109-118.

46.   Duan, L.; Guli, M.; Zhang, Y.; Yi, H.; Haque, F.; Uddin, A., The Air Effect in the Burn-in Thermal Degradation of Nonfullerene Organic Solar Cells. *Energy Technology* **2020**, *8*, 1901401.

Chapter 3

Interfacial Engineering of Non-Fullerene Acceptor IT-4F Based Organic Solar Cells

In this chapter, the role of interface layers (the region between the electrodes layer and the active layer) is presented. The introduction of an interlayer in the standard device architecture of thin-film OSC consisting of the active layer sandwiched between the anode and cathode electrodes modifies the performance considerably.[1] in the absence of the interlayers; the recombination losses present significantly reduce the device parameters; V_{OC}, J_{SC}, and FF.[2-5] The introduction of interface layers of certain organic solar cells OSCs can mitigate the loss in the performance parameters. The purpose of the interlayers is to enable unipolar charge carrier extraction from the photoactive layer to the respective electrode. The electron transport layer (ETL) and hole transport layer (HTL) with suitable orbital energy levels are introduced to minimize the undesirable charge carrier accumulation and surface recombination at the interface (**Figure.3.1**).[6] These buffer layers are important tools in the interfacial engineering of the OSCs to maximize the performance of a given D-A combination.[5, 7] For instance, the PCE of P3HT:PC$_{60}$BM BHJ OSC has increased to 4.2% by introducing suitable ETL and HTL from 2.3% without interlayers.[8] The key benefits of interlayers are:-

    i.   Reduces the energy level mismatch between the active layer and electrode

    ii.   Better contact selectivity and reduced charge carrier accumulation and recombination

    iii.   Passivation of charge trap sites at the active layer – electrode interface

    iv.   Prohibits the chemical reaction between the organic layer and the metal electrode

    v.   Minimizes the moisture ingression into the photoactive organic layer
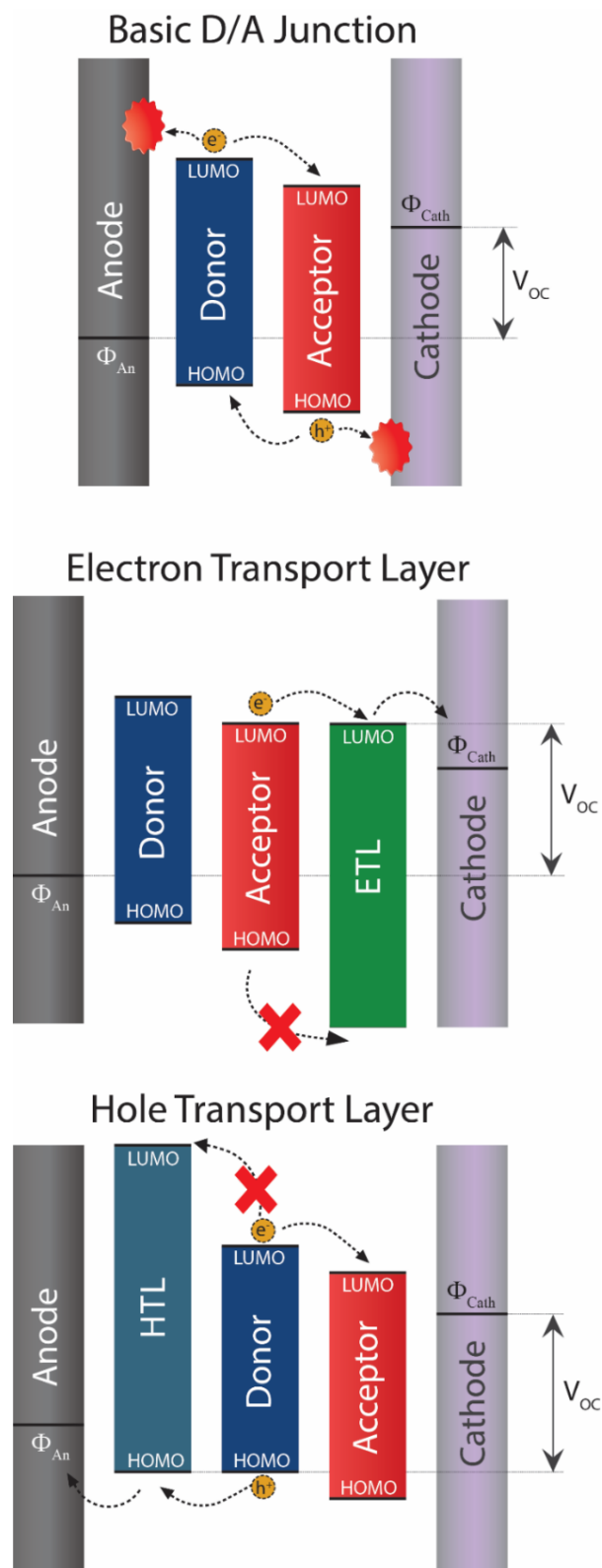
Figure.3.1. Schematic represents the energy band diagram of the organic solar cell with (a) basic donor-acceptor junction, (b) only electron transport layer and (c) only hole transport layer, respectively, to illustrate the function of transport layers in the OSC device architecture.

The standard device architecture involves an ETL and an HTL with an optimized thickness and matched optoelectronic properties. In some cases, multiple interlayers are also used to enhance the efficiency of the OSCs.[9-10] The following section provides a brief overview of interlayers and interfacial modifications used in OSCs with examples.

The interfacial modifications in OSCs can be broadly classified into (1) interlayers to reduce energy level mismatch and charge transport barrier and (2) interfacial modifications to enhance photon harvesting.[10-11]

Table 3.1. Survey of reported interlayers and interface modifications in organic solar cells.

Interlayers	Examples	Ref.
Metals	Ca, Mg, Ba	12
Metal oxides	ZnO, MoO$_x$, NiO, V$_2$O$_5$, WO$_3$	13-17
Organic conjugated molecules	NDIs, PDIs	18-21
Organic polymers	PEDOT:PSS	22-24
Organic dyes	Perylene bisimide	25-26
Interfacial dipoles	PEIE, PFN, PFN-Br	27-29
Ionic liquids	[BMIM]BF4	30
Optical spacers	TiO$_x$	31
Plasmonic nanoparticles	Au NPs, Ag NPs	32

The low work function of alkali metal and alkaline earth metals (Ca, Mg, Ba, LiF salt) are cathode interlayers (ETL) which reduce the work function of metal electrodes and enhance the electron extraction in the device.[33-34] These materials are mostly used in organic light-emitting diodes (OLEDs) and are also utilised in OSCs. The thermal evaporation method is used to deposit these layers in the device. Metal oxides (ZnO, MoO_x, TiO_2) are another important class of interlayers and are widely used in standard device architecture.[35-36] ZnO is the most extensively used ETL in the inverted device architecture of OSCs. The relatively high electron mobility, solution processability, high transparency in the visible region, excellent stability and suitable energy levels (valance band ~ -7.8 eV and conduction band ~ -4.4 eV) make ZnO film a well-suited cathode buffer layer in OSCs with inverted device architecture. The ZnO buffer layer is mostly fabricated using the sol-gel method, and it can also be fabricated from ZnO nanoparticle dispersion and, in some cases, using the atomic layer deposition (ALD) method.[14] The standard ETL in all the devices fabricated in this thesis also uses the ZnO film, and the fabrication process of the ZnO layer is discussed in detail in the following section.

The use of interfacial dipoles (PEIE, PFN) at the BHJ/electrode interface can create a local electric field by forming electronic dipoles at the interface, which further help extract the electrons. Interfacial dipole layers are relatively thin and can be incorporated with other ETL such as ZnO.[37] Apart from this, organic molecules such as PDIs, NDIs and fullerene derivatives can also be used as the ETL due to their high electron mobility and compatibility with the acceptor molecules in the BHJ layer.[20-21]

The organic polymer PEDOT:PSS (mixture of two ionomers) is a widely used HTL owing to the properties of good film-forming capability, high transparency in the visible region and tunable conductivity ($10^{-4} – 10^3$ S/cm^{-1}).[38] The high work function of PEDOT:PSS film (5.0 – 5.2 eV) is suitable to align with the anode and the HOMO level of the BHJ active layer.[7, 22, 39]

The optical spacers (TiO_x, ZnO) and plasmonic nanoparticles (Au NPs, Ag NPs) are interfacial modifications to enhance photon harvesting and thereby improve the J_{SC} of the OSCs. The optical spacer is an optically transparent layer that helps to maximize the absorption of back-reflected photons by facilitating constructive interference of incoming and reflected light at the active layer. The optimized thickness of the optical spacer leads to the constructive interference of incident and reflected light at the BHJ layer and increases the number of photogenerated carriers and J_{SC}. The plasmonic nanoparticles interlayer help to scatter the incident light at the BHJ interface and thereby enhances the photo-absorption of the active layer. The incoming light which passes through the thin active layer without being absorbed due to the low-thickness (~100 nm) of the BHJ layer can be trapped at the active layer by the photon scattering of plasmonic nanoparticles.[9, 32]

This chapter discusses the utility of the $PC_{70}BM$ interlayer between electron transport layer ZnO and the active layer in inverted OSCs of PBDB-T-2Cl:IT-4F BHJ. The presence of a $PC_{70}BM$ interlayer can significantly improve the device performance and exhibit a 33% enhancement in PCE compared to control devices. The combination of ZnO/$PC_{70}BM$ as an electron transport layer in this specific NFA (IT-4F) based BHJ helps to reduce interfacial transport and surface recombination losses to result in high J_{SC}.[40]

3.1. Device Fabrication of Organic Solar Cells

The chemical structure of PBDB-T-2Cl, IT-4F and $PC_{70}BM$ is shown in **Figure.3.2**. PBDB-T-2Cl and IT-4F were purchased from Solarmer materials Inc (China). Phenyl-C71-butyric acid methyl ester ($PC_{70}BM$) was purchased from Luminescent Technologies (Taiwan). All chemicals used as received.
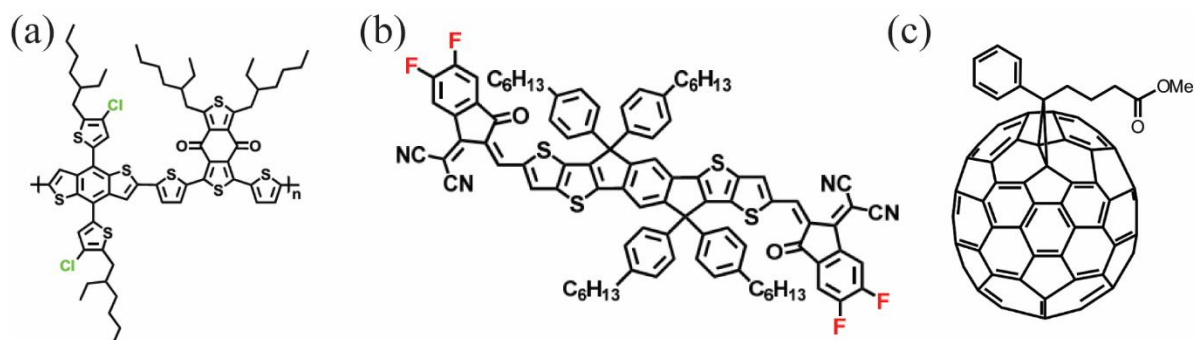
Figure.3.2. The chemical structures of (a) PBDB-T-2Cl, (b) IT-4F and (c) PC$_{70}$BM.

The structure of inverted OSC devices with interlayer is ITO/ZnO/ PC$_{70}$BM/PBDB-T-2Cl:IT-4F/MoO$_3$/Ag, shown in **Figure.3.3a**. Zinc oxide (ZnO) nanoparticle dispersion (from Sigma-Aldrich) in ethanol was spin-coated on precleaned and patterned indium tin oxide (ITO) substrates (sheet resistance ~7 □/sq) to obtain ≈ 40 nm thick ZnO film. ZnO layer was thermally annealed in air at 120 °C for 30 minutes. The interlayer devices were fabricated by spin-coating PC$_{70}$BM (dissolved in chlorobenzene with a concentration of 10 mg mL^{-1}) at 3500 rpm for 1min on the ZnO layer, followed by thermal annealing at 120°C for 15 min inside a nitrogen-rich glove box. Thermal annealing of the PC$_{70}$BM layer ensures the solidification of the film and reduces the complete dissolving or washing away of the layer when the BHJ layer is cast on top of it. The spin-coating of the interlayer was optimized to obtain a thickness of the PC$_{70}$BM layer ~20 nm. 20 mg/ml solution of PBDB-T-2Cl:IT-4F (1:1.2 ratio of donor and acceptor polymers) in chlorobenzene: Diiodooctane (99.5:0.5 v/v) solvent was used to form BHJ active layer films. The active layer formed was obtained from spin-coating at 1500 rpm for 60 s on the ZnO-coated ITO substrates inside a nitrogen-rich glovebox. Dynamic spin coating was employed for a quick dispensation of the BHJ layer due to the commonality of solvent. The O$_2$ and H$_2$O levels in the glovebox are maintained to < 0.5 ppm and < 2 ppm,

respectively. The devices (electrode area ≈ 0.09 cm^2) were completed by thermal evaporation of ≈ 10 nm layer of molybdenum oxide and a 100 nm layer of silver.

3.2. Current-Voltage Characteristics

The introduction of the PC$_{70}$BM interlayer distinctly improves the device performance, as observed in the J-V characteristics of OSCs shown in **Figure 3.3.b**. The summary of results from tests of a large number of devices (~ 120) forming a reasonable data set is provided in **Table 3.2**. reveals this definite trend.
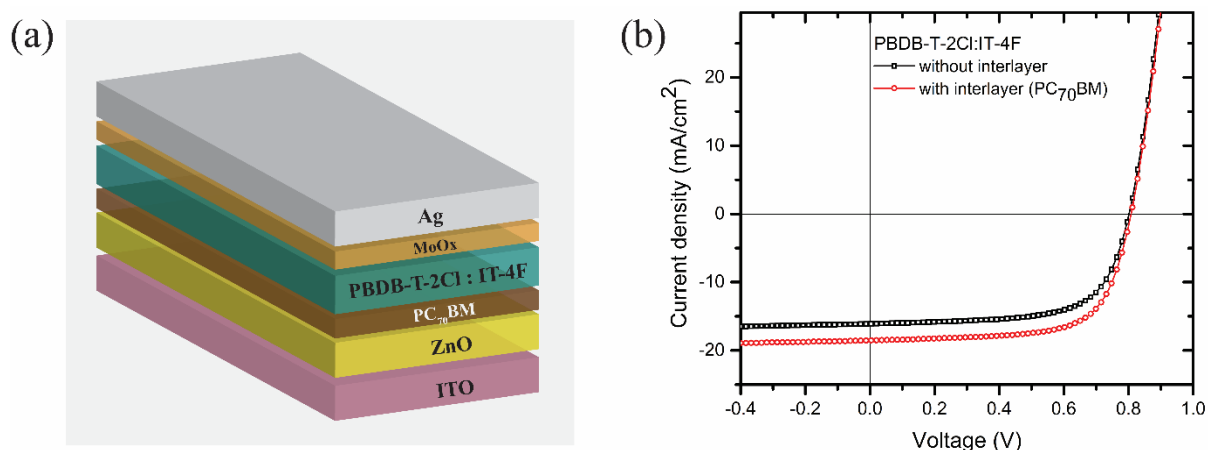
Figure.3.3. (a) Device architecture of inverted BHJ Organic Solar Cell with the PC$_{70}$BM interlayer (b) Typical J-V characteristics of the PBDB-T-2Cl: IT-4F solar cells with and without PC$_{70}$BM interlayer under simulated AM1.5G (100 mW cm^{-2}) illumination.

It must be noted that the PC$_{70}$BM interlayer needs to have an optimum thickness (~ 20 nm) to extract the best performance parameters (thickness determined from ellipsometry data) by fitting the B-spline method using complete EASE software). PBDB-T-2Cl:IT-4F BHJ OSC for this 20 nm-PC$_{70}$BM interlayer results in efficiency as high as 12.1% accompanied by a short circuit current density J$_{SC} \approx 23$ mA/cm^2 (**Figure.3.4a**). The statistics of the performance metrics

carried over a sizable number (100) of devices reveal an increase of average PCE by 33 % (change of PCE from 8.4% to 11.2%). The efficiency enhancement is largely due to the significant improvement in J_{SC} from 15.7 mA/cm^2 to 20.7 mA/cm^2, along with a mild improvement in fill factor (FF) and V_{OC}.

Table 3.2. The Solar cell parameters of PBDB-T-2Cl: IT-4F solar cells without and with PC$_{70}$BM interlayer under simulated AM1.5G (100 mW cm^{-2}) illumination.

Device	V_{oc} (V)	J_{sc} (mAcm^{-2})	Fill Factor (%)	Efficiency (%)	R_S[a)] (Ωcm^2)	R_{Sh}[b)] (Ωcm^2)
Without interlayer	0.800 ± 0.004	15.70 ± 0.28	66.70 ± 0.40	8.44 ± 0.09	5.4	2.9×10^5
With interlayer	0.810 ± 0.004	20.69 ± 1.83	67.41 ± 1.17	11.23 ± 0.79	1.9	9.6×10^4

(a) calculated from dark J-V curve at 1.2 V; b) calculated from the dark J-V curve in the regime around 0 V.

This response is consistent with the scenario of high J_{SC} due to reduced barriers and a nearly unchanged V_{OC} which is controlled mainly by the bulk D and A molecular levels. The efficient electron extraction using the PC$_{70}$BM interlayer shows the formation of a better interface between the active layer and cathode in the device. However, it may be noted that there is a mild reduction in the shunt resistance (R_{sh}), with the FF nearly unchanged. This set of observations can be interpreted in terms of the inevitable mixing of the BHJ active layer at the interface of PC$_{70}$BM/BHJ is expected due to the commonality of the solvent used for the interface and bulk layers and eventually leading to change in the surface morphology of the BHJ. FF and R_{sh} are known to be impacted by the morphology and non-ohmicity in the charge extraction at the anode side.[41]
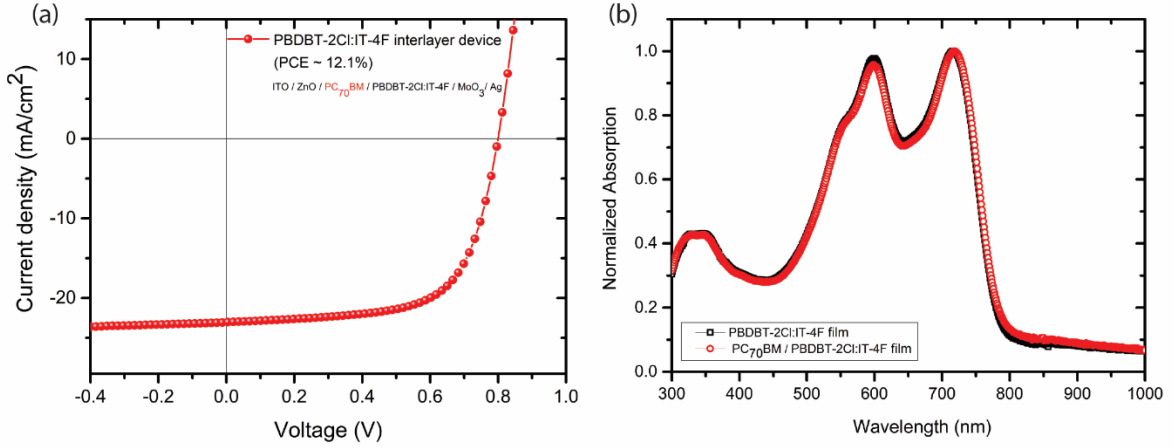
Figure.3.4. (a) J-V characteristic of the PBDB-T-2Cl: IT-4F champion interlayer device under simulated AM1.5G (100 mW cm^{-2}) illumination and (b) Absorption spectra of thin films of PBDB-T-2Cl: IT-4F BHJ and PBDB-T-2Cl: IT-4F BHJ coated on PC$_{70}$BM layer.

The absorption spectra of PBDB-T-2Cl:IT-4F BHJ thin film and PBDB-T-2Cl:IT-4F BHJ thin film coated on PC$_{70}$BM layer shown in **Figure.3.4b** indicates the enhancement in J$_{SC}$ is not due to the improved light absorption of the PC$_{70}$BM layer. The dark J-V characteristics of control and interlayer devices are shown in **Figure.3.5a**, which illustrates that the leakage current is lower in the interlayer device. Furthermore, the interlayer device shows an improved rectification ratio indicative of better contact selectivity obtained by the PC$_{70}$BM layer in the device.[42-44] These features correlate with the efficient charge carrier extraction behaviour of interlayer devices under illumination.[45-46] Differential diode ideality factor (η_{id}) obtained from dark J-V sheds light on recombination processes involved in the device.[2, 47-48] It is estimated from the slope in the exponential region of the dark J-V curve using the relation,

$$\eta_{id} = \left(\frac{KT}{q} \frac{\partial \ln{(J)}}{\partial V} \right)^{-1} \tag{39}$$

The calculated η_{id} at different voltages for control and interlayer devices is depicted in **Figure.3.5b**. A reduction in the ideality factor for the interlayer device ($\eta_{id} \sim 1.5$) in comparison with the control device ($\eta_{id} \sim 2$) is suggestive of reduced bimolecular recombination and improved device performance.
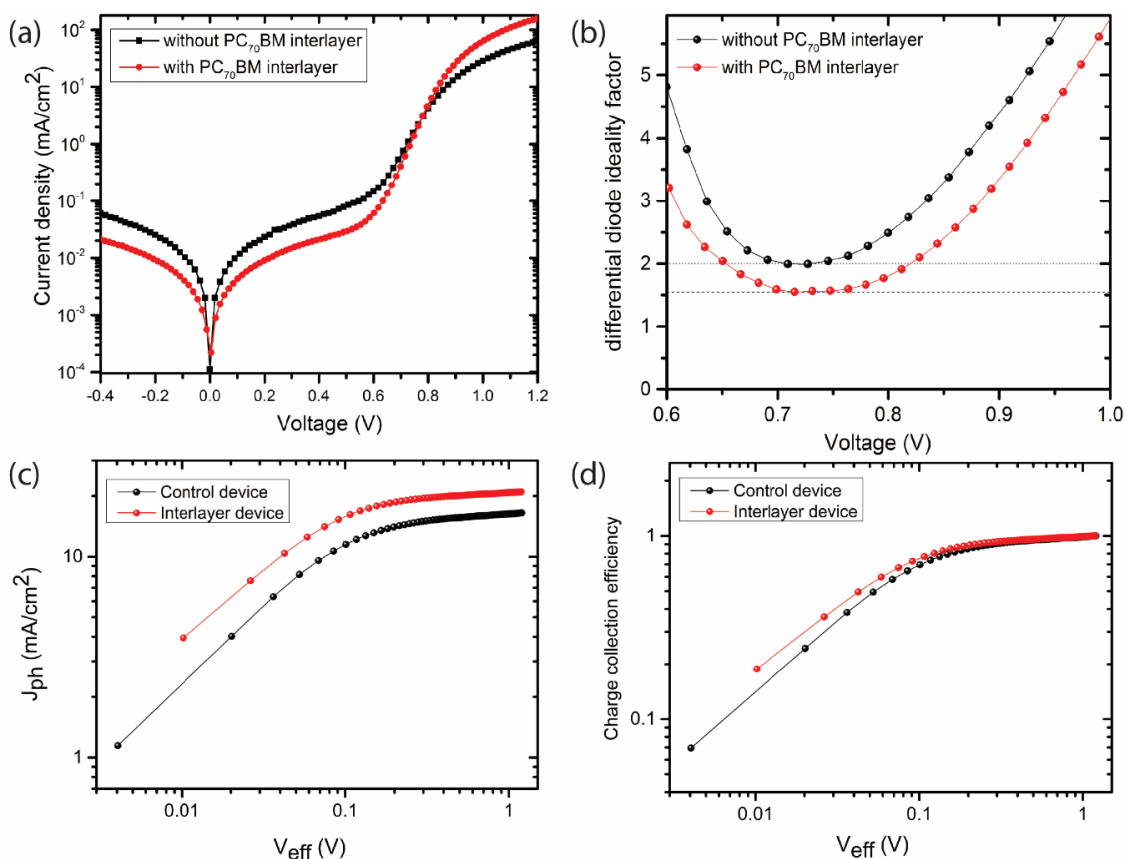
Figure.3.5. (a) Typical dark J-V characteristics, (b) differential diode ideality factor obtained from dark J-V characteristics of the PBDB-T-2Cl: IT-4F solar cells without and with $PC_{70}BM$ interlayer (ideality factor for control device ~ 2.04 and interlayer device ~ 1.55) (c) J_{ph} and (d) charge collection efficiency of the PBDB-T-2Cl: IT-4F solar cells and with the inclusion of $PC_{70}BM$ interlayer.

Photocurrent density (J_{ph}) as a function of effective voltage (V_{eff}) for the control and the interlayer devices are studied to gain insights into the efficiency enhancement of interlayer devices.[49-50] The double logarithmic plot of $J_{ph}(V_{eff})$ at room temperature is shown in **Figure.3.5.c**. $J_{ph} = J_L - J_D$, where J_L and J_D are the current densities measured under AM1.5G illumination and dark, respectively. $V_{eff} = V_o - V$ where V_o corresponds to the voltage where $J_{ph}=0$ and V is the applied voltage. At low V_{eff} (< 0.1 V), J_{ph} has a linear dependence on the voltage for both types of devices. In this region of $J_{ph}(V)$, dJ_{ph}/dV for the interlayer device is

less than dJ_{ph}/dV for the control device. This trend is also consistent with models suggesting decreased recombination and enhanced charge collection for the interlayer device.[50-51] At higher V_{eff} (> 1 V), all generated electron-hole pairs are assumed to be dissociated and collected at the electrode, and J_{ph} becomes saturated. J_{ph} saturates towards J_{sat} for both the devices above $V_{eff} \approx 0.4$ V. The charge collection efficiency is estimated from J_{ph}/J_{sat} as shown in **Figure.3.5d**, and it clearly indicates the increase in the case of the interlayer devices. Since both the devices have identical anode contacts, interfacial properties at the cathode due to the $PC_{70}BM$ interlayer resulted in enhanced charge collection in the interlayer device.[52-54]

The light intensity-dependent J(V) response also highlights the role of the $PC_{70}BM$ interlayer. J_{SC} was studied as a function of light intensity for control and interlayer devices, as shown in **Figure.3.6**. J_{SC} (intensity) has the form of $J_{SC} = CI^{\alpha}(\alpha \leq 1)$, where C is a constant. α assumes a value in the range of 0.5 to 1, and $\alpha < 1$ corresponds to the dominant bimolecular recombination.[55-57] The α estimate for the interlayer devices (0.92) is marginally higher than that of control devices (0.91).
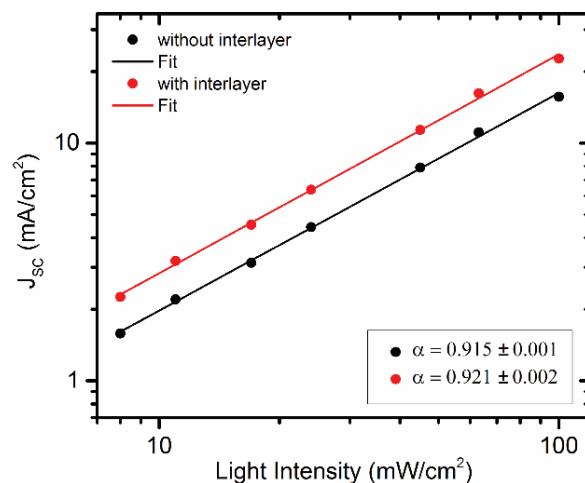
Figure.3.6. Light-intensity dependence of J_{SC} for PBDB-T-2Cl:IT-4F solar cells without and with $PC_{70}BM$ interlayer. Neutral density filters are used to vary the intensity of AM 1.5G 1 sun illumination.

112

On the other hand, the LUMO energy level of ZnO is ≈ -4.4 eV and for $PC_{70}BM$ is ≈ -4.0 eV. These levels indicate the pathway for the photogenerated electrons in the BHJ via an intermediate state and provide a low-loss mechanism for charge extraction at the cathode.[58-59]

3.3. Charge Transport Study using Impedance Spectroscopy

The process in the bulk and interface can be closely followed by frequency-domain impedance measurements, $Z(\omega)$. The relaxation processes associated with the physical processes have their signatures in $Z(\omega)$ studies. This method has been utilized to follow various charge transport and recombination processes with different time scales in an operating device.[60-61] Here, a small sinusoidal voltage perturbation of varying frequency applied to the device along with a constant DC voltage and subsequent relaxation is studied. A wide enough frequency range of the ac voltage from 10 Hz to 2 MHz was selected for the measurement to obtain information on electrical processes with various response time scales. **Figure.3.7a** shows the Nyquist plot of control and $PC_{70}BM$ interlayer devices obtained in the dark and under open-circuit conditions. The response $-Z''$(-imaginary part of $Z(\omega)$) vs Z'(real part of $Z(\omega)$) of the optimized control and interlayer, devices reveal a single semi-circular arc, and a simple equivalent of RC element provides a description of the response.

Equivalent circuit analysis (**Table.3.3**) indicates a significant reduction in charge transport resistance (R_{CT}) for the $PC_{70}BM$ interlayer device, again confirming the enhanced contact-selectivity for electron transport and efficient charge collection.[30, 62-63] The nearly unchanged C_1 of ≈ 40 nF cm^{-2} for both control and interlayer devices implies that the frequency shifts in $Z(\omega)$ primarily arise from changes in the device resistance.[64-65] Bode plots (magnitude of the impedance and phase *vs* frequency) show the dependence of frequency with better clarity on high-frequency response explicitly. Bode plots of control and interlayer devices (**Figure 3b,c**)

113

depict the reduction in charge transport resistance due to the $PC_{70}BM$ interlayer as a shift in peak towards a high-frequency region ($\sim 10^5$ Hz) in comparison with the control device ($\sim 5 \times 10^4$ Hz).
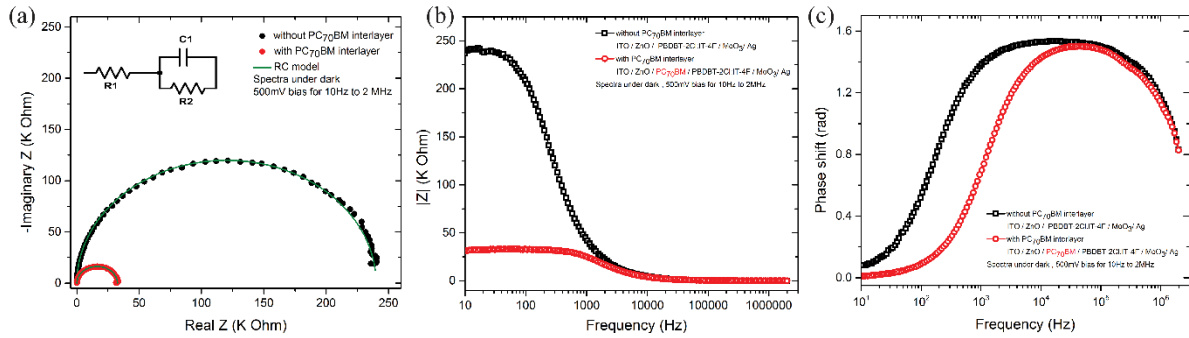
Figure.3.7. (a) Nyquist plot of the PBDB-T-2Cl: IT-4F solar cells without and with PC70BM interlayer at room temperature and under dark conditions. Bode plots of (b) magnitude of impedance and (c) phase angle of devices without and with PC70BM interlayer. The upper left inset in (a) shows the equivalent circuit for experimental data fitting (R_1 series resistance, $R_2=R_{CT}$ charge transport resistance and $C_1=C_g$ geometric capacitance).

Table.3.3. Summary of parameters from equivalent circuit analysis of PBDB-T-2Cl: IT-4F cells and cells with $PC_{70}BM$ interlayer.

	$R_1(\Omega cm^2)$	$R_2(k\Omega cm^2)$	$C_1 \ (nFcm^{-2})$
Without interlayer	1.75	21.59	39.1
With interlayer	1.79	2.93	42.2

(R_1 series resistance due to the contacts at ITO and anode, $R_2=R_{CT}$ charge transport resistance and C_1 represents geometric capacitance).

3.4. Charge Transport Study using Photocurrent Noise Spectroscopy

Electric noise spectroscopy is a facile tool to probe intrinsic processes and device stability in electronic devices.[66] The fluctuations in the time-series of photocurrent $I_{ph}(t)$ under steady-incident illumination are the manifestation of different inherent processes, such as trap-mediated charge transport in the bulk and interfacial barrier-limited transport.[66-67] The parameters describing the $1/f$ behaviour, such as the range and onset of the power spectral density (PSD), provide a quantitative tool to compare the devices.[67] It has earlier demonstrated in PTB7-Th:PC$_{70}$BM devices the improved charge collection efficiency and better contact selectivity result in a reduction in the magnitude of the fluctuation amplitude and consequently the PSD.[13] In general, low-noise amplitude (PSD) of the fluctuations in the $I_{ph}(t)$ time series correlates with improved device performance.[67]
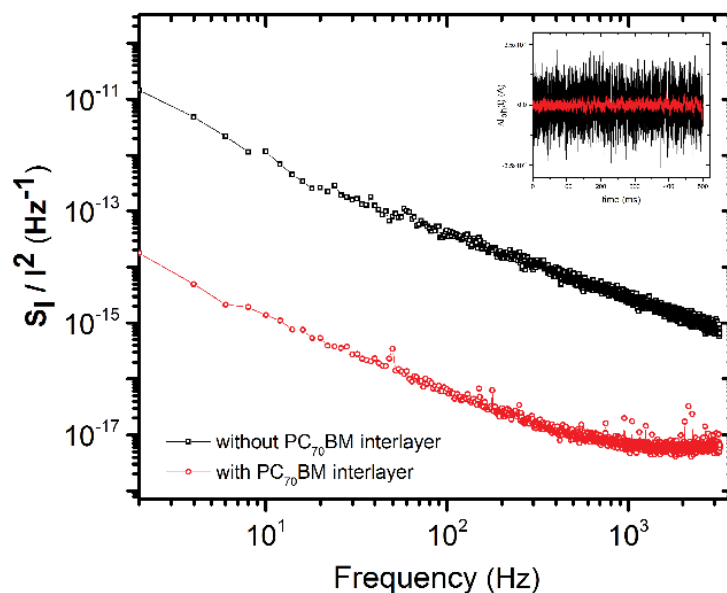
Figure.3.8. Normalized PSD of photocurrent noise spectra at 300 K (obtained from time-series measurements using dynamic signal analyzer ~104 samples s^{-1} for 40 s, under steady-state DC light levels of ~ 10 mW cm-2) of the PBDB-T-2Cl: IT-4F solar cells along with the presence of PC70BM interlayer. The upper right inset shows the photocurrent fluctuations in the time domain.

Table.3.4. Normalized PSD values at 2 Hz and the frequency exponent calculated by fitting to Hooge's model of PBDB-T-2Cl: IT-4F solar cells without and with $PC_{70}BM$ interlayer.

Device	S_I/I^2 Hz^{-1} (at 2 Hz)	γ
Without interlayer	1.45 x 10^{-11}	1.25
With interlayer	1.77 x 10^{-14}	1.27

In the present study, the noise spectra of control and interlayer devices provide further insight into the enhanced performance of the interlayer device and confirm the underlying trend. Normalized PSD (NPSD) of control and interlayer devices captured under steady-state low noise white light illumination is shown in **Figure.3.8**. Noise spectra in the frequency domain follow $1/f^\gamma$ behaviour, typical for the organic solar cells with γ in the range of 0.8 – 1.4 in conventional devices.[66, 68] A γ value of ~1.3 (**Table.3.4**) was obtained for the devices with a reduction in NPSD in three orders of magnitude for interlayer devices (1.77 x 10^{-14} Hz^{-1}) in comparison with the control device (1.45 x 10^{-11} Hz^{-1}) indicating improved charge collection and reduced charge transport barrier.

3.5. Summary

In summary, the introduction of interface layers can maximize the performance of certain organic solar cells (OSCs). It is demonstrated that high-efficiency non-fullerene acceptor (NFA) based solar cells can be further improved upon the insertion of $PC_{70}BM$ as an interlayer between the electron transport layer and the active layer. The introduction of ~20 nm thick interlayer of $PC_{70}BM$ between the cathode-buffer layer, and the BHJ active layer of PBDB-T-2Cl:IT-4F, is an effective strategy to enhance the PCE of the solar cell. The combination of

ZnO and $PC_{70}BM$ layers between the cathode and bulk heterojunction (BHJ) active layer appear to serve as a better selective contact by reducing the charge transport barrier and recombination. The enhanced short-circuit current density (J_{SC}) is characterized by a low series resistance (< 2 Ωcm^2), improved charge collection efficiency and power conversion efficiency (PCE). The improvement is primarily due to the enhanced J_{SC} and has been traced to reduced interfacial charge transport barriers and increased charge collection efficiency. Furthermore, the $PC_{70}BM$ interlayer suppresses the interfacial recombination and provides better contact selectivity. Impedance and noise spectroscopy studies corroborate these findings and validate the interpretations.

References

1.   Yu, G.; Gao, J.; Hummelen, J. C.; Wudl, F.; Heeger, A. J., Polymer Photovoltaic Cells: Enhanced Efficiencies Via a Network of Internal Donor-Acceptor Heterojunctions. *Science* **1995**, *270*, 1789-1791 0036-8075.

2.   Street, R. A.; Schoendorf, M.; Roy, A.; Lee, J. H., Interface State Recombination in Organic Solar Cells. *Physical Review B* **2010**, *81*, 205307.

3.   Li, J.; Jiu, T.; Li, B.; Kuang, C.; Chen, Q.; Ma, S.; Shu, J.; Fang, J., Inverted Polymer Solar Cells with Enhanced Fill Factor by Inserting the Potassium Stearate Interfacial Modification Layer. *Applied Physics Letters* **2016**, *108*, 181602 0003-6951.

4.   Nian, L.; Zhang, W.; Zhu, N.; Liu, L.; Xie, Z.; Wu, H.; Würthner, F.; Ma, Y., Photoconductive Cathode Interlayer for Highly Efficient Inverted Polymer Solar Cells. *Journal of the American Chemical Society* **2015**, *137*, 6995-6998.

5.   Yin, Z.; Wei, J.; Zheng, Q., Interfacial Materials for Organic Solar Cells: Recent Advances and Perspectives. *Advanced Science* **2016**, *3*, 1500362.

6.   Zhang, F.; Ceder, M.; Inganäs, O., Enhancing the Photovoltage of Polymer Solar Cells by Using a Modified Cathode. *Advanced Materials* **2007**, *19*, 1835-1838.

7.   Walker, B.; Choi, H.; Kim, J. Y., Interfacial Engineering for Highly Efficient Organic Solar Cells. *Current Applied Physics* **2017**, *17*, 370-391.

8.   Liao, H.-H.; Chen, L.-M.; Xu, Z.; Li, G.; Yang, Y., Highly Efficient Inverted Polymer Solar Cell by Low Temperature Annealing of Cs 2 Co 3 Interlayer. *Applied physics letters* **2008**, *92*, 156 0003-6951.

9.   Ahmad, N.; Zhou, H.; Fan, P.; Liang, G., Recent Progress in Cathode Interlayer Materials for Non-Fullerene Organic Solar Cells. *EcoMat* **2022**, *4*, e12156 2567-3173.

10.   Lan, W.; Gu, J.; Wu, S.; Peng, Y.; Zhao, M.; Liao, Y.; Xu, T.; Wei, B.; Ding, L.; Zhu, F., Toward Improved Stability of Nonfullerene Organic Solar Cells: Impact of Interlayer and Built-in Potential. *EcoMat* **2021**, *3*, e12134 2567-3173.

11.   Yip, H.-L.; Jen, A. K. Y., Recent Advances in Solution-Processed Interfacial Materials for Efficient and Stable Polymer Solar Cells. *Energy & Environmental Science* **2012**, *5*, 5994-6011.

12.   Reese, M. O.; White, M. S.; Rumbles, G.; Ginley, D. S.; Shaheen, S. E., Optimal Negative Electrodes for Poly (3-Hexylthiophene):[6, 6]-Phenyl C61-Butyric Acid Methyl Ester Bulk Heterojunction Photovoltaic Devices. *Applied Physics Letters* **2008**, *92*, 35 0003-6951.

13.   Chen, S.; Small, C. E.; Amb, C. M.; Subbiah, J.; Lai, T. h.; Tsang, S. W.; Manders, J. R.; Reynolds, J. R.; So, F., Inverted Polymer Solar Cells with Reduced Interface Recombination. *Advanced Energy Materials* **2012**, *2*, 1333-1337 1614-6832.

14.   Liang, Z.; Zhang, Q.; Jiang, L.; Cao, G., Zno Cathode Buffer Layers for Inverted Polymer Solar Cells. *Energy & Environmental Science* **2015**, *8*, 3442-3476.

15.   Irwin, M. D.; Buchholz, D. B.; Hains, A. W.; Chang, R. P. H.; Marks, T. J., P-Type Semiconducting Nickel Oxide as an Efficiency-Enhancing Anode Interfacial Layer in Polymer Bulk-Heterojunction Solar Cells. *Proceedings of the National Academy of Sciences* **2008**, *105*, 2783-2787 0027-8424.

16.   Huang, J.-S.; Chou, C.-Y.; Liu, M.-Y.; Tsai, K.-H.; Lin, W.-H.; Lin, C.-F., Solution-Processed Vanadium Oxide as an Anode Interlayer for Inverted Polymer Solar Cells Hybridized with Zno Nanorods. *Organic Electronics* **2009**, *10*, 1060-1065 1566-1199.

17.   Tao, C.; Ruan, S.; Xie, G.; Kong, X.; Shen, L.; Meng, F.; Liu, C.; Zhang, X.; Dong, W.; Chen, W., Role of Tungsten Oxide in Inverted Polymer Solar Cells. *Applied Physics Letters* **2009**, *94*, 29 0003-6951.

18.   Yao, J.; Qiu, B.; Zhang, Z.-G.; Xue, L.; Wang, R.; Zhang, C.; Chen, S.; Zhou, Q.; Sun, C.; Yang, C., Cathode Engineering with Perylene-Diimide Interlayer Enabling over 17% Efficiency Single-Junction Organic Solar Cells. *Nature communications* **2020**, *11*, 1-10 2041-1723.

19.   Yao, J.; Chen, Q.; Zhang, C.; Zhang, Z. G.; Li, Y., Perylene-Diimide-Based Cathode Interlayer Materials for High Performance Organic Solar Cells. *SusMat 2692-4552* **2022**.

20.   Li, Z.; Yang, D.; Zhao, X.; Li, Z.; Zhang, T.; Wu, F.; Yang, X., New Pdi-Based Small-Molecule Cathode Interlayer Material with Strong Electron Extracting Ability for Polymer Solar Cells. *RSC advances* **2016**, *6*, 101645-101651.

21.   Liu, M.; Fan, P.; Hu, Q.; Russell, T. P.; Liu, Y., Naphthalene-Diimide-Based Ionenes as Universal Interlayers for Efficient Organic Solar Cells. *Angewandte Chemie* **2020**, *132*, 18288-18292 0044-8249.

22.   Tait, J. G.; Worfolk, B. J.; Maloney, S. A.; Hauger, T. C.; Elias, A. L.; Buriak, J. M.; Harris, K. D., Spray Coated High-Conductivity Pedot: Pss Transparent Electrodes for Stretchable and Mechanically-Robust Organic Solar Cells. *Solar Energy Materials and Solar Cells* **2013**, *110*, 98-106 0927-0248.

23.   Liu, Q., et al., 18% Efficiency Organic Solar Cells. *Science Bulletin* **2020**, *65*, 272-275.

24.   Savva, A.; Georgiou, E.; Papazoglou, G.; Chrusou, A. Z.; Kapnisis, K.; Choulis, S. A., Photovoltaic Analysis of the Effects of Pedot: Pss-Additives Hole Selective Contacts on the Efficiency and Lifetime Performance of Inverted Organic Solar Cells. *Solar Energy Materials and Solar Cells* **2015**, *132*, 507-514 0927-0248.

25.   Wen, X.; Zhang, Y.; Xie, G.; Rausch, R.; Tang, N.; Zheng, N.; Liu, L.; Würthner, F.; Xie, Z., Phenol-Functionalized Perylene Bisimides as Amine-Free Electron Transporting Interlayers for Stable Nonfullerene Organic Solar Cells. *Advanced Functional Materials* **2022**, *32*, 2111706 1616-301X.

26. Schmidt, D.; Son, M.; Lim, J. M.; Lin, M. J.; Krummenacher, I.; Braunschweig, H.; Kim, D.; Würthner, F., Perylene Bisimide Radicals and Biradicals: Synthesis and Molecular Properties. *Angewandte Chemie* **2015**, *127*, 14186-14190 0044-8249.

27. Zhou, Y.; Fuentes-Hernandez, C.; Shim, J.; Meyer, J.; Giordano, A. J.; Li, H.; Winget, P.; Papadopoulos, T.; Cheun, H.; Kim, J., A Universal Method to Produce Low–Work Function Electrodes for Organic Electronics. *Science* **2012**, *336*, 327-332 0036-8075.

28. Duan, C.; Zhang, K.; Guan, X.; Zhong, C.; Xie, H.; Huang, F.; Chen, J.; Peng, J.; Cao, Y., Conjugated Zwitterionic Polyelectrolyte-Based Interface Modification Materials for High Performance Polymer Optoelectronic Devices. *Chemical Science* **2013**, *4*, 1298-1307.

29. Xiong, S.; Hu, L.; Hu, L.; Sun, L.; Qin, F.; Liu, X.; Fahlman, M.; Zhou, Y., 12.5% Flexible Nonfullerene Solar Cells by Passivating the Chemical Interaction between the Active Layer and Polymer Interfacial Layer. *Advanced Materials* **2019**, *31*, 1806616 0935-9648.

30. Yu, W.; Huang, L.; Yang, D.; Fu, P.; Zhou, L.; Zhang, J.; Li, C., Efficiency Exceeding 10% for Inverted Polymer Solar Cells with a Zno/Ionic Liquid Combined Cathode Interfacial Layer. *Journal of Materials Chemistry A* **2015**, *3*, 10660-10665.

31. Kim, J. Y.; Kim, S. H.; Lee, H. H.; Lee, K.; Ma, W.; Gong, X.; Heeger, A. J., New Architecture for High-Efficiency Polymer Photovoltaic Cells Using Solution-Based Titanium Oxide as an Optical Spacer. *Advanced materials* **2006**, *18*, 572-576 0935-9648.

32. Uddin, A.; Yang, X., Surface Plasmonic Effects on Organic Solar Cells. *Journal of nanoscience and nanotechnology* **2014**, *14*, 1099-1119 1533-4880.

33. Jiang, C. Y.; Sun, X. W.; Kyaw, A. K. K.; Li, Y. N., Low Work Function Metal Modified Ito as Cathode for Inverted Polymer Solar Cells. *Solar Energy Materials and Solar Cells* **2010**, *94*, 1618-1621 0927-0248.

34.   Gupta, V.; Kyaw, A. K. K.; Wang, D. H.; Chand, S.; Bazan, G. C.; Heeger, A. J., Barium: An Efficient Cathode Layer for Bulk-Heterojunction Solar Cells. *Scientific reports* **2013**, *3*, 1-6 2045-2322.

35.   Chen, S.; Manders, J. R.; Tsang, S.-W.; So, F., Metal Oxides for Interface Engineering in Polymer Solar Cells. *Journal of Materials Chemistry* **2012**, *22*, 24202-24212.

36.   Boucle, J.; Ackermann, J., Solid-State Dye-Sensitized and Bulk Heterojunction Solar Cells Using Tio2 and Zno Nanostructures: Recent Progress and New Concepts at the Borderline. *Polymer International* **2012**, *61*, 355-373 0959-8103.

37.   Hu, L.; Liu, Y.; Mao, L.; Xiong, S.; Sun, L.; Zhao, N.; Qin, F.; Jiang, Y.; Zhou, Y., Chemical Reaction between an Itic Electron Acceptor and an Amine-Containing Interfacial Layer in Non-Fullerene Solar Cells. *Journal of Materials Chemistry A* **2018**, *6*, 2273-2278.

38.   Kirchmeyer, S.; Reuter, K., Scientific Importance, Properties and Growing Applications of Poly (3, 4-Ethylenedioxythiophene). *Journal of Materials Chemistry* **2005**, *15*, 2077-2088.

39.   Dasi, G.; Lavanya, T.; Sathiyan, G.; Gupta, R. K.; Garg, A.; Amaladass, P.; Thangaraju, K., Improved Hole Injection/Extraction Using Pedot: Pss Interlayer Coated onto High Temperature Annealed Ito Electrode for Efficient Device Performances. *Superlattices and Microstructures* **2021**, *156*, 106953 0749-6036.

40.   Azeez, A.; Narayan, K. S., Enhanced Device Performance Via Interfacial Engineering in Non-Fullerene Acceptor Based Organic Solar Cells. *Applied Physics Letters* **2020**, *117*, 043302 0003-6951.

41.   Gupta, D.; Mukhopadhyay, S.; Narayan, K., Fill Factor in Organic Solar Cells. *Solar Energy Materials and solar cells* **2010**, *94*, 1309-1313.

42.   Kaewprajak, A.; Kumnorkaew, P.; Sagawa, T., Influence of Binary Additives into the Solvent for Preparation of Polymer and Fullerene Bulk Heterojunction Solar Cells by Convective Deposition Method. *Organic Electronics* **2019**, *73*, 18-25.

43.   Li, P.; Wu, B.; Yang, Y. C.; Huang, H. S.; Yang, X. D.; Zhou, G. D.; Song, Q. L., Improved Charge Transport Ability of Polymer Solar Cells by Using Npb/Moo3 as Anode Buffer Layer. *Solar Energy* **2018**, *170*, 212-216.

44.   Kang, Q.; Ye, L.; Xu, B.; An, C.; Stuard, S. J.; Zhang, S.; Yao, H.; Ade, H.; Hou, J., A Printable Organic Cathode Interlayer Enables over 13% Efficiency for 1-Cm2 Organic Solar Cells. *Joule* **2019**, *3*, 227-239.

45.   Liu, B., et al., Boosting Efficiency and Stability of Organic Solar Cells Using Ultralow-Cost Biocl Nanoplates as Hole Transporting Layers. *ACS Applied Materials & Interfaces* **2019**, *11*, 33505-33514.

46.   Zhang, W.; Lan, W.; Lee, M. H.; Singh, J.; Zhu, F., A Versatile Solution-Processed Moo3/Au Nanoparticles/Moo3 Hole Contact for High Performing Pedot:Pss-Free Organic Solar Cells. *Organic Electronics* **2018**, *52*, 1-6.

47.   Cowan, S. R.; Leong, W. L.; Banerji, N.; Dennler, G.; Heeger, A. J., Identifying a Threshold Impurity Level for Organic Solar Cells: Enhanced First-Order Recombination Via Well-Defined Pc84bm Traps in Organic Bulk Heterojunction Solar Cells. *Advanced Functional Materials* **2011**, *21*, 3083-3092.

48.   Kirchartz, T.; Pieters, B. E.; Kirkpatrick, J.; Rau, U.; Nelson, J., Recombination Via Tail States in Polythiophene:Fullerene Solar Cells. *Physical Review B* **2011**, *83*, 115209.

49.   Mihailetchi, V. D.; Xie, H. X.; de Boer, B.; Koster, L. J. A.; Blom, P. W. M., Charge Transport and Photocurrent Generation in Poly(3-Hexylthiophene): Methanofullerene Bulk-Heterojunction Solar Cells. *Advanced Functional Materials* **2006**, *16*, 699-708.

50. Mihailetchi, V. D.; Koster, L. J. A.; Hummelen, J. C.; Blom, P. W. M., Photocurrent Generation in Polymer-Fullerene Bulk Heterojunctions. *Physical Review Letters* **2004**, *93*, 216601.

51. Min, J., et al., Alkyl Chain Engineering of Solution-Processable Star-Shaped Molecules for High-Performance Organic Solar Cells. *Advanced Energy Materials* **2014**, *4*, 1301234.

52. Vijayan, R.; Azeez, A.; Narayan, K. S., Enhanced Stability and Optimized Morphology Induced by Electric-Field-Assisted Annealing of Bulk Heterojunction Solar Cells. *Solar RRL* **2019**, *3*, 1900120.

53. Zhang, M.; Gao, W.; Zhang, F.; Mi, Y.; Wang, W.; An, Q.; Wang, J.; Ma, X.; Miao, J.; Hu, Z., Efficient Ternary Non-Fullerene Polymer Solar Cells with Pce of 11.92% and Ff of 76.5%. *Energy & Environmental Science* **2018**, *11*, 841-849.

54. Yang, L.; Tumbleston, J. R.; Zhou, H.; Ade, H.; You, W., Disentangling the Impact of Side Chains and Fluorine Substituents of Conjugated Donor Polymers on the Performance of Photovoltaic Blends. *Energy & Environmental Science* **2013**, *6*, 316-326.

55. Kyaw, A. K. K.; Wang, D. H.; Gupta, V.; Leong, W. L.; Ke, L.; Bazan, G. C.; Heeger, A. J., Intensity Dependence of Current–Voltage Characteristics and Recombination in High-Efficiency Solution-Processed Small-Molecule Solar Cells. *ACS Nano* **2013**, *7*, 4569-4577.

56. Riedel, I.; Parisi, J.; Dyakonov, V.; Lutsen, L.; Vanderzande, D.; Hummelen, J. C., Effect of Temperature and Illumination on the Electrical Characteristics of Polymer–Fullerene Bulk-Heterojunction Solar Cells. *Advanced Functional Materials* **2004**, *14*, 38-44.

57. Wetzelaer, G.-J. A. H.; Kuik, M.; Blom, P. W. M., Identifying the Nature of Charge Recombination in Organic Solar Cells from Charge-Transfer State Electroluminescence. *Advanced Energy Materials* **2012**, *2*, 1232-1237.

58.   Banerjee, S.; Gupta, S. K.; Singh, A.; Garg, A., Buffer Layers in Inverted Organic Solar Cells and Their Impact on the Interface and Device Characteristics: An Experimental and Modeling Analysis. *Organic Electronics* **2016**, *37*, 228-238.

59.   Wang, K.; Liu, C.; Meng, T.; Yi, C.; Gong, X., Inverted Organic Photovoltaic Cells. *Chemical Society Reviews* **2016**, *45*, 2937-2975.

60.   Bisquert, J., Theory of the Impedance of Electron Diffusion and Recombination in a Thin Layer. *The Journal of Physical Chemistry B* **2002**, *106*, 325-333.

61.   von Hauff, E., Impedance Spectroscopy for Emerging Photovoltaics. *The Journal of Physical Chemistry C* **2019**, *123*, 11329-11346.

62.   Guerrero, A.; Montcada, N. F.; Ajuria, J.; Etxebarria, I.; Pacios, R.; Garcia-Belmonte, G.; Palomares, E., Charge Carrier Transport and Contact Selectivity Limit the Operation of Ptb7-Based Organic Solar Cells of Varying Active Layer Thickness. *Journal of Materials Chemistry A* **2013**, *1*, 12345-12354.

63.   Azmi, R.; Aqoma, H.; Hadmojo, W. T.; Yun, J.-M.; Yoon, S.; Kim, K.; Do, Y. R.; Oh, S.-H.; Jang, S.-Y., Low-Temperature-Processed 9% Colloidal Quantum Dot Photovoltaic Devices through Interfacial Management of P–N Heterojunction. *Advanced Energy Materials* **2016**, *6*, 1502146.

64.   Boix, P. P.; Guerrero, A.; Marchesi, L. F.; Garcia-Belmonte, G.; Bisquert, J., Current-Voltage Characteristics of Bulk Heterojunction Organic Solar Cells: Connection between Light and Dark Curves. *Advanced Energy Materials* **2011**, *1*, 1073-1078.

65.   Guerrero, A.; Ripolles-Sanchis, T.; Boix, P. P.; Garcia-Belmonte, G., Series Resistance in Organic Bulk-Heterojunction Solar Devices: Modulating Carrier Transport with Fullerene Electron Traps. *Organic Electronics* **2012**, *13*, 2326-2332.

66.   Bag, M.; Vidhyadhiraja, N. S.; Narayan, K. S., Fluctuations in Photocurrent of Bulk Heterojunction Polymer Solar Cells—a Valuable Tool to Understand Microscopic and Degradation Processes. *Applied Physics Letters* **2012**, *101*, 043903.

67.   Vijayan, R.; Azeez, A.; Narayan, K. S., Toward Reliable High Performing Organic Solar Cells: Molecules, Processing, and Monitoring. *APL Materials* **2020**, *8*, 040908.

68.   Barone, C.; Lang, F.; Mauro, C.; Landi, G.; Rappich, J.; Nickel, N. H.; Rech, B.; Pagano, S.; Neitzert, H. C., Unravelling the Low-Temperature Metastable State in Perovskite Solar Cells by Noise Spectroscopy. *Scientific Reports* **2016**, *6*, 34675.

Chapter 4

Comprehensive Investigation of Light and Temperature Induced Degradation in Non-Fullerene Acceptor IT-4F Based Organic Solar Cells

Recent advancements in the power conversion efficiency (PCE) of non-fullerene acceptor-based bulk heterojunction (BHJ) OSCs indicate a promising future for commercial feasibility.[1-3] Currently, PCE exceeds 18% for single-junction binary and ternary devices; with the existing donor-acceptor (D-A) combination, 20% PCE is within reach.[4-8] The molecular design strategy has largely focused on improving performance efficiency.[9] More recently, efforts to improve long-term stability have gathered momentum.[10-13] For OSCs to become a mature technology and commercially successful, a longer device lifetime is necessary, along with high performance.[14-15] Background of device degradation and stability aspects of OSCs with emphasis on NFA-based systems has been provided in Chapter 1. It was emphasized that a comprehensive understanding of factors contributing to device stability and degradation mechanisms is required to optimize OSC devices for high efficiency over long lifetimes.[16-17] The present chapter focuses on these issues in the specific BHJ systems based on the NFA acceptor IT-4F.

Recent studies on degradation in non-fullerene acceptors (NFAs) such as IT-4F based devices reveal several years of a lifetime for encapsulated devices under certain aging conditions.[18] The various options increasingly available for encapsulation and packaging can be used to prolong the device performance.[19-20] However, the inherent instability of the device constituents towards external factors such as UV exposure and thermal cycling need to be quantified and understood.

A typical OSC device with a laboratory-standard barrier layer undergoes a more rapid degradation during the initial period of operation as compared to the subsequent stages. This initial drop, called the "burn-in" period, is system-specific and exhibits a decay time-scale of a few hours to hundreds of hours.[21] The "burn-in" degradation is significant in OSCs; in some cases, they constitute nearly 50% of the initial performance. For instance, in PCE11: $PC_{70}BM$ OSCs, a drop of 39% in PCE is observed after 120 hours, even in dark conditions.[22] Similarly, in PBDB-T: ITIC OSCs, a reduction in PCE of over 50% was observed for aging under continuous one sun illumination for 5 hours.[23] A thermal stress of 85°C in the presence of air for initial 5 hours in PTB7-TH: IEICO-4F based OSCs was also shown to reduce the PCE by over 70%.[24]

In this regard, understanding the burn-in loss mechanisms and material-device engineering to reduce the burn-in time and loss is essential.[25] The factors causing the degradation of OSCs during the operation are discussed in chapter 1. Amongst these, light-induced degradation (LID) and temperature-induced degradation (TID) are the major cause of the rapid deterioration of encapsulated device performance. Photochemical and thermochemical degradation, which occurs in the presence of oxygen and moisture, are also significant.[26-27] The chemical reaction between different layers in the device and the chemical stability of the active layer materials themselves to sustain continuous photoexcitation also becomes decisive in device stability.[28] The instabilities induced by atmospheric factors like oxygen and moisture can be minimized through encapsulation.[16, 19] It must be noted that cost-effective plastic-based encapsulation can only protect the device partially from the atmospheric factors, while glass-based encapsulation is not entirely appropriate for flexible devices.[29-30]

In this direction, the present studies reveal the effects of LID and TID during the initial period (for the initial 10 hours and 120 hours) of NFA-based single-junction binary OSC in an inert

atmosphere. Degradation and aging studies were carried out with different initial conditions (UV dosage, thermal history, presence or absence of additives) by monitoring the cell parameters over a sufficiently long duration to arrive at the trajectory trend of the device. These studies also emphasize the need for a standardized protocol of OSCs, where the relative UV component dosage metrics are also specified.

4.1. PBDB-T-2Cl:IT-4F Inverted Organic Solar Cells

PBDB-T-2Cl donor blended with NFA IT-4F based BHJ in an inverted device architecture is selected for the studies and uses the more stable inverted device architecture.[31-33] The NFA molecule IT-4F selected for the present study is one of the highly stable ITIC derivatives mainly due to the fluorination of the end group.[18] The inverted device ITO/ZnO/PBDB-T-2Cl:IT-4F/MoO$_3$/Ag, along with the additive 1,8-diiodooctane (DIO) used in the BHJ solution processing, is used to arrive at optimized active layer morphology for high performing devices.[34] The materials PBDB-T-2Cl and IT-4F were purchased from Solarmer materials Inc (China). 1,8- diiodooctane were purchased from Sigma Aldrich. All chemicals were used as received in the solar cell device fabrication. Zinc oxide (ZnO) nanoparticle dispersion (purchased from Sigma-Aldrich) in ethanol was spin-coated on precleaned and patterned indium tin oxide (ITO) substrates to obtain 40 nm ZnO film. ZnO layer was thermally annealed in air at 120 °C for half an hour. For PBDB-T-2Cl:IT-4F, BHJ solutions of 1:1.2 ratio of donor and acceptor with polymer concentration at 20 mg/ml in chlorobenzene:diiodooctane (99.5:0.5 v/v) solvent. BHJ solutions were kept for stirring overnight at 40 °C. The active layer was then spin-coated at 1500 rpm for 60 s on the ZnO-coated ITO substrates inside a nitrogen-rich glovebox. The devices (electrode area $\approx$ 9 mm^2) were completed

by thermal evaporation of a 10 nm layer of molybdenum oxide and a 100 nm layer of silver at a base pressure of 10^{-6} mbar.

High-performance devices with performance parameters similar to the reported values were consistently obtained for a large number of devices (>100) which were needed to conclusively establish the trends observed in these studies. The narrow distribution of the parameters (short circuit current density J_{SC}, open-circuit voltage V_{OC}, fill factor FF) from the devices with a specified set of processing conditions and dosage metrics were taken into account in the analysis and interpretation of the results.
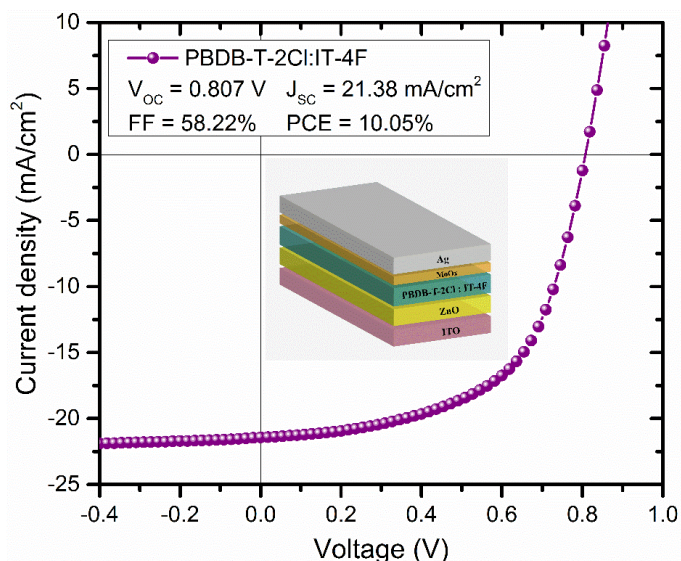
Figure.4.1. Typical J-V characteristics of the PBDB-T-2Cl:IT-4F solar cells under simulated AM1.5G (100 mW/cm^2) illumination (inset shows the device architecture used for the study).

The current-voltage characteristic (J(V)) of a typical device is shown in **Figure.4.1**, along with the device architecture in the inset. Typical PBDB-T-2Cl:IT-4F devices exhibited efficiency centred around 10% with J_{SC} exceeding 20 mA/cm^2. For the accelerated-ageing studies, the stresses (light and heat) are applied to these unencapsulated devices housed in inert chambers immediately after

the first J-V measurement. These devices can be classified under "perfectly encapsulated" devices undergoing selective degradation. Long-term monitoring of device storage life for more than 1000 hours was also carried out to understand the storage life of these devices, as shown in **Figure.4.2**. Even after 1000 hours, the device performance parameters are above T80 lifetime (time taken to reduce the initial efficiency to 80% of its initial value). It must be noted that during the storage life monitoring, the devices are exposed to short-term AM1.5G 1 Sun illumination to record the J-V characteristics at regular intervals of time.
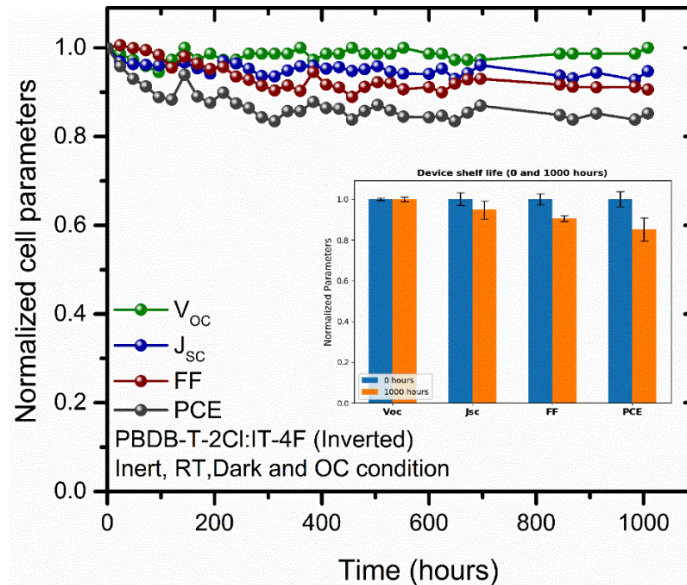
Figure.4.2. Normalized cell parameters of PBDB-T-2Cl:IT-4F solar cells monitored for more than 1000 hours during the storage life in an inert and dark atmosphere (inset bar chart shows the relative change in the parameters of fresh and 1000 hours aged devices).

4.2. Monitoring the evolution of current-voltage characteristics

For the present studies, devices exhibiting PCE greater than 8% were chosen as the minimum PCE on which the degradation process was initiated. J(V) of these devices were then monitored over a period of 10 hours when UV exposure and thermal conditions were maintained on these devices

in an inert atmosphere for 10 hours. **Figure.4.3** shows the normalized cell parameters, including V_{OC}, J_{SC}, FF, and PCE of the devices exposed continuously to 1 sun (AM1.5G) illumination, 1 sun (AM1.5G) illumination with a UV-cut filter (to remove UV components < 400 nm from the incident light) and subjected to continuous thermal stress of 70°C for a ten-hour duration in an inert condition. These three accelerating aging stresses were applied in parallel but separately and isolatedly to the devices. These selective stability test conditions enable identifying the degradation processes initiated by light and heat exclusively in an encapsulated device. And it is anticipated that the results from this study will serve as a guideline for designing stable NFAs for OSCs. In the case of devices exposed to continuous one sun illumination, it is observed that a significant reduction in PCE of ≈ 38% is observed that is accompanied by a reduction in V_{OC} of ~ 28% (**Table.4.1**). The insertion of a UV-blocking filter substantially mitigates the degradation rate in the reduction of PCE to only a 16% drop from the initial value over a period of ten hours and is accompanied by a smaller reduction in V_{OC} (~ 3%) over the same duration. This observation indicates that the initial burn-in due to UV-induced degradation occurs predominantly via mechanisms that primarily affect V_{OC}. Previous reports attributed the photochemical reaction of UV-induced radicals of leftover-DIO with NFA-ITIC as the mechanism which expedites the device degradation.[35] Koster et al. have also shown in the fullerene-based device that the remnant-DIO can act as a photo-acid, and upon UV-illumination, the formation of electronic traps can lead to accelerated ageing of the device.[36] In this context, it is noted that in our studies, the UV-induced trend is present even in the absence of additives like DIO. In the present case, factors non-related to morphological changes also appear to contribute to UV-induced degradation. The UV-blocked studies of the NFA cells are consistent with the reported results of a much slighter and gradual decrease in efficiency.[37]
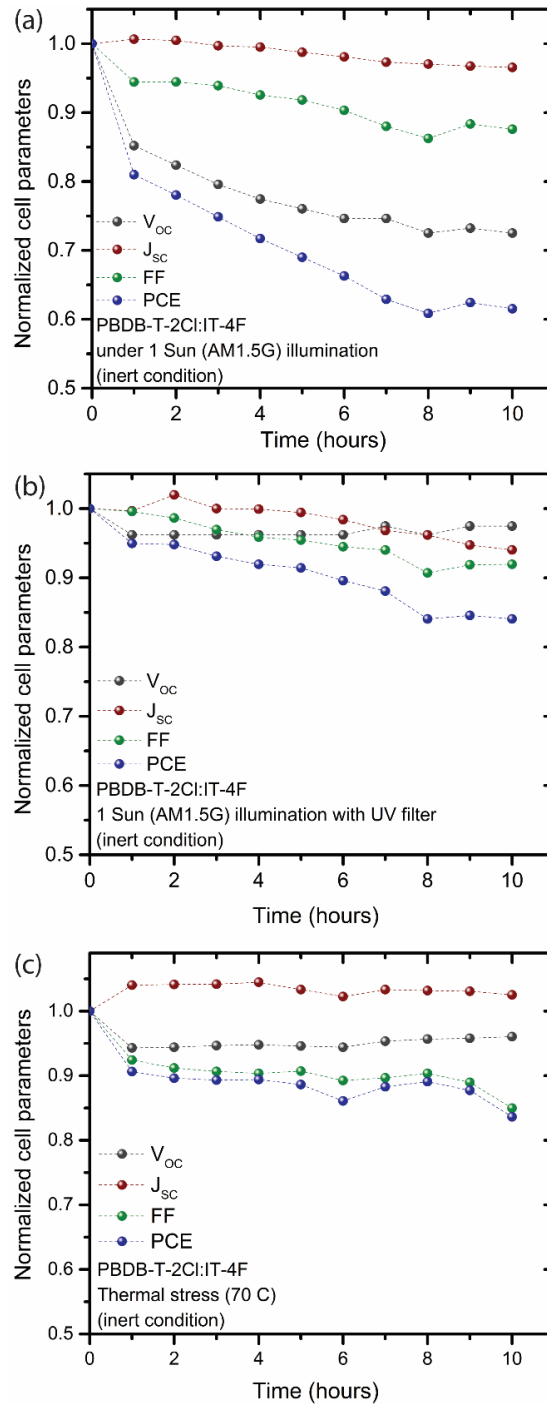
Figure.4.3. Normalized J-V parameters of PBDB-T-2Cl:IT-4F solar cells under (a) simulated AM1.5G 1 sun (100 mW/cm^2) illumination (b) simulated AM1.5G 1 sun (100 mW/cm^2) illumination with a UV-cut filter introduced to remove the UV components and (c) thermal stress of 70°C for the initial 10 hours of device operation continuously in an inert condition, data points represent average values of measurements.

Table.4.1. Percentage reduction in solar cell parameters of PBDB-T-2Cl:IT-4F devices after continuous exposure to ageing stresses for 10 hours (Figure.4.3). The quantities represent the average of results obtained from six devices, each with the error range for the PCE represented by the maximum deviation from this value.

Aging Stress (10 hours)	V_{OC} (%) reduction	J_{SC} (%) reduction	FF (%) reduction	PCE (%) reduction average with error range
1 Sun illumination	27.5	3.4	12.5	38.5 ± 8.6
1 Sun illumination (with UV-cut filter)	2.5	5.9	8.1	15.9 ± 6.4
Thermal stress (70°C)	3.9	2.5	15.0	16.3 ± 5.1

Since the UV spectral component, which constitutes about 4.6% of the AM1.5G light source, appeared to play a crucial role (**Appendix C** shows the analysis of the spectral distribution of AM1.5G solar spectra). Light sources of exclusive UV ($\lambda \sim 350 - 400$ nm, $P_{out} \sim 1$ mW/cm^2) and white light ($\lambda \sim 400 - 700$ nm, $P_{out} \sim 35$ mW/cm$^2 \sim 0.3$ Sun) were utilized to isolate the contributions (illumination spectra of the light sources are shown in **Figure.4.4**). The advantage of these light sources was that long hours (> 500 hours) of exposure inside a glove-box environment is possible. In the present studies, results from devices exposed separately to a white light (UV-free) illumination and UV-illumination for 120 hours in the inert atmosphere were examined. Optimized control devices made using a 0.5% volume fraction of DIO, along with additive-free devices, were also studied with this combination of UV-illumination and UV-free white light (**Figure.4.5**). Percentage reduction in the performance parameters (V_{OC}, J_{SC}, FF and PCE) of OSCs under various accelerated ageing conditions are summarised in **Table.4.2**. OSCs, which are continuously exposed to white light illumination, maintained more than 90% of their

initial efficiency even after 120 hours. While in contrast, devices exposed to UV-illumination suffered from a severe PCE loss of close to 65% of its initial value, accompanied by a 34% decrease in V_{OC}. This is nearly consistent with the earlier short duration (10 hours of AM1.5G illumination) measurements. On the other hand, devices fabricated without DIO also dropped from the high-efficiency values by 55%. The V_{OC} drop (~ 21%) for the DIO-free devices was comparatively smaller in the overall contribution to the PCE decrease. The J_{SC} decrease for the DIO-free devices was similar to ~ 20% in these devices. A significant reduction in FF (~ 27%) was observed in both devices, and in the case of the DIO-free device, it formed the dominant factor in the decay during the burn-in period. This indicates that apart from additive-solvent-assisted UV reaction inducing morphology changes and instabilities, the photochemical changes of BHJ constituents are present. The donor and acceptor molecules under continuous UV excitation over a long period result in a transformation in such a manner to affect both V_{OC} and, ultimately, J_{SC}.
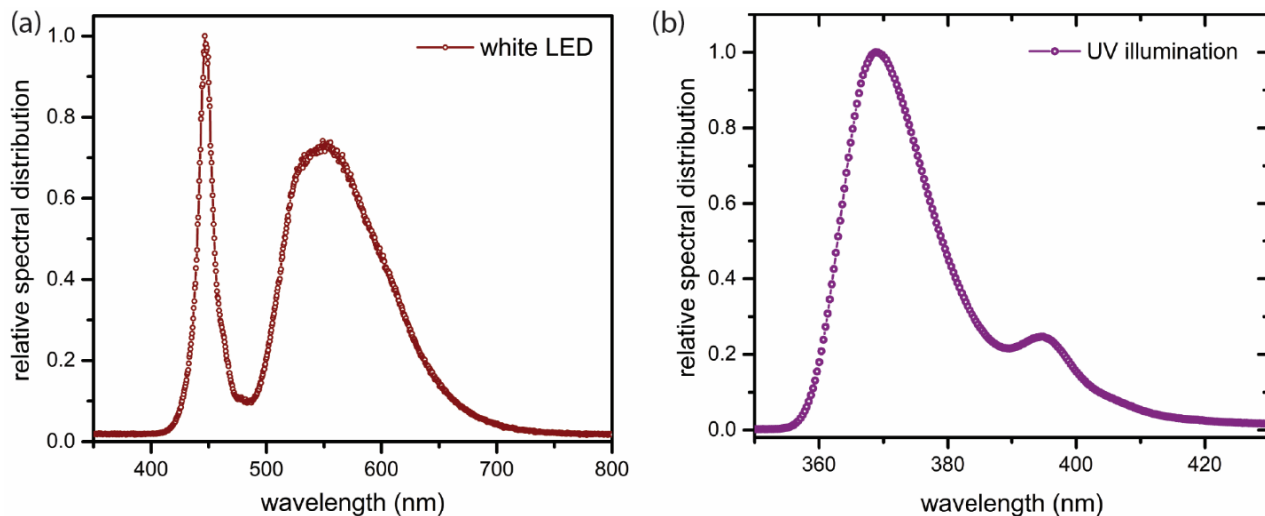
Figure.4.4. The illumination spectra of light sources (a) white LED and (b) UV- LED used for the stability study.
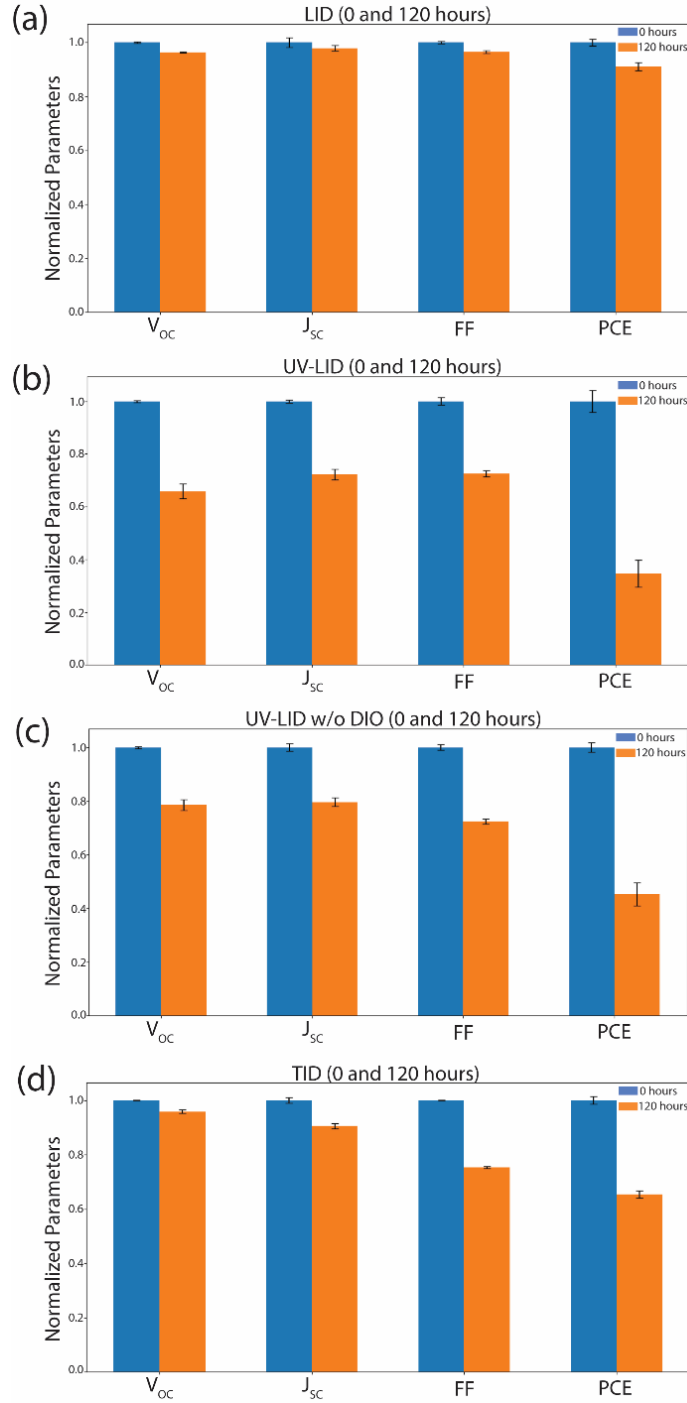
Figure.4.5. Normalized J-V parameters of PBDB-T-2Cl:IT-4F solar cells under (a) white light illumination (UV-free), (b) UV-light illumination, (c) UV-light illumination on devices fabricated without using solvent additive DIO, and (d) thermal stress of 70°C, respectively for the initial 120 hours of device operation continuously in an inert condition (error bar indicated and an average of 6 representative devices).

Table.4.2. Percentage reduction in solar cell parameters of PBDB-T-2Cl:IT-4F devices after continuous exposure to aging stresses for 120 hours (**Figure.4.5**). The quantities represent the average of results obtained from six devices, each with the error range for the PCE represented by the maximum deviation from this value.

Aging Stress (120 hours)	V_{OC} (%) reduction	J_{SC} (%) reduction	FF (%) reduction	PCE (%) reduction
White light (non-UV) illumination	3.6	2.1	3.4	8.9 ± 2.4
UV-light illumination	34.0	27.6	27.3	65.4 ± 3.1
UV-light illumination (devices w/o DIO additive)	21.4	20.2	27.6	54.6 ± 2.8
Thermal stress (70°C)	4.1	9.4	24.6	34.6 ± 1.7

4.3. Spectroscopy signature of photochemical degradation

To further understand the large drop in performance metrics of the device and to elucidate the role of active layer components under UV exposure, Fourier-transform infrared (FT-IR) measurements were studied. The IR-spectra of the BHJ film (without DIO) indicates a distinct shift in the region (~ 1564 cm^{-1}), corresponding to the aromatic C=C group of the acceptor IT-4F molecule. This shift to lower wavenumber (~ 1562 cm^{-1}) upon UV exposure of short duration ~ 5 hours (**Figure.4.6**) is observed only for the BHJ blend and not present for the UV-exposed pure donor and acceptor samples. This trend suggests the role of the modification of D-A ground state interaction. A broadening of the CT manifold can possibly explain the decrease in Voc. [38-43] The other possibility is the weakening of conjugation in the acceptor molecule giving rise to increasing barrier-mediated charge transport pathways.[44] It is known that oxidative degradation and associated disruption in

the charge transport pathways within the BHJ layer are due to UV exposure.[45] UV-induced photochemical changes such as C-H bond rearrangements and the formation of metastable carbon
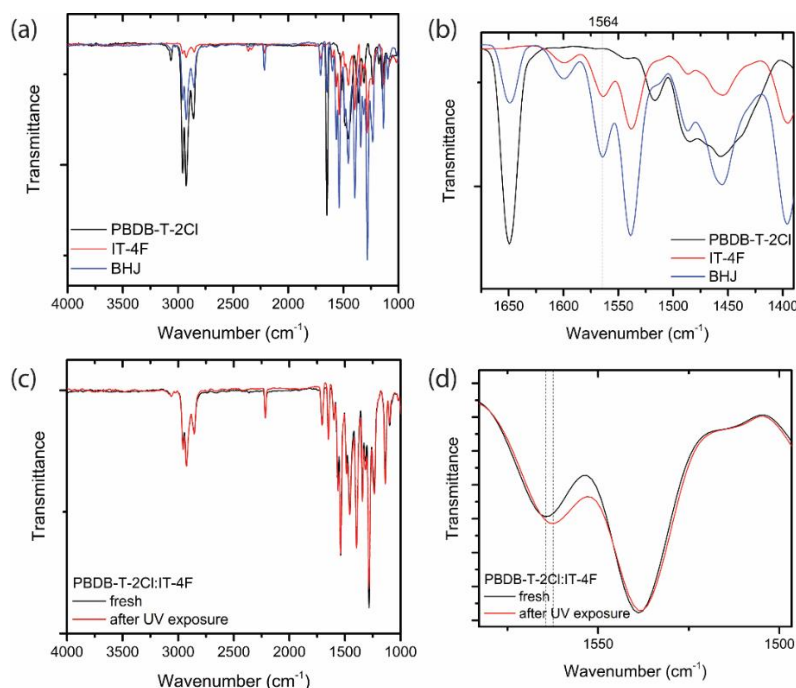
Figure.4.6. (a), (b) Typical FT-IR spectra of pristine PBDB-T-2Cl, IT-4F and BHJ films (c) spectra of fresh and UV-light exposed BHJ film and (d) show the band shift associated with IT-4F molecule.

dangling bonds at the D-A interface are known to expedite degradation in inert conditions.[46] Photocatalytic reaction of NFA in the presence of electron transport layer ZnO results in breaking of the double bond connecting electron-donating and accepting groups within the acceptor molecule.[47] The preparation of ZnO solution via sol-gel method involves dehydration reaction of $Zn(OH)_4^{2-}$ leading to the formation of hydroxyl groups on ZnO surface. The presence of a large number of hydroxyl groups on the ZnO surface is known and can expedite the photocatalytic reaction resulting in the formation of hydroxyl radicals (•OH). These hydroxyl radicals possess a strong oxidizing ability which can decompose the organic layer. Further, it was shown that the

presence of a high density of surface defects in low-temperature solution-processed ZnO and the UV excitation results in the formation of hydroxyl radicals (•OH), which can decompose the vinyl group in ITIC and its derivative NFAs such as IT-4F.[31, 47] This process can lead to breaking the conjugated structure and consequently weakens the charge transport, particularly at the interface with the interlayer.[47] Similar results and features of the optimized devices using both types of ZnO (sol-gel method and nanoparticle dispersion) were observed. A combination of these mechanisms may be at play for the present system.

It should be mentioned that degradation caused by thermal stress belongs to a different class of decay, where the device evolves at a much slower rate. For example, the initial 10 hours of thermal stress (70°C) maintains the device efficiency above 80% of its initial value with a marginal increase in J_{SC}. Improved thermal stability of NFA-based devices in comparison with fullerene counterparts is known, and the degradation is found to occur mainly due to a significant drop in the FF.[48-50] An average drop in efficiency of 16.3% after 10 hours of thermal stress is observed mainly due to the reduction in device FF by 15% (**Figure.4.5**). This feature is more visible with the extended thermal stress for a period of 120 hours. The average drop in PCE is nearly 34%, with a significant contribution from FF reduction (**Figure.4.5**). V_{OC} loss after 120 hours of thermal stress is still minimal (~ 4%), which indicates bulk-related recombination losses are not significant. This observation is consistent with the moderately improved thermal stability of NFA-based BHJs and the thermal stress for this short period having a comparatively less detrimental impact on the active layer.[28, 51]

These changes in the device performance are not readily observed in the optical absorption spectra of the individual layers. Absorption spectra of PBDB-T-2Cl:IT-4F BHJ film show negligible changes even after 120 hours of accelerated ageing stresses (**Figure.4.7b**). In contrast, the external

quantum efficiency (EQE) spectra of the device, which is the ratio of the number of charges extracted out of the device to the number of incident photons at different λ, provide a better insight into the degradation. Processes contributing to EQE include absorption, exciton diffusion to the D-A interface, charge generation and collection. **Figure.4.7a** shows typical EQE spectra of the initial device state and undergoing accelerated ageing conditions. A uniform reduction in EQE for devices exposed to UV light for a period of 120 hours over a wavelength range of 500-750 nm is observed. The overall decrease in EQE spectra in the active layer absorption window correlates with a substantial reduction in PCE (more than 50%). UV-induced photo-degradation of the BHJ active layer and interlayers, especially the interlayer close to the transparent electrode, has shown to exhibit a broadband decrease in EQE.[52] This indicates, in general, losses are likely to arise from changes in interfacial characteristics.
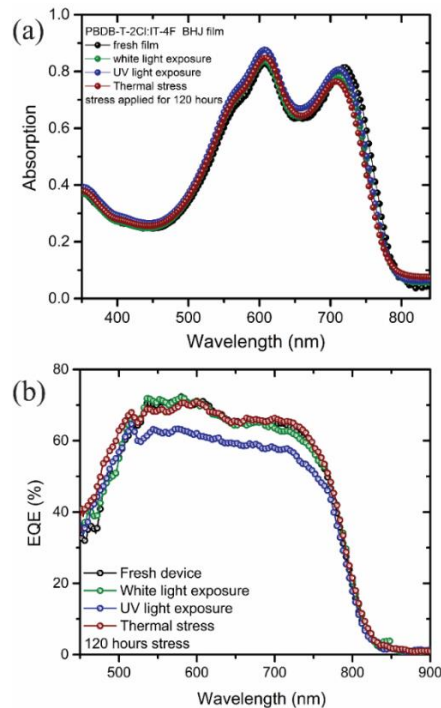
Figure.4.7. (a) Normalized absorption spectra of fresh and 120 hours aged PBDB-T-2Cl:IT-4F BHJ thin films and (b) typical EQE characteristics of fresh devices and devices exposed to various accelerated ageing stresses for 120 hours in an inert condition.

The dark J-V characteristics of fresh devices and devices exposed to the various accelerated ageing conditions (**Figure.4.8**) indicate higher leakage current under reverse bias in devices after UV-induced degradation. This correlates with the large burn-in loss associated with UV-induced degradation. Furthermore, UV-induced degradation causes a large drop in the device rectification ratio as compared to other degradation routes. These observations indicate the reduction in charge carrier extraction efficiency of the devices after accelerated ageing stresses and correlate with the observed reduction in V_{OC} and FF.[53-55]
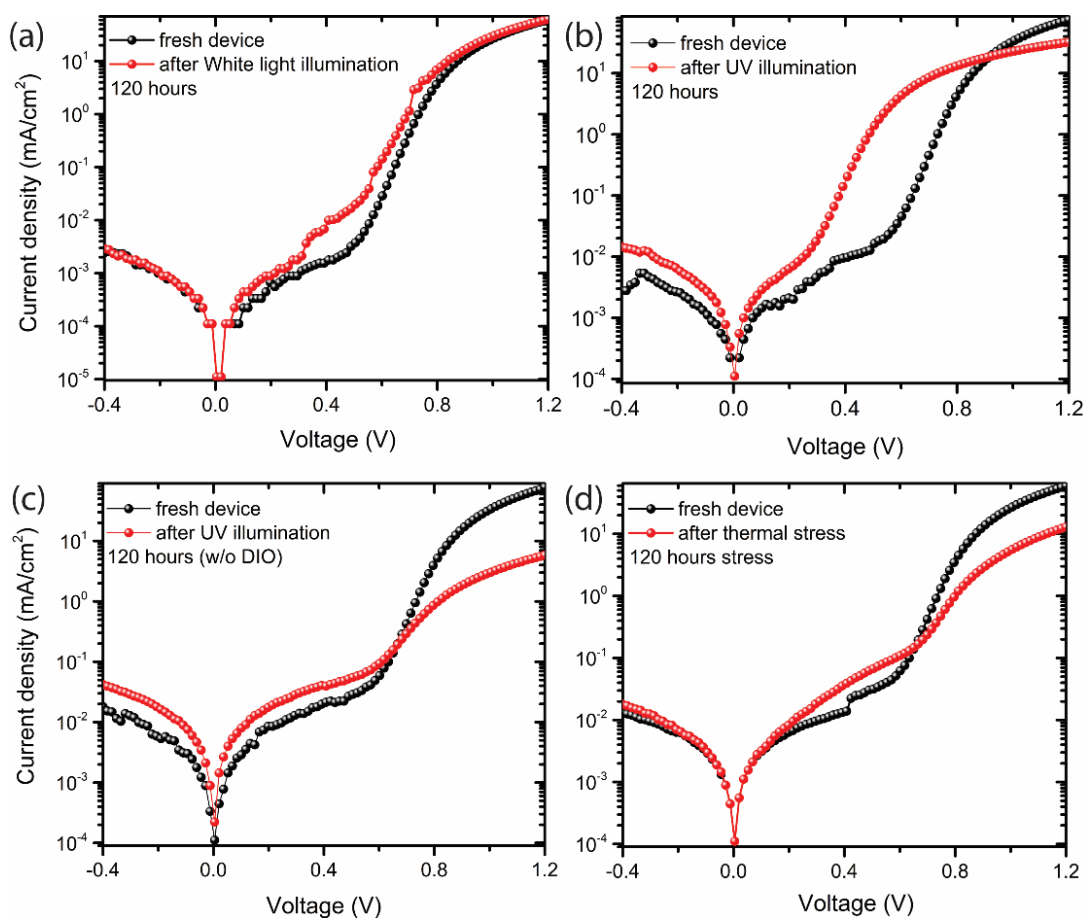
Figure.4.8. Typical dark J-V characteristic of PBDB-T-2Cl:IT-4F solar cells at room temperature before and after accelerated ageing stresses continuously for 120 hours (a) white light illumination (b) UV illumination (c) UV illumination on devices fabricated without using solvent additive DIO and (d) thermal stress of 70°C respectively in an inert condition.

141

Additionally, a qualitative but clear trend of the acceptor molecule modifications near the ZnO interlayer with UV exposure was observed by studies during the fabrication process. UV-light was introduced onto the deposited layers during the fabrication procedure for a 1-hour duration. A set of devices were exposed to UV after spin coating the ZnO layer, and another set was exposed to UV after coating both the ZnO layer and BHJ active layer. UV light was introduced from the glass-ITO side as well as from the polymer side. After the exposure, the device fabrication was completed and studied. The key features observed were: (i) No changes in performance parameters were observed for devices where only the ZnO layer was exposed and was used as control samples (ii) for devices where the ZnO-BHJ interfaces were exposed to UV illumination, a PCE drop of nearly 5% observed in comparison to the control devices (**Table.4.3**). Subsequently, devices in which the ZnO-BHJ interface is exposed to UV-illumination during fabrication degrade (in the dark as well as light) rapidly compared to the non-exposed devices. The role of the UV-exposed BHJ device appears to affect the ZnO/BHJ interface region as compared to the bulk of the BHJ active layer.

Table.4.3. Photovoltaic parameters (V_{OC}, J_{SC}, FF and PCE) of fresh and 10 hours aged PBDB-T-2Cl:IT-4F devices without and with UV exposure to ZnO/BHJ interface during fabrication.

	V_{OC} (V)	J_{SC} (mA/cm^2)	FF (%)	PCE (%)
Device A	0.88 ± 0.001	18.01 ± 0.41	53.10 ± 0.36	8.42 ± 0.23
Device B	0.88 ± 0.001	17.47 ± 0.37	52.28 ± 1.94	8.01 ± 0.48
Device A (after 10 hours UV exposure)	0.87 ± 0.005	15.92 ± 0.37	48.58 ± 0.43	6.70 ± 0.23
Device B (after 10 hours UV exposure)	0.84 ± 0.02	15.17 ± 0.14	46.93 ± 0.38	6.00 ± 0.14

Device A represents ITO/ZnO layers exposed to UV during fabrication, and Device B represents ITO/ZnO/BHJ layer exposed to UV during fabrication.

4.4. Surface morphology characterization using AFM

Atomic Force Microscopy (AFM) imaging studies were carried out to gain insights into the modification of surface morphology of the BHJ blend film after UV exposure and thermal stress. **Figure.4.9** shows AFM-topography images (5 μm × 5 μm) of fresh-BHJ films and films exposed to UV-light and thermal stress. The estimated root-mean-square (RMS) surface roughness values of these images over a large number of samples (at least five films in each case) reveal a trend. Fresh PBDB-T-2Cl:IT-4F BHJ film deposited on ITO/ZnO surface indicates a smooth and uniform surface with RMS surface roughness (Rq) of 4.94 nm. After accelerated ageing stresses, the RMS surface roughness value increases in comparison to fresh BHJ films. UV-light exposed devices show a higher increase in RMS surface roughness (5.43 nm) in comparison with film exposed to thermal stress (5.19 nm). The higher RMS surface roughness suggests strong aggregation behaviour in the UV-light exposed and thermally degraded films, which are consistent with solar cell performance parameters and J-V characteristics.[24, 56]
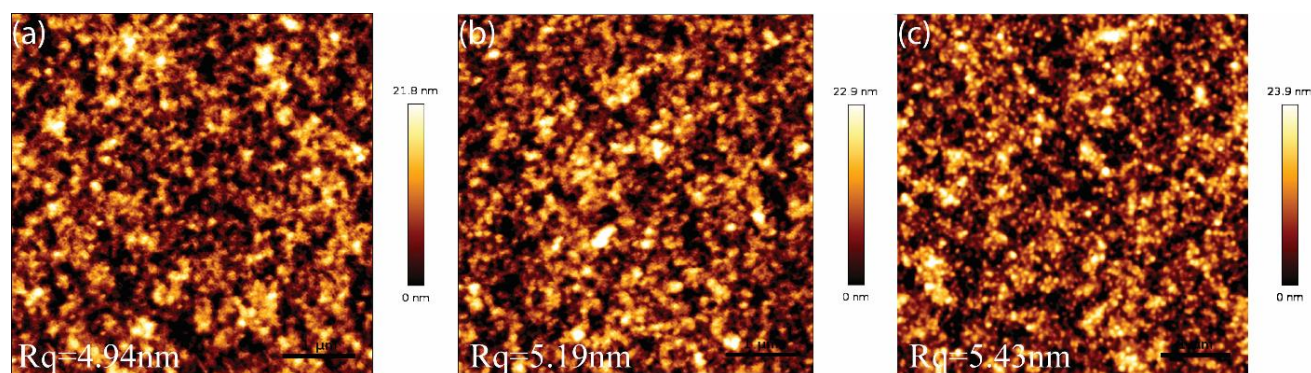
Figure.4.9. Representative AFM morphology images (5μm×5μm) of (a) fresh PBDB-T-2Cl:IT-4F BHJ film (b) PBDB-T-2Cl:IT-4F BHJ film exposed to thermal stress and (c) PBDB-T-2Cl:IT-4F BHJ film exposed to UV-light respectively (all films deposited on ITO/ZnO surface and estimated RMS surface roughness indicted).

4.5.   Impedance and Intensity-modulated photocurrent spectroscopy measurements

Photo-physical processes in the bulk and interface of the device can be followed by looking into the relaxation processes associated with the impedance spectroscopy (IS) measurement $Z(\omega)$. Charge transport and recombination processes of various time scale is reflected in the $Z(\omega)$, while IS represents the resistive and capacitive processes in the device.[57-58] A suitable equivalent circuit can model the photo-physical processes governing the device performance.[59-62] The IS measurements are performed on devices under different ageing conditions for a wide range of frequencies spanning from 10 Hz to 5 MHz under illumination. **Figure.4.10** shows the impedance spectra of fresh devices and devices with a different history of exposure. The results reveal significant elicits the role of (white light, UV light and temperature) stress, which can be depicted by a simple RC equivalent network.[59] The equivalent circuit used to analyze the results can be represented by series resistance (R_S) and two parallel R-C networks in series with it (**Figure.4.11**). If there are two distinct and separable processes, R_1 and C_1 can represent the bulk and R_2 and C_2 can represent the interfacial resistance and capacitance, respectively.[59] In the present case, the interfacial component can be assumed to represent BHJ regions in the proximity of the ZnO buffer layer. Equivalent circuit analysis results of fresh and aged devices are summarised in **Table.4.4**. After UV-induced degradation, a significant increase in the bulk and interfacial resistance (~ 3 times) was observed. While the marginal increase in bulk resistance and interfacial resistance after white light (UV-free) exposure is consistent with J-V monitoring results. Notably, in the case of UV-induced degradation in additive-free devices, the increase in bulk resistance (R_1) from ~ 9.1 to 13.6 Ohm-cm^2 is not substantial as compared to the interfacial resistance increase from ~ 3.8 to 14.8 Ohm-cm^2. This observation indicates the detrimental role of residual solvent additive in the

UV-exposed BHJ film. While the reduction in bulk and interfacial capacitance after UV exposure correlates with the observed reduction in V_{OC} and PCE.[62-65]
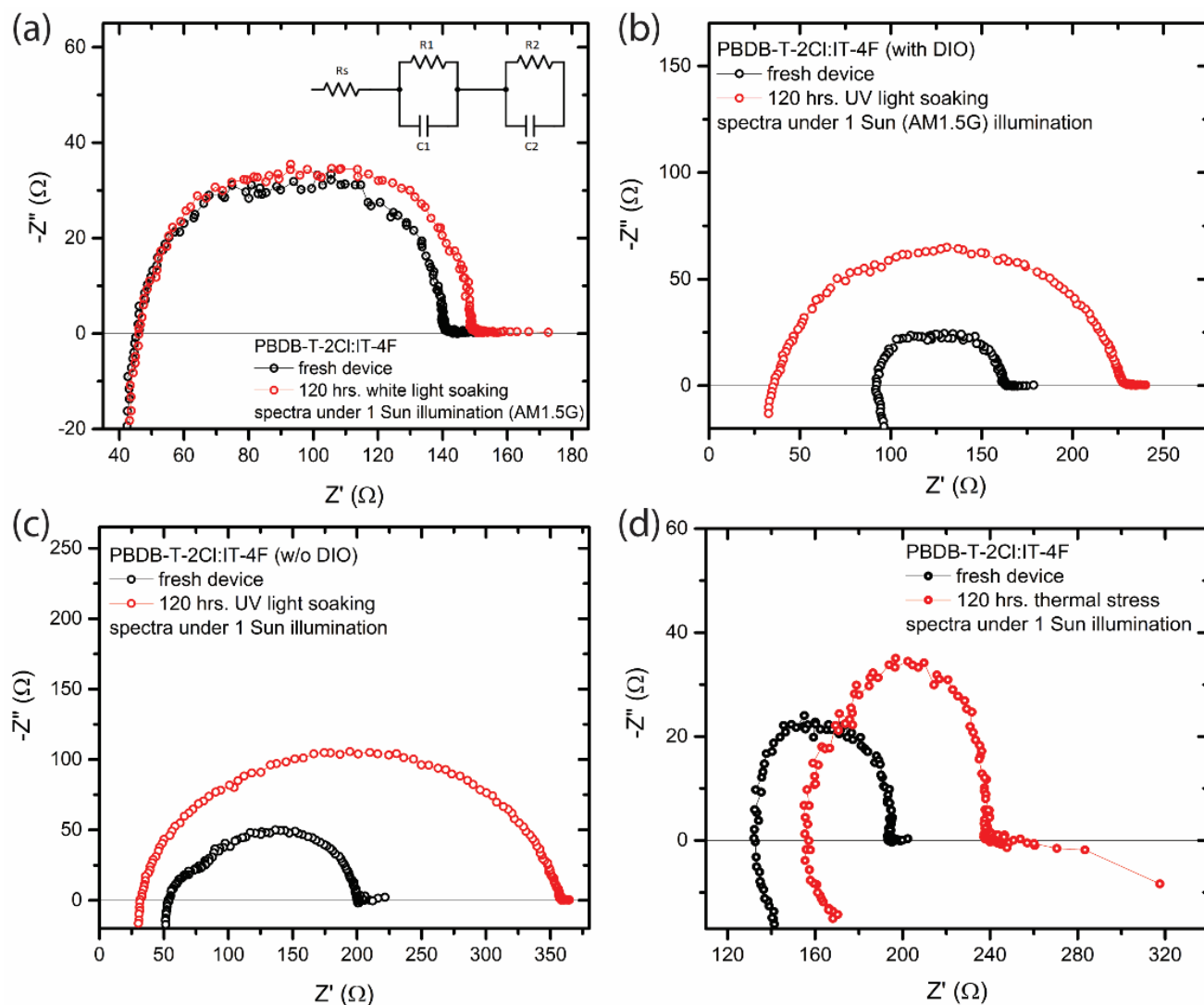
Figure.4.10. Nyquist plot of PBDB-T-2Cl:IT-4F solar cells at room temperature under the illumination condition before and after accelerated ageing stresses applied continuously for 120 hours (a) white light illumination (b) UV illumination (c) UV illumination on devices fabricated without using solvent additive DIO and (d) thermal stress of 70°C respectively in an inert condition. Inset in (a) shows the equivalent circuit used for the analysis.
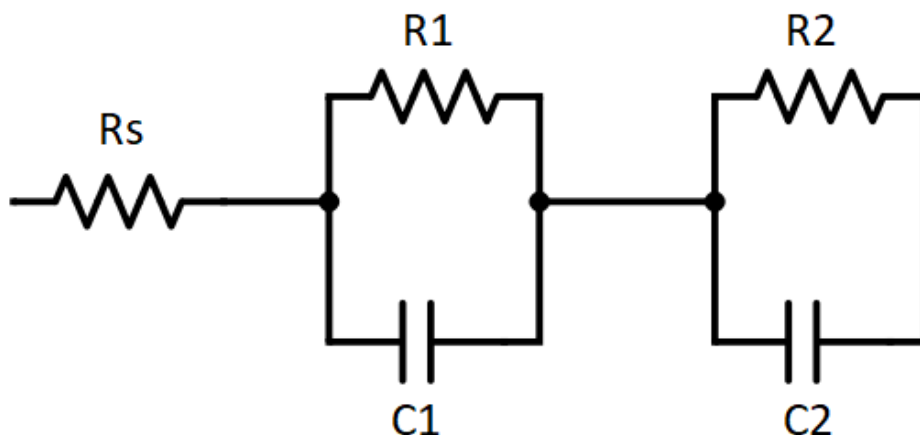
Figure.4.11. The equivalent circuit model used to analyze impedance spectroscopy results (R_S represents the series resistance contribution mostly from the contacts at ITO and anode, R_1, C_1 represent the bulk and R_2, C_2 represent the interface).

Table.4.4. Summary of parameters from equivalent circuit analysis (R_1, C_1 represents the bulk and R_2, C_2 represents the interface) of impedance spectroscopy measurement (Figure.4.10) performed on fresh and aged PBDB-T-2Cl:IT-4F devices (error bar ± arrived from the analysis represented in percentage %).

Aging stress	White light		UV-light		UV-light (w/o DIO)		Thermal	
	fresh	120 h.	fresh	120 h.	fresh	120 h.	fresh	120 h.
R_S (Ohm-cm^2)	4.25 ± 1.8%	4.32 ± 2.0%	8.52 ± 0.9%	3.68 ± 2.3%	5.15 ± 1.7%	3.57 ± 3.6%	12.23 ± 0.7%	14.46 ± 0.9%
R_1(Ohm-cm^2)	4.43 ± 2.0%	4.82 ± 2.0%	3.60 ± 2.7%	9.21 ± 1.1%	9.06 ± 1.3%	13.56 ± 1.3%	3.51 ± 3.6%	3.44 ± 6.1%
C_1 (F)	1.16E-8 ± 9.3%	9.63E-9 ± 9.6%	1.71E-8 ±12.4%	7.56E-9 ± 5.1%	8.37E-8 ± 5.6%	5.74E-8 ± 5.2%	1.95E-8 ± 13.6%	1.13E-7 ±24.8%
R_2 (Ohm-cm^2)	4.11 ± 2.4%	4.45 ± 2.5%	2.60 ± 4.2%	7.59 ± 1.5%	3.81 ± 2.8%	14.80 ± 1.0%	1.78 ± 7.8%	3.94 ± 4.9%
C_2 (F)	8.48E-8 ±10.3%	7.01E-8 ±10.7%	1.42E-7 ± 18.4%	6.92E-8 ± 6.4%	1.68E-8 ±14.5%	6.54E-9 ± 4.7%	1.74E-7 ±30.0%	3.07E-8 ± 18.2%

In the case of devices undergoing TID, the impedance analysis shows a substantial increase in interfacial resistance (R_2) of the device ~ 1.8 to 3.9 Ohm-cm^2 after thermal stress. The unchanged bulk resistance (R_1) in this duration is indicative of the integrity of the bulk morphology of the BHJ active layer.[28, 51] Further, increased bulk capacitance (C_1) can be attributed to the rearrangement of BHJ domains facilitating the transport of photogenerated carriers in bulk. At the same time, the reduced interfacial capacitance (C_2) indicates the interfacial modification, which is unfavourable for the charge transport at the interface and results in severe FF reduction.[51, 66]
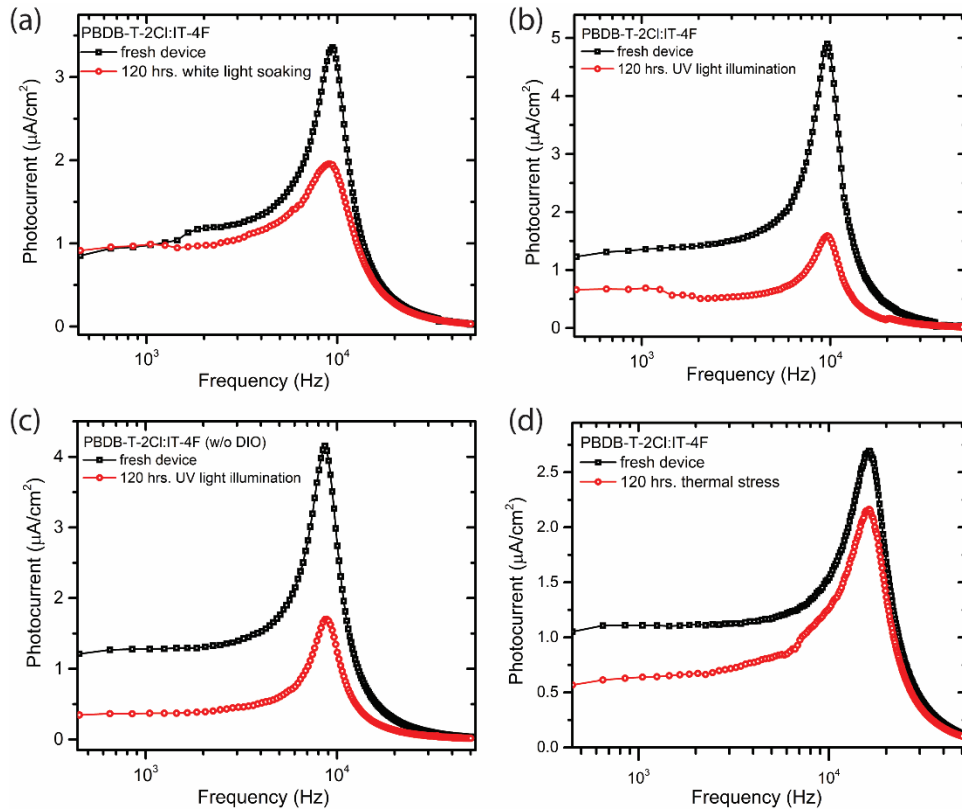
Figure.4.12. Frequency-dependent photocurrent response (IMPS) of PBDB-T-2Cl:IT-4F solar cells at room temperature before and after accelerated ageing stresses continuously for 120 hours (a) white light illumination (b) UV illumination (c) UV illumination on devices fabricated without using solvent additive DIO and (d) thermal stress of 70°C respectively in an inert condition.

To gain further insight into the charge transport and trap-assisted recombination processes in fresh and aged devices, Intensity-modulated photocurrent spectroscopy (IMPS) measurements were performed. [67-68] Contrary to the IS, in IMPS, light intensity modulation at reference frequency (500 Hz - 50 kHz) generates (ac) steady-state photocurrent.[67] **Figure.4.12** shows the photocurrent response $I_{ph}(\omega)$ of the fresh devices and devices exposed to different accelerated ageing conditions for 120 hours. The photocurrent response generally consists of three regions, a low-frequency region in which $I_{ph}(\omega)$ is nearly independent of frequency. After which, $I_{ph}(\omega)$ starts increasing with frequency and reaches a distinct maximum of I_{max} at a frequency $\omega_{max,}$ followed by a rapid decrease at a high frequency beyond the distinct maxima. It was earlier demonstrated that the mid-frequency distinct maxima are largely independent of external parameters, while the low-frequency region originates from the trap-assisted non-geminate recombination.[67] Results reveal that the distinct maxima of $I_{ph}(\omega)$ are not shifted after accelerated aging, and at very high frequencies, fresh and aged devices resemble a similar $I_{ph}(\omega)$ behaviour. In addition, an overall reduction in the magnitude of $I_{ph}(\omega)$ with aging is observed. In the case of white light exposure for 120 hours, the $I_{ph}(\omega)$ response (**Figure.4.12a**) is almost unchanged in the low-frequency region, while a moderate reduction in the magnitude of $I_{ph}(\omega)$ at mid-frequencies is observed. This trend is consistent with the J-V and IS studies. Photocurrent responses with UV-induced degradation (**Figure.4.12b**) show a clear reduction of $I_{ph}(\omega)$ in the low-frequency region. The difference in magnitude of $I_{ph}(\omega)$ at maxima is comparatively higher for devices fabricated with solvent additive (**Figure.4.12c**). Photocurrent responses of devices exposed to thermal stress show comparatively less reduction in the magnitude of $I_{ph}(\omega)$ at maxima (**Figure.4.12d**). These series of studies on UV and thermal exposure of this BHJ system clearly points to characteristic modifications. The

spectroscopic and device characterization results indicate that the degradation mechanisms under UV light can be interpreted in terms of two spatial zones within the device.

4.6.   Summary

In summary, isolated effects of light and temperature induced degradation in non-fullerene acceptor IT-4F based organic solar cells during the burn-in period are systematically studied. For light-induced degradation studies, the devices were exposed to simulated AM1.5G solar illumination to replicate the real-time working condition. The insights gained during this analysis were utilised to study the device degradation in custom-made spectrally resolved stability test conditions (UV and non-UV illumination). Results reveal that the UV-induced instabilities affect the performance parameters more severely than non-UV light and thermal stresses. These trends in PCE were observed even in the absence of residual solvent additive DIO in the BHJ. The results suggest modifications of the acceptor molecule near the interlayer. The decrease in PCE for DIO-treated samples exhibited a larger share of V_{OC} drop, while for the DIO-free devices, the reduction in FF was dominant. Furthermore, photostability under continuous white light (non-UV) illumination reiterates the advantage of indoor applicability of organic devices, and a well-suited encapsulant can significantly improve thermal stability. Impedance spectroscopy and IMPS measurements corroborate and quantify these findings in terms of circuit parameters. The results point out the importance of developing strategies for blocking UV components or converting them into higher wavelength (luminescent downshifting) can be extremely beneficial in the long-term stability of the organic solar cells.

References

1.   Karki, A.; Gillett, A. J.; Friend, R. H.; Nguyen, T. Q., The Path to 20% Power Conversion Efficiencies in Nonfullerene Acceptor Organic Solar Cells. *Advanced Energy Materials* **2020**, 2003441.

2.   Wadsworth, A.; Moser, M.; Marks, A.; Little, M. S.; Gasparini, N.; Brabec, C. J.; Baran, D.; McCulloch, I., Critical Review of the Molecular Design Progress in Non-Fullerene Electron Acceptors Towards Commercially Viable Organic Solar Cells. *Chemical Society Reviews* **2019**, *48*, 1596-1625.

3.   Shi, Q.; Wu, J.; Wu, X.; Peng, A.; Huang, H., Perylene Diimide-Based Conjugated Polymers for All-Polymer Solar Cells. *Chemistry–A European Journal* **2020**, *26*, 12510-12522.

4.   Liu, Q., et al., 18% Efficiency Organic Solar Cells. *Science Bulletin* **2020**, *65*, 272-275.

5.   Lin, Y.; Nugraha, M. I.; Firdaus, Y.; Scaccabarozzi, A. D.; Aniés, F.; Emwas, A.-H.; Yengel, E.; Zheng, X.; Liu, J.; Wahyudi, W., A Simple N-Dopant Derived from Diquat Boosts the Efficiency of Organic Solar Cells to 18.3%. *ACS Energy Letters* **2020**, *5*, 3663-3671.

6.   Lin, Y.; Adilbekova, B.; Firdaus, Y.; Yengel, E.; Faber, H.; Sajjad, M.; Zheng, X.; Yarali, E.; Seitkhan, A.; Bakr, O. M., 17% Efficient Organic Solar Cells Based on Liquid Exfoliated Ws2 as a Replacement for Pedot: Pss. *Advanced materials* **2019**, *31*, 1902965.

7.   Firdaus, Y.; Le Corre, V. M.; Khan, J. I.; Kan, Z.; Laquai, F.; Beaujuge, P. M.; Anthopoulos, T. D., Key Parameters Requirements for Non-Fullerene-Based Organic Solar Cells with Power Conversion Efficiency> 20%. *Advanced Science* **2019**, *6*, 1802028.

8.   Chen, L. X., Organic Solar Cells: Recent Progress and Challenges. ACS Publications: 2019.

9.   Zhao, W.; Li, S.; Yao, H.; Zhang, S.; Zhang, Y.; Yang, B.; Hou, J., Molecular Optimization Enables over 13% Efficiency in Organic Solar Cells. *Journal of the American Chemical Society* **2017**, *139*, 7148-7151.

10.   Vijayan, R.; Azeez, A.; Narayan, K., Toward Reliable High Performing Organic Solar Cells: Molecules, Processing, and Monitoring. *APL Materials* **2020**, *8*, 040908.

11.   Vijayan, R.; Azeez, A.; Narayan, K. S., Enhanced Stability and Optimized Morphology Induced by Electric-Field-Assisted Annealing of Bulk Heterojunction Solar Cells. *Solar RRL* **2019**, *3*, 1900120.

12.   Kam, Z.; Wang, X.; Zhang, J.; Wu, J., Elimination of Burn-in Open-Circuit Voltage Degradation by Zno Surface Modification in Organic Solar Cells. *ACS applied materials & interfaces* **2015**, *7*, 1608-1615.

13.   Li, Y.; Li, T.; Lin, Y., Stability: Next Focus in Organic Solar Cells Based on Non-Fullerene Acceptors. *Materials Chemistry Frontiers* **2021**.

14.   Riede, M.; Spoltore, D.; Leo, K., Organic Solar Cells—the Path to Commercial Success. *Advanced Energy Materials* **2021**, *11*, 2002653 1614-6832.

15.   Li, Y.; Li, T.; Lin, Y., Stability: Next Focus in Organic Solar Cells Based on Non-Fullerene Acceptors. *Materials Chemistry Frontiers* **2021**, *5*, 2907-2930.

16.   Wang, Y.; Lee, J.; Hou, X.; Labanti, C.; Yan, J.; Mazzolini, E.; Parhar, A.; Nelson, J.; Kim, J.-S.; Li, Z., Recent Progress and Challenges toward Highly Stable Nonfullerene Acceptor-Based Organic Solar Cells. *Advanced Energy Materials* **2021**, *11*, 2003002.

17.   Li, W.; Liu, D.; Wang, T., Stability of Non-Fullerene Electron Acceptors and Their Photovoltaic Devices. *Advanced Functional Materials* **2021**, *31*, 2104552 1616-301X.

18.   Du, X.; Heumueller, T.; Gruber, W.; Classen, A.; Unruh, T.; Li, N.; Brabec, C. J.,
Efficient Polymer Solar Cells Based on Non-Fullerene Acceptors with Potential Device Lifetime
Approaching 10 Years. *Joule* **2019**, *3*, 215-226.

19.   Uddin, A.; Upama, M. B.; Yi, H.; Duan, L., Encapsulation of Organic and Perovskite
Solar Cells: A Review. *Coatings* **2019**, *9*, 65.

20.   Juillard, S.; Planes, E.; Matheron, M.; Perrin, L.; Berson, S.; Flandin, L., Mechanical
Reliability of Flexible Encapsulated Organic Solar Cells: Characterization and Improvement.
ACS applied materials & interfaces **2018**, *10*, 29805-29813.

21.   Mateker, W. R.; McGehee, M. D., Progress in Understanding Degradation Mechanisms
and Improving Stability in Organic Photovoltaics. *Advanced materials* **2017**, *29*, 1603940.

22.   Li, N.; Perea, J. D.; Kassar, T.; Richter, M.; Heumueller, T.; Matt, G. J.; Hou, Y.; Güldal,
N. S.; Chen, H.; Chen, S., Abnormal Strong Burn-in Degradation of Highly Efficient Polymer
Solar Cells Caused by Spinodal Donor-Acceptor Demixing. *Nature communications* **2017**, *8*, 1-
9.

23.   Upama, M. B.; Wright, M.; Mahmud, M. A.; Elumalai, N. K.; Soufiani, A. M.; Wang, D.;
Xu, C.; Uddin, A., Photo-Degradation of High Efficiency Fullerene-Free Polymer Solar Cells.
Nanoscale **2017**, *9*, 18788-18797.

24.   Duan, L.; Guli, M.; Zhang, Y.; Yi, H.; Haque, F.; Uddin, A., The Air Effect in the Burn-
in Thermal Degradation of Nonfullerene Organic Solar Cells. *Energy Technology* **2020**, *8*,
1901401.

25.   Heumueller, T.; Mateker, W. R.; Sachs-Quintana, I. T.; Vandewal, K.; Bartelt, J. A.;
Burke, T. M.; Ameri, T.; Brabec, C. J.; McGehee, M. D., Reducing Burn-in Voltage Loss in

Polymer Solar Cells by Increasing the Polymer Crystallinity. *Energy & Environmental Science* **2014**, *7*, 2974-2980.

26.   Norrman, K.; Krebs, F. C., Lifetimes of Organic Photovoltaics: Using Tof-Sims and 18o2 Isotopic Labelling to Characterise Chemical Degradation Mechanisms. *Solar energy materials and solar cells* **2006**, *90*, 213-227.

27.   Speller, E. M.; Clarke, A. J.; Aristidou, N.; Wyatt, M. F.; Francàs, L.; Fish, G.; Cha, H.; Lee, H. K. H.; Luke, J.; Wadsworth, A., Toward Improved Environmental Stability of Polymer: Fullerene and Polymer: Nonfullerene Organic Solar Cells: A Common Energetic Origin of Light-and Oxygen-Induced Degradation. *ACS energy letters* **2019**, *4*, 846-852.

28.   Speller, E. M.; Clarke, A. J.; Luke, J.; Lee, H. K. H.; Durrant, J. R.; Li, N.; Wang, T.; Wong, H. C.; Kim, J.-S.; Tsoi, W. C., From Fullerene Acceptors to Non-Fullerene Acceptors: Prospects and Challenges in the Stability of Organic Solar Cells. *Journal of Materials Chemistry A* **2019**, *7*, 23361-23377.

29.   Matteocci, F.; Cinà, L.; Lamanna, E.; Cacovich, S.; Divitini, G.; Midgley, P. A.; Ducati, C.; Di Carlo, A., Encapsulation for Long-Term Stability Enhancement of Perovskite Solar Cells. *Nano Energy* **2016**, *30*, 162-172.

30.   Corsini, F.; Griffini, G., Recent Progress in Encapsulation Strategies to Enhance the Stability of Organometal Halide Perovskite Solar Cells. *Journal of Physics: Energy* **2020**, *2*, 031002.

31.   Sherafatipour, G.; Benduhn, J.; Patil, B. R.; Ahmadpour, M.; Spoltore, D.; Rubahn, H.-G.; Vandewal, K.; Madsen, M., Degradation Pathways in Standard and Inverted Dbp-C 70 Based Organic Solar Cells. *Scientific reports* **2019**, *9*, 1-11.

32.	Wang, K.; Liu, C.; Meng, T.; Yi, C.; Gong, X., Inverted Organic Photovoltaic Cells. *Chemical Society Reviews* **2016**, *45*, 2937-2975.

33.	Zhang, S.; Qin, Y.; Zhu, J.; Hou, J., Over 14% Efficiency in Polymer Solar Cells Enabled by a Chlorinated Polymer Donor. *Advanced Materials* **2018**, *30*, 1800868.

34.	Wienhold, K. S.; Körstgens, V.; Grott, S.; Jiang, X.; Schwartzkopf, M.; Roth, S. V.; Müller-Buschbaum, P., Effect of Solvent Additives on the Morphology and Device Performance of Printed Nonfullerene Acceptor Based Organic Solar Cells. *ACS applied materials & interfaces* **2019**, *11*, 42313-42321.

35.	Classen, A.; Heumueller, T.; Wabra, I.; Gerner, J.; He, Y.; Einsiedler, L.; Li, N.; Matt, G. J.; Osvet, A.; Du, X., Revealing Hidden Uv Instabilities in Organic Solar Cells by Correlating Device and Material Stability. *Advanced Energy Materials* **2019**, *9*, 1902124.

36.	Doumon, N. Y.; Wang, G.; Qiu, X.; Minnaard, A. J.; Chiechi, R. C.; Koster, L. J. A., 1, 8-Diiodooctane Acts as a Photo-Acid in Organic Solar Cells. *Scientific reports* **2019**, *9*, 1-14.

37.	Tournebize, A.; Mattana, G.; Gorisse, T. r. s.; Bousquet, A.; Wantz, G.; Hirsch, L.; Chambon, S., Crucial Role of the Electron Transport Layer and Uv Light on the Open-Circuit Voltage Loss in Inverted Organic Solar Cells. *ACS applied materials & interfaces* **2017**, *9*, 34131-34138.

38.	Azzouzi, M.; Yan, J.; Kirchartz, T.; Liu, K.; Wang, J.; Wu, H.; Nelson, J., Nonradiative Energy Losses in Bulk-Heterojunction Organic Photovoltaics. *Physical Review X* **2018**, *8*, 031055.

39.	Azzouzi, M.; Kirchartz, T.; Nelson, J., Factors Controlling Open-Circuit Voltage Losses in Organic Solar Cells. *Trends in Chemistry* **2019**, *1*, 49-62 2589-5974.

40.   Furukawa, S.; Komiyama, H.; Yasuda, T., Controlling Open-Circuit Voltage in Organic

Solar Cells by Terminal Fluoro-Functionalization of Narrow-Bandgap Π-Conjugated Molecules.

The Journal of Physical Chemistry C **2016**, *120*, 21235-21241 1932-7447.

41.   Department of Chemistry, I. S. U., An Introduction to Laboratory

Practices in Organic Chemistry. **2015**.

42.   Tremolet de Villers, B. J.; O'Hara, K. A.; Ostrowski, D. P.; Biddle, P. H.; Shaheen, S. E.;

Chabinyc, M. L.; Olson, D. C.; Kopidakis, N., Removal of Residual Diiodooctane Improves

Photostability of High-Performance Organic Solar Cell Polymers. *Chemistry of Materials* **2016**,

28, 876-884 0897-4756.

43.   Hu, L.; Liu, Y.; Mao, L.; Xiong, S.; Sun, L.; Zhao, N.; Qin, F.; Jiang, Y.; Zhou, Y.,

Chemical Reaction between an Itic Electron Acceptor and an Amine-Containing Interfacial

Layer in Non-Fullerene Solar Cells. *Journal of Materials Chemistry A* **2018**, *6*, 2273-2278.

44.   Lee, H. K. H.; Durrant, J. R.; Li, Z.; Tsoi, W. C., Stability Study of Thermal Cycling on

Organic Solar Cells. *Journal of Materials Research* **2018**, *33*, 1902-1908 0884-2914.

45.   Jeong, J.; Seo, J.; Nam, S.; Han, H.; Kim, H.; Anthopoulos, T. D.; Bradley, D. D.; Kim,

Y., Significant Stability Enhancement in High-Efficiency Polymer: Fullerene Bulk

Heterojunction Solar Cells by Blocking Ultraviolet Photons from Solar Light. *Advanced Science*

2016, *3*, 1500269.

46.   Fungura, F.; Lindemann, W. R.; Shinar, J.; Shinar, R., Carbon Dangling Bonds in

Photodegraded Polymer: Fullerene Solar Cells. *Advanced Energy Materials* **2017**, *7*, 1601420.

47.   Park, S.; Son, H. J., Intrinsic Photo-Degradation and Mechanism of Polymer Solar Cells:

The Crucial Role of Non-Fullerene Acceptors. *Journal of Materials Chemistry A* **2019**, *7*, 25830-

25837.

48.   Cheng, P.; Li, G.; Zhan, X.; Yang, Y., Next-Generation Organic Photovoltaics Based on Non-Fullerene Acceptors. *Nature Photonics* **2018**, *12*, 131-142.

49.   Alagiriswamy, A.; Narayan, K., Electronic Defect Studies of Ladder-Type Polymers. *Journal of applied physics* **2002**, *91*, 3021-3027.

50.   Yu, L.; Qian, D.; Marina, S.; Nugroho, F. A.; Sharma, A.; Hultmark, S.; Hofmann, A. I.; Kroon, R.; Benduhn, J.; Smilgies, D.-M., Diffusion-Limited Crystallization: A Rationale for the Thermal Stability of Non-Fullerene Solar Cells. *ACS applied materials & interfaces* **2019**, *11*, 21766-21774.

51.   Chen, B.; Qiao, X.; Liu, C.-M.; Zhao, C.; Chen, H.-C.; Wei, K.-H.; Hu, B., Effects of Bulk and Interfacial Charge Accumulation on Fill Factor in Organic Solar Cells. *Applied Physics Letters* **2013**, *102*, 86_1.

52.   Patel, J. B.; Tiwana, P.; Seidler, N.; Morse, G. E.; Lozman, O. R.; Johnston, M. B.; Herz, L. M., Effect of Ultraviolet Radiation on Organic Photovoltaic Materials and Devices. *ACS applied materials & interfaces* **2019**, *11*, 21543-21551.

53.   Zhang, W.; Lan, W.; Lee, M. H.; Singh, J.; Zhu, F., A Versatile Solution-Processed Moo3/Au Nanoparticles/Moo3 Hole Contact for High Performing Pedot: Pss-Free Organic Solar Cells. *Organic Electronics* **2018**, *52*, 1-6.

54.   Azeez, A.; Narayan, K., Enhanced Device Performance Via Interfacial Engineering in Non-Fullerene Acceptor Based Organic Solar Cells. *Applied Physics Letters* **2020**, *117*, 043302.

55.   Liu, B., et al., Boosting Efficiency and Stability of Organic Solar Cells Using Ultralow-Cost Biocl Nanoplates as Hole Transporting Layers. *ACS Applied Materials & Interfaces* **2019**, *11*, 33505-33514.

56.   Li, S.; Ye, L.; Zhao, W.; Yan, H.; Yang, B.; Liu, D.; Li, W.; Ade, H.; Hou, J., A Wide Band Gap Polymer with a Deep Highest Occupied Molecular Orbital Level Enables 14.2% Efficiency in Polymer Solar Cells. *Journal of the American Chemical Society* **2018**, *140*, 7159-7167.

57.   Bisquert, J., Theory of the Impedance of Electron Diffusion and Recombination in a Thin Layer. *The Journal of Physical Chemistry B* **2002**, *106*, 325-333.

58.   Von Hauff, E., Impedance Spectroscopy for Emerging Photovoltaics. *The Journal of Physical Chemistry C* **2019**, *123*, 11329-11346.

59.   Zhou, H.; Zhang, Y.; Seifter, J.; Collins, S. D.; Luo, C.; Bazan, G. C.; Nguyen, T. Q.; Heeger, A. J., High-Efficiency Polymer Solar Cells Enhanced by Solvent Treatment. *Advanced materials* **2013**, *25*, 1646-1652.

60.   Fabregat-Santiago, F.; Garcia-Belmonte, G.; Mora-Sero, I.; Bisquert, J., Characterization of Nanostructured Hybrid and Organic Solar Cells by Impedance Spectroscopy. *Physical chemistry chemical physics* **2011**, *13*, 9083-9118.

61.   Aprilia, A.; Wulandari, P.; Suendo, V.; Hidayat, R.; Fujii, A.; Ozaki, M., Influences of Dopant Concentration in Sol–Gel Derived Azo Layer on the Performance of P3ht: Pcbm Based Inverted Solar Cell. *Solar energy materials and solar cells* **2013**, *111*, 181-188.

62.   Gehan, T. S.; Ellis, C. L.; Venkataraman, D.; Bag, M., Origin of Low Open-Circuit Voltage in Surfactant-Stabilized Organic-Nanoparticle-Based Solar Cells. *ACS applied materials & interfaces* **2020**, *12*, 8183-8188.

63.   Chauhan, A.; Gusain, A.; Jha, P.; Veerender, P.; Koiry, S.; Sridevi, C.; Aswal, D.; Gupta, S.; Taguchi, D.; Manaka, T., Interfacial Charge Trapping in the Polymer Solar Cells and Its Elimination by Solvent Annealing. *AIP Advances* **2016**, *6*, 095012.

64.   Park, H. S.; Han, Y. W.; Lee, H. S.; Jeon, S. J.; Moon, D. K., 13.2% Efficiency of Organic Solar Cells by Controlling Interfacial Resistance Resulting from Well-Distributed Vertical Phase Separation. *ACS Applied Energy Materials* **2020**, *3*, 3745-3754.

65.   Shivanna, R.; Rajaram, S.; Narayan, K., Role of Charge-Transfer State in Perylene-Based Organic Solar Cells. *ChemistrySelect* **2018**, *3*, 9204-9210.

66.   Gupta, D.; Bag, M.; Narayan, K., Correlating Reduced Fill Factor in Polymer Solar Cells to Contact Effects. *Applied Physics Letters* **2008**, *92*, 70.

67.   Bag, M.; Narayan, K., Universality in the Intensity-Modulated Photocurrent in Bulk-Heterojunction Polymer Solar Cells. *Physical Review B* **2010**, *82*, 075308.

68.   Grimm, R. T.; Deb, P.; Walwark Jr, D. J.; Viets, C.; Grey, J. K., Implications of Trap-Assisted Nongeminate Charge Recombination on Time-and Frequency-Domain Photocurrent Degradation Signatures of Organic Solar Cells. *The Journal of Physical Chemistry C* **2020**, *124*, 16838-16848.

Chapter 5

Insights into the Role of PC₇₀BM as the Third Component in Y6 Acceptor Based Ternary Blend Organic Solar Cells

Insights into the Role of PC$_{70}$BM as the Third Component in Y6 Acceptor Based Ternary Blend Organic Solar Cells

The possibility of introducing a third component in a binary mixture-based photoactive film offers a significant control in obtaining high performing OSCs. Ternary blend organic solar cells (TBOSCs) have received enormous attention as a facile strategy.[1-4] A TBOSC consists of three photoactive materials in the BHJ (either two donors and an acceptor or two acceptors and one donor), with the obvious added feature of increasing the operating spectral range.[5] As introduced in chapter 1 (Section 1.5), the role of the third component in the BHJ layer has more implications than merely improving the absorption window.[6-7] For instance, it has been demonstrated that the third component can effectively optimize the binary BHJ active layer morphology and enhance the charge transport, leading to superior device performance.[8-10] With the advent of novel NFAs the ternary blend strategy has become a critical technique for obtaining record efficiencies (~19%) in OSCs.[11-12] The simultaneous advantage of increased photon harvesting and reduced fabrication complexity compared to multi-junction devices makes TBOSCs an important strategy that needs to be further explored.

The availability of a large number of D-A combinations, along with the rapid increase in the synthesis of new D-A molecules, necessitates a general understanding of the role of the third component.[13] The correlation of the device performance parameters (V_{OC}, J_{SC} and FF) with the optoelectronic properties of constituent materials and their stoichiometry in the blend still needs to be understood. The device physics of TBOSCs is largely dependent on the choice of a third component, and in most cases, multiple energy and charge transport mechanisms can

159

be present.[2] The important models based on the role of third components in photon harvesting and charge transport are (1) energy transfer, (2) charge transfer, (3) parallel-model and (4) alloy model.[2, 14-16] These models were briefly presented in chapter 1, and in most of the cases, multiple processes coexist in a typical TBOSC system.[2] The impact of the third component on device stability is also critical since a trade-off between efficiency and stability is necessary for the development of OSCs as a mature and commercially viable technology.[17-20] In this chapter, the role of fullerene derivative acceptor $PC_{70}BM$ as the third component in the PM7:Y6 BHJ blend is studied. The PM7 donor blended with the NFA Y6 forms the control device ($D:A_1$=1:1.2) and an optimized ternary system with $PC_{70}BM$ as a third additive component ($D:A_1:A_2$=1:1.2:0.2) subjected to the study. The charge transport dynamics and stability aspects with emphasis on 'burn-in' degradation under accelerated aging stresses are examined.

5.1. Device fabrication of ternary blend organic solar cells

The PM7 donor blended with the Y6 acceptor constitutes the active layer of control devices, and the fullerene derivative $PC_{70}BM$ constitutes the third component in the ternary devices. The molecular structure and orbital energy levels, along with the thin film absorption spectra, are shown in **Figure.5.1**. The rationale behind selecting the acceptor molecule $PC_{70}BM$ as the third component is its complementary absorption and comparatively large band gap ($E_g \sim 2.0$ eV). In this study, binary and ternary devices are fabricated with the inverted device architecture ITO/ZnO/BHJ Active layer/MoO_3/Ag, as shown in **Figure.5.1b**. PM7, Y6 and $PC_{70}BM$ were purchased from Luminescence Technology Corp. (Taiwan). All chemicals were used as received. Zinc oxide (ZnO) sol-gel precursor was spin-coated on precleaned and patterned indium tin oxide (ITO) substrates to obtain 40 nm ZnO film. ZnO sol-gel precursor was prepared by dissolving 100 mg Zinc acetate dihydrate [$Zn(CH_3COO)2.2H_2O$] in 1 ml of

2- methoxy ethanol and 28 µl ethanolamine as a stabilizer. Zinc acetate dihydrate, 2-methoxy ethanol and ethanolamine all were procured from Sigma Aldrich.
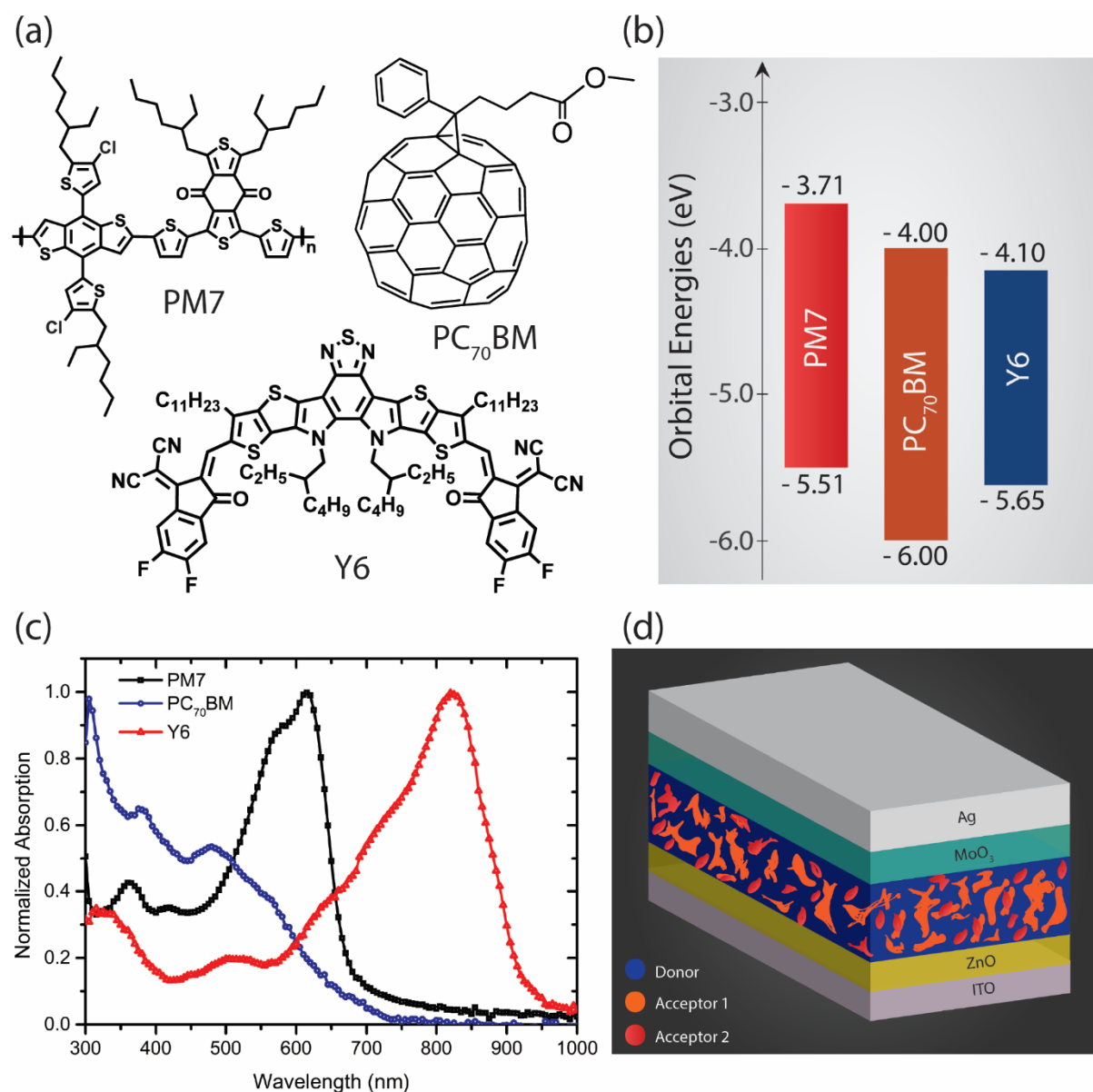
Figure.5.1. (a) The chemical structure, (b) Orbital energy levels of the donor (PM7) and acceptor (Y6 and PC$_{70}$BM) molecules, (c) Normalized absorption spectra of pristine films of donor PM7, acceptors Y6 and PC$_{70}$BM and (d) device architecture of ternary blend organic solar cells used for the study.

161

ZnO layer was thermally annealed in air at 200 °C for half an hour. For the PM7:Y6 binary device, BHJ solutions of 1:1.2 ratio of donor and acceptor with polymer concentration at 16 mg/ml in chloroform solvent were used to cast the film. For PM7:Y6:$PC_{70}BM$, BHJ solutions of 1:1.2:0.2 ratio of donor and acceptors with polymer concentration at 16 mg/ml in chloroform solvent were used. BHJ solutions were kept for stirring overnight at 40 °C. The active layer was then spin-coated at 2000 rpm for 60 s on the ZnO-coated ITO substrates inside a nitrogen-rich glovebox. Then the active layer was thermally annealed at 100 °C for 5 minutes inside the glovebox. The devices (electrode area ≈ 9 mm2) were completed by thermal evaporation of an 8 nm layer of molybdenum oxide and a 100 nm layer of silver at a base pressure of 10^{-6} mbar.

PM7:Y6 binary devices with an optimized D-A_1 ratio of 1:1.2 exhibited efficiency of around 12.85% with open-circuit voltage 0.830 V and J_{SC} exceeding 25 mA/cm^2. The addition of $PC_{70}BM$ acceptor in small proportion to the PM7:Y6 BHJ system resulted in pronounced improvement in V_{OC} ~0.854 V and enhanced PCE (~13.13%). It must be noted that the improved device performance is obtained with an optimized donor-acceptor ratio D-A_1-A_2=1:1.2:0.2 for the ternary blend.

5.2. Current-voltage characteristics and charge transport studies

The current-voltage characteristic (J(V)) of a typical PM7:Y6 binary and PM7:Y6:$PC_{70}BM$ ternary devices are shown in **Figure.5.2c**. The presence of the third component, $PC_{70}BM$, in the BHJ resulted in an average enhancement of PCE from 12.85% to 13.13%. This efficiency enhancement is accompanied by an increase in the V_{OC} by ~ 3% (0.830 V to 0.854 V) along with an improvement in device J_{SC}.
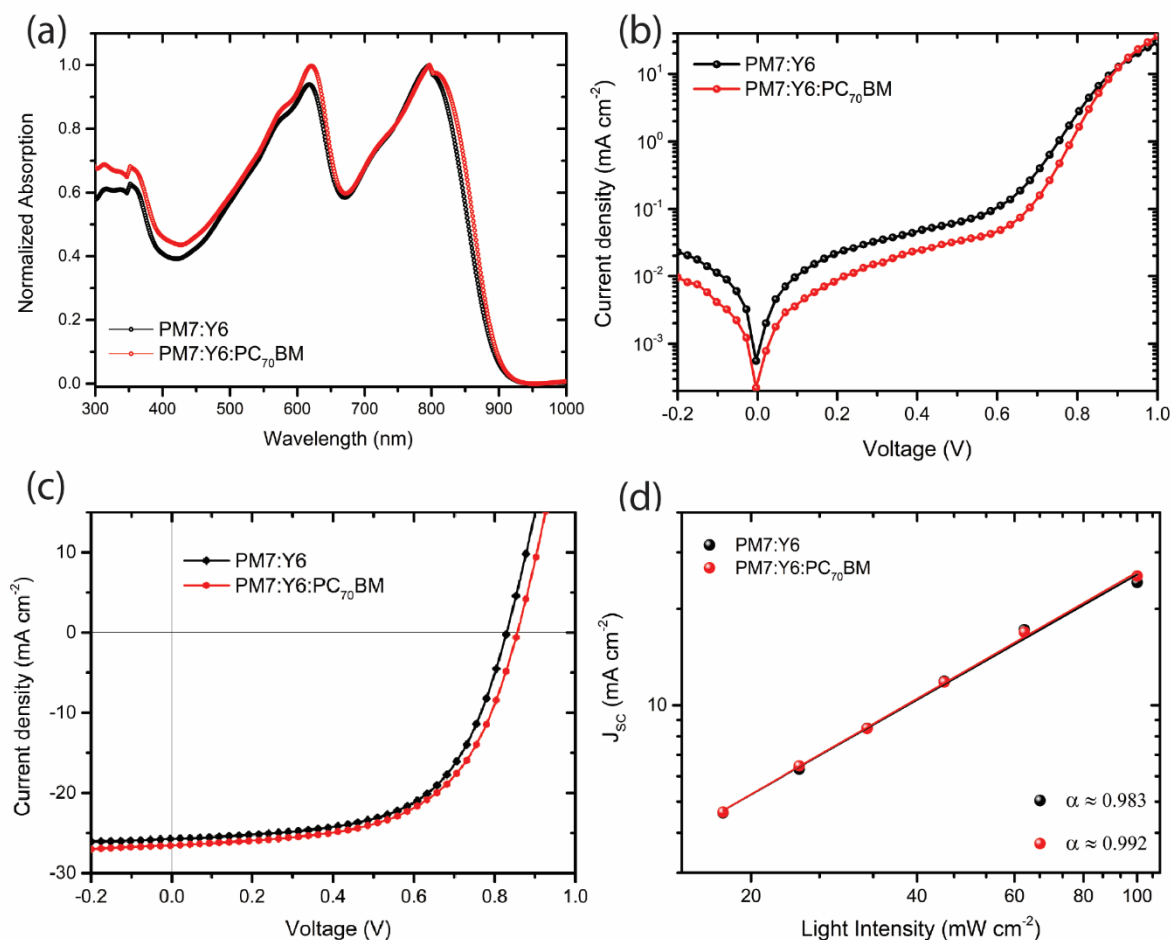
Figure.5.2. (a) Normalized absorption spectra of PM7:Y6 and PM7:Y6:PC$_{70}$BM BHJ thin films, (b) typical dark J-V characteristics, (c) typical J-V characteristics under simulated AM1.5G (100 mW cm^{-2}) illumination and (d) Intensity dependent short-circuit current density of PM7:Y6 and PM7:Y6:PC$_{70}$BM bulk heterojunction organic solar cells respectively.

Table.5.1. summarizes the performance parameters of PM7:Y6 binary and PM7:Y6:PC$_{70}$BM ternary OSCs. The presence of comparatively large band gap acceptor molecule PC$_{70}$BM (HOMO $\approx$ -6.0 eV, LUMO $\approx$ -4.0 eV) with the LUMO level lying between that of donor PM7 and acceptor Y6 (**Figure.5.1b**) improved the V$_{OC}$ of the ternary blend devices.[21] The rationale behind the choice of third component PC$_{70}$BM molecules such as complementary absorption (**Figure.5.1c**), better electron mobility, and parallel energetically favourable carrier transport pathways with the donor PM7 primarily led to the efficiency enhancement of ternary devices.

Table.5.1. Solar cell parameters of PM7:Y6 and PM7:Y6:PC$_{70}$BM bulk heterojunction organic solar cells under simulated AM1.5G (100 mW cm^{-2}) illumination (quantities represent the average of results obtained from six devices).

	V_{OC} (V)	J_{SC} (mA/cm^2)	FF (%)	PCE (%)
PM7:Y6	0.830 ± 0.005	25.73 ± 0.17	60.13 ± 1.09	12.85 ± 0.24
PM7:Y6:PC$_{70}$BM	0.854 ± 0.002	26.18 ± 0.24	58.71 ± 0.90	13.13 ± 0.16

The absorption spectra of PM7:Y6 and PM7:Y6: PC$_{70}$BM BHJ thin films shown in **Figure.5.2a** indicate marginally improved absorption for ternary BHJ film for wavelength below 600 nm. Typical dark J-V characteristics of the binary and ternary device are shown in **Figure.5.2b** indicate a reduced leakage current for TBOSCs. Further, an improved rectification ratio of TBOSCs indicates comparatively more balanced charge transport and better charge collection in the device. The light intensity-dependent J(V) characteristics further highlight the beneficial role of the third component in the active layer. J_{SC} as a function of the light intensity for binary and ternary devices is shown in **Figure.5.2d.** The light intensity dependence of J_{SC} has the form $J_{SC}=CI^{\alpha}$ ($\alpha \leq 1$), where C is a constant. For an ideal solar cell, α must be unity, and the deviation is an indicator of dominant bimolecular recombination. Both binary and ternary blend devices showing α value close to unity indicate improved charge transport properties in these systems. The value of α is marginally lower in the binary device ($\sim$ 0.98) as compared to the ternary device ($\sim$ 0.99), indicating reduced bimolecular recombination in TBOSCs.[22-25]

In order to get a comprehensive picture, PM7:PC$_{70}$BM binary BHJ OSCs were also fabricated, and a typical J-V characteristic is shown in **Figure.5.3.** PM7:PC$_{70}$BM devices exhibit a high $V_{OC} \approx$ of 0.96 V and a similar FF ($\approx$ 59%), but a significantly reduced $J_{SC} \approx$ 14.5 mA cm^{-2} lead to a PCE $\approx$ 8.3%. The comparatively low PCE of PM7:PC$_{70}$BM OSCs is expected due to reduced photon harvesting in the NIR region resulting in low J_{SC}. The effective band gap (energy difference between HOMO of the donor and LUMO of the acceptor) of the

PM7:PC$_{70}$BM blend is ~ 1.51 eV as compared to 1.41 eV for the PM7:Y6 blend, indicating a comparatively high V$_{OC}$ can be expected in the system. But it must be noted that predicting the V$_{OC}$ based on the effective band gap may not be accurate in all cases. When a third component is introduced in the BHJ, this appears to be more complex and depends on the stoichiometry of the third component and morphology optimization, along with other factors.[26-30]
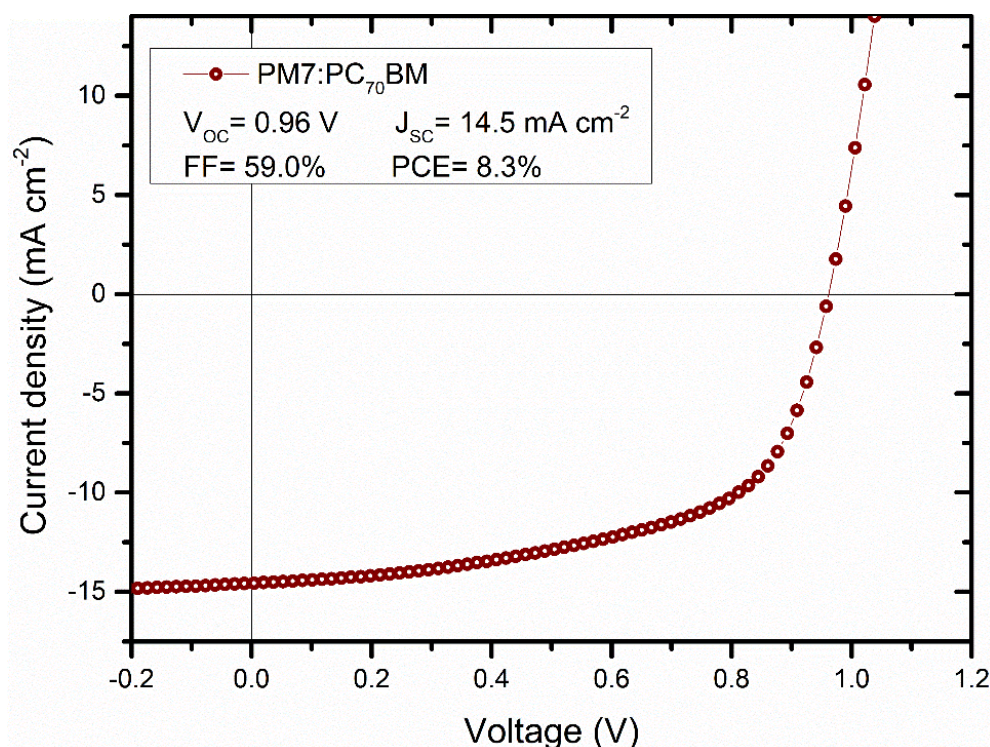
Figure.5.3. Typical J-V characteristics of the PM7:PC$_{70}$BM solar cells under simulated AM1.5G (100 mW/cm^2) illumination. The device exhibits a high V$_{OC}$ ~ 0.96 V as compared to PM7:Y6 (V$_{OC}$ ~ 0.830 V) and PM7:Y6:PC$_{70}$BM (V$_{OC}$ ~ 0.854 V) devices.

In order to identify the origin of V$_{OC}$ and its relation with material energetics in a ternary system, a combined approach of experimental and simulation studies needs to be carried out. The availability of a wide range of D-A combinations makes the direct estimation of V$_{OC}$ tedious.[31-35] A preliminary attempt to identify the origin of V$_{OC}$ is carried out by fabricating OSC using the acceptor molecule IT-4F instead of Y6 and presented in **Appendix A**. However,

further studies are needed to elucidate the role of the third component in the V_{OC} of the TBOSCs.
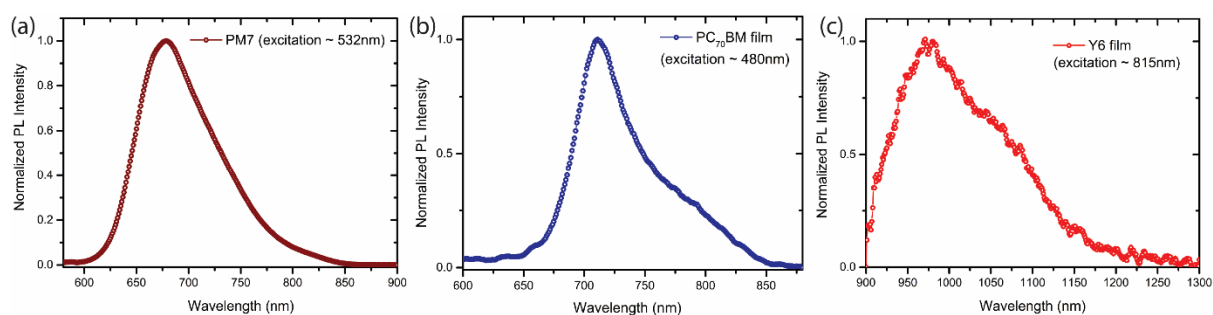
Figure.5.4. The normalized photoluminescence (PL) spectra of (a) PM7, (b) PC$_{70}$BM and (c) Y6 thin films, respectively (the excitation wavelength is indicated in the figure).

The steady-state photoluminescence (PL) spectra of constituent D-A materials are shown in **Figure.5.4**. The PL spectra indicate an overlap between the emission of donor PM7 and acceptor Y6, suggesting the possibility of energy transfer from FRET donor PM7 to FRET acceptor Y6. Recent ultrafast transient absorption spectroscopy result shows a signature of energy transfer between PM7 and Y6.[36] Apart from the favourable charge transfer and energy transfer, Y6 is also shown to have the capability to form a CT state within the molecule.[37] These advantages of the donor and acceptor components are expected to be similar in both binary and ternary blend systems. The PL spectra of PC$_{70}$BM overlap with the Y6 molecule (from 670-820 nm), but the weak PL emission of the PC$_{70}$BM ($\lambda \sim 715$ nm) molecule suggests a negligible gain from the energy transfer mechanism.[38] At the same time, the J-V characteristics of individual binary BHJ OSCs (PM7:Y6 and PM7:PC$_{70}$BM) indicate a parallel-like model of charge transport in the PM7:Y6:PC$_{70}$BM TBOSCs. It is worth mentioning that the existence of the alloy model in a ternary blend system has been challenged recently, which fundamentally arises from the complexity of microstructure morphology and energetics of the constituents in the BHJ.[39]
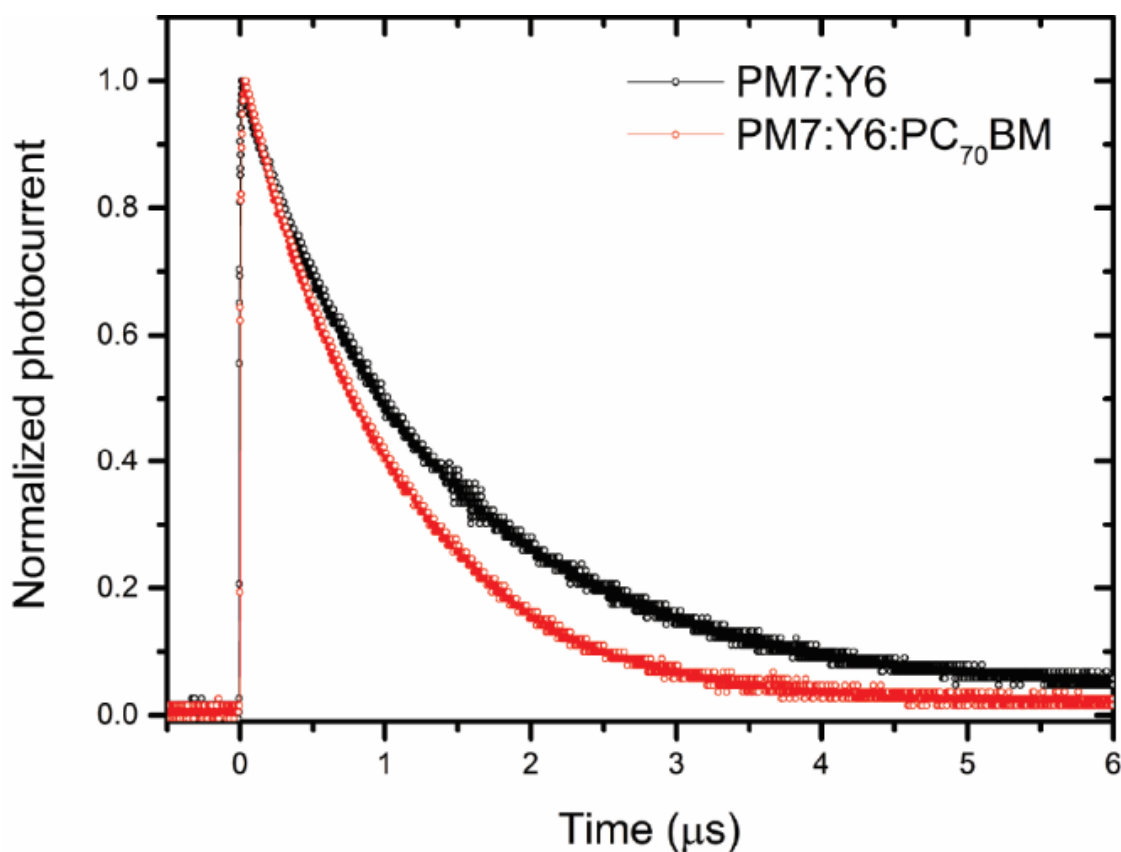
Figure.5.5. Typical transient photocurrent decay profile of PM7:Y6 and PM7:Y6:PC$_{70}$BM organic solar cells (the device is excited using a 532 nm pulsed laser).

Transient photocurrent techniques were employed to gain further insight into the charge carrier dynamics. In this technique, a sub-ns light pulse is used to excite the device, and the carrier generation can be considered almost instantaneous. The resulting photocurrent decay profile provides information about the charge carrier extraction and recombination dynamics.[40-42] During the TPC measurement, the device is held at short-circuit condition, and the TPC decay profile provides information on the distribution of carrier extraction time and charge carrier density. The transient photocurrent decay profile of binary and ternary devices (excitation $\lambda \sim$ 532 nm) is shown in **Figure.5.5.** The ternary device shows a faster photocurrent decay than binary devices indicating an improved charge extraction in TBOSCs.

167
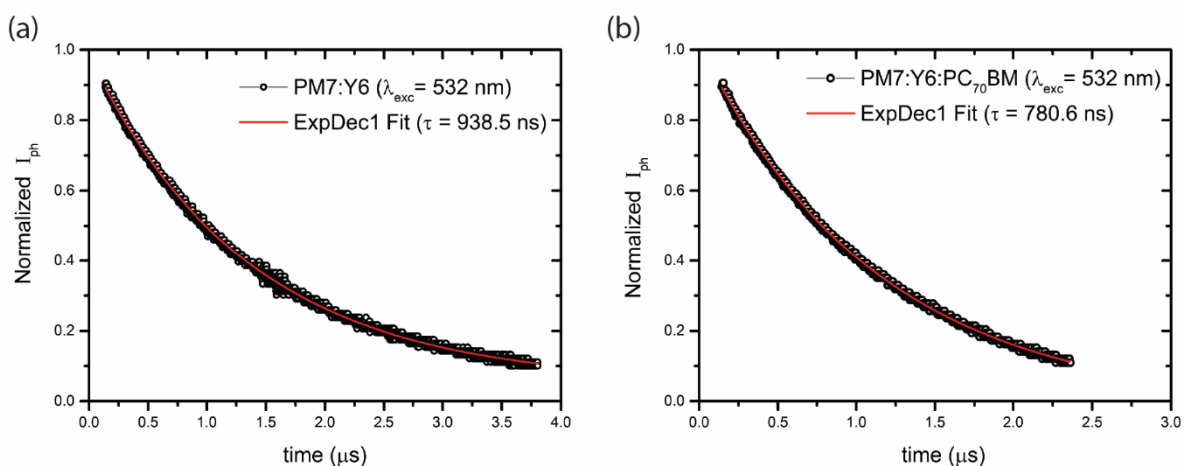
Figure.5.6. Mono-exponential decay fit of TPC profile obtained for PM7:Y6 (decay time constant $\tau \sim$ 938.5 ns) and PM7:Y6:PC$_{70}$BM (decay time constant $\tau \sim$ 780.6 ns) organic solar cells, respectively.

The mono-exponential decay profile (**Figure.5.6**) of transient photocurrent reveals that an effective carrier extraction duration was reduced to ~ 780 ns in the ternary device as compared to the binary device (~ 940 ns). The shorter carrier extraction time in TBOSC can be possibly attributed to the reduced recombination rates in the device with the addition of the third component, PC$_{70}$BM.

Additionally, a signature of reduced recombination losses in ternary blend devices was also observed from electroluminescence (EL) measurement. A red-shifted peak in the EL spectra for the ternary blend device (~ 925 nm = 1.34 eV) in comparison with the binary blend (~ 860 nm = 1.44 eV) indicates a marginally reduced CT state energy in the ternary system due to the presence of a small amount of additive third component PC$_{70}$BM.[43] In contrast, improved V$_{OC}$ of the TBOSCs (~ 0.854 V) clearly indicates a suppressed recombination loss which can be attributed to the morphological optimization of the blend.[44-48] Nonetheless, further estimation and quantification of recombination losses using complementary techniques are needed.
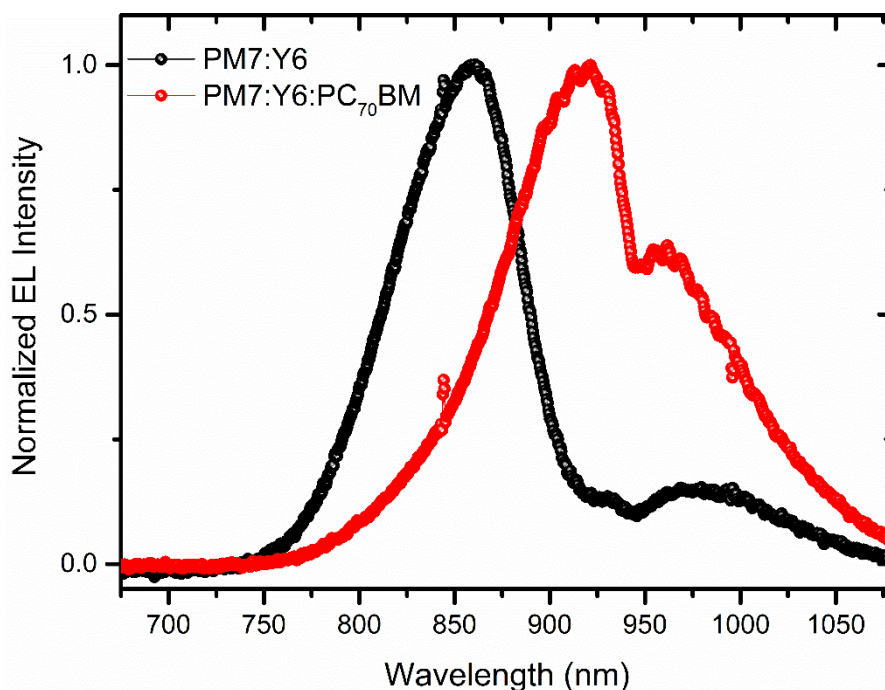
Figure.5.7. Normalized electroluminescence (EL) spectra of PM7:Y6 and PM7:Y6:PC$_{70}$BM organic solar cells (a red-shifted main peak ~ 925 nm observed for the ternary blend as compared to binary blend ~ 860 nm).

5.3. Stability implications from the third component

The degradation trajectory of a typical OSC usually consists of an initial rapid decay of J-V parameters followed by a comparatively slow decay till the failure of the device. Initial device degradation or the burn-in loss is substantial in OSC and has been discussed in chapters 1 and 4 for the binary BHJ systems. It is found that prolonged light exposure and temperature-induced degradation (LID and TID) are among the severe aging factors for an encapsulated device. The device degradation here is largely associated with the molecular properties of the D-A components and their compatibility. Previous studies on burn-in degradation of NFA-based OSCs reveal that the UV component present in the light exposure constitutes the major factor for the decay of encapsulated devices.[49] Temperature-induced degradation is a critical loss channel and it impacts the BHJ active layer morphology the most. In the present study, the investigation is constricted to the UV-light induced and temperature-induced "burn-in"

169

degradation in this Y6 acceptor-based binary and ternary devices. In a manner similar to the previous studies on IT-4F based BHJ systems, the unencapsulated ternary devices were exposed to different aging stress in an inert environment. As described earlier (chapter 4), this stability test condition has the advantage that the device can be considered 'perfectly encapsulated', and the contribution of UV-light and thermal stress can be isolated. This indicates the penetration of oxygen and moisture into the device during the course of the study due to the limitations of encapsulation is negligible, and the photochemical and thermochemical reaction of the commonly used UV-curable epoxy materials can be avoided due to continuous exposure to the aging stresses. The primary objective of this study is to understand the role of the third component in device stability by comparing the degradation trajectories of PM7:Y6 binary and PM7:Y6:PC$_{70}$BM ternary devices. In the present case, as the third component, PC$_{70}$BM mostly impacts the BHJ active layer morphology; the TID is anticipated to play a critical role in the stability comparison of the binary and ternary devices. Accelerated aging stresses were applied continuously for 24 hours immediately after the first J-V measurement on binary and ternary devices in an inert condition to isolate the effects of degradation from UV light ($\lambda \sim 350 - 400$ nm, P$_{out} \sim 1$ mW/cm^2, RT~ 300 K and open-circuit condition) and temperature (100°C, dark and open-circuit condition). **Figure.5.7.** shows the normalized J-V parameters of binary and ternary devices before and after the TID and UV-LID, respectively. **Table.5.2**. summarizes the trend of TID and UV-LID and clearly shows that TBOSCs possess superior stability over binary counterparts. Results reveal that the UV-LID follow a similar pattern in both binary and ternary device, with a marginal improvement in stability for ternary blend devices (Figure.5.7b and Table.5.2). In contrast, TID is significantly minimal in ternary devices as compared to the binary counterpart (Figure.5.7a and Table.5.2).
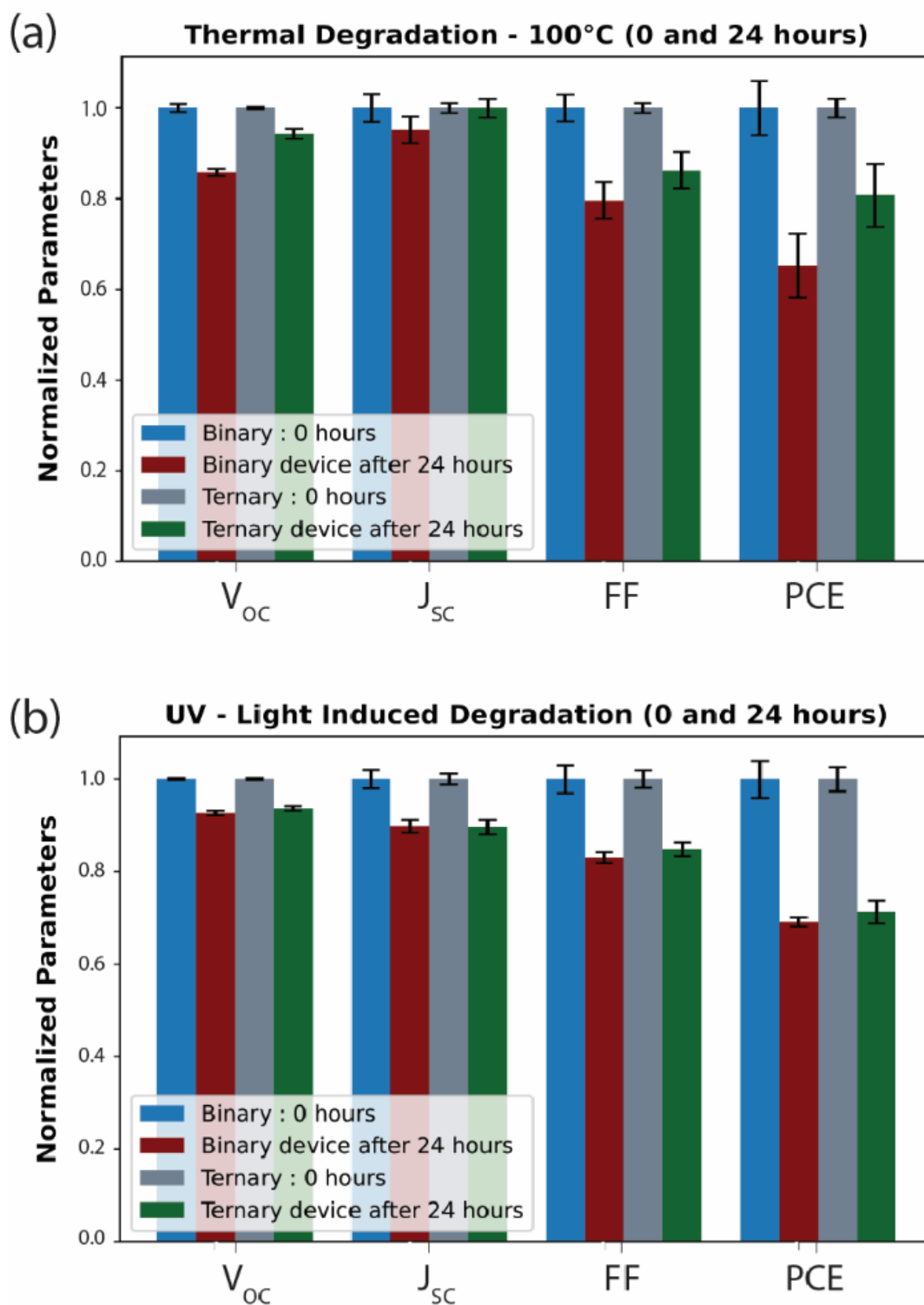
Figure.5.8. Normalized J–V parameters of PM7:Y6 binary and PM7:Y6:PC$_{70}$BM ternary organic solar cells under (a) thermal stress of 100 °C in the dark and (b) UV-light illumination, respectively, for the initial 24 h continuously in inert condition (error bar indicated for an average of six representative devices).

The percentage reduction in the efficiency from the initial PCE value after 24 hours of continuous UV-light exposure for the ternary device (~ 28.7%) is marginally less than the binary device (~ 30.9%) due to the slow decay in V_{OC} and FF of ternary devices. One of the major routes for the UV light-induced degradation in NFAs-based OSCs is due to the photocatalytic reaction of the acceptor molecule and the cathode interlayer ZnO. The presence of surface defects in the ZnO layer coupled with the photoexcitation leads to the trapping of electrons and holes in these states. These electrons can undergo a redox reaction with the adsorbed water molecules in the ZnO layer due to the processing at ambient conditions resulting in the generation of hydroxyl free radicals (·OH). The hydroxyl free radicals are known to weaken the charge transport pathways by decomposing the small molecule acceptors.[49-52] The similar device architecture of both binary and ternary devices indicates the magnitude of ZnO/BHJ interfacial degradation is proportionate. It must be noted that the quantity of Y6 acceptor maintained the same in ternary BHJ, and the $PC_{70}BM$ was introduced as an additive component contributing ~14% of the total acceptor phase (1:1.2:0.2).

The large increase in the energetic disorder and Urbach energy in the BHJ blend upon UV-light soaking can potentially disrupt the charge transport and collection in the device.[53] These sub-bandgap defect states can trap the charge carriers, leading to an enhancement in the recombination losses. Even though the morphological degradation is thermodynamically driven, light-induced morphological degradation and molecular fragmentation at room temperature can possibly accelerate the performance deterioration.[54-55] It is speculated that degradation factors affect ternary devices with $PC_{70}BM$ by reducing the J_{SC} in comparison to the binary device due to factors affecting carrier generation, such as fullerene dimerisation.[56] At the same time, a marginal improvement in V_{OC} retainment after light soaking is expected due to a better microstructure morphology of the BHJ layer due to the addition of the third component.[52, 57-58] A stable morphology can suppress the interfacial recombination losses in

the device. This aspect is evident in the surface morphology characterization of the binary and ternary BHJ films discussed in the following section.

Table.5.2. Percentage reduction in solar cell parameters of PM7:Y6 binary and PM7:Y6:PC$_{70}$BM ternary devices after continuous exposure to aging stresses (temperature and light) for 24 hours in inert conditions. The quantities represent the average of results obtained from six devices.

Aging Stress (24 hours)		ΔV_{OC} (% reduction)	ΔJ_{SC} (% reduction)	ΔFF (% reduction)	ΔPCE (% reduction)
Temperature (100°C)	PM7:Y6	14.2	4.8	20.4	34.8
	PM7:Y6:PC$_{70}$BM	5.7	0.1	13.8	19.3
UV-light	PM7:Y6	7.3	10.2	16.9	30.9
	PM7:Y6:PC$_{70}$BM	6.3	10.4	15.2	28.7

The TID study demonstrates the critical role of the third component, PC$_{70}$BM, in improving the thermal stability of PM7:Y6 binary devices. Even after 24 hours of thermal stress (100°C), ternary devices maintain efficiency above 80% of the initial value with significant retainment in device V_{OC} (decay ~5.7%). In contrast, the binary device undergoes much faster TID with ~34.8% initial PCE loss and a large V_{OC} loss (~14.2%).

Having similar architecture and interlayers, the key difference in the ternary active layer morphology brought in by the addition of an optimal amount of PC$_{70}$BM appears to help reduce the interfacial recombination. Reduced interfacial recombination losses in the ternary device are reflected in the better retainment of the V_{OC} even after 24 hours of continuous thermal stress. This key feature essentially indicates the utility of PC$_{70}$BM in tuning the microstructure so as to reduce recombination loss and improve the stability using the ternary strategy in Y6 acceptor-based devices. **Figure.5.8**. shows representative AFM surface morphology images of

binary and ternary blend films coated on a glass substrate and on ZnO coated ITO substrates before and after thermal stress is applied. A large number of scans on BHJ films in both configurations reveal a definite trend. Results indicate strong aggregation behaviour of PM7:Y6 blend upon thermal stress has been prevented effectively by the addition of a small quantity of third component $PC_{70}BM$.
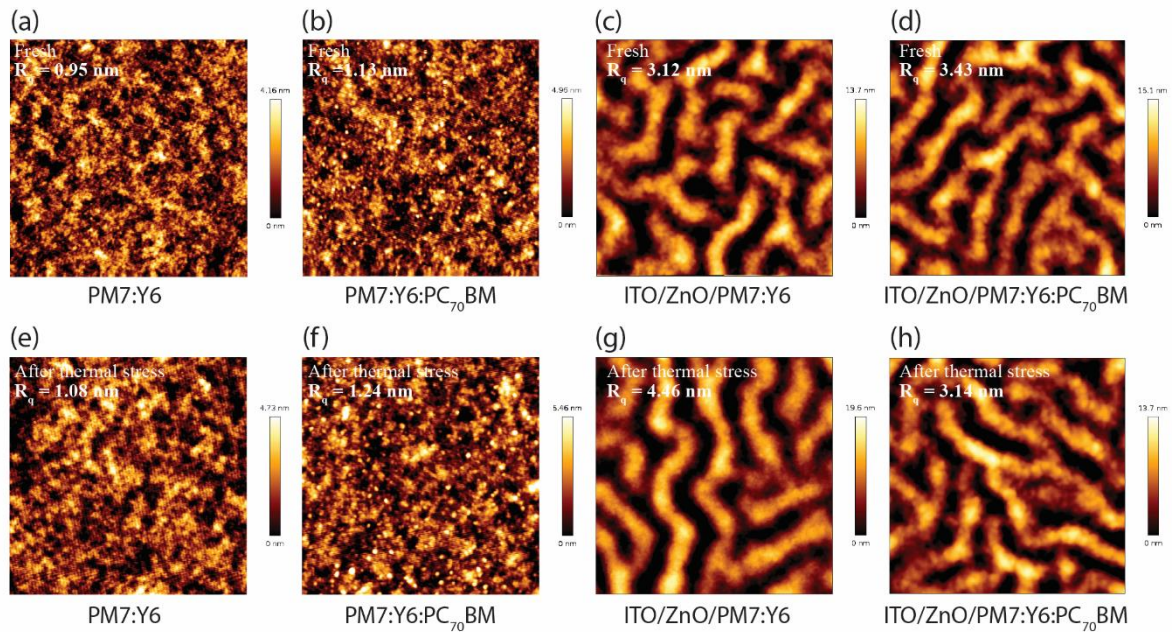
Figure.5.9. Representative AFM morphology images (3μm×3μm) of fresh thin films of (a) PM7:Y6, (b) PM7:Y6:PC_{70}BM, (c) ITO/ZnO/PM7:Y6, (d) ITO/ZnO/PM7:Y6:PC_{70}BM and thermal stress applied thin films of (e) PM7:Y6, (f) PM7:Y6:PC_{70}BM, (g) ITO/ZnO/PM7:Y6, (h) ITO/ZnO/PM7:Y6:PC_{70}BM respectively (estimated RMS surface roughness indicted).

The BHJ films coated on glass substrate show an increase in the root-mean-square roughness (R_q) after accelerated thermal stress of 100°C for 24 hours in an inert condition. The R_q value of binary BHJ film increased to 1.08 nm from 0.95 nm, and for the ternary BHJ film, the R_q value increased to 1.24 nm from 1.13 nm. The increase in the RMS roughness after thermal stress is indicative of the aggregation in the film, and the change is comparatively greater for

binary BHJ film (13.76%) as compared to ternary BHJ film (10.03%), suggesting the morphological stability and optimization from the presence of third component $PC_{70}BM$.[49, 55, 59] This trend is pronounced in films cast on standard interlayer in the device configuration (ITO/ZnO/BHJ film). The R_q value of PM7:Y6 increased from 3.12 nm to 4.46 nm, indicating a strong aggregation behaviour in the presence of ZnO interlayer with an increase of ~ 42.90%. In contrast, $PM7:Y6:PC_{70}BM$ ternary film did not exhibit a significant change in the surface roughness, and the R_q value decreased to 3.14 nm from 3.43 nm. It is evident from this trend that the optimal addition of $PC_{70}BM$ in PM7:Y6 BHJ film improves the microstructure for better device stability.

Table.5.3. Percentage change in the RMS-roughness (R_q) value of PM7:Y6 and $PM7:Y6:PC_{70}BM$ films before and after accelerated thermal stress of 100°C for 24 hours in inert conditions (↓ indicates a reduction in RMS roughness).

Film	ΔR_q
PM7:Y6	13.76%
$PM7:Y6:PC_{70}BM$	10.03%
ITO/ZnO/PM7:Y6	42.90%
$ITO/ZnO/PM7:Y6:PC_{70}BM$	8.50%↓

It was shown that the thermal transition temperature of the BHJ blend constituents plays a critical role in the morphological stability of the active layer. For materials with similar molecular weight, high thermal transition temperature helps to reduce rapid diffusion and aggregate formation within the BHJ active layer.[20, 60] An earlier study on degradation (chapter 4) demonstrated a significantly improved thermal stability in a binary BHJ OSC with the acceptor molecule being an ITIC derivative having a comparatively large thermal transition temperature (~ 160°C). The low thermal transition temperature (~ 102°C) of the Y6 molecule is an important reason behind its poor thermal stability in contrast with ITIC derivatives. It was

shown that the morphology could be stabilised if the third component in the blend with a high thermal transition, such as $PC_{70}BM$ (~ 160°C), with suitable electronic properties.[20] The UV-LID also indicate a similar trend of reduced interfacial recombination and better charge transport in the ternary devices. This is evident from the percentage reduction in V_{OC} after light soaking is smaller (6.3%) in the ternary devices as compared to binary counterparts (7.3%). But it appears that UV-LID is significant in both the devices, and the beneficial role of the third component is comparatively minimal. The results point out that the thermal degradation is severe in this Y6 acceptor-based system, and the role of the third component is significant.

5.4. Summary

In summary, the addition of an optimal amount of acceptor molecule $PC_{70}BM$ as the third component in PM7:Y6 binary bulk heterojunction OSC provides a pathway to improve the performance. The presence of trace amounts of the third component $PC_{70}BM$ in the active layer significantly improved the open-circuit voltage and power conversion efficiency. Steady-state electrical characterizations reveal reduced charge transport barriers and improved charge collection in ternary blend organic solar cells. The crucial aspect of the third component in enhancing the thermal stability and photostability is characterized by an optimized morphology of the ternary blend active layer. A clear trend of better retainment of the open-circuit voltage in the ternary blend device during accelerated aging reflects reduced interfacial charge carrier recombination. Surface morphology characterization confirms that enhanced thermal stability manifests reduced well-known aggregate formation of Y6 molecules in the BHJ due to the presence of $PC_{70}BM$. This work demonstrates the utility of $PC_{70}BM$ as the third component to simultaneously improve the efficiency and stability of Y6 acceptor-based organic solar cells.

References

1.   Bi, P.; Hao, X., Versatile Ternary Approach for Novel Organic Solar Cells: A Review. *Solar RRL* **2019**, *3*, 1800263 2367-198X.

2.   Zhao, C.; Wang, J.; Zhao, X.; Du, Z.; Yang, R.; Tang, J., Recent Advances, Challenges and Prospects in Ternary Organic Solar Cells. *Nanoscale* **2021**, *13*, 2181-2208.

3.   Yu, R.; Yao, H.; Hou, J., Recent Progress in Ternary Organic Solar Cells Based on Nonfullerene Acceptors. *Advanced Energy Materials* **2018**, *8*, 1702814 1614-6832.

4.   An, Q.; Zhang, F.; Zhang, J.; Tang, W.; Deng, Z.; Hu, B., Versatile Ternary Organic Solar Cells: A Critical Review. *Energy & Environmental Science* **2016**, *9*, 281-322.

5.   Adil, M. A.; Iqbal, M. J.; Zhang, J.; Wei, Z., Unconventional Third Components for Ternary Organic Solar Cells. *Materials Today Energy* **2021**, *21*, 100728 2468-6069.

6.   Gasparini, N.; Salleo, A.; McCulloch, I.; Baran, D., The Role of the Third Component in Ternary Organic Solar Cells. *Nature Reviews Materials* **2019**, *4*, 229-242 2058-8437.

7.   Xu, W.; Gao, F., The Progress and Prospects of Non-Fullerene Acceptors in Ternary Blend Organic Solar Cells. *Materials Horizons* **2018**, *5*, 206-221.

8.   Liu, T.; Yang, T.; Ma, R.; Zhan, L.; Luo, Z.; Zhang, G.; Li, Y.; Gao, K.; Xiao, Y.; Yu, J., 16% Efficiency All-Polymer Organic Solar Cells Enabled by a Finely Tuned Morphology Via the Design of Ternary Blend. *Joule* **2021**, *5*, 914-930 2542-4351.

9.   Chang, L.; Sheng, M.; Duan, L.; Uddin, A., Ternary Organic Solar Cells Based on Non-Fullerene Acceptors: A Review. *Organic Electronics* **2021**, *90*, 106063 1566-1199.

10.   Xu, X.; Li, Y.; Peng, Q., Ternary Blend Organic Solar Cells: Understanding the Morphology from Recent Progress. *Advanced Materials* **2022**, 2107476 0935-9648.

11.   Zhu, L.; Zhang, M.; Xu, J.; Li, C.; Yan, J.; Zhou, G.; Zhong, W.; Hao, T.; Song, J.; Xue, X., Single-Junction Organic Solar Cells with over 19% Efficiency Enabled by a Refined Double-Fibril Network Morphology. *Nature Materials* **2022**, 1-8 1476-4660.

12.   Cui, Y.; Xu, Y.; Yao, H.; Bi, P.; Hong, L.; Zhang, J.; Zu, Y.; Zhang, T.; Qin, J.; Ren, J., Single-Junction Organic Photovoltaic Cell with 19% Efficiency. *Advanced Materials* **2021**, *33*, 2102420 0935-9648.

13.   Karuthedath, S.; Paleti, S. H. K.; Sharma, A.; Yin, H.; Alshehri, N.; De Castro, C. S. P.; Ramos, N.; Khan, J. I.; Martin, J.; Li, G., Mixing of Nfas Ionization Energies: An Additional Tool to Tune the Quantum Efficiency of Ternary Solar Cells. *arXiv preprint arXiv:2112.06245* **2021**.

14.   Bi, P.; Zheng, F.; Yang, X.; Niu, M.; Feng, L.; Qin, W.; Hao, X., Dual Förster Resonance Energy Transfer Effects in Non-Fullerene Ternary Organic Solar Cells with the Third Component Embedded in the Donor and Acceptor. *Journal of Materials Chemistry A* **2017**, *5*, 12120-12130.

15.   Mohapatra, A. A.; Tiwari, V.; Patil, S., Energy Transfer in Ternary Blend Organic Solar Cells: Recent Insights and Future Directions. *Energy & Environmental Science* **2021**, *14*, 302-319.

16.   Li, M.-Y.; Pan, Y.-Q.; Sun, G.-Y.; Geng, Y., Charge Transfer Mechanisms Regulated by the Third Component in Ternary Organic Solar Cells. *The journal of physical chemistry letters* **2021**, *12*, 8982-8990 1948-7185.

17.   Ming, S.; Wu, H.; Wang, X.; Huang, H.; Xue, W.; Xu, X.; Tang, Z.; Ma, W.; Bo, Z., High-Efficiency Ternary Nonfullerene Organic Solar Cells with Record Long-Term Thermal Stability. *Journal of Materials Chemistry A* **2020**, *8*, 22907-22917.

18.   Yang, W.; Luo, Z.; Sun, R.; Guo, J.; Wang, T.; Wu, Y.; Wang, W.; Guo, J.; Wu, Q.; Shi, M., Simultaneous Enhanced Efficiency and Thermal Stability in Organic Solar Cells from a Polymer Acceptor Additive. *Nature communications* **2020**, *11*, 1-10 2041-1723.

19.   Zhao, W.; Qian, D.; Zhang, S.; Li, S.; Inganäs, O.; Gao, F.; Hou, J., Fullerene-Free Polymer Solar Cells with over 11% Efficiency and Excellent Thermal Stability. *Advanced materials* **2016**, *28*, 4734-4739 0935-9648.

20.   Qin, Y.; Balar, N.; Peng, Z.; Gadisa, A.; Angunawela, I.; Bagui, A.; Kashani, S.; Hou, J.; Ade, H., The Performance-Stability Conundrum of Btp-Based Organic Solar Cells. *Joule* **2021**, *5*, 2129-2147 2542-4351.

21.   Chen, G.; Sasabe, H.; Sano, T.; Wang, X.-F.; Hong, Z.; Kido, J.; Yang, Y., Chloroboron (Iii) Subnaphthalocyanine as an Electron Donor in Bulk Heterojunction Photovoltaic Cells. *Nanotechnology* **2013**, *24*, 484007 0957-4484.

22.   Kyaw, A. K. K.; Wang, D. H.; Gupta, V.; Leong, W. L.; Ke, L.; Bazan, G. C.; Heeger, A. J., Intensity Dependence of Current–Voltage Characteristics and Recombination in High-Efficiency Solution-Processed Small-Molecule Solar Cells. *ACS Nano* **2013**, *7*, 4569-4577.

23.   Riedel, I.; Parisi, J.; Dyakonov, V.; Lutsen, L.; Vanderzande, D.; Hummelen, J. C., Effect of Temperature and Illumination on the Electrical Characteristics of Polymer–Fullerene Bulk-Heterojunction Solar Cells. *Advanced Functional Materials* **2004**, *14*, 38-44.

24.   Wetzelaer, G.-J. A. H.; Kuik, M.; Blom, P. W. M., Identifying the Nature of Charge Recombination in Organic Solar Cells from Charge-Transfer State Electroluminescence. *Advanced Energy Materials* **2012**, *2*, 1232-1237.

25.   Azeez, A.; Narayan, K. S., Enhanced Device Performance Via Interfacial Engineering in Non-Fullerene Acceptor Based Organic Solar Cells. *Applied Physics Letters* **2020**, *117*, 043302 0003-6951.

26.   Yan, Y.; Zhang, Y.; Liu, Y.; Shi, Y.; Qiu, D.; Deng, D.; Zhang, J.; Wang, B.; Adil, M. A.; Amin, K., Simultaneously Decreasing the Bandgap and Voc Loss in Efficient Ternary Organic Solar Cells. *Advanced Energy Materials* **2022**, *12*, 2200129 1614-6832.

27.   Zhan, L.; Li, S.; Li, Y.; Sun, R.; Min, J.; Bi, Z.; Ma, W.; Chen, Z.; Zhou, G.; Zhu, H., Desired Open-Circuit Voltage Increase Enables Efficiencies Approaching 19% in Symmetric-Asymmetric Molecule Ternary Organic Photovoltaics. *Joule* **2022**, *6*, 662-675 2542-4351.

28.   Pan, J.; Shi, Y.; Yu, J.; Zhang, H.; Liu, Y.; Zhang, J.; Gao, F.; Yu, X.; Lu, K.; Wei, Z., Π-Extended Nonfullerene Acceptors for Efficient Organic Solar Cells with a High Open-Circuit Voltage of 0.94 V and a Low Energy Loss of 0.49 Ev. *ACS Applied Materials & Interfaces* **2021**, *13*, 22531-22539 1944-8244.

29.   Baik, S.; Kim, D. W.; Kang, H.-S.; Hong, S. H.; Park, S.; An, B.-K.; Park, S. Y., Itic Derivative Acceptors for Ternary Organic Solar Cells: Fine-Tuning of Absorption Bands, Lumo Energy Levels, and Cascade Charge Transfer. *Sustainable Energy & Fuels* **2022**, *6*, 110-120.

30.   Palacios-Gómez, D. A.; Huerta Flores, A. M.; MacKenzie, R. C. I.; Pearson, C.; Alanazi, F.; Mendis, B. G.; Groves, C., Differing Impacts of Blended Fullerene Acceptors on the Performance of Ternary Organic Solar Cells. *ACS Applied Energy Materials* **2021**, *4*, 10867-10876 2574-0962.

31.   Tang, W.; Peng, W.; Zhu, M.; Jiang, H.; Wang, W.; Xia, H.; Yang, R.; Inganäs, O.; Tan, H.; Bian, Q., 17.25% High Efficiency Ternary Solar Cells with Increased Open-Circuit Voltage Using a High Homo Level Small Molecule Guest Donor in a Pm6: Y6 Blend. *Journal of Materials Chemistry A* **2021**, *9*, 20493-20501.

32.   Castro-Chacón, A.; Castro-Carranza, A.; Amargós-Reyes, O.; Maldonado, J.-L.; Hernández-Cristóbal, O.; Guzmán-Caballero, D.; Mejía, I.; Vázquez, A.; Gutowski, J. r.;

Nolasco, J. C., Relationship between the V Oc Tuning Effect and the Interface Activation Energy Due to the Third Component Concentration in Ternary Organic Solar Cells. *ACS Applied Energy Materials* **2022**, *5*, 4288-4295 2574-0962.

33.   Li, H.; Zhang, Z.-G.; Li, Y.; Wang, J., Tunable Open-Circuit Voltage in Ternary Organic Solar Cells. *Applied Physics Letters* **2012**, *101*, 163302 0003-6951.

34.   Lee, M.-H., A Machine Learning–Based Design Rule for Improved Open-Circuit Voltage in Ternary Organic Solar Cells. *Advanced Intelligent Systems* **2020**, *2*, 1900108 2640-4567.

35.   Li, Y.; Cai, Y.; Xie, Y.; Song, J.; Wu, H.; Tang, Z.; Zhang, J.; Huang, F.; Sun, Y., A Facile Strategy for Third-Component Selection in Non-Fullerene Acceptor-Based Ternary Organic Solar Cells. *Energy & Environmental Science* **2021**, *14*, 5009-5016.

36.   Ravichandran Shivanna , A. A. M., Satyaprasad P Senanayak , Alexander Gillett , Satish Patil , Richard Friend Energy Transfer Mediated Charge Generation in the Efficient Pm6:Y6 Organic Solar Cells. *Proceedings of Online Conference on Perovskites for Energy Harvesting: From Fundamentals to Devices (PERENHAR)* **2020**.

37.   Wan, P.; Chen, X.; Liu, Q.; Mahadevan, S.; Guo, M.; Qiu, J.; Sun, X.; Tsang, S.-W.; Zhang, M.; Li, Y., Direct Observation of the Charge Transfer States from a Non-Fullerene Organic Solar Cell with a Small Driving Force. *The Journal of Physical Chemistry Letters* **2021**, *12*, 10595-10602 1948-7185.

38.   Gao, J.; Wang, J.; An, Q.; Ma, X.; Hu, Z.; Xu, C.; Zhang, X.; Zhang, F., Over 16.7% Efficiency of Ternary Organic Photovoltaics by Employing Extra Pc71bm as Morphology Regulator. *Science China Chemistry* **2020**, *63*, 83-91 1869-1870.

39.   Huang, X.; Liu, X.; Ding, K.; Forrest, S. R., Is There Such a Thing as a Molecular Organic Alloy? *Materials Horizons* **2020**, *7*, 244-251.

40.   Fu, J.; Chen, S.; Yang, K.; Jung, S.; Lv, J.; Lan, L.; Chen, H.; Hu, D.; Yang, Q.; Duan, T., A "Σ-Hole"-Containing Volatile Solid Additive Enabling 16.5% Efficiency Organic Solar Cells. *Iscience* **2020**, *23*, 100965 2589-0042.

41.   Palomares, E.; Montcada, N. F.; Méndez, M.; Jiménez-López, J.; Yang, W.; Boschloo, G., Photovoltage/Photocurrent Transient Techniques. In *Characterization Techniques for Perovskite Solar Cell Materials*, Elsevier: 2020; pp 161-180.

42.   Yang, K.; Chen, S.; Fu, J.; Jung, S.; Ye, J.; Kan, Z.; Hu, C.; Yang, C.; Xiao, Z.; Lu, S., Molecular Lock Induced by Chloroplatinic Acid Doping of Pedot: Pss for High-Performance Organic Photovoltaics. *ACS Applied Materials & Interfaces* **2020**, *12*, 30954-30961 1944-8244.

43.   Shivanna, R.; Rajaram, S.; Narayan, K. S., Role of Charge-Transfer State in Perylene-Based Organic Solar Cells. *ChemistrySelect* **2018**, *3*, 9204-9210 2365-6549.

44.   Tang, Z.; Wang, J.; Melianas, A.; Wu, Y.; Kroon, R.; Li, W.; Ma, W.; Andersson, M. R.; Ma, Z.; Cai, W., Relating Open-Circuit Voltage Losses to the Active Layer Morphology and Contact Selectivity in Organic Solar Cells. *Journal of Materials Chemistry A* **2018**, *6*, 12574-12581.

45.   Zhang, T.; Birgersson, E.; Luther, J., Relating Morphological Characteristics to the Open-Circuit Voltage of Organic Bulk-Heterojunction Solar Cells. *Applied Physics Express* **2015**, *8*, 024301 1882-0786.

46.   Credgington, D.; Hamilton, R.; Atienzar, P.; Nelson, J.; Durrant, J. R., Non-Geminate Recombination as the Primary Determinant of Open-Circuit Voltage in Polythiophene: Fullerene Blend Solar Cells: An Analysis of the Influence of Device Processing Conditions. *Advanced Functional Materials* **2011**, *21*, 2744-2753 1616-301X.

47.   Schlenker, C. W.; Thompson, M. E., The Molecular Nature of Photovoltage Losses in Organic Solar Cells. *Chemical communications* **2011**, *47*, 3702-3716.

48.   Ray, B.; Lundstrom, M. S.; Alam, M. A., Can Morphology Tailoring Improve the Open Circuit Voltage of Organic Solar Cells? *Applied Physics Letters* **2012**, *100*, 7 0003-6951.

49.   Azeez, A.; Narayan, K. S., Dominant Effect of Uv-Light-Induced "Burn-in" Degradation in Non-Fullerene Acceptor Based Organic Solar Cells. *The Journal of Physical Chemistry C* **2021**, *125*, 12531-12540 1932-7447.

50.   Hu, L.; Liu, Y.; Mao, L.; Xiong, S.; Sun, L.; Zhao, N.; Qin, F.; Jiang, Y.; Zhou, Y., Chemical Reaction between an Itic Electron Acceptor and an Amine-Containing Interfacial Layer in Non-Fullerene Solar Cells. *Journal of Materials Chemistry A* **2018**, *6*, 2273-2278.

51.   Park, S.; Son, H. J., Intrinsic Photo-Degradation and Mechanism of Polymer Solar Cells: The Crucial Role of Non-Fullerene Acceptors. *Journal of Materials Chemistry A* **2019**, *7*, 25830-25837.

52.   Günther, M.; Blätte, D.; Oechsle, A. L.; Rivas, S. S.; Yousefi Amin, A. A.; Müller-Buschbaum, P.; Bein, T.; Ameri, T., Increasing Photostability of Inverted Nonfullerene Organic Solar Cells by Using Fullerene Derivative Additives. *ACS Applied Materials & Interfaces* **2021**, *13*, 19072-19084 1944-8244.

53.   Upama, M. B.; Wright, M.; Mahmud, M. A.; Elumalai, N. K.; Soufiani, A. M.; Wang, D.; Xu, C.; Uddin, A., Photo-Degradation of High Efficiency Fullerene-Free Polymer Solar Cells. *Nanoscale* **2017**, *9*, 18788-18797.

54.   Zhang, C.; Heumueller, T.; Gruber, W.; Almora, O.; Du, X.; Ying, L.; Chen, J.; Unruh, T.; Cao, Y.; Li, N., Comprehensive Investigation and Analysis of Bulk-Heterojunction Microstructure of High-Performance Pce11: Pcbm Solar Cells. *ACS applied materials & interfaces* **2019**, *11*, 18555-18563 1944-8244.

55.   Zhu, Y.; Gadisa, A.; Peng, Z.; Ghasemi, M.; Ye, L.; Xu, Z.; Zhao, S.; Ade, H., Rational Strategy to Stabilize an Unstable High-Efficiency Binary Nonfullerene Organic

Solar Cells with a Third Component. *Advanced Energy Materials* **2019**, *9*, 1900376 1614-6832.

56.   Eklund, P. C.; Rao, A. M.; Zhou, P.; Wang, Y.; Holden, J. M., Photochemical Transformation of C60 and C70 Films. *Thin solid films* **1995**, *257*, 185-203 0040-6090.

57.   Gasparini, N.; Paleti, S. H. K.; Bertrandie, J.; Cai, G.; Zhang, G.; Wadsworth, A.; Lu, X.; Yip, H.-L.; McCulloch, I.; Baran, D., Exploiting Ternary Blends for Improved Photostability in High-Efficiency Organic Solar Cells. *ACS Energy Letters* **2020**, *5*, 1371-1379 2380-8195.

58.   Feng, H.; Song, X.; Zhang, Z.; Geng, R.; Yu, J.; Yang, L.; Baran, D.; Tang, W., Molecular Orientation Unified Nonfullerene Acceptor Enabling 14% Efficiency as-Cast Organic Solar Cells. *Advanced Functional Materials* **2019**, *29*, 1903269 1616-301X.

59.   Xiong, S.; Fukuda, K.; Lee, S.; Nakano, K.; Dong, X.; Yokota, T.; Tajima, K.; Zhou, Y.; Someya, T., Ultrathin and Efficient Organic Photovoltaics with Enhanced Air Stability by Suppression of Zinc Element Diffusion. *Advanced Science* **2022**, 2105288 2198-3844.

60.   Mateker, W. R.; McGehee, M. D., Progress in Understanding Degradation Mechanisms and Improving Stability in Organic Photovoltaics. *Advanced materials* **2017**, *29*, 1603940 0935-9648.

Summary and Future Directions

6.1. Summary

This thesis reports efficiency enhancement strategies for bulk heterojunction organic solar cells based on non-fullerene acceptors and presents a comprehensive understanding of the degradation mechanism with emphasis on the 'burn-in' period, which is particularly important in organic solar cells. The first part of the thesis focused on improving the efficiency of non-fullerene acceptor IT-4F based inverted OSCs using $PC_{70}BM$ as a cathode interlayer. The studies demonstrated that the introduction of $\sim 20\,nm$ thick interlayer of $PC_{70}BM$ between cathode buffer layer ZnO and the BHJ active layer of PBDB-T-2Cl:IT-4F significantly improved the short-circuit current density along with marginal improvement in open-circuit voltage and fill factor. After introducing the interlayer, an efficiency close to 11.3% was achieved with short-circuit current density exceeding 20 mA/cm^2. The contact selectivity of the device at the cathode interface improved by incorporating the $PC_{70}BM$ interlayer and the standard electron transport layer ZnO. A detailed analysis of the current-voltage characteristics reveals that the thin $PC_{70}BM$ interlayer can reduce the charge transport barriers and help achieve more balanced carrier transport and better charge collection. Impedance spectroscopy and photocurrent noise measurements corroborate these findings. The equivalent circuit modelling of the impedance spectra shows a significant reduction in the charge transport resistance (R_{CT}) by nearly an order of magnitude in the device with a $PC_{70}BM$ interlayer. A low level of photocurrent fluctuations ($\sim 10^{-14}\,Hz^{-1}$) in the interlayer device compared with the control device ($\sim 10^{-11}\,Hz^{-1}$) correlates with the reduced charge transport barrier identified using

the impedance spectroscopy analysis. The studies suggested the potential of $PC_{70}BM$ as an interlayer material to further improve the performance of NFA IT-4F based OSCs.

In the next part of the thesis, a comprehensive investigation of light-induced and temperature-induced degradation in IT-4F acceptor-based organic solar cells were studied with emphasis on the initial period of operation ('burn-in' period). It is well known that 'burn-in' degradation is significant in organic solar cells, unlike other photovoltaic technologies. Various factors contribute to the device degradation, in which light and temperature-induced degradation were found to be critical. The mechanism of light and temperature-induced degradation in one of the high stabilities reported non-fullerene acceptor IT-4F based organic solar cells with the more stable inverted device geometry was investigated. Monitoring current-voltage characteristics upon accelerated aging stresses in inert conditions revealed that significant degradation occurs due to the light illumination than the moderate thermal stress. Further, spectrally resolved photostability measurements (UV-light and non-UV white light) demonstrated that the UV components present in the light illumination are the dominant factor causing rapid deterioration of the device performance. Steady-state optoelectronic measurements and spectroscopic studies provide significant insights into the degradation mechanisms, including the development of substantial bulk and interfacial charge transport barriers and the weakening of the conjugation in the acceptor molecule. Further, attempts were made to understand the detrimental effects of the commonly used solvent additive DIO (1,8-diiodooctane) in device degradation. It is found that though solvent additives are detrimental, the inherent instability of the active layer components is critical in rapid degradation. The study suggests the importance of preventing UV components through suitable barrier layers or through luminescent downshifting to prolong the lifetime of organic solar cells.

The final section of the thesis focused on improving the OSC device performance using the ternary blend strategy. Ternary blend strategy in which three photo-active materials constitute

the active layer is a route to enhance photon harvesting without the fabrication complexities of multi-junction devices. In this work, the fullerene derivative acceptor molecule $PC_{70}BM$ is introduced as the third component in the Y6 acceptor-based OSCs. Wide-bandgap $PC_{70}BM$ with complementary absorption significantly improved the open-circuit voltage and the PCE of the binary OSCs. Insights into charge transport and recombination dynamics in the devices are analyzed using steady-state and transient techniques. Transient photocurrent results reveal a fast charge carrier extraction in the ternary system with a time constant $\tau \sim 730$ ns, indicating reduced recombination and transport barrier. The role of the third component, $PC_{70}BM$, in the device stability is critical, and it has been found that thermal stress acts as a dominant factor in degradation over the UV light in Y6 acceptor-based devices. The morphological modification of the BHJ active layer indicates a suppressed interfacial recombination due to the third component, $PC_{70}BM$, having a comparatively high thermal transition temperature. Light and temperature-induced degradation studies reveal the optimized BHJ morphology of ternary OSCs in prolonging the device lifetime. The morphological modification in the BHJ active layer due to the third component, $PC_{70}BM$, reduced the interfacial recombination and rapid degradation of the ternary device compared to the binary counterpart. This work pinpoints the potential of fullerene derivative acceptor $PC_{70}BM$ in improving the efficiency and stabilizing the NFA-based single-junction organic solar cells.

In summary, this thesis described methods to improve the device performance of non-fullerene acceptors IT-4F and Y6-based organic solar cells using interfacial modification and ternary blend strategies. In addition to this, a systematic study of the degradation mechanism in these devices and disintegration of the influence of various aging factors along with implications toward strategies to improve the stability are presented. This thesis proposes strategies and provides insights to improve the efficiency and stability of organic solar cells using state-of-the-art non-fullerene acceptors. It is envisioned that the inferences are drawn from this study

help improve the performance of non-fullerene acceptor-based bulk heterojunction organic solar cells and serve as valuable information for the design of more stable active layer components in the future.

6.2. Future Directions

A detailed investigation and in-depth understanding of photochemical and thermochemical changes of the bulk heterojunction active layer components induced by various factors (intrinsic factors, role of various transport layers, external factors) during light and temperature-induced degradation is imperative. It is evident that the degradation mechanism is system-specific, and hence a detailed study is needed to frame general guidelines for the design of new donor-acceptor materials. This investigation is particularly relevant to nailing down strategies to develop 'burn-in' free OSCs.

Most of the stability studies in organic solar cells are conducted by continuous exposure to aging stress factors for various time durations. The degradation studies with emphasis on cycles of photo-thermal stress are seldom emphasized. As far as the outdoor applications are concerned, the cycling stress conditions are particularly important, and the insights in terms of inherent material stability and the pattern of degradation due to external factors need to be understood. The understanding of the presence of reversible degradation processes in the system, along with the trajectory of performance decay under cycling stress conditions, comprise a valuable set of information in regards to the feasibility of commercial organic solar cells.

The correlation of open-circuit voltage of a ternary blend system with the constituent material energetics and the stoichiometry of individual components needs to be identified. The role of the third component in a ternary blend system can vary depending on the optoelectronic properties of the binary BHJ components. The availability of a large number of material combinations and rapidly increasing high-performing material collections make it a tedious task. Particularly when the ternary blend systems outperform the binary counterparts and

voltage loss is the dominant loss pathway, it is necessary to identify the correlation of open-circuit voltage to the material properties.

The BHJ active layer morphology has a significant impact on the efficiency parameters and the device stability. It is evident that in many D-A combinations of the ternary blend, the morphology has a significant impact on improving the device stability. Apart from molecular design strategies, the morphology control and optimization of ternary blends using additional strategies such as solvent annealing and electric field-assisted thermal annealing and understanding its correlation to the device lifetime needs to be explored in detail. Recent studies report that many ternary blend devices are more stable than their binary counterpart, but these studies are, in general, focused either on a specific aging stress factor or short-term monitoring. A standard protocol where the stability reports are reasonably comparable with different combinations also needs to be developed.

The combination of frequency-domain techniques such as impedance spectroscopy, intensity-modulated photocurrent spectroscopy, and time-domain noise spectroscopy can provide quantitative information and insights into device photo-physics. In-depth understanding and quantification of defect distribution, recombination losses and various other charge transport barriers and their evolution during degradation using combined time-domain and frequency-domain experimental tools could serve as a valuable tool to correlate aging with transport parameters. A common equivalent circuit modelling to the results of this combined experimental technique can provide a rapid assessment of the device performance with insights into the material structure-property relationship and the device architecture.

Appendices

Appendix A:

Device performance analysis of IT-4F based ternary blend organic solar cells
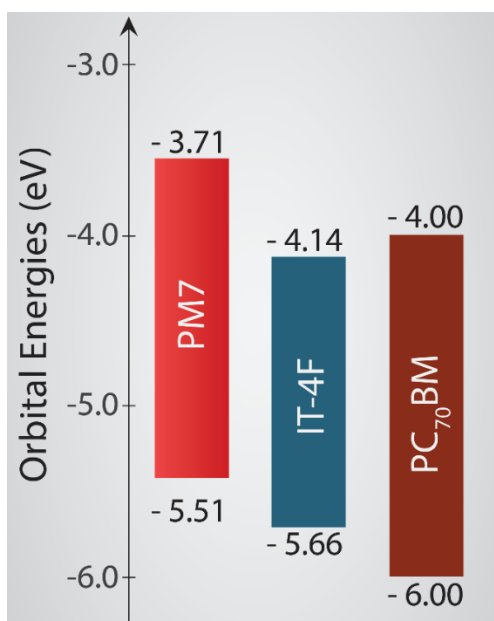
Figure.A.1. The orbital energy diagram of donor PM7 and acceptors IT-4F and PC$_{70}$BM.

In this study, the device performance of PM7:IT-4F:PC$_{70}$BM ternary blend OSCs are investigated. The key difference in this ternary system is the presence of comparatively stable non-fullerene acceptor molecule IT-4F instead of Y6. The fullerene derivative acceptor PC$_{70}$BM retained as the third component. **Figure.A.1.** show the orbital energy diagram of the three components and the devices fabricated in the standard inverted architecture (ITO/ZnO/BHJ/MoO$_x$/Ag). The solvent additive DIO used to obtain an optimized BHJ active layer morphology during the device fabrication. The typical J-V characteristics of PM7:IT-4F:PC$_{70}$BM ternary device along with PBDB-T-2Cl:IT-4F and PM7:PC$_{70}$BM binary devices

are shown in **Figure.A.2**. and the results are summarized in **Table.A.1**. PM7:IT-4F binary OSC show a high PCE ($\approx$ 10.1%) as compared to the PM7:PC$_{70}$BM binary ($\approx$ 8.2%) and PM7:IT-4F:PC$_{70}$BM ternary ($\approx$ 8.9%) OSCs. PM7:PC$_{70}$BM binary device exhibit highest $V_{OC} \approx$ 0.96 V, whereas the ternary device shows V_{OC} ($\approx$ 0.85 V) between that of both the binary devices. Despite having high V_{OC}, the low PCE in PM7:PC$_{70}$BM device can be understood due to the reduced photo absorption in this blend which is evident from low J_{SC} and FF. It must be noted that the efficiency of the TBOSC is slightly lower as compared to the NFA IT-4F based binary device due to reduced J_{SC} and FF. The V_{OC} of the devices show a similar trend as that Y6 based system discussed previously in chapter.5. The presence of a wide band gap acceptor as a third component improves the V_{OC}, which appears as in direct relation with the effective bandgap for parallel-like charge transport model. Further studies on dependence of V_{OC} to the stoichiometry of third component in the BHJ is needed.
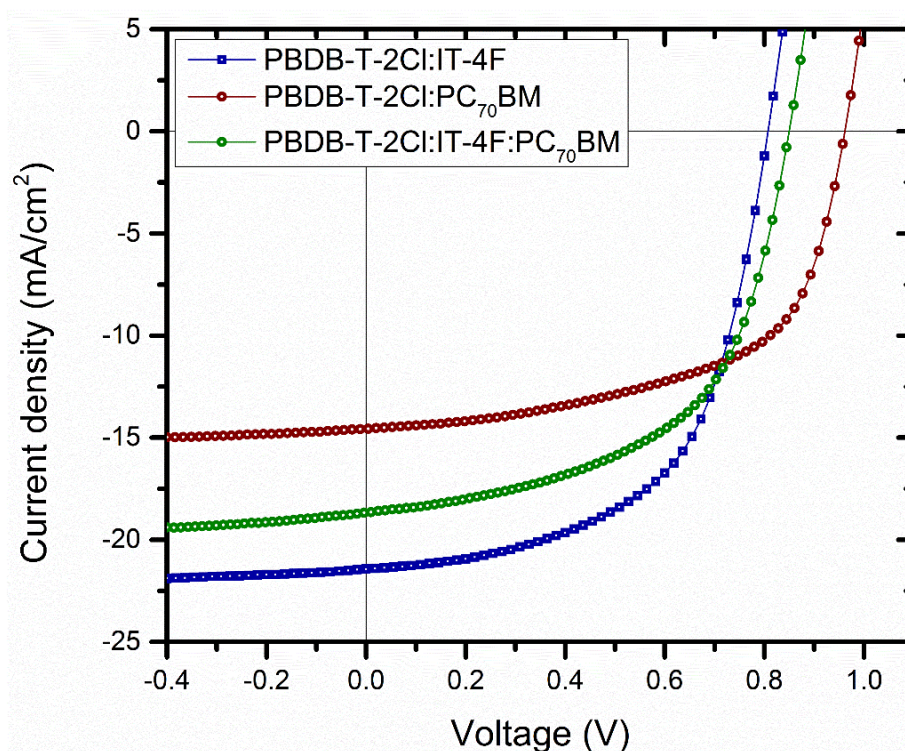

Figure.A.2. Typical J-V characteristics of PBDB-T-2Cl:IT-4F, PBDB-T-2Cl:PC$_{70}$BM and PBDB-T-2Cl:IT-4F:PC$_{70}$BM bulk heterojunction organic solar cells under simulated AM1.5G (100 mWcm^{-2}) illumination.

Table.A.1. Solar cell parameters of PBDB-T-2Cl:IT-4F, PBDB-T-2Cl:PC$_{70}$BM and PBDB-T-2Cl:IT-4F:PC$_{70}$BM bulk heterojunction organic solar cells under simulated AM1.5G (100 mWcm^{-2}) illumination.

BHJ System	V_{OC} (V)	J_{SC} (mA/cm^2)	FF (%)	PCE (%)
Binary BHJ (PBDB-T-2Cl:IT-4F)	0.800 ± 0.003	19.67 ± 1.26	59.12 ± 2.3	9.4 ± 0.40 (10.1)
Binary BHJ (PBDB-T-2Cl:PC$_{70}$BM)	0.961 ± 0.002	13.43 ± 0.56	58.31 ± 0.67	7.5 ± 0.50 (8.2)
Ternary BHJ (PBDB-T-2Cl:IT-4F:PC$_{70}$BM)	0.850 ± 0.003	17.51 ± 0.56	55.42 ± 0.67	8.2 ± 0.36 (8.9)

To gain insights into the degradation pattern, the stability aspects of all the devices are systematically studied during initial period of operation by applying accelerated aging stresses similar to the conditions discussed in chapter 4. All the devices were exposed to accelerated aging stresses of 1 Sun illumination and a thermal stress of ≈ 70°C in an inert condition for 10 hours. **Figure.A.3.** shows the degradation pattern of binary and ternary devices and the results are summarized in **Table.A.2.** and **Table.A.3**. Interestingly, PM7:IT-4F binary BHJ OSCs exhibits excellent thermal stability and comparatively better photostability in contrast to PM7:Y6 OSCs discussed in chapter.5. The key advantage of introducing PC$_{70}$BM as a third component is in slowing down V$_{OC}$ decay during the degradation under 1 Sun illumination. Intrinsically high thermal stability of IT-4F and extraordinary absorption suggests the presence of PC$_{70}$BM as a third component is not vital for improving the device performance.
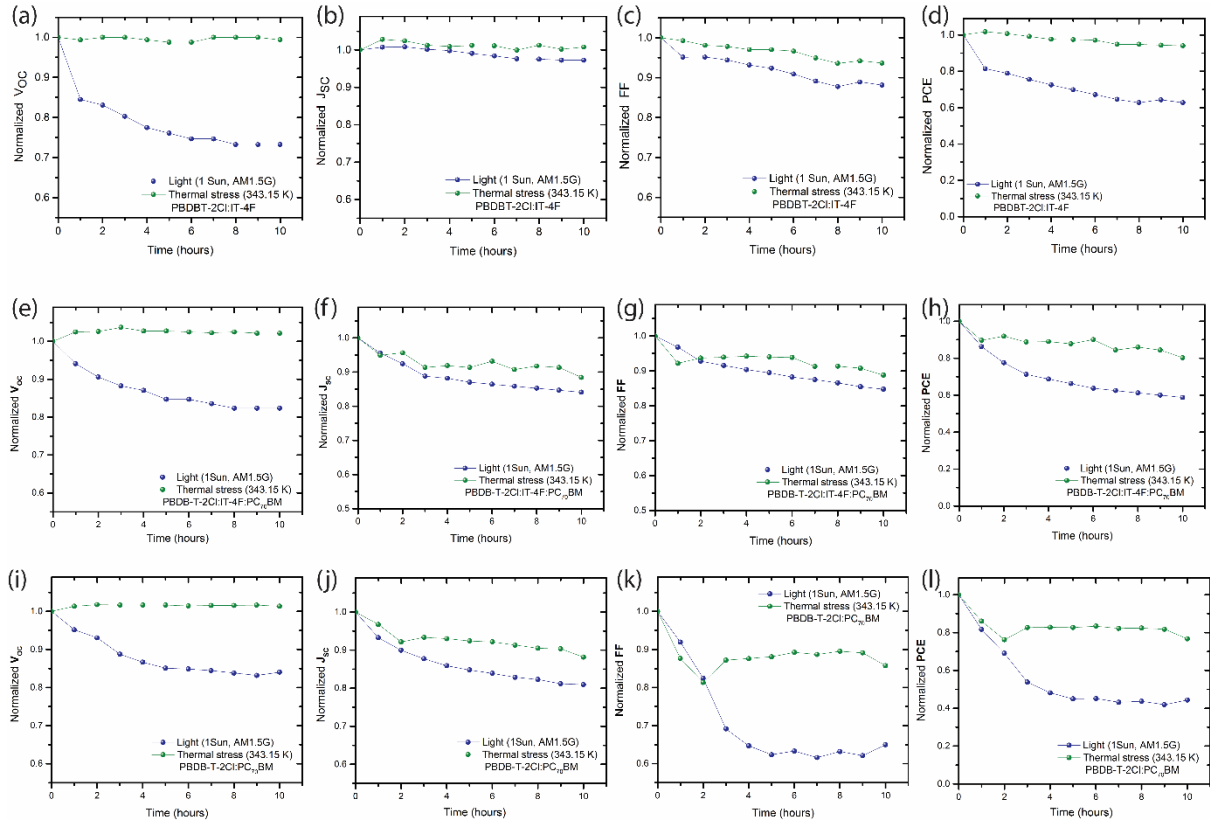
Figure.A.3. Normalized J-V parameters of PBDB-T-2Cl:IT-4F (a-d), PBDB-T-2Cl:IT-4F:PC$_{70}$BM (e-h) and PBDB-T-2Cl:PC$_{70}$BM (i-l) solar cells under simulated AM1.5G 1 sun (100 mWcm^{-2}) illumination and thermal stress of 70°C, respectively for the initial 10 hours of device operation continuously in an inert condition, data points represent average values of measurements.

Table.A.2. Percentage reduction in solar cell parameters of PBDB-T-2Cl:IT-4F devices after continuous exposure to ageing stresses for 10 hours (Figure 2). The quantities represent the average of results obtained from six devices each with the error-range for the PCE represented by the maximum deviation from this value.

| LID	V$_{OC}$	J$_{SC}$	FF	PCE
PM7:IT-4F	26.7	2.7	11.8	37.2
PM7:PC$_{70}$BM	16.0	19.1	35.0	55.7
PM7:IT-4F:PC$_{70}$BM	17.6	15.9	15.2	41.2

Table.A.3. Percentage reduction in solar cell parameters of PBDB-T-2Cl:IT-4F devices after continuous exposure to ageing stresses for 10 hours (Figure 2). The quantities represent the average of results obtained from six devices each with the error-range for the PCE represented by the maximum deviation from this value.

TID	V_{OC}	J_{SC}	FF	PCE
PM7:IT-4F	0.6	$0.8^{\uparrow}$	6.3	5.9
PM7:PC$_{70}$BM	$1.3^{\uparrow}$	11.8	14.3	23.3
PM7:IT-4F:PC$_{70}$BM	$2.1^{\uparrow}$	11.5	11.2	19.7

Organic Solar Cells Timeline
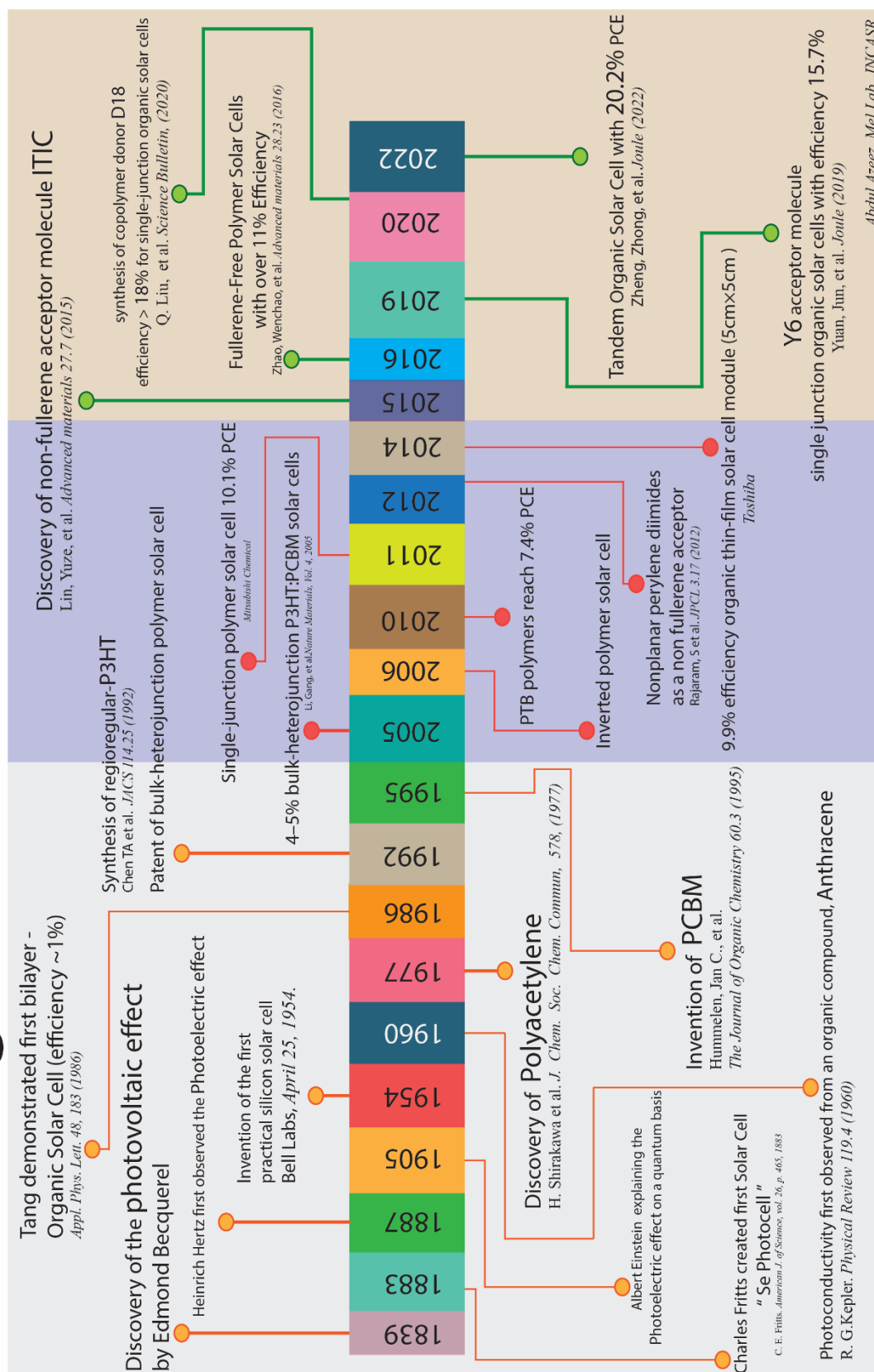
Appendix C:

Spectral distribution analysis of AM1.5G illumination
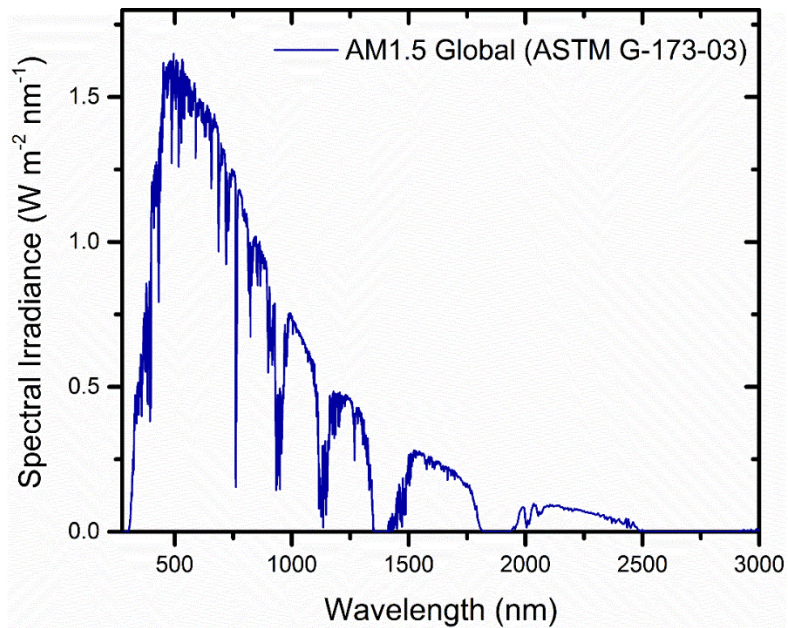
Figure.C.1. The spectral irradiance of the standard AM1.5 Global spectrum used for the characterization of solar cells

Table C.1. Percentage contribution of different wavelength region in the AM1.5G solar spectra.

Wavelength (nm)	Percentage of total irradiance
300-400	4.6 %
400-500	14.0 %
500-600	15.1 %
600-700	13.9 %
700-800	11.3 %
800-900	9.4 %
900-1000	5.6 %
>1000	26.0 %

Table C.2. Percentage contribution of the UV components (300-400 nm) in the AM1.5G solar spectra.

Wavelength (nm)	Power (W/m^2)	Percentage of total irradiance
300-350	13.77	1.4 %
350-400	32.33	3.2 %

Appendix D:

1- Matlab code used for the calculation of noise power spectral density from time-domain data

```
%% Details of the Code
% The PSD is computed by taking the time series file and splitting into
% frames of a specific frequency range, which can be different from the
% settings at DSA.Thus this program can change the lower and
% higher frequency ranges and is also good for averaging. Here the nfft is
% radix-2 and not in terms of resolution lines of signal analyzer. But the
% PSD is plotted in resolution lines which depends on the user input
% frequency range  values.
%% Molecular Electronics LAB

function DSA_PSD _zeta
format long
clear all

%% Initializing all parameters from the measurement settings

fres = 1600; % input('Enter the frequency resolution: ');
fspan =400;% input('Enter the frequency span of time capture in DSA(in Hz):
12800');

sf = fspan*2.56;              % sampling frequency, sf does not depend on
                             % frequency resolution of DSA
% lowf = fspan/fres;      % lower frequency in DSA
T =60;% input('Enter the total duration of time capture:10 ');
% minf=1/T;               % lowest frequency possible
fl = 0.25;% input('Enter the lower frequency of plot: ');
fu = 400;% input('Enter the upper frequency of plot: ');
t = 1/fl;                % this should be the time capture for one PSD plot
Av= input('Enter the gain at preamplifier (only exponent): ');
Av=1*10^(0);
%% Calling the saved file into MatLAB
data_file = input('Enter the file name of time series capture: ','s');
fid = fopen(data_file,'r');
data= dlmread(data_file);
X= data(:,1);                % X has all the data points of time capture
```

```matlab
X=X./(Av);
len_X= length(X);                              % len_X
%% Initialize parameters for obtainig PSD plots

len_T = T*sf;
len_t= t*sf;                   % data points required for one PSD plot

nfft = 2.56*(fu/fl);% nfft
%(p=nextpow2(len_t);nfft=2^p;nfft) this line can also be used, but only
% when the lower frequency ranges are similar or when more no.of  points are
% taken for a particular freq span. Like 8192 data pts for 4096 fft pts

Navg = len_T/len_t;

x = zeros(len_t,1);
PSD_total = zeros(nfft,1);
psd_x = zeros(nfft,1);
ptr=0;

for i= 1:Navg

    x = X(1+ptr:len_t+ptr,1);

    psd_x = (fft(x,nfft))./(nfft);
    psd_x = abs(psd_x);
    psd_x = (psd_x.^2);



    PSD_total=PSD_total+psd_x;
    ptr= ptr+len_t;

end

freq=0:fl:fu;          % size(freq)
                       % freq(1,1:4)

PSD_total = PSD_total/Navg;

PSD_total=PSD_total(1:((nfft/2)+1),1);
```

```matlab
PSD_total(2:end-1,1) = PSD_total(2:end-1,1);


% Do not multiply the elements of PSD with 2, even if the elements are same
% and are folded with respect to zero level. The correct form is taking
% only one side (or only one half) along with the zero level.


PSD_plt=plot(log10(freq),log10(PSD_total(1:((nfft/2.56)+1))));
xlabel('Frequency (Hz)')
title(data_file)
% saveas(PSD_plt,sprintf('.bmp'))


%% Saving the PSD plot into text file
freq=transpose(freq);
PSD_write=zeros((fu/fl)+1,2);
PSD_write(:,1)= freq(:,1);
PSD_write(:,2)= PSD_total(1:((nfft/2.56)+1),1);
dlmwrite('PSD_OSC_400Hz_60s.txt',PSD_write,'precision',16,'delimiter',',',
'newline','pc')
fclose all
    end
```

2- Python code used for the plotting the bar graphs of J-V monitoring results

```python
import matplotlib
import matplotlib.pyplot as plt
import numpy as np


labels = ['Voc', 'Jsc', 'FF', 'PCE']
fresh = [1, 1, 1, 1]
degraded = [1, 0.94709, 0.90581, 0.85192]
E1 = [5.476e-3,0.03067,0.0266,0.0383]
E2 = [0.01095,0.04534,0.0141,0.0572]


x = np.arange(len(labels))  # the label locations
width = 0.3  # the width of the bars


fig, ax = plt.subplots()
rects1 = ax.bar(x - width/2, fresh, width, label='0 hours',yerr = E1,capsize=5)
rects2 = ax.bar(x + width/2, degraded, width, label='1000 hours',yerr = E2,capsize=5)#120 hours


# Add some text for labels, title and custom x-axis tick labels, etc.
ax.set_ylabel('Normalized Parameters',fontsize='large')
ax.set_title('Device shelf life (0 and 1000 hours)', fontsize='large', fontweight='bold')
ax.set_xticks(x)
ax.set_xticklabels(labels,fontsize='large', fontweight='bold')
ax.legend()
fig.tight_layout()
plt.show()
```

3- Python code to plot Bode plot and Cole-Cole plot from impedance spectroscopy measurement

```python
from matplotlib import pyplot as plt
from matplotlib import style
import numpy as np


w,x,y = np.loadtxt('BHJOSC_10Hz_2MHz_20mV.txt',
                   unpack = True,
                   delimiter ='\t')


E = float(input('Amplitude of the bias voltage in Volts '))
A = int(input('enter the value of Gain of Pre Amplifier '))
x1 = x/A
Z= E/x1
Z1 = Z*np.cos(y*(np.pi/180))
Z2 = Z*np.sin(y*(np.pi/180))
M = np.sqrt((Z1*Z1)+(Z2*Z2))
N = (Z1*Z1)+(Z2*Z2)


u = np.linspace(10, 1000000, num=len(Z1))


C1 = Z2/(6.28*w*N)


C2 = Z1/(6.28*w*N)


f = open('C1_BHJOSC_10Hz_2MHz_20mV.txt','w')
for i in range(len(Z1)):
    f.write("{}\t{}\n".format(w[i],C1[i]))
f.close()

"""
h = open('Output_BHJOSC_10Hz_2MHz_20mV.txt','w')
for i in range(len(u)):
    h.write("{}\t{}\n".format(u[i],C2[i]))
h.close()
```

203

```python
plt.figure(1)
plt.scatter(C1,C2)
plt.title('Cole-Cole Plot')
plt.ylabel('Imaginary Z (KOhm)')
plt.xlabel('Real Z (KOhm)')

plt.figure(2)
plt.scatter(u,M/1000)
plt.title('Bode Plot_1')
plt.ylabel('|Z| (KOhm)')
plt.xlabel('Frequency (Hz)')
plt.figure(3)
plt.scatter(u,y)
plt.title('Bode Plot_2')
plt.ylabel('THETA (Degree)')
plt.xlabel('Frequency (Hz)')
"""
#plt.show(1)
#plt.show(2)
#plt.show(3)
```

4- Wolfram Mathematica code used for the fitting of intensity dependent short-circuit current density results

```
SetDirectory["F:\\Solar Cells_My Device\\Ternary\\LIGHT\\INTENSITY\\FIT"]
F:\Solar Cells_My Device\Ternary\LIGHT\INTENSITY\FIT

DATA = Import["D3_Jsc_10hrs.txt"]
17     2.86
24     4.02
32     5.12
45     7.21
63     10.27
100    14.31

MyData = ImportString[DATA]
{{17, 2.86}, {24, 4.02}, {32, 5.12}, {45, 7.21}, {63, 10.27}, {100, 14.31}}

ListPlot[MyData, Joined → False]
```
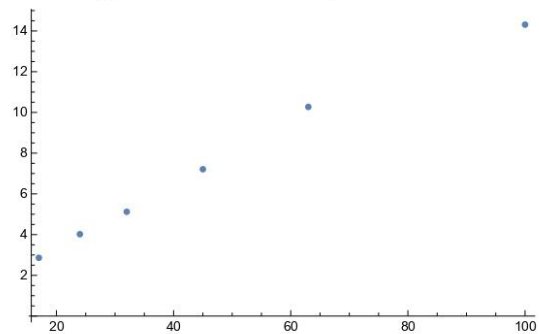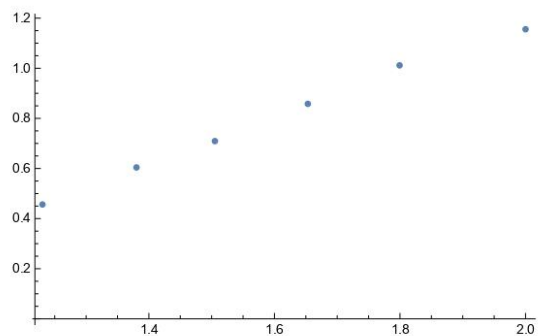


```
TRUEDATA = Log[10, MyData]
```

$$\left\{\left\{\frac{Log[17]}{Log[10]}, 0.456366\right\}, \left\{\frac{Log[24]}{Log[10]}, 0.604226\right\}, \left\{\frac{Log[32]}{Log[10]}, 0.70927\right\},\right.$$
$$\left.\left\{\frac{Log[45]}{Log[10]}, 0.857935\right\}, \left\{\frac{Log[63]}{Log[10]}, 1.01157\right\}, \{2, 1.15564\}\right\}$$
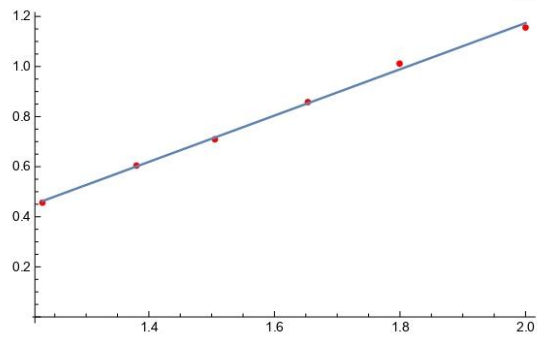
```
ListPlot[TRUEDATA]
```



```
FindFit[TRUEDATA, (m * x) + c, {m (1), c}, x]
{m → 0.923888, c → -0.674182}
```

```
Show[ListPlot[TRUEDATA, PlotStyle → Red],
  Plot[m x + c /. {m → 0.923888, c → -0.674182}, {x, Log[17]/Log[10], 2}]]
```

Appendix E:

The procedure of TPC data fitting

Nonlinear Curve Fit (ExpDec1) (06-04-2022 14:47:07)
Parameters

		Value	Standard Error
fitTernary C8	y0	-0.01428	0.00127
	A1	1.03109	9.04149E-4
	t1	1.12616	0.00367
	k	0.88797	0.00289
	tau	0.7806	0.00254

Reduced Chi-sqr = 3.07079713854E-5
COD(R^2) = 0.99936099478238
Iterations Performed = 4
Total Iterations in Session = 4
Fit converged. Chi-Sqr tolerance value of 1E-9 was reached.
k, tau are derived parameter(s).

Statistics

	fitTernary C8
Number of Points	1110
Degrees of Freedom	1107
Reduced Chi-Sqr	3.0708E-5
Residual Sum of Squares	0.03399
Adj. R-Square	0.99936
Fit Status	Succeeded(100)

Fit Status Code :
100 : Fit converged. Chi-Sqr tolerance value of 1E-9 was reached.

Summary

	y0		A1		t1		k	tau	Statistics	
	Value	Standard Error	Value	Standard Error	Value	Standard Error	Value		Reduced Chi-Sqr	Adj. R-Square
fitTernary C8	-0.01428	0.00127	1.03109	9.04149E-4	1.12616	0.00367	0.88797	0.7806	3.0708E-5	0.99936

ANOVA

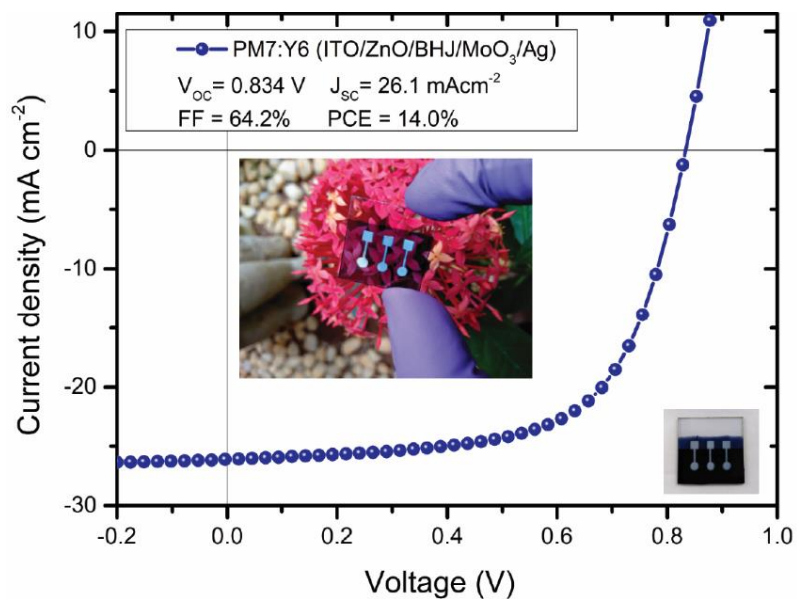|		DF	Sum of Squares	Mean Square	F Value	Prob>F
fitTernary C8	Regression	3	215.34031	71.7801	2.33751E6	0
	Residual	1107	0.03399	3.0708E-5		
	Uncorrected Total	1110	215.3743			
	Corrected Total	1109	53.19788			

Fitted Curves Plot
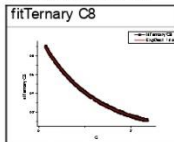
Residual vs. Independent Plot
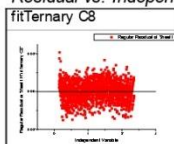
Figure.F.1. Typical J-V characteristics of a champion PM7:Y6 BHJ organic solar cell under simulated AM1.5G (100 mW/cm^2) illumination (inset show the devices).

Figure.F.2. Photograph of a typical organic solar cell fabricated in our laboratory highlights the semitransparency feature of the BHJ thin film.